



# *The Journal of* Gemmology

Volume 38 / No. 5 / 2023



Imperial Crown of  
the Holy Roman  
Empire (Part 1)

Cobalt-bearing  
Spinel from  
Tanzania

Nephrite Jade  
from Washington  
State, USA

Copper Minerals  
in Chalcedony  
from Indonesia



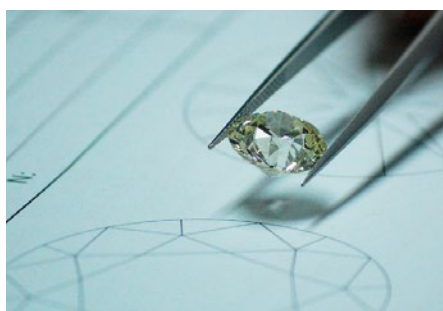
SCHWEIZERISCHES GEMMOLOGISCHES INSTITUT  
SWISS GEMMOLOGICAL INSTITUTE  
INSTITUT SUISSE DE GEMMOLOGIE



ORIGIN DETERMINATION · TREATMENT DETECTION

DIAMOND GRADING · PEARL TESTING

EDUCATION · RESEARCH



THE SCIENCE OF GEMSTONE TESTING™



## COLUMNS

### What's New

417

Big Sherlock Diamond Detector | Gemtrue Arete Synthetic Diamond Tester | Geospatial Analysis of Afghanistan's Gem Production | GIT Lab Note on Purplish Orange Dumortierite | Gold Demand Trends 2022 | *Grassroots Research on Local Diamond Mining Impact* Project | JNA's *Gemsworld* 2023 | *The Journal's* Cumulative Index and Bibliography Lists Updated | Laboratory-grown Diamond Market Research Report | Gem Connection Podcasts | Vicenzaoro 2022 Presentations

### Gem Notes

420

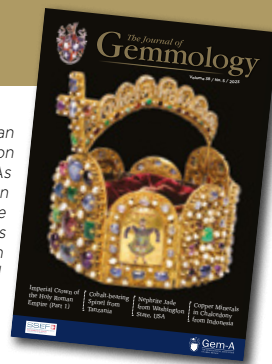
Amethyst/Carnelian Association from Madagascar | Aquamarine Crystal with Large Mobile Bubble | Rhodonite from Washington State, USA | Talc Chinese Seal Stone | Native Copper Inclusions in Cu-Bearing Tourmaline | Photochromism and Phosphorescence of Tugtupite | Diamond with Mobile Diamond Inclusion | Reddish Orange Diamond Coloured by Hematite | CVD-Grown Diamond with Unusual Fluorescence Colour Appearance | Pink-Orange CVD-grown Synthetic Diamonds with Ni Impurities | Treated Orange Pink HPHT-grown Synthetic Diamond with 776.4 nm PL Peak | Tin Glass-filled Ruby | Reconstructed Turquoise Imitation

442



Photo by Huixin Zhao

**Cover photo:** The Imperial Crown of the Holy Roman Empire dates to the High Middle Ages, and is on display at the Imperial Treasury Vienna in Austria. As part of an interdisciplinary research project, an article on pp. 448-473 of this issue focuses on the spectroscopic study of its gemstones. The crown's dimensions are 24.4 cm tall and up to 28.6 cm in diameter. Photo © KHM-Museumsverband (Christian Mendez); reproduced with permission.



## ARTICLES

### The Imperial Crown of the Holy Roman Empire, Part I: Photoluminescence and Raman Spectroscopic Study of the Gemstones

448

By Lutz Nasdala, Teresa Lamers, H. Albert Gilg, Chutimun Chanmuang N., Martina Griesser, Franz Kirchweiger, Annalena Erlacher, Miriam Böhmeler and Gerald Giester

### Cobalt-bearing Blue Spinel from Lukande, near Mahenge, Tanzania

474

By Michael S. Krzemnicki, Alex Leuenberger and Walter A. Balmer

### Nephrite Jade from Washington State, USA, Including a New Variety Showing Optical Phenomena

494

By Jean-Pierre Jutras, Cara Williams, Bear Williams and George R. Rossman

### Copper Minerals in Chalcedony from Obi Island, Indonesia

512

By Joel Ivey and Brendan M. Laurs

477



Photo by A. Leuenberger

518



Courtesy of Bud Standley

### Conferences

522

AGA Tucson Conference

### Learning Opportunities

528

### Gem-A Notices

524

### New Media

532

The Journal is published by Gem-A in collaboration with SSEF.



**Gem-A**  
THE GEMMOLOGICAL ASSOCIATION  
OF GREAT BRITAIN



# The Journal of Gemmology

## EDITORIAL STAFF

Editor-in-Chief  
**Brendan M. Laurs**  
brendan.laurs@gem-a.com

Executive Editor  
Alan D. Hart

Editorial Assistant  
**Carol M. Stockton**

Editor Emeritus  
**Roger R. Harding**

## ASSOCIATE EDITORS

**Ahmadjan Abduriyim**  
Tokyo Gem Science LLC,  
Tokyo, Japan

**Raquel Alonso-Perez**  
Harvard University,  
Cambridge, Massachusetts,  
USA

**Edward Boehm**  
RareSource, Chattanooga,  
Tennessee, USA

**Maggie Campbell Pedersen**  
London

**Alan T. Collins**  
King's College London

**Alessandra Costanzo**  
National University of  
Ireland Galway

**John L. Emmett**  
Crystal Chemistry, Brush  
Prairie, Washington, USA

**Emmanuel Fritsch**  
University of Nantes,  
France

**Rui Galopim de Carvalho**  
Gem Education Consultant,  
Lisbon, Portugal

**Al Gilbertson**  
Gemological Institute  
of America, Carlsbad,  
California

**Lee A. Groat**  
University of British  
Columbia, Vancouver,  
Canada

**Thomas Hainschwang**  
GGTL Laboratories,  
Balzers, Liechtenstein

**Henry A. Hänni**  
GemExpert, Basel,  
Switzerland

**Jeff W. Harris**  
University of Glasgow

**Alan D. Hart**  
Gem-A, London

**Ulrich Henn**  
German Gemmological  
Association, Idar-Oberstein

**Jaroslav Hyršl**  
Prague, Czech Republic

**Brian Jackson**  
National Museums  
Scotland, Edinburgh

**Mary L. Johnson**  
Mary Johnson Consulting,  
San Diego, California, USA

**Stefanos Karamelas**  
Laboratoire Français de  
Gemmologie, Paris, France

**Lore Kiefert**  
Dr. Lore Kiefert Gemmology  
Consulting, Heidelberg,  
Germany

**Hiroshi Kitawaki**  
Central Gem Laboratory,  
Tokyo, Japan

**Michael S. Krzemnicki**  
Swiss Gemmological  
Institute SSEF, Basel

**Shane F. McClure**  
Gemological Institute  
of America, Carlsbad,  
California

**Jack M. Ogden**  
London

**Federico Pezzotta**  
Natural History Museum  
of Milan, Italy

**Gérard Panczer**  
Claude Bernard University  
Lyon 1, France

**Jeffrey E. Post**  
Smithsonian Institution,  
Washington DC, USA

**George R. Rossman**  
California Institute of  
Technology, Pasadena, USA

**Karl Schmetzer**  
Petershausen, Germany

**Dietmar Schwarz**  
Bellerophon Gemlab,  
Bangkok, Thailand

**Menahem Sevdemish**  
Gemwizard Ltd, Ramat  
Gan, Israel

**Andy H. Shen**  
China University of  
Geosciences, Wuhan

**Guanghai Shi**  
China University of  
Geosciences, Beijing

**James E. Shigley**  
Gemological Institute  
of America, Carlsbad,  
California

**Christopher P. Smith**  
American Gemological  
Laboratories Inc.,  
New York, New York

**Elisabeth Strack**  
Gemmologisches Institut  
Hamburg, Germany

**Tay Thye Sun**  
Far East Gemological  
Laboratory, Singapore

**Frederick 'Lin' Sutherland**  
Port Macquarie, New  
South Wales, Australia

**Pornsawat Wathanakul**  
Kasetsart University,  
Bangkok, Thailand

**Chris M. Welbourn**  
Reading, Berkshire

**Bear Williams**  
Stone Group Laboratories  
LLC, Jefferson City,  
Missouri, USA

**J. C. (Hanco) Zwaan**  
Naturalis Biodiversity  
Center, Leiden,  
The Netherlands



21 Ely Place  
London EC1N 6TD  
UK

t: + 44 (0)20 7404 3334  
f: + 44 (0)20 7404 8843  
e: [information@gem-a.com](mailto:information@gem-a.com)  
w: <https://gem-a.com>

Registered Charity No. 1109555  
A company limited by guarantee and  
registered in England No. 1945780  
Registered office: Palladium House,  
1-4 Argyll Street, London W1F 7LD

## PRESIDENT

Richard Drucker

## VICE PRESIDENTS

David J. Callaghan  
Alan T. Collins  
Nigel Israel

## HONORARY FELLOWS

Gaetano Cavalieri  
Terrence S. Coldham  
Richard Drucker  
Emmanuel Fritsch

## HONORARY DIAMOND MEMBER

Martin Rapaport

## CHIEF EXECUTIVE OFFICER

Alan D. Hart

## COUNCIL

Justine L. Carmody – Chair  
Nevin Bayoumi-Stefanovic  
Maggie Campbell Pedersen  
Kate Flitcroft  
Joanna Hardy  
Philip Sadler  
Pia Tonna

## BRANCH CHAIRMEN

Midlands – Craig O'Donnell  
North East – Mark W. Houghton  
North West – Liz Bailey  
South West – Rachael Boothroyd

## COVERED BY THE FOLLOWING ABSTRACTING AND INDEXING SERVICES:

Clarivate Analytics' (formerly Thomson Reuters/ISI) Science Citation Index Expanded (in the Web of Science), Journal Citation Reports (Science Edition) and Current Contents (Physical, Chemical and Earth Sciences); Elsevier's Scopus; Australian Research Council's Excellence in Research for Australia (ERA) Journal List; China National Knowledge Infrastructure (CNKI Scholar); EBSCO's Academic Search Ultimate; ProQuest (Cambridge Scientific Abstracts); GeoRef; CrossRef; Chemical Abstracts (CA Plus); Mineralogical Abstracts; Index Copernicus ICI Journals Master List; Gale Academic OneFile; British Library Document Supply Service; and Copyright Clearance Center's RightFind application.



## CONTENT SUBMISSION

The Editor-in-Chief is glad to consider original articles, news items, conference reports, announcements and calendar entries on subjects of gemmological interest for publication in *The Journal of Gemmology*. A guide to the various sections and the preparation of manuscripts is given at <https://gem-a.com/membership/journal-of-gemmology/submissions>, or contact the Editor-in-Chief.

## SUBSCRIPTIONS

Gem-A members receive *The Journal* as part of their membership package, full details of which are given at <https://gem-a.com/membership>. Laboratories, libraries, museums and similar institutions may become direct subscribers to *The Journal*; download the form from *The Journal's* home page.

## ADVERTISING

Enquiries about advertising in *The Journal* should be directed to [advertising@gem-a.com](mailto:advertising@gem-a.com). For more information, see <https://gem-a.com/component/edocman/media-kit>.

## COPYRIGHT AND REPRINT PERMISSION

For full details of copyright and reprint permission contact the Editor-in-Chief. *The Journal of Gemmology* is published quarterly by Gem-A, The Gemmological Association of Great Britain. Any opinions expressed in *The Journal* are understood to be the views of the contributors and not necessarily of the publisher.

## DESIGN & PRODUCTION

Zest Design, London. <http://www.zest-uk.com>

## PRINTER

Park Communications Ltd, London.  
<http://www.parkcom.co.uk>



© 2023 Gem-A (The Gemmological Association of Great Britain)  
ISSN 1355-4565 (Print), ISSN 2632-1718 (Online)



# What's New

## INSTRUMENTATION

### Big Sherlock Diamond Detector

New from Yehuda in September 2022, the Big Sherlock has the same detection-rate technology as the Sherlock Holmes 2.0 (see *The Journal*, Vol. 38, No. 3, 2022, p. 213). In addition, however, it can check up to 108 rings at a time or about 1,000 carats of loose diamonds, utilising a larger visible checking area of  $20 \times 30 \times 10$  cm. An app is available, and with cloud-based storage the results can be accompanied by photos, certificate SKUs and more. A USD10/month subscription fee (covering all Yehuda detectors) comes with updates and storage for about 1,000 test results. Visit <https://www.yehuda.com/big-sherlock>.



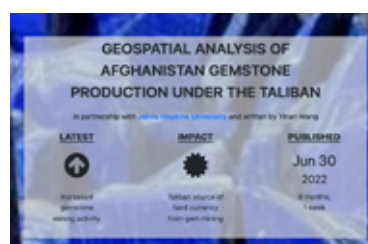
### Gemtrue Arete Synthetic Diamond Tester

Arete is the newest synthetic diamond tester from Gemtrue, released in February 2023. It is designed to distinguish between natural and synthetic diamonds (CVD and HPHT), as well as synthetic moissanite and other simulants. It can be used with both loose and mounted samples (in closed- or open-backed settings), as small as 0.2 ct and in the D-to-J colour range. The unit measures  $192 \times 42 \times 21$  mm, with a colour touch screen and retractable probe. Test results are displayed on the screen, as well as audible. Visit <https://www.gemtrue.com/products/dk10200-gemtrue-arete>.

## NEWS AND PUBLICATIONS

### Geospatial Analysis of Afghanistan's Gem Production

A June 2022 online report, which is available at [https://www.tearline.mil/public\\_page/geospatial-analysis-of-afghanistan-gemstone-production-under-the-taliban/](https://www.tearline.mil/public_page/geospatial-analysis-of-afghanistan-gemstone-production-under-the-taliban/), examines the status of gem production in Afghanistan following the Taliban's takeover. The report was prepared for Tearline—a non-profit group partnered with the U.S. National Geospatial-Intelligence Agency to provide information to the public about under-reported areas worldwide—in conjunction with Johns Hopkins University, Maryland, USA. Based on geospatial analysis, four major gem-mining areas (Sar-e Sang, Panjshir, Dara-e-Pech



and Mawi/Nilaw) show signs of active mining or newly constructed infrastructure, and only one area (Paprok) does not display any signs of recent activity. There are no indications of increased military activity in any of these areas. Material from Afghanistan continues to reach world markets via Pakistan.

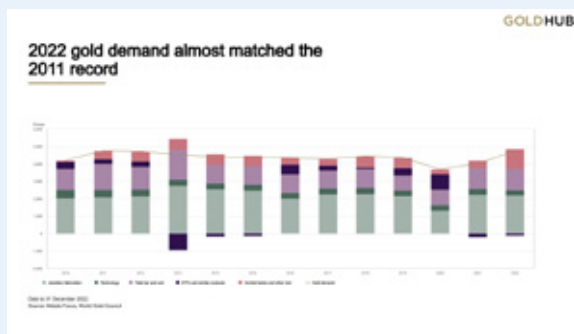
## GIT Lab Note on Purplish Orange Dumortierite

In January 2023, the Gem and Jewelry Institute of Thailand's Gem Testing Laboratory reported on a faceted 0.24 ct dumortierite that was purplish orange rather than showing typical blue colouration. The stone had RIs of 1.684–1.724 (birefringence = 0.040) and an SG value of 3.37, consistent with data previously reported for dumortierite. The report also includes EDXRF chemical data, as well as Raman and UV-Vis-NIR spectra. It can be downloaded at <https://git.or.th/en/information-service/27/76/detail/2419>.



## Gold Demand Trends 2022

In January 2023, the World Gold Council issued its annual full-year Gold Demand Trends report, which



covers 2022 and the fourth quarter of 2021. Notably, 2022 was the strongest year for gold demand in more than a decade, rising 18%. However, due in part to higher gold prices, jewellery use for 2022 was down 3% from the previous year, with a particularly steep decline in China that was offset by the rest of the world. Total annual supply rose 2%, with mine production at a four-year high. Visit <https://www.gold.org/goldhub/research/gold-demand-trends/gold-demand-trends-full-year-2022>, to read a summary or download more detailed reports after creating an account and signing in.

## Grassroots Research on Local Diamond Mining Impact Project

During the first half of 2022, the Kimberley Process Civil Society Coalition released a series of 2021–2022 reports on human rights and the socio-economic and environmental impact of diamond mining in seven African countries: Cameroon, Central African Republic, Côte d'Ivoire, Democratic Republic of Congo, Guinea, Lesotho and Sierra Leone. Download an executive summary or a full report (in English and/or French) for each country at <https://tinyurl.com/bp63tdck>.



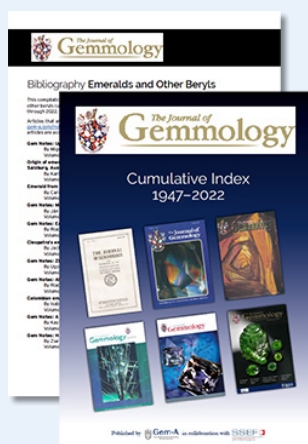
## JNA's Gemsworld 2023



The 2023 issue of JNA's *Gemsworld* publication was released in January, with articles covering market trends and demand forecasts for coloured stones and jewellery, the International Colored Gemstone Association, Greenland ruby, laboratory-grown emeralds, Miranda

Group's business strategy and mine-to-market initiatives. Download the 48-page publication at <https://tinyurl.com/2p9y73v5>.





## The Journal's Cumulative Index and Bibliography Lists Updated

*The Journal of Gemmology's* cumulative index and subject bibliographies have been updated to cover all issues since its inception in 1947 through 2022. All are available as PDF files which can be searched for specific authors, as well as topics. The subject bibliographies cover articles and notes published in *The Journal* on the following topics: asterism and chatoyancy, biogenic gems, chrysoberyl and alexandrite, colour-change gems, corundum, diamond, emerald and other beryls, feldspar, garnet, historical gems and jewels, jade and jade-like materials, opal, pearl, quartz-family gems, spinel and tourmaline. Download the PDFs at <https://gem-a.com/membership/journal-of-gemmology>.

## Laboratory-grown Diamond Market Research Report

In December 2022, USA-based market-research group The MVEye released its *Global Voices* international laboratory-grown diamond consumer and trade market research report. This study (the third in a series headed by the International Grown Diamond Association) included 1,200 consumers in Canada and the USA, and 178 retailers in Australia, Canada, the European Union, New Zealand, the United Kingdom and the USA. The results indicate that growth in consumer demand for synthetic diamonds has started to impact the market for natural ('mined') diamonds. The main reason given



for the appeal of synthetics is their price, but the report also describes other factors. Of the retailers included in the study, 72% sell laboratory-grown diamonds. The full report is available for purchase at <https://www.themveye.com/premium-reports.php>.

## OTHER RESOURCES

### Gem Connection Podcasts



Since December 2020, Gem Connection podcasts hosted by Susan Thornton have been available on Spotify. The most recent ones (February 2023) focus on laboratory-grown diamonds, and previous episodes cover historical topics, jewellery designers and more. Visit <https://open.spotify.com/show/7kIAVQ1DLfRE5OcWufdUNZ>.

Brendan M. Laurs

### Vicenzaoro 2022 Presentations

Videos of presentations and panel discussions at the September 2022 Vicenzaoro show are available at <https://tinyurl.com/cjd4rxs3> (in English and Italian). Topics are wide-ranging and include gem carving, retail strategies, gem and design trends, supply chain regulations, and vintage and antique jewellery.



**What's New** provides announcements of new instruments/technology, publications, online resources and more. Inclusion in What's New does not imply recommendation or endorsement by Gem-A. Entries were prepared by Carol M. Stockton unless otherwise noted.

# Gem Notes

## COLOURED STONES

### Unusual Amethyst and Carnelian Association from Madagascar

Amethyst has long been a popular gem material, and carnelian—or orange chalcedony—has also been known for centuries. In December 2022, while visiting the gem and mineral market in Antsirabe, Madagascar, author FR encountered some unusual faceted stones that were a combination of amethyst and carnelian. The parcel consisted of about 30 gemstones with a total weight of about 380 carats (4.80–47.05 ct each). The rough material was reportedly produced at an underground quartz mine located in the Ambatofinandrahna area of the Amoron'i Mania region in central Madagascar, where it was extracted from a small pocket in an amethyst vein. At the time of writing, this pocket was the only one of this material discovered there, and the mining operations had temporarily ceased due to the rainy season.

Five representative gemstones were selected from the parcel for testing (Figure 1). The amethyst portions contained various internal features, including irregular fissures, partially healed fractures, and in some cases colour zoning that followed the rhombohedral growth directions, as is typical for macro-crystalline quartz. The carnelian areas appeared quite homogeneous or displayed banded colouration that was typically aligned parallel to the rhombohedral growth directions of the adjacent amethyst. However, with increasing distance from the amethyst, the angles of the banding softened and appeared more like curves. This suggests that the carnelian formed after the amethyst, filling residual space around the amethyst crystals.

Microscopic examination of the amethyst revealed many short, brush-like bundles or tufts with the appearance of goethite (Figure 2). The base of each tuft was most often aligned on the same plane as the others, and they radiated towards the outward faces of the amethyst crystal. Some of these brush-like inclusions could also be observed in what looked like carnelian, but they were, in fact, hosted by colourless or pale-coloured



**Figure 1:** An unusual association of amethyst with carnelian shows various colour patterns in these five faceted gemstones that were examined for this report (8.15–46.85 ct). Composite photo by F. Rossetto.

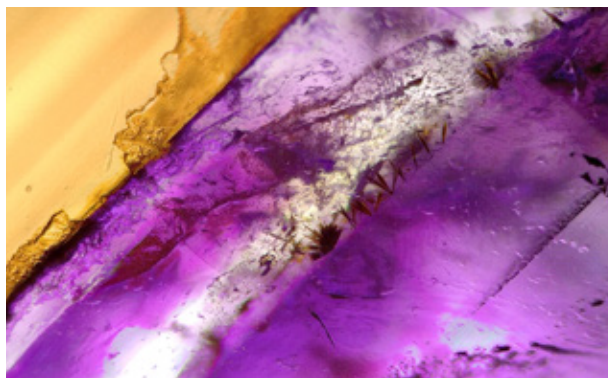


**Figure 2:** Internal features seen at the amethyst-carnelian boundary consist of colour zoning in both materials and tufts (about 0.1 mm long) with the appearance of goethite along a layer in the amethyst. Photomicrograph by T. Cathelineau; image width 2.8 mm in transmitted light.



**Table I:** Gemmological properties of five faceted samples of amethyst-carnelian from Madagascar.

Property	Amethyst portion	Carnelian portion
Colour	Pale to strong purple	Orange to red-orange, sometimes light brownish orange
Pleochroism	Weak; shades of purple	None
Diaphaneity	Almost always transparent	Translucent
RIs	1.544-1.553	1.535-1.539
Birefringence	0.009	0.004
Optic character	Uniaxial positive	Could not be determined
Chelsea Colour Filter	Dark grey	Red
Polariscope	Alternates dark and light four times through 360° rotation (anisotropic), with some anomalous extinction	Stays light through 360° rotation (polycrystalline)
Lustre	Vitreous	
Magnetism	No reaction to N52 neodymium magnet	
Fluorescence	Inert to long- and short-wave UV radiation	
Hydrostatic SG	2.50 (carnelian predominant) to 2.62 (amethyst predominant)	

quartz zones surrounded by carnelian, which gave the impression they were within the latter. In addition, a few black, round platelets were seen in the amethyst, and numerous tiny, orange, round platelets were present in the banded areas of the carnelian. These platelets were likely iron compounds, possibly hematite. Along the boundary with the amethyst, the carnelian was slightly undercut during the faceting process.

Gemmological properties obtained from the five samples are summarised in Table I, and are consistent with those previously reported for amethyst and carnelian (cf. O'Donoghue 2006; Boulliard 2015; AFG 2021). The unusual combination of these gem materials in the same faceted stones resulted in a rather striking overall appearance.

*Franck Rossetto FGA (contact@wg-company.com)  
Vitrolles, France*

*Thierry Cathelineau  
Paris, France*

## References

- AFG (ed) 2021. *Gemmes*, 4th edn. Association Française de Gemmologie, Paris, France, 270 pp.
- Boulliard, J.-C. 2015. *Pierres Précieuses: Guide Pratique d'Identification / Precious Stones: Practical Identification Guide*. Publibook, Paris, France, 384 pp.
- O'Donoghue, M. (ed) 2006. *Gems*, 6th edn. Butterworth-Heinemann, Oxford, 873 pp.

## Aquamarine Crystal Containing a Large Multiphase Inclusion with a Mobile Bubble

Large fluid inclusions with mobile gas bubbles, sometimes accompanied by movable solids, are rarely encountered and intriguing internal features in some gem materials, especially quartz. Dr Edwin Roedder summarised the rarity of such 'bubble crystals' in the *Photoatlas of Inclusions in Gemstones* (Gübelin & Koivula 1986, p. 62): 'For every such large inclusion in nature there are untold billions of very small fluid inclusions, however, only visible with a microscope.'

Recently, the authors examined a spectacular aquamarine crystal (Figure 3) with a very large multiphase inclusion. It was shown to the authors by Alexander Kreis

(Kreis Jewellery GmbH & Co. KG, Niederwörresbach, Germany) during the September 2022 Intergem show in Idar-Oberstein, Germany. The crystal was reportedly from Marambaia, Brazil, and consisted of a transparent greenish blue doubly-terminated hexagonal prism that weighed 155.77 g and measured 119.1 × 29.1 × 21.9 mm. The prism faces showed distinct striations, as are sometimes seen on beryl crystals.

The aquamarine contained a large multiphase inclusion that extended along approximately one-half of the crystal (Figures 3 and 4). It encapsulated an elongated cavity measuring approximately 52 × 19.5 mm,



**Figure 3:** The aquamarine crystal described here measures  $119.1 \times 29.1 \times 21.9$  mm and weighs 155.77 g. A large multiphase inclusion is visible at lower left, starting at the base of the brownish area. Photo by Q. Wang.

oriented parallel to the *c*-axis, which started at a growth plane and tapered to a point at its other end. It contained a large bubble that moved freely as the crystal was rocked and tilted, and this gaseous inclusion could be ‘broken’ into two bubbles as it passed by an irregularity near the cavity’s wider end. A video showing the movement of the bubble inside the inclusion is available at <https://blog.dgemg.com/forschung/2-uncategorised/105-beryll-mehrphaseneinschluss.html>. The cavity also contained many dark, slightly brownish, dust-like solid particles, which were also movable. However, it was not possible to capture a photo or video of these solids due to the pronounced striations on the crystal’s surface. Next to the large

cavity was another, smaller multiphase inclusion, also with a movable bubble.

Another aquamarine crystal with a large fluid inclusion containing a mobile gas bubble was described recently by Laurs (2020). This note cited Kesler *et al.* (2013, p. 398), who mentioned perhaps the first documentation of such inclusions in beryl (translated from German by Albert Gilg):

In the 13th century...Albertus Magnus, a German medieval scholar and Archbishop of Cologne, wrote a book on lapidary (*‘de mineralibus’*) with a note on fluid inclusions in beryl, that states ‘Beryl is a shining and transparent gemstone of pale colour. The most precious kind is the one, in which you see water moving when you turn him’.

The fluid phase in the crystal described here was indeed water, as identified by Raman spectroscopy. Raman analysis of the gaseous phase, however, gave no signal.

Beryl from granitic pegmatites commonly contains fluid inclusions, especially as elongated two-phase inclusions oriented parallel to the *c*-axis. Sunagawa and Urano (2000), and also Sunagawa (2005), attributed their formation to growth-dissolution-regrowth processes controlled by variations in the supply and composition of the pegmatitic fluids. When crystal growth in the direction of the *c*-axis is blocked by impurities, then cavities (negative crystals) can form behind these particles, which encapsulate the pegmatitic fluid. During cooling, such fluids lose volume, and a contraction bubble forms.

For crystal collectors, the aquamarine specimen described here is itself highly desirable, but the presence of a large multiphase inclusion makes it exceptional. Fortunately, even though much of this aquamarine is of facetable quality, it will be kept in its natural state as a crystal.

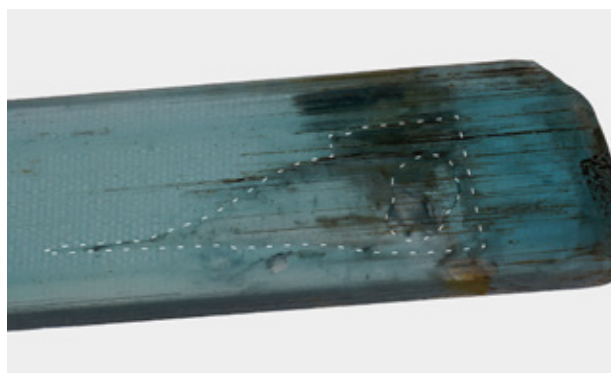


**Figure 4:** The shape of the multiphase inclusion is outlined here with the aquamarine crystal immersed in water. The inclusion measures  $52 \times 19.5$  mm, and the bubble (also outlined) is nearly 10 mm long. Photo by T. Stephan.



Dr Tom Stephan (t.stephan@dgemg.com)  
 German Gemmological Association  
 Idar-Oberstein, Germany

Stefan Müller  
 DSEF German Gem Lab  
 Idar-Oberstein, Germany

## References

- Gübelin, E.J. & Koivula, J.I. 1986. *Photoatlas of Inclusions in Gemstones*. ABC Edition, Zurich, Switzerland, 532 pp.
- Kesler, S.E., Bodnar, R.J. & Mernagh, T.P. 2013. Role of fluid and melt inclusion studies in geologic research. *Geofluids*, **13**(4), 398–404, <https://doi.org/10.1111/gfl.12055>.
- Laurs, B.M. 2020. Gem Notes: Aquamarine crystal with ‘enhydro’ inclusion from Brazil. *Journal of Gemmology*, **37**(3), 235–237.
- Sunagawa, I. 2005. *Crystals: Growth, Morphology, & Perfection*. Cambridge University Press, New York, New York, USA, 308 pp.
- Sunagawa, I. & Urano, A. 2000. Beryl crystals from pegmatites: Morphology and mechanism of crystal growth. *Journal of Gemmology*, **26**(1), 521–533, <https://doi.org/10.15506/JoG.1999.26.8.521>.

## A New Occurrence of Rhodonite Associated with Nephrite Jade in Washington State, USA

Gem- and ornamental-quality massive rhodonite ( $\text{MnSiO}_3$ ) is commonly found in close association with nephrite jade, as seen at various localities such as north-western Canada (Simandl *et al.* 1999), Washington State (Ream 2022) and Italy (Diella *et al.* 2014). Recently, a new occurrence of rhodonite was discovered at Jade Leader Corp.’s DJ project in Washington (see the article on this nephrite deposit on pp. 494–511 of this issue).

This rhodonite occurrence was first recognised in the field by the author in 2017, leading to initial efforts at cutting and shaping the material to assess its workability and general attractiveness, and this yielded encouraging results. Further exploration in 2018 and 2019 defined two distinct but poorly exposed *in situ* occurrences of

rhodonite, with surface expressions measuring about  $4.1 \times 6.2$  m and  $2.2 \times 5.3$  m (e.g. Figure 5). These are located about 110 m apart and are hosted in a regional-scale serpentinite unit. Due to weathering and forested areas between these two surface showings, the level of continuity between them cannot be ascertained without further exploration work such as trenching.

In excess of 2,500 kg of rhodonite material has been extracted so far, for rough inventory as well as for cutting cabochons, beads and spheres (e.g. Figures 6 and 7). The extracted material consists of blocks of massive rhodonite ranging from 1–2 kg to more than 150 kg. In addition, a boulder with an estimated weight of 4,500 kg has been recovered, and is being assessed for use in a large sculptural work (Figure 8).



**Figure 5:** The surface expression of one of the two rhodonite outcrops found to date at the DJ project in Washington (shown here with the author) exhibits a typical black appearance due to staining by manganese oxide. Photo by J.-P. Jutras.



**Figure 6:** These rhodonite samples consist of a partially polished block (2.5 kg) with various cabochons and beads cut from the material. The round beads are 7.5–10.5 mm in diameter and the barrel-shaped beads are 13.5 × 12.5 mm. Photo by J.-P. Jutras.



**Figure 7:** This image provides a more detailed view of the cut-and-polished rhodonite (shown here resting on glass), consisting of a 2.3 × 1.8 cm cabochon and a 6.0 × 2.5 cm polished slab. Photo by J.-P. Jutras.

Several polished samples were examined for this report. The material consists of medium-grained polyminerallc aggregates that are dominantly pink to reddish pink (rhodonite) with some white-to-grey areas (calcite and quartz) and attractive black patterning (manganese oxides). No RI reading could be obtained with a refractometer (probably due to the mixture of minerals present), and the hydrostatic SG value obtained from four samples ranged from 3.02 to 4.01 (average 3.43), reflecting the varying amounts of accessory minerals. The material is inert to long- and short-wave UV radiation, and the Mohs hardness was determined to be 5½–6½. These properties are consistent with those of massive rhodonite (e.g. O'Donoghue 2006).

Further development of the deposit will take place according to market demand.

Jean-Pierre Jutras (jp@gold.ca)  
Jade Leader Corp.  
Calgary, Alberta, Canada



**Figure 8:** This large block was sliced from a rhodonite-bearing boulder weighing about 4,500 kg that was recovered at the DJ project. The material's carving potential is being evaluated for a life-size meditating female figure by international award-winning stone and jade sculptor Georg Schmerholz. Photo by J.-P. Jutras.

## References

- Diella, V., Adamo, I & Bocchio, R. 2014. Gem-quality rhodonite from Val Malenco (Central Alps, Italy). *Periodico di Mineralogia*, **83**(2), 207–221, <https://doi.org/10.2451/2014PM0012>.
- O'Donoghue, M. (ed) 2006. *Gems*, 6th edn. Butterworth-Heinemann, Oxford, 873 pp. (see pp. 443–444).
- Ream, L.R. 2022. *Nephrite Jade of Washington and Associated Gem Rocks: Their Origin, Occurrence and Identification*. LR Ream Publishing, Coeur d'Alene, Idaho, USA, 128 pp.
- Simandl, G.J., Paradis, S. & Nelson, J.L. 1999. Jade and rhodonite deposits, British Columbia, Canada. In: Bon, R.L., Riordan, R.F., Tripp, B.T. & Krukowski, S.T. (eds) *Proceedings of the 35th Forum on the Geology of Industrial Minerals – The Intermountain West Forum 1999*. Utah Geological Survey, Salt Lake City, Utah, USA, 163–171.

## A Chinese Seal Stone Consisting of Yellow Talc

Recently, a large yellow Chinese seal stone (Figure 9) was submitted to author TTS for testing among other yellow samples. This particular one weighed 1,592.5 g and measured 123.69 × 71.70 × 71.30 mm. It was soft

and had a waxy appearance and soapy feel, resembling what is known as *Tianhuang stone* in China (i.e. the kaolinite-group minerals dickite and/or nacrite; cf. Tay *et al.* 2017). It yielded a spot RI reading around 1.55,





**Figure 9:** (a) This large yellow Chinese seal stone (1,592.5 g) has scenic carvings on the four sides of the squarish block. (b) The base has Chinese characters and is stained red due to the ink used on the stamp pad. Photos by Tay Thye Sun.

which was slightly blurred due to the softness of the material. It fluoresced weak chalky blue to long-wave UV radiation, and was inert to short-wave UV. Under  $10\times$  magnification, the stone showed whitish cloud-like features (Figure 10a) typical of Tianhuang materials and some dark yellow veins (Figure 10b).

The RI was not diagnostic enough to identify the material, so a small amount of powder was extracted from inconspicuous areas on the sides of the specimen for further analysis. A pressed powder disc consisting of 150 mg potassium bromide and 1 mg powdered sample was prepared for Fourier-transform infrared (FTIR) spectroscopy. The sample was analysed with a Bruker Alpha FTIR spectrometer at the National University of

Singapore's Department of Pharmacy in the range of  $4000\text{--}400\text{ cm}^{-1}$  ( $4\text{ cm}^{-1}$  resolution). The transmittance spectrum showed a series of bands that provided a good match with a talc reference spectrum (Figure 11). According to the literature (Schroeder 2002; Blanchard *et al.* 2018), the sharp feature at  $3677\text{ cm}^{-1}$  is attributed to the stretching vibration of an O-H bond without a hydrogen bond, while the broad peak at about  $3440\text{ cm}^{-1}$  is due to a hydrogen-bonded O-H stretching vibration. The main IR absorption band at  $1019\text{ cm}^{-1}$  is due to an Si-O stretching vibration, and the band at  $670\text{ cm}^{-1}$  corresponds to O-H bending.

The same powdered sample of the seal stone was analysed by Raman spectroscopy using a Bruker

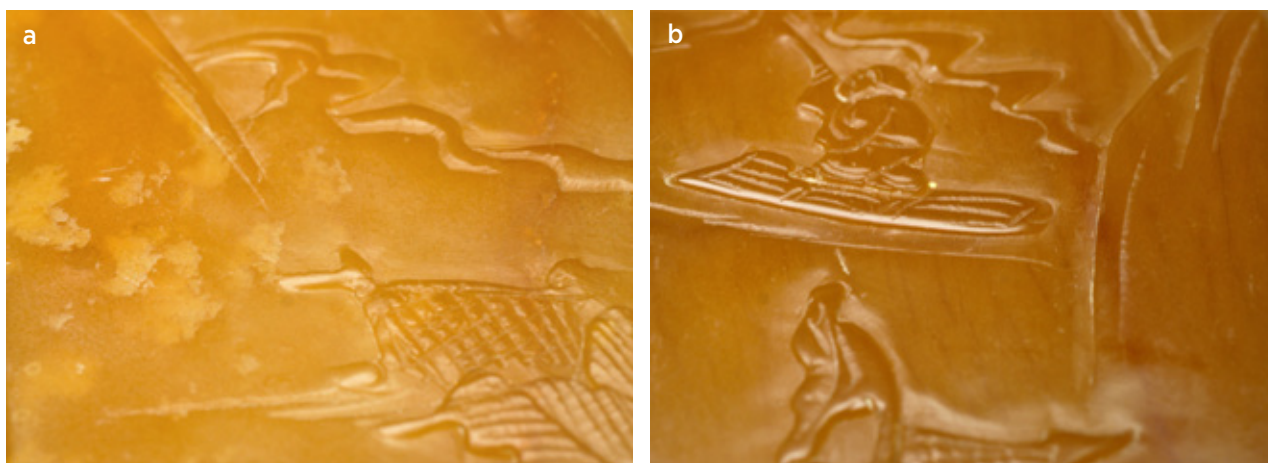


**Figure 10:** Magnification of the seal stone shows (a) whitish cloud-shaped features and (b) dark yellow veins. Photomicrographs by Tay Thye Sun; magnified  $10\times$ .

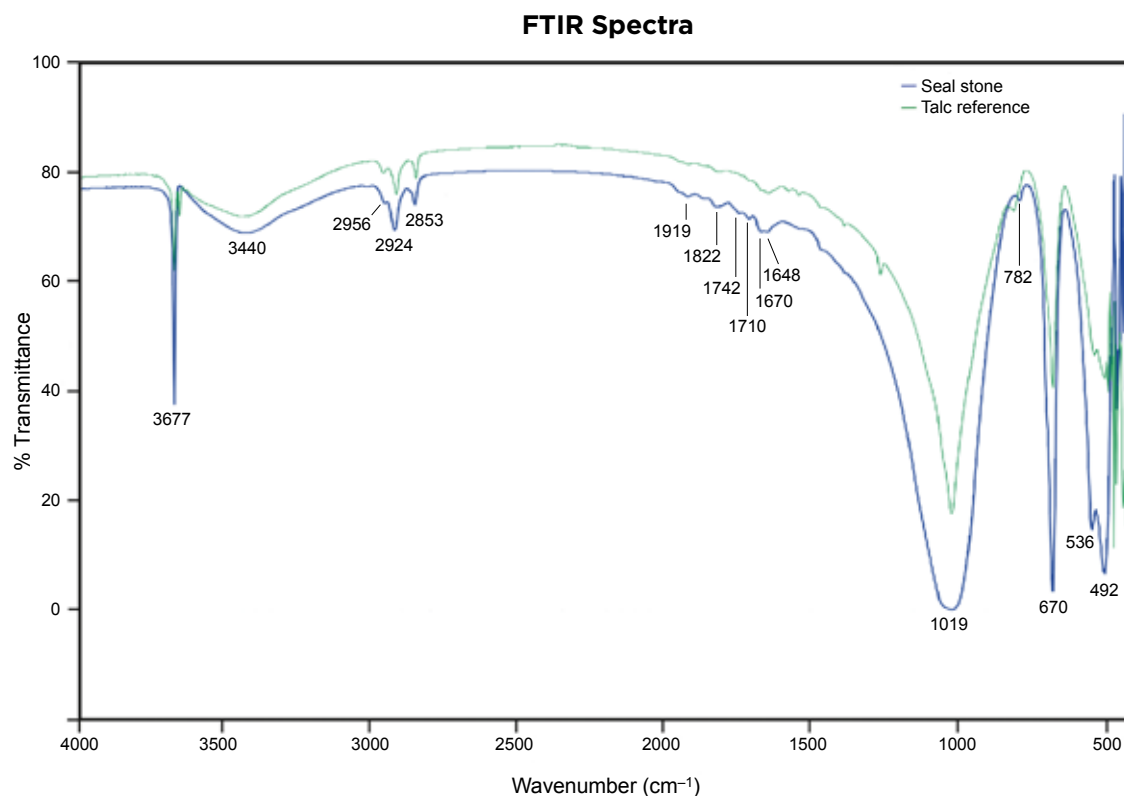


**Figure 11:** FTIR spectroscopy of a powdered sample of the seal stone reveals a good match to a powdered talc reference sample (steatite from Australia).

Senterra spectrometer equipped with a solid-state 532 nm Nd-YAG laser. We used a laser power of 20 mW, a measurement time of 100 s, an aperture of 50  $\mu\text{m}$  and a 50 $\times$  objective. Raman peaks at 677, 434, 364, 292, 196, 109 and 68  $\text{cm}^{-1}$  were recorded, which are typical for talc, as demonstrated by comparison to Raman spectra of two reference standards (talc 529 powder from the Mineralogy and Petrology section of the University of Basel, and talc R050087 from the RRUFF database; see

<https://rruff.info/talc/display=default/R050087>).

Although this yellow specimen looks very much like Tianhuang stone, it turned out to be talc. Our investigation showed that a combination of FTIR and Raman spectroscopy can unambiguously identify such agglomerated masses of layer silicates.

*Acknowledgement:* Many thanks to Bill Loh for allowing the yellow stone to be analysed and to Eng Chun Heng for technical assistance.

TAY Thye Sun FGA (tay@gem.com.sg)

Far East Gemological Laboratory  
Singapore

Prof. Dr Leander Franz  
Department of Environmental Sciences  
University of Basel, Switzerland

Prof. Dr Koh Hwee Ling  
National University of Singapore

LI Jianjun  
National Gold & Diamond Testing Center  
Shandong Institute of Metrology  
Shandong, China

## References

- Blanchard, M., Méheut, M., Delon, L., Poirier, M., Micoud, P., Le Roux, C. & Martin, F. 2018. Infrared spectroscopic study of the synthetic Mg-Ni talc series. *Physics and Chemistry of Minerals*, **45**(9), 843–854, <https://doi.org/10.1007/s00269-018-0966-x>.
- Schroeder, P.A. 2002. Infrared spectroscopy in clay science. In: Rule, A. & Guggenheim, S. (eds) *Teaching Clay Science*. Clay Minerals Society, Aurora, Colorado, USA, 182–206, <https://doi.org/10.1346/CMS-WLS-11>.
- Tay, T.S., Franz, L. & Li, J. 2017. Gem Notes: Tianhuang, an unusual yellow stone: Dickite or nacrite? *Journal of Gemmology*, **35**(6), 472–474.

## Further Characterisation of Native Copper Inclusions in Cu-Bearing Tourmaline

Native copper inclusions have been reported in Cu-bearing gem tourmaline from Paraíba State in Brazil since its discovery in the late 1980s (Fritsch *et al.* 1990). Similar native copper inclusions have been found in other gem materials, such as Oregon sunstone (labradorite feldspar; e.g. Badur 2022). However, the native copper inclusions in Oregon sunstone generally have a more uniform size and distribution than those in copper-bearing tourmaline. Native copper inclusions in tourmaline have been mentioned in the literature only occasionally, probably since they are rather rare (Fritsch *et al.* 1990; Koivula *et al.* 1992; Brandstätter & Niedermayr 1994; Hartley 2018).

Brandstätter and Niedermayr (1994) observed thin, flat, gold-coloured dendritic inclusions of native copper extending parallel to the *c*-axis of Paraíba tourmaline, with the copper clusters scattered irregularly through the host crystal. Previously, Koivula *et al.* (1992) proposed a growth scenario for this type of inclusion as epigenetic exsolution from the host Cu-bearing tourmaline. That is, the inclusions formed along fractures in the host crystal after its crystallisation, with the copper being derived from the tourmaline rather than being added from external sources. Brandstätter and Niedermayr (1994) found that the CuO concentration in Paraíba tourmaline decreased towards the native copper inclusions. Thus, they also proposed epigenetic exsolution formation as being more plausible than syngenetic precipitation of native copper at the growing tourmaline's surface.

Recently, the authors investigated a crystal fragment of Cu-bearing elbaite from Paraíba State (Figure 12). This yellowish green to bluish green sample was reportedly

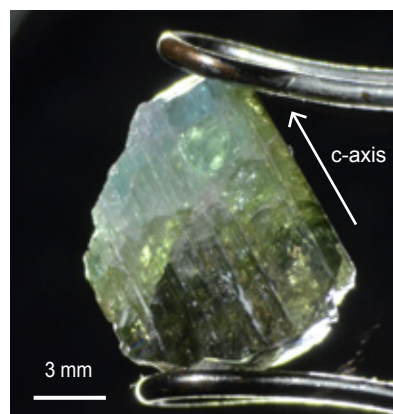


**Figure 12:** A crystal fragment of Cu-bearing elbaite, reportedly from Paraíba State in Brazil, was examined to study its copper-bearing inclusions. Photo by H. A. O. Wang.

untreated, and it contained up to 4,000 ppm Cu, as determined by laser ablation inductively coupled plasma time-of-flight mass spectrometry at SSEF. We observed numerous native copper inclusions in the sample (e.g. Figure 13a). The inclusions were clustered in a rather large planar area, and they showed mainly one orientation along the *c*-axis of the host tourmaline, with their planar surfaces being mostly parallel to one another. We also observed abundant transparent inclusions (Figure 13b) that showed a morphology and orientation similar to that of the native copper inclusions (e.g. Figure 14a). As far as we know, this type of transparent inclusion has not been reported previously in Cu-bearing tourmaline. We interpret these to be fluid inclusions because we occasionally observed round gas bubbles inside them.

To further characterise the native copper inclusions, we first used a focused ion beam scanning electron microscope (FIB-SEM) to expose the cross-section of one typical platelet inclusion. The backscattered electron

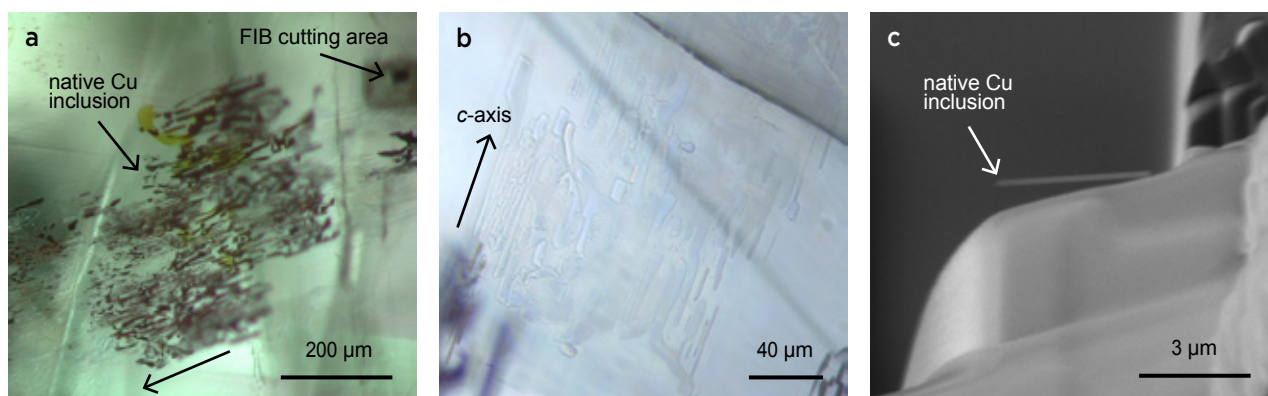


**Figure 13:** (a) A native copper inclusion in the tourmaline in Figure 12 is shown with an optical microscope using transmitted light. (b) Also present are occasional transparent inclusions with round gas bubbles and with a morphology similar to that of the native copper inclusions. (c) A backscattered electron (BSE) image of the cross-section of a native copper platelet shows a homogeneous thickness of about 150 nm. Photomicrographs by H. A. O. Wang and BSE image by D. Mathys.



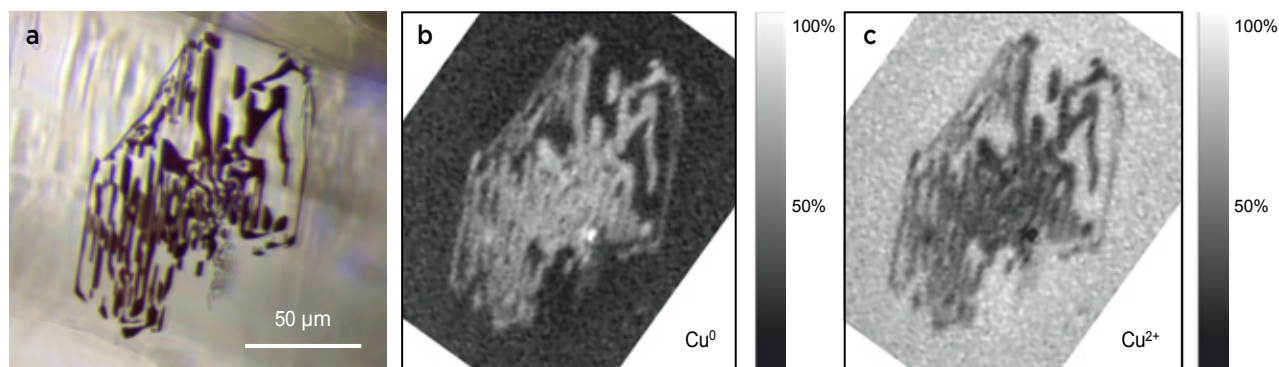


**Figure 14:** (a) Another native copper inclusion in the tourmaline in Figure 12 is seen here using an optical microscope with transmitted light. High-spatial-resolution redox maps of (b) metallic copper ( $\text{Cu}^0$ ) and (c) oxidised copper ( $\text{Cu}^{2+}$ ) are shown for the same view, and reveal that the inclusion consists of  $\text{Cu}^0$  rather than  $\text{Cu}^{2+}$ . The scale on the right side of each map indicates the ratio of the corresponding Cu speciation to the total amount of copper. Photomicrograph by H. A. O. Wang and redox maps by D. Grolimund.

image of this inclusion is shown in Figure 13c; it had a thickness of about 150 nm and measured about 3–4 μm long. Interestingly, its length:thickness ratio was greater than that of native copper platelets in Oregon sunstone (as estimated from figures 11 and 14 in Badur 2022). To our knowledge, the gold-coloured platelet inclusions in Paraíba tourmaline were previously assumed to be composed of native copper, but without direct analytical evidence. Using spatially resolved synchrotron radiation X-ray absorption spectroscopy (specifically, micro-XANES), we revealed the characteristic local oxidation state of copper in a typical platelet inclusion and also in the host tourmaline. The chemical and electronic contrast revealed by this method can depict the electronic state of Cu (i.e. via copper ‘redox maps’), including the distribution of metallic ( $\text{Cu}^0$ ) and oxidised ( $\text{Cu}^{2+}$ ) copper. Figure 14 shows these distributions for a typical inclusion located approximately 5 μm beneath the tourmaline’s surface. The metallic Cu distribution in the redox maps (Figure 14b, c) correlates with the shape of the inclusion in the photomicrograph (Figure 14a), and shows that the copper is present as  $\text{Cu}^0$ . These results are the first direct proof that the gold-coloured platelet inclusions in Cu-bearing Paraíba tourmaline consist of native copper in its metallic state.

Additional observations, especially the presence of fluid inclusions with a morphology similar to that of the native copper inclusions, suggest that epigenetic exsolution might not easily explain the formation of this type of native copper inclusion. Instead, syngenetic (epitaxial) growth of native copper during the formation of the host tourmaline seems a more likely scenario. Nevertheless, we cannot fully exclude the formation of such inclusions as thin-film dendritic fracture-fillings after the formation of the host tourmaline, with the native

copper being precipitated by fluid infiltration.

Further detailed research is ongoing to better understand these native copper inclusions in Brazilian Cu-bearing tourmaline. This study also demonstrates that cutting-edge micro-analytical methods new to gemmology (in this case, FIB-SEM and micro-XANES) have the potential to provide new insights to characterise gem materials and their formation.

Dr Hao A. O. Wang *FGA* ([gemlab@ssef.ch](mailto:gemlab@ssef.ch))  
Swiss Gemmological Institute SSEF  
Basel, Switzerland

Dr Daniel Grolimund  
microXAS Beamline, Swiss Light Source  
Paul Scherrer Institute, Villigen, Switzerland

Prof. Dr Leander Franz  
Department of Environmental Sciences  
University of Basel, Switzerland

Daniel Mathys  
Nano Imaging Lab, Swiss Nanoscience Institute  
University of Basel, Switzerland

Prof. Dr Rainer Schultz-Güttler  
Institute of Geosciences, University of São Paulo, Brazil

Dr Michael S. Krzemnicki *FGA*  
Swiss Gemmological Institute SSEF and  
Department of Environmental Sciences  
University of Basel, Switzerland

## References

- Badur, C.B. 2022. *An investigation of native copper in plagioclase, Lake and Harney Counties, Oregon*. Master’s thesis, Auburn University, Alabama, USA, 76 pp., <https://etd.auburn.edu/handle/10415/8200>.

Brandstätter, F. & Niedermayr, G. 1994. Copper and tenorite inclusions in cuprian-elbaite tourmaline from Paraíba, Brazil. *Gems & Gemology*, **30**(3), 178–183, <https://doi.org/10.5741/gems.30.3.178>.

Fritsch, E., Shigley, J.E., Rossman, G.R., Mercer, M.E., Muhlmeister, S.M. & Moon, M. 1990. Gem-quality cuprian-elbaite tourmalines from São José da Batalha,

Paraíba, Brazil. *Gems & Gemology*, **26**(3), 189–205, <https://doi.org/10.5741/gems.26.3.189>.

Hartley, A. 2018. Gem Notes: Native copper inclusions in a Cu-bearing tourmaline. *Journal of Gemmology*, **36**(3), 203.

Koivula, J.I., Kammerling, R.C. & Fritsch, E. 1992. Gem News: Tourmaline with distinctive inclusions. *Gems & Gemology*, **28**(3), 204.

## Photochromism and Phosphorescence of Tugtupite

Tugtupite belongs to the sodalite mineral group, with an ideal chemical formula of  $\text{Na}_4\text{BeAlSi}_4\text{O}_{12}\text{Cl}$ . It is named after its type locality at Tugtup Agtakôrfia in Greenland (Sørensen 1960). Tugtupite has been rarely used as a gem material since 1965 (Jensen & Petersen 1982). Almost all gem-quality tugtupite comes from the Taseq and Kvaneeld areas of the Ilímaussaq complex in Greenland. It is usually cut and polished into cabochons; faceted stones are seldom encountered due to the common presence of fractures and a distinct cleavage on {101}.

Tugtupite provides an example of a gem material that shows photochromism, meaning that it reversibly changes colour upon exposure to visible light or UV radiation (Blumentritt & Fritsch 2021). Specifically, it becomes dark red when exposed to UV radiation (or is irradiated by X-rays), and the colour fades to a paler red, pink or white when kept in the dark or exposed to bright light for a few minutes. This colour behaviour is probably due to an electron trapped in a Cl vacancy and associated sulphur polyanions (Blumentritt & Fritsch 2021).

Recently, the authors had an opportunity to examine a 1.76 ct faceted tugtupite. The stone had RIs of 1.497–1.500 (birefringence = 0.003), which is consistent with the literature (Jensen & Petersen 1982; Anthony *et al.* 1990). FTIR and Raman spectroscopy confirmed it was tugtupite. Microscopic observation revealed several colourless and irregular mineral crystals and fluid inclusions.

The stone was initially pink, and turned red immediately upon exposure to long-wave UV radiation (Figure 15). After the UV lamp was turned off, the stone returned to pink after several minutes. This chromatic change was repeatable. However, several small white parts of the sample showed no distinct change in colour (again, see Figure 15), and Raman analysis of those areas identified them as feldspar, which explains the absence of photochromism there.

Visible-near infrared (Vis-NIR) spectra were collected using a GEM 3000 spectrometer for both the pink and

red colour states of the sample (Figure 16). In its pink state, the stone displayed two primary broad bands centred around 390 and 515 nm, with a weak band at approximately 700 nm. However, in its red state after exposure to UV radiation, the stone displayed only a single major band centred around 520 nm.

A SYNTHdetect diamond-screening instrument (McGuinness *et al.* 2020) was used to test the phosphorescence of the tugtupite sample, because this time-gated luminescence imaging system (with a UV source of < 220 nm) can detect very short-lived phosphorescence that usually cannot be seen with the unaided eye. We chose nine exposure delay times ranging from 11 to 40,000  $\mu\text{s}$  (or 0.04 s) to demonstrate the sample's phosphorescence behaviour. The instrument recorded intense yellow phosphorescence that gradually faded to near-darkness during this time period (Figure 17, top row). A prominent red hue appeared at 4,700  $\mu\text{s}$ , and the yellow was nearly gone at 17,000  $\mu\text{s}$ . The overall phosphorescence faded distinctly at 30,000  $\mu\text{s}$  and it could be barely seen at 40,000  $\mu\text{s}$ .



**Figure 15:** This 1.76 ct faceted tugtupite turned from pink to red immediately when exposed to long-wave UV radiation of 365 nm. Stone courtesy of Xiaokang Xiong; composite photo by Huixin Zhao.

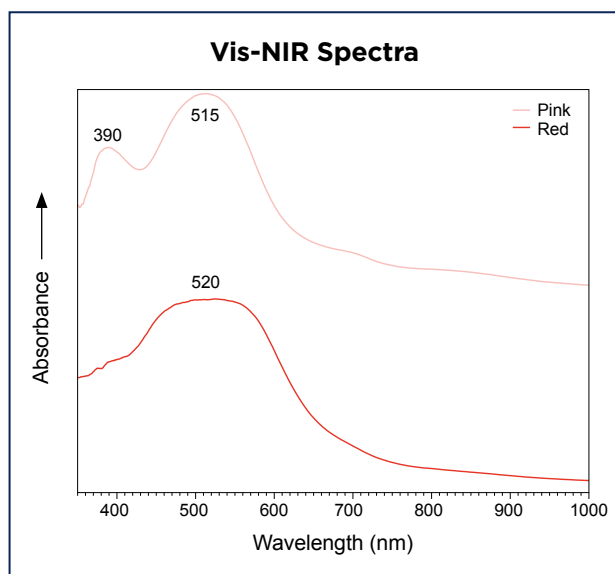


**Figure 16:** Vis-NIR spectra of the tugtupite recorded in both its pink and red states reveal distinct differences in the major absorption features. The spectra were collected only using the spectrometer's visible light source (i.e. without the UV source) to avoid any impact on the sample's colouration.

To better evaluate colour changes shown by the phosphorescence, we performed a colour analysis in RGB (red, green and blue) mode, as shown in Figure 17. While

the first row shows the observed phosphorescence in RGB mode, the second row is in RG mode (red and green, without blue), the third row is in RB mode (red and blue, without green), and the fourth row is in GB mode (green and blue, without red). As shown in the second row, subtracting the blue component has only a small impact on the observed phosphorescence, with the yellow hue being more obvious. Subtracting the green component gives rise to a series of highly saturated red colours, while omitting the red component results in nearly a pure green appearance. The contributions of the three colours to the sample's phosphorescence can therefore be ranked as follows: red > green >> blue. Considering the nearly equal contributions of green and red, with red contributing more than green, the overall phosphorescence of this tugtupite samples can be best described as orangey red.

To the authors' knowledge, this is the first time that the phosphorescence characteristics of tugtupite have been documented, although Robbins (1983) briefly mentioned that tugtupite occasionally shows eye-visible blue-white phosphorescence, similar to that of hackmanite. The application of the SYNTHdetect instrument provides new information on the luminescence properties of this interesting gem material.

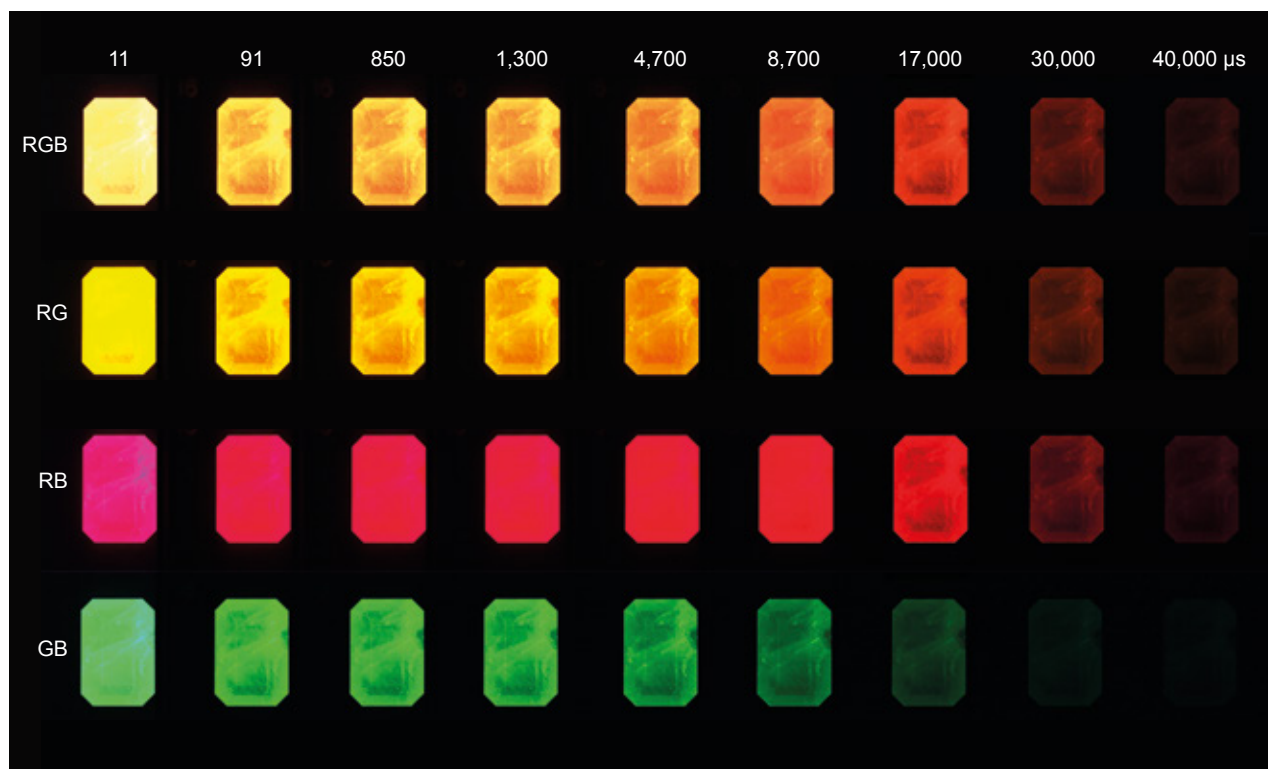


**Figure 17:** The short-lived phosphorescence of the tugtupite sample is shown with exposure delay times ranging from 11 to 40,000  $\mu$ s (or 0.04 s), as obtained with a SYNTHdetect instrument. The top row shows the overall appearance of the phosphorescence (RGB mode), while subsequent rows display RG mode (second row), RB mode (third row) and GB mode (fourth row). Composite photo by Y. Gao.



Yujie Gao and Xueying Sun  
(shirley.sun@guildgemlab.com)  
Guild Gem Laboratories  
Shenzhen, China

## References

- Anthony, J.W., Bideaux, R.A., Bladh, K.W. & Nichols, M.C. 1990. *Handbook of Mineralogy: Elements, Sulfides and Sulfosalts*. Mineral Data Publishing, Tucson, Arizona, USA, 588 pp.
- Blumentritt, F. & Fritsch, E. 2021. Photochromism and photochromic gems: A review and some new data (part 1). *Journal of Gemmology*, **37**(8), 780–800, <https://doi.org/10.15506/jog.2021.37.8.780>.
- Jensen, A. & Petersen, O.V. 1982. Tugtupite: A gemstone from Greenland. *Gems & Gemology*, **18**(2), 90–94, <https://doi.org/10.5741/gems.18.2.90>.
- McGuinness, C.D., Wassell, A.M., Lanigan, P.M.P. & Lynch, S.A. 2020. Separation of natural from laboratory-grown diamond using time-gated luminescence imaging. *Gems & Gemology*, **56**(2), 220–229, <https://doi.org/10.5741/gems.56.2.220>.
- Robbins, M.A. 1983. *The Collector's Book of Fluorescent Minerals*. Springer Science + Business Media, New York, New York, USA, xiii + 289 pp., <https://doi.org/10.1007/978-1-4757-4792-8>.
- Sørensen, H. 1960. Beryllium minerals in a pegmatite in the nepheline syenites of Ilímaussaq, South West Greenland. *Report of the 21st Session, Norden. Denmark, Finland, Iceland, Norway, Sweden, 1960; Proceedings of Section 17: Minerals and Genesis of Pegmatites*. Berlingske Bogtrykkeri, Copenhagen, Denmark, 31–35.

## DIAMONDS

### Diamond within Diamond: An Analysis of the 'Beating Heart'

De Beers Institute of Diamonds recently analysed an unusual 0.33 ct rough diamond with an internal cavity enclosing a smaller crystal that is free to move around (Figure 18). Although undoubtedly a rare phenomenon of diamond formation, previous examples have been documented in the literature, including the so-called Matryoshka diamond from Siberia, Russia, which has been widely publicised since its discovery in October 2019 (e.g. Fritsch 2021).

De Beers Institute of Diamonds was initially alerted to the specimen in October 2022, when it was noted as a potentially interesting natural anomaly by De Beers Sightholder VD Global, based in India. The rough diamond was recovered by De Beers Group at one of its four global mining locations (Botswana, Canada, Namibia and South Africa) and arrived at the De Beers Institute of Diamonds facility in Maidenhead in November 2022. It was later named the 'Beating Heart' diamond by VD Global in recognition of its unusual structure.

To determine its properties and to assess the factors and conditions that may have contributed to its unusual physical structure, the diamond was analysed by various techniques, including optical and scanning electron microscopy (SEM), FTIR spectroscopy, and fluorescence and phosphorescence imaging. It was D colour and FTIR spectroscopy showed it was type IaAB. Macle

twin planes visible as herringbone patterns were seen on the surfaces of both the inner and host diamonds. Stepped surfaces led from the outer diamond into the interior cavity, and small black inclusions were visible near the cavity opening alongside brown radiation staining/spots (Figure 18b). Their brown colour is due to natural heating of radiation-damage features that were originally green and derived from radioactive decay of elements adjacent to the diamond during its geological history (Eaton-Magaña & Moe 2016). What appeared to be a small macle twin crystal was trapped inside the cavity but remained free to move within the interior space.

SEM imagery of the surface of both the outer and inner diamonds (Figure 19) showed etch features on both of them, including trigons (some truncated) and some hexagonal pits. These features are consistent with a high proportion of CO<sub>2</sub> in the fluid phase responsible for the etching. Generally 50–90% CO<sub>2</sub> results in trigons that have a truncated appearance, whereas > 90% CO<sub>2</sub> results in hexagonal features (Fedortchouk 2019).

Other notable findings include a disparity in fluorescence between the outer and inner crystals (Figure 20), which was seen with both the DiamondView and SYNTHdetect instruments developed by De Beers Group Ignite. The outer diamond had characteristic blue fluorescence, whereas the smaller interior crystal

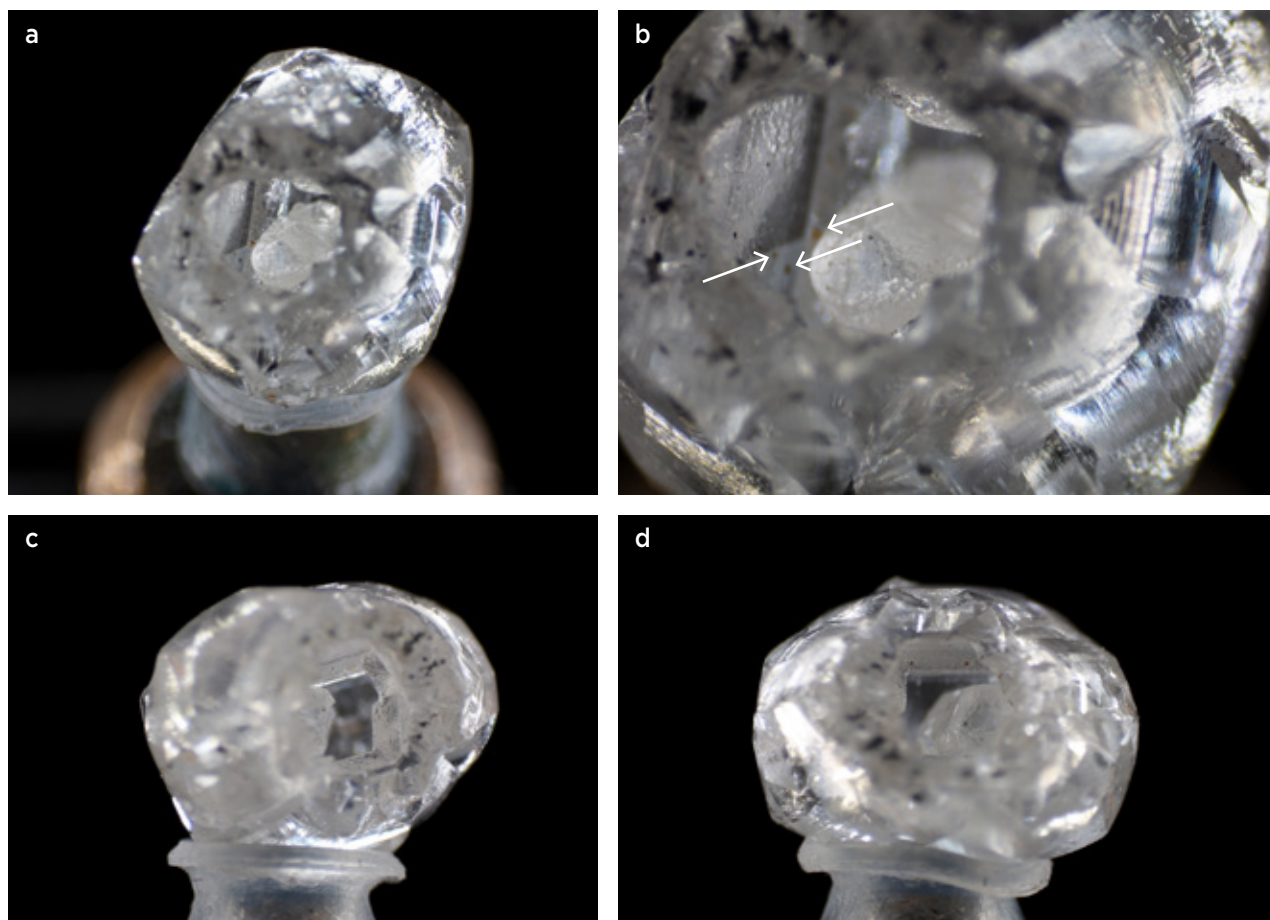


**Figure 18:** Optical images of the 0.33 ct Beating Heart diamond reveal a small diamond crystal nestled inside the larger host. The photos show (a) the overall appearance of the specimen, (b) a closer view, and (c) and (d) different positions of the mobile interior diamond. Note also the stepped surfaces, black inclusions and brown radiation stains (see arrows) visible in image b. Photos by Danny Bowler.

showed brighter blue fluorescence. This difference in intensity could relate to variations in nitrogen content and/or aggregation state between the host diamond and its included crystal.

Initial conclusions made by the De Beers Institute of Diamonds suggest that the cavity was formed due to preferential etching of an intermediate layer of poor-quality fibrous diamond. Only the better-quality material ‘survived’ this process—the outer diamond and

the core—which in this case led to a diamond freely moving within the host diamond.

The Beating Heart joins a small group of similar rough diamond specimens that house a mobile crystal within a larger crystal. It is fascinating to imagine the journey it experienced during its formation, subsequent etching and dissolution, until its delivery to the earth’s surface via eruption of the host kimberlite. A specimen such as this demonstrates why natural diamond formation and

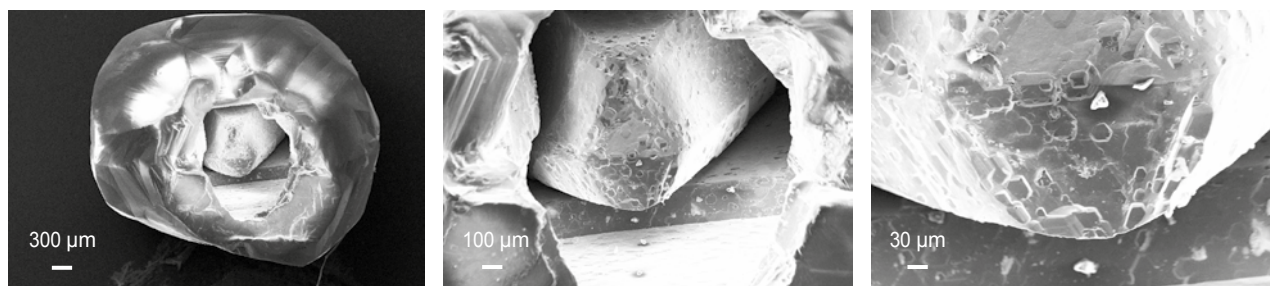


**Figure 19:** SEM images reveal the etch features visible on both the smaller internal diamond and the interior crystal faces of the host. Images by Ivan Nikiforov.

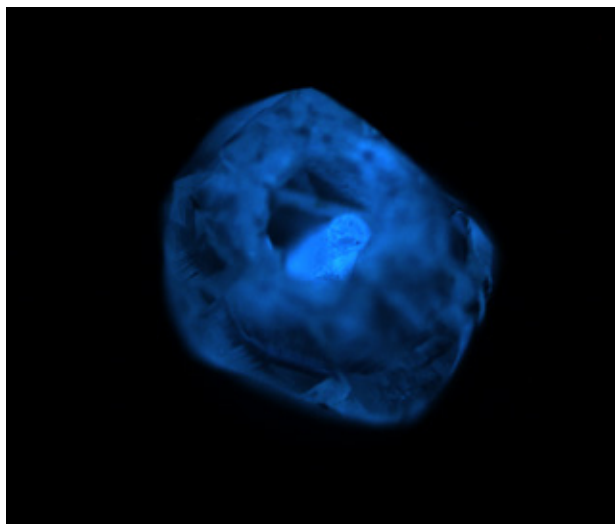


**Figure 20:** Seen here with the DiamondView instrument, both the host diamond and internal crystal show blue fluorescence, but the latter has more intense luminescence. Photo by S. Sibley.

origin is such a fascinating area of study, and why it is important to strive for advancements in testing and analysis that can contribute to our knowledge of natural diamond growth.

The Beating Heart diamond is registered on the Tracr blockchain platform and can be seen by scanning the following QR code:



Samantha Sibley DGA  
(Samantha.Sibley@debeersgroup.com)  
De Beers Group  
London, United Kingdom

## References

- Eaton-Magaña, S.C. & Moe, K.S. 2016. Temperature effects on radiation stains in natural diamonds. *Diamond and Related Materials*, **64**, 130–142, <https://doi.org/10.1016/j.diamond.2016.02.009>.
- Fedortchouk, Y. 2019. A new approach to understanding diamond surface features based on a review of experimental and natural diamond studies. *Earth-Science Reviews*, **193**, 45–65, <https://doi.org/10.1016/j.earscirev.2019.02.013>.
- Fritsch, E. 2021. Revealing the formation secrets of the Matryoshka diamond. *Journal of Gemmology*, **37**(5), 528–533, <https://doi.org/10.15506/JoG.2021.37.5.528>.

## Reddish Orange Diamond Coloured by Hematite

Diamonds coloured by inclusions are most commonly black, and their inclusions are usually graphite, or rarely may consist of magnetite, hematite and natural iron. Those with iron-bearing phases mostly come from the Siberian region of Russia (Eaton-Magaña *et al.* 2019). To our knowledge, other coloured diamonds very rarely owe their colouration to inclusions.

Recently, an unusual 0.40 ct reddish orange diamond (Figure 21) was submitted to NGTC's Shenzhen laboratory. Microscopic examination revealed numerous feathers with unevenly distributed reddish orange colouration, as well as reddish brown pinpoints (Figure 22).

The colour origin of pink-to-red diamonds is typically attributed to the 550 nm band or, very rarely, NV centres (Gaillou *et al.* 2010). However, the UV-Vis-NIR absorption spectrum of the present diamond showed Fe<sup>3+</sup> absorption bands at about 400 and 850 nm (Szalai *et al.* 2013; Figure 23a). With first-order derivative reflectance spectroscopy (cf. Bou-Orm *et al.* 2020), a band near 570 nm associated with hematite was obtained (Figure 23b). In addition, Raman spectroscopy with 532 nm laser excitation revealed peaks related to the vibration modes of hematite at 224, 244, 291, 409,

500, 612 and 665 nm, and provided a good match to a hematite reference spectrum in the RRUFF database (<https://rruff.info/R050300>).

These results, combined with the distribution of the colouration along fractures, indicates that this diamond



**Figure 21:** This 0.40 ct pear-shaped modified brilliant-cut diamond owes its colour to hematite. Photo by Wenfang Zhu.



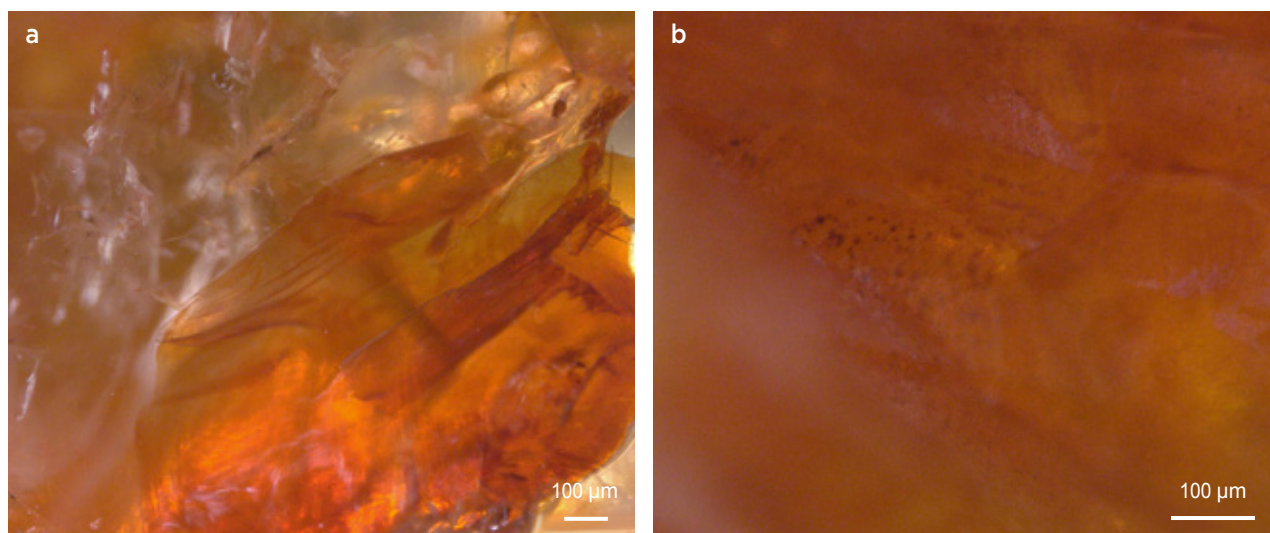


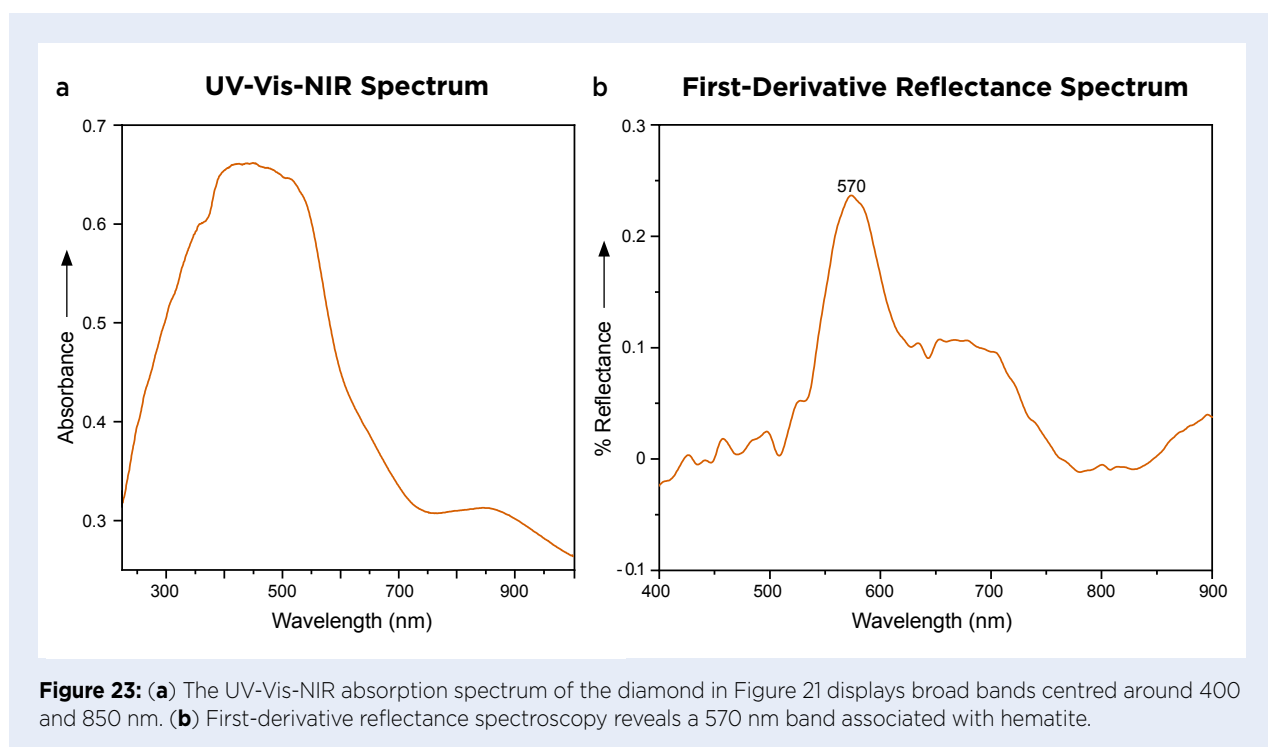
**Figure 22:** Microscopic examination of the 0.40 ct diamond shows (a) unevenly distributed reddish orange staining in feathers, as well as (b) reddish brown pinpoints. Photomicrographs by W. Zhu.

is coloured by an epigenetic staining of hematite, which probably occurred during its deposition in a placer deposit. Although it is not uncommon to find oxide staining within fractures in diamonds, this is the first time NGTC has encountered a reddish orange-appearing diamond coloured by hematite, which to the authors' knowledge has not been reported previously.

When secondary minerals affect the overall colour of a diamond, rather than having a localised impact, then this must be taken into account when colour grading.

The degree to which epigenetic minerals influence colouration is difficult to quantify, thus presenting a challenge when grading a stone's colour. In addition, exposure to bleaching agents may affect the colour stability of such a diamond, so its colour grade should be considered valid only at the time of grading.

*Wenfang Zhu (zhuwf@ngtc.com.cn), Huihuang Li,  
Xiaoxia Zhu and Ying Ma  
NGTC, Shenzhen, China*



## References

- Bou-Orm, N., AlRomaithi, A.A., Elrmeithi, M., Ali, F.M., Nazzal, Y., Howari, F.M. & Al Aydaros, F. 2020. Advantages of first-derivative reflectance spectroscopy in the VNIR-SWIR for the quantification of olivine and hematite. *Planetary and Space Science*, **188**, article 104957, <https://doi.org/10.1016/j.pss.2020.104957>.
- Eaton-Magaña, S., Ardon, T., Breeding, C.M. & Shigley, J.E. 2019. Natural-color fancy white and fancy black diamonds: Where color and clarity converge. *Gems & Gemology*, **55**(3), 320–337, <https://doi.org/10.5741/gems.55.3.320>.
- Gaillou, E., Post, J.E., Bassim, N.D., Zaitsev, A.M., Rose, T., Fries, M.D., Stroud, R.M., Steele, A. *et al.* 2010. Spectroscopic and microscopic characterizations of color lamellae in natural pink diamonds. *Diamond and Related Materials*, **19**(10), 1207–1220, <https://doi.org/10.1016/j.diamond.2010.06.015>.
- Szalai, Z., Kiss, K., Jakab, G., Sipos, P., Belucz, B. & Németh, T. 2013. The use of UV-VIS-NIR reflectance spectroscopy to identify iron minerals. *Astronomische Nachrichten*, **334**(9), 940–943, <https://doi.org/10.1002/asna.201211965>.

## SYNTHETICS AND SIMULANTS

### CVD-Grown Diamond with Unusual Fluorescence Colour Appearance

Rapidly improving chemical vapour deposition (CVD) technology can now produce large, high-quality, near-colourless and colourless laboratory-grown diamonds. Manufacturers can control the growth rate, morphology and purity to obtain products of desirable quality. For example, the addition of oxygen favours single-crystal over polycrystalline growth, and the presence of nitrogen enhances the growth rate by eight-fold (Harris & Weiner 1989; Jin & Moustakas 1994; Liang *et al.* 2009; Eaton-Magaña & D’Haenens-Johansson 2012). However, the presence of nitrogen during the formation of CVD-grown diamonds turns them yellowish or light brown; this colouration is associated with nitrogen-vacancy-hydrogen complexes (NVH<sup>-</sup>; Liang *et al.* 2009). The concentration of NVH<sup>-</sup> centres can be reduced by either high pressure, high temperature (HPHT) or low pressure, high temperature (LPHT) annealing, so most near-colourless CVD-grown diamonds undergo post-growth treatment.

Recently a 1.27 ct CVD-grown diamond (7.00 × 6.93 × 4.26 mm, G colour and VS<sub>1</sub> clarity) was submitted to Gemological Science International’s (GSI) Mumbai laboratory for post-growth treatment identification. The specimen showed anomalous fluorescence behaviour when viewed in the DiamondView instrument: as it was rotated in the face-down position, it displayed a fluorescence colour that appeared to change from greenish blue to violet. As shown in Figure 24, at the initial orientation (0°) it appeared to luminesce greenish blue, while at 180° rotation, it showed both violet and greenish blue fluorescence. This is seen more distinctly in Figure 25, which at 180° rotation reveals a growth

plane dividing the pavilion into two parts—an upper portion that fluoresces greenish blue and a lower part that luminesces violet. The sample also phosphoresced a weak greenish blue, which was stronger in the upper portion of the sample. The growth plane was oriented at an angle of approximately 45°–50° relative to the table facet, and therefore the visibility of the violet-luminescent zone changed as the sample was rotated. This caused the variations in the apparent fluorescence colour upon rotation of the sample.

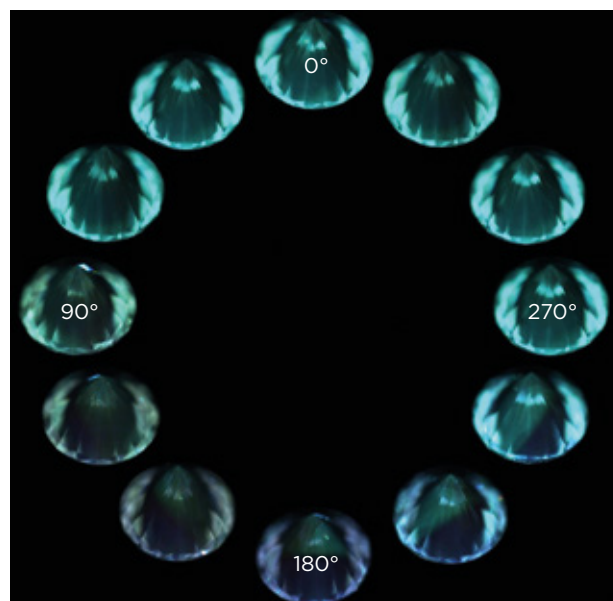


**Figure 24:** DiamondView fluorescence images of the 1.27 ct CVD-grown diamond show an apparent change in fluorescence colour from greenish blue to a combination of violet and greenish blue as the diamond is rotated. Composite photo by R. G. Patil.

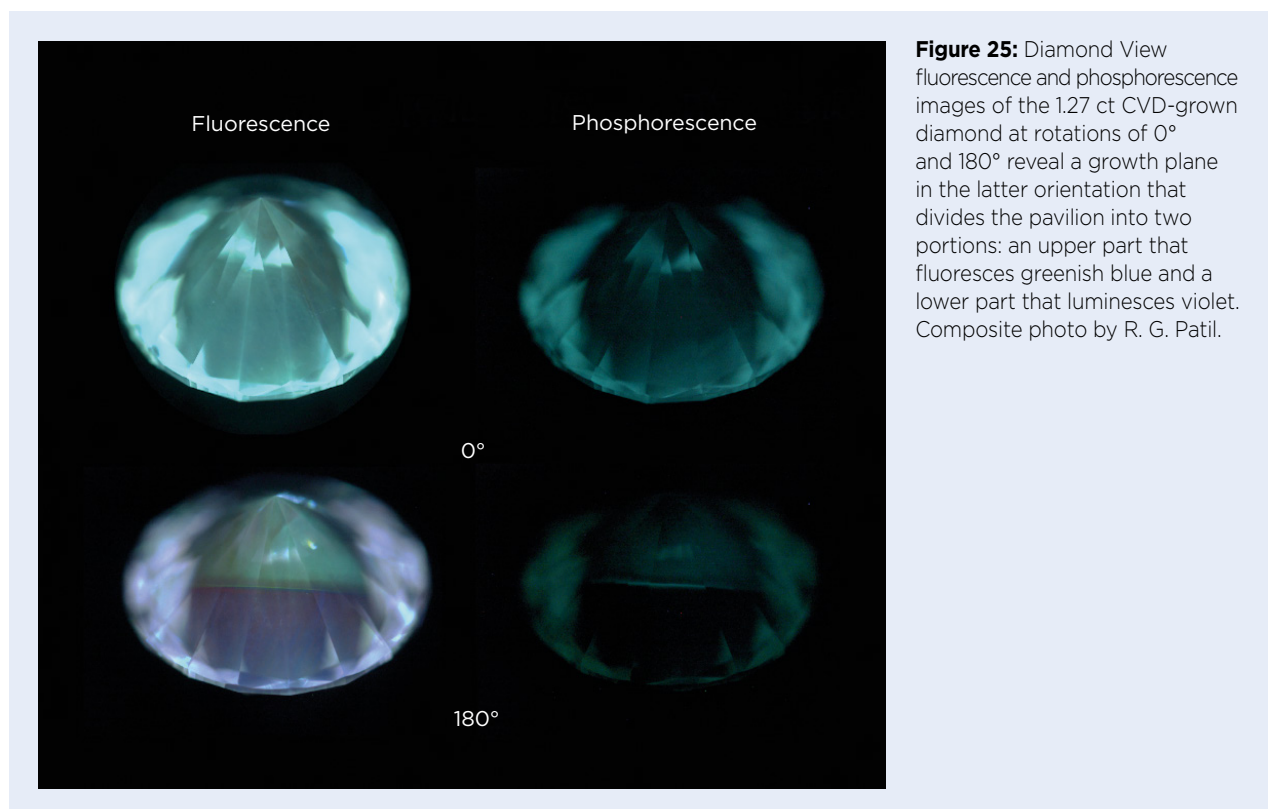


**Figure 25:** Diamond View fluorescence and phosphorescence images of the 1.27 ct CVD-grown diamond at rotations of 0° and 180° reveal a growth plane in the latter orientation that divides the pavilion into two portions: an upper part that fluoresces greenish blue and a lower part that luminesces violet. Composite photo by R. G. Patil.

The specimen was further tested with FTIR and photoluminescence (PL) spectroscopy (at liquid-nitrogen temperature). FTIR spectroscopy revealed that it was type IIa, with no hydrogen-related absorptions at either 3107 or 3123  $\text{cm}^{-1}$ . PL spectroscopy with 532 nm laser excitation showed  $[\text{Si-V}]^-$  emissions at 737 and 766 nm, a characteristic feature of CVD-grown diamonds (Figure 26). The PL spectra also showed weak emissions from NV centres at 575.0 and 637.0 nm. The absence of a 596/597 nm doublet in the PL spectra provides evidence of post-growth treatment for colour enhancement (Eaton-Magaña & Shigley 2016).

We infer that the abrupt boundary between the different zones of fluorescence and phosphorescence is due to intentional or unintentional variations in deposition conditions or interruptions during CVD growth, which modified the impurity content of the synthetic diamond. The luminescence colouration of diamond is related to various defect centres, and the distribution and concentration of defects create distinctive patterns during diamond growth naturally or in a laboratory. Nearly all diamonds luminesce in the DiamondView due to the instrument's ultra-short-wave UV excitation, with energy greater than the diamond's band gap (i.e. wavelength < 225 nm and energy > 5.5 eV). As-grown colourless, near-colourless or brown CVD synthetic diamonds usually luminesce

orange, red or pink, or show a mottled distribution of purple, red and blue due to NV centres (Eaton-Magaña & Shigley 2016; D'Haenens-Johansson *et al.* 2022). Decolourisation via post-growth treatment (i.e. HPHT annealing) alters the pre-existing NV centres or creates new defects, as evidenced by various emission peaks that can be observed with PL spectroscopy. Consequently, the fluorescence colour of as-grown CVD synthetic diamonds changes from red, pink, orange

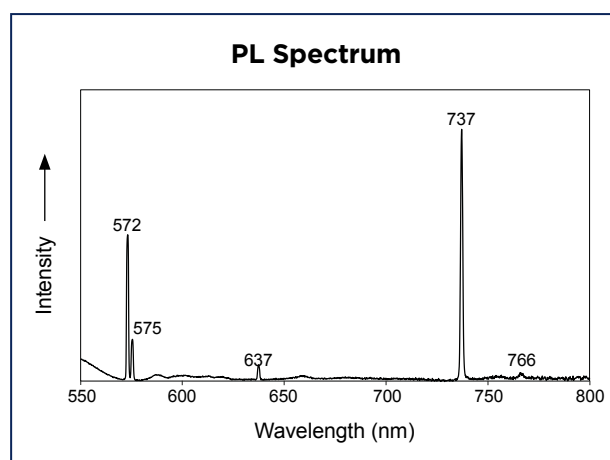


**Figure 26:** PL spectroscopy of the 1.27 ct synthetic diamond with 532 nm laser excitation shows weak emissions from NV centres at 575 and 637 nm, as well as CVD-specific emissions at 737 and 766 nm from the  $[\text{Si-V}]^-$  centre. The feature at 572 nm is the first-order Raman line.



or purple to green or greenish blue after treatment. Furthermore, HPHT-annealed CVD-grown diamonds show strong green to greenish blue phosphorescence that may be associated with N–B donor-acceptor pairs (Eaton-Magaña & Shigley 2016; D’Haenens-Johansson *et al.* 2022). The addition of traces of nitrogen and boron influences the growth rate of CVD-grown diamond, and the presence of boron significantly reduces the concentration of defects (D’Haenens-Johansson *et al.* 2022). A nonuniform distribution of N and B impurities is inferred to be responsible for the unusual luminescence pattern observed for this synthetic diamond.

## References

- D’Haenens-Johansson, U.F.S., Butler, J.E. & Katruscha, A.N. 2022. Synthesis of diamonds and their identification. *Reviews in Mineralogy and Geochemistry*, **88**(1), 689–753, <https://doi.org/10.2138/rmg.2022.88.13>.
- Eaton-Magaña, S. & D’Haenens-Johansson, U.F.S. 2012. Recent advances in CVD synthetic diamond quality. *Gems & Gemology*, **48**(2), 124–127, <https://doi.org/10.5741/gems.48.2.124>.
- Eaton-Magaña, S. & Shigley, J.E. 2016. Observations on CVD-grown synthetic diamonds: A review. *Gems & Gemology*, **52**(3), 222–245, <https://doi.org/10.5741/gems.52.3.222>.

Researchers and scientists continuously experiment with growth technology to increase the growth rate and reduce the overall cost of producing laboratory-grown diamonds. The diamond described here could be part of such experimentation. More such unusual features in laboratory-grown diamonds are likely to be encountered in the future.

Dr Ramchandra G. Patil  
([ramchandrap@gemscience.net](mailto:ramchandrap@gemscience.net))  
Gemological Science International  
Mumbai, India

- Harris, S.J. & Weiner, A.M. 1989. Effects of oxygen on diamond growth. *Applied Physics Letters*, **55**(21), 2179–2181, <https://doi.org/10.1063/1.102350>.
- Jin, S. & Moustakas, T.D. 1994. Effect of nitrogen on the growth of diamond films. *Applied Physics Letters*, **65**(4), 403–405, <https://doi.org/10.1063/1.112315>.
- Liang, Q., Yan, C., Meng, Y., Lai, J., Krasnicki, S., Mao, H. & Hemley, R.J. 2009. Recent advances in high-growth rate single-crystal CVD diamond. *Diamond and Related Materials*, **18**(5–8), 698–703, <https://doi.org/10.1016/j.diamond.2008.12.002>.

## Pink-Orange CVD-grown Synthetic Diamonds with Ni Impurities

HPHT-grown synthetic diamonds often contain Ni impurities and, sometimes, traces of Si (Eaton-Magaña *et al.* 2017). CVD-grown synthetics generally contain Si, but only rarely Ni, and natural diamonds can contain both Si and Ni impurities (Li *et al.* 2021). However, while colourless CVD-grown diamonds with Ni have been reported previously (Barrie 2020), to the authors’ knowledge no pink CVD synthetic diamonds containing both Si and Ni have been documented in the literature. Recently, the National Gemstone Testing Center’s (NGTC) Guangzhou laboratory encountered two pink-orange CVD-grown synthetic diamonds (Figure 27)—a 1.23 ct heart-shape brilliant and a 1.45 ct round brilliant—that were found to contain both of these impurities.

Both samples fluoresced moderate and strong orange to long- and short-wave UV radiation, respectively. In the DiamondView, they displayed intense orange-red fluorescence, with darker parallel banding seen from the pavilion side (Figure 28), as well as moderately strong orange-red phosphorescence for several seconds.

Inspection with a microscope also showed a layered structure.

Based on their FTIR spectra, both synthetic diamonds were classified as type Ib, with weak absorptions at



**Figure 27:** These pink-orange CVD-grown diamonds (1.23 ct heart-shape and 1.45 ct round brilliant) were found to contain Ni impurities in addition to the expected traces of Si. Photos by Zhenping Lu.

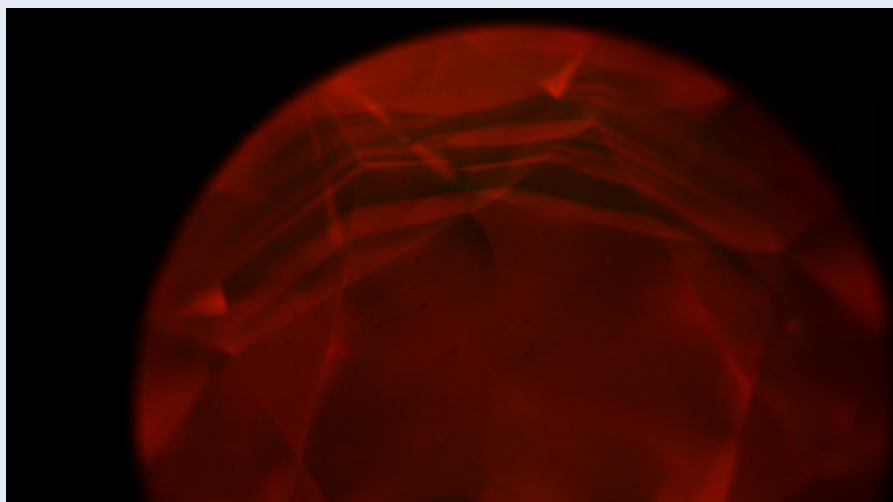


**Figure 28:** In the DiamondView, both of the synthetic diamonds emitted orange-red fluorescence caused by prominent NV centres, as seen here for the 1.45 ct sample. Photo by Zhenping Lu.

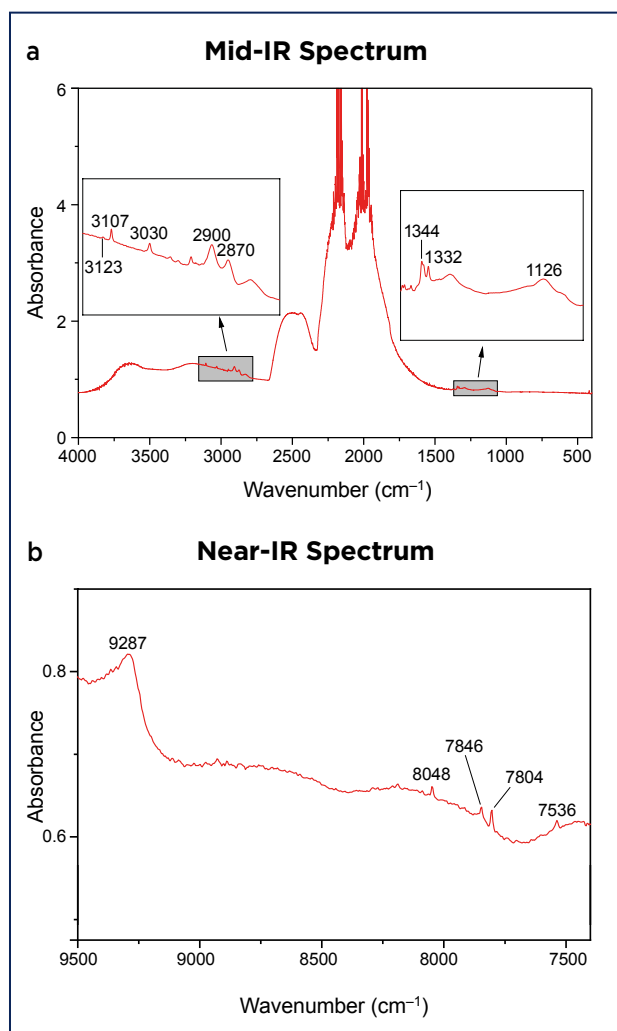


**Figure 29:** Representative IR absorption spectra are shown (a) in the mid-IR range for the 1.45 ct sample and (b) in the near-IR range for the 1.23 ct specimen. Both of these synthetic diamonds are type Ib with small amounts of single-substitutional nitrogen and the presence of hydrogen-related impurities.

1344, 1332 and  $1126\text{ cm}^{-1}$  indicating small amounts of single-substitutional nitrogen (Figure 29a). The mid-infrared region showed the presence of hydrogen-related impurities (cf. Moe *et al.* 2014), with absorptions at 3123 ( $\text{NVH}^0$ ), 3107 ( $\text{N}_3\text{VH}$ ), 3030, 2900 and  $2870\text{ cm}^{-1}$ . Additional hydrogen-related features (cf. Liang *et al.* 2009) were recorded in the near-infrared region at 7846, 7804 and  $7536\text{ cm}^{-1}$  (Figure 29b). Also, an absorption at  $9287\text{ cm}^{-1}$  is attributed to irradiation treatment (Lv *et al.* 2015).

The UV-Vis-NIR spectrum, recorded at liquid-nitrogen temperature, displayed a strong  $\text{NV}^-$  absorption (zero-phonon line at 637.0 nm), a peak at 594.3 (595 nm centre) that is typical of diamonds which have undergone irradiation and annealing, and a doublet at 736.6/737.0 nm attributed to the  $[\text{Si-V}]^-$  defect that appears almost exclusively in CVD synthetic diamonds. The NV centre strongly absorbs light in the green-to-orange region, creating a transmission window in the red region, and the intensity of the resulting pink-to-red colouration (in this case, pink-orange) depends on the concentration of these optical centres (Wang & Johnson 2010).

Photoluminescence spectra obtained at liquid-nitrogen temperature with various excitation wavelengths (Figure 30) showed the presence of a weak but distinct  $[\text{Si-V}]^-$  doublet (736.6/736.9 nm), prominent  $\text{NV}^0$  (575 nm) and  $\text{NV}^-$  (637 nm) centres, numerous peaks in the 486–502 nm region, strong H3 (503.2 nm) and H2 (986 nm) centres, and weak Ni-related peaks (883 and 884 nm). Furthermore, none of the spectra showed evidence of  $[\text{Si-V}]^0$  (946 nm) and 596/597 nm centres. The absence of the latter feature, along with the presence of H3 and H2 centres, suggests that these two diamonds were exposed to HPHT treatment before irradiation.

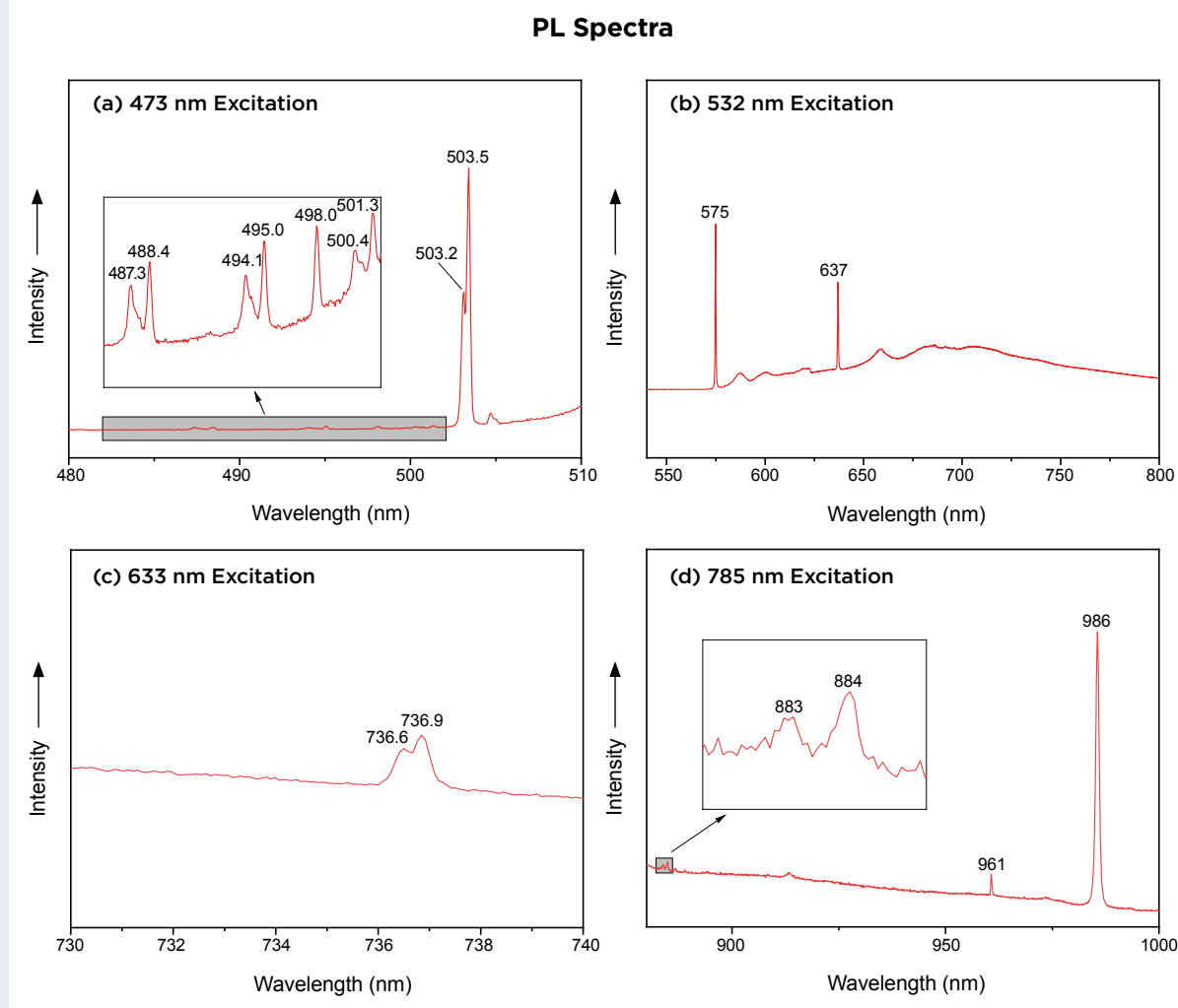


**Figure 30:** Representative PL spectra of the synthetic diamonds at liquid-nitrogen temperature indicate that both were exposed to HPHT treatment before irradiation. The spectra were collected using various laser excitation wavelengths: (a) 473 nm, (b) 532 nm, (c) 633 nm and (d) 785 nm. Spectra a and c were obtained from the 1.23 ct sample, and b and d were collected from the 1.45 ct specimen.

Zhenping Lu (luzp@ngtc.com.cn), Yang Wang,  
Zhonghua Song, Yuhan Cheng and Di Pan  
NGTC, Guangzhou and Beijing, China

## References

- Barrie, E. 2020. Lab Notes: HPHT-processed CVD laboratory-grown diamonds with low color grades. *Gems & Gemology*, **56**(2), 289–290.
- Eaton-Magaña, S., Shigley, J.E. & Breeding, C.M. 2017. Observations on HPHT-grown synthetic diamonds: A review. *Gems & Gemology*, **53**(3), 262–284, <https://doi.org/10.5741/gems.53.3.262>.
- Li, Y., Song, Z., Ma, Y. & Xu, Y. 2021. Characteristics of natural diamond containing silicon and nickel impurities. International Gems and Jewelry Academic Conference, online, 19–20 November, 27–30.
- Liang, Q., Yan, C., Meng, Y., Lai, J., Krasnicki, S., Mao, H. & Hemley, R.J. 2009. Recent advances in high-growth rate single-crystal CVD diamond. *Diamond and Related Materials*, **18**(5–8), 698–703, <https://doi.org/10.1016/j.diamond.2008.12.002>.
- Lv, X., Lu, T., Yang, L., Song, Z., Zhang, J. & Chen, C. 2015. Identification of irradiated colored diamonds by 9287  $\text{cm}^{-1}$  absorption band. *International Gems and Jewelry Academic Conference*, Beijing, China, 51–56.
- Moe, K.S., Wang, W. & D’Haenens-Johansson, U. 2014. Lab Notes: Yellow CVD synthetic diamond. *Gems & Gemology*, **50**(2), 154–155.
- Wang, W. & Johnson, P. 2010. Lab Notes: Red CVD synthetic diamond with multiple treatments. *Gems & Gemology*, **46**(1), 52–54.



## Treated Orange Pink HPHT-grown Synthetic Diamond with 776.4 nm PL Peak

Many pink-to-red synthetic diamonds currently in the jewellery market owe their colour to multiple enhancement processes, including HPHT treatment combined with irradiation and annealing. Treatment involving irradiation and annealing generates strong absorption from nitrogen-vacancy (NV) centres, which are responsible for both a pink body colour and strong orange-red fluorescence (Johnson 2010).

Most HPHT-grown synthetic pink diamonds have a purplish hue. Recently, a 0.40 ct sample exhibiting an attractive orange pink colour (Figure 31) was submitted to the National Gemstone Testing Center's (NGTC) Guangzhou laboratory for identification. Microscopic observation revealed distinct colour zoning. Viewed from the pavilion, the sample was dark brownish pink in the {100} sectors and orange pink in the {111} sectors. The mid-IR spectrum showed weak bands at 1344 and 1332  $\text{cm}^{-1}$  (Figure 32).

When exposed to long-wave (365 nm) UV radiation, the sample exhibited strong red fluorescence, which suggests it had a significant concentration of NV centres. In the DiamondView, it displayed intense orange fluorescence and strong green phosphorescence that lasted for several seconds (Figure 33). DiamondView imaging also revealed cuboctahedral growth, indicative of the diamond's HPHT synthetic origin. As seen in Figure 33, cubic {100} sectors were evident when viewed from the pavilion, along with octahedral {111} sectors. The phosphorescence was strongest in the latter sectors.



**Figure 31:** This 0.40 ct HPHT-grown synthetic diamond shows an unusual orange pink colour. Photo by Zhenping Lu.

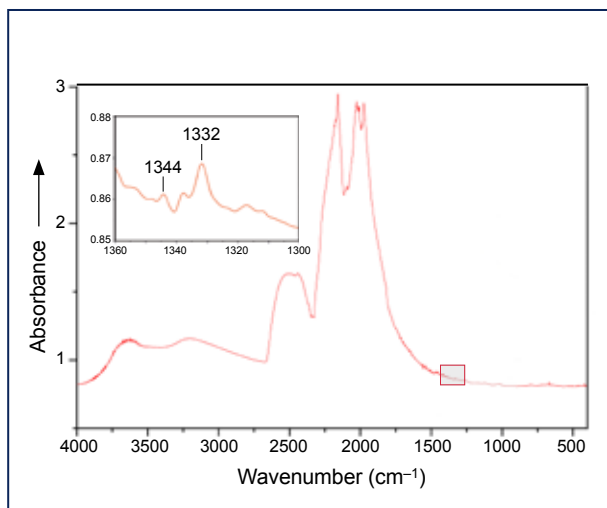


**Figure 32:** The FTIR spectrum of the 0.40 ct synthetic diamond shows absorption features at 1344 and 1332  $\text{cm}^{-1}$ .

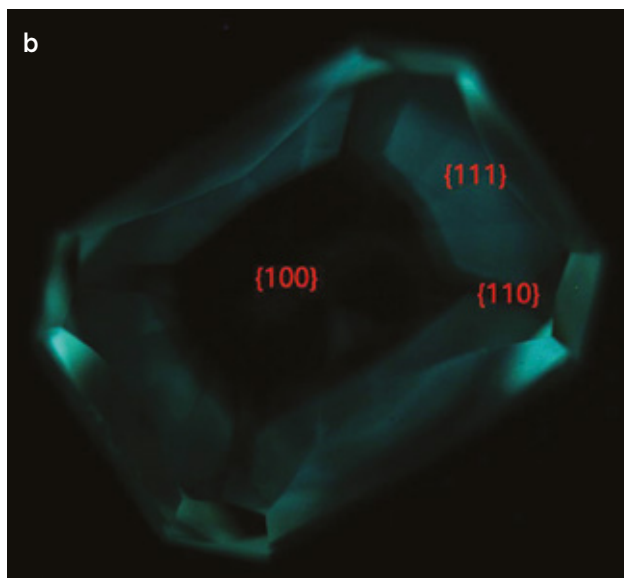
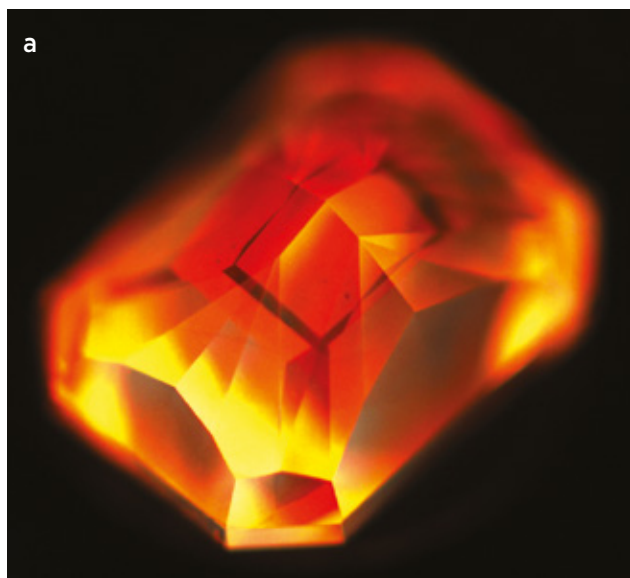


**Figure 33:** DiamondView images of the 0.40 ct laboratory-grown diamond show (a) zoned fluorescence patterns typical of HPHT synthetics and (b) green phosphorescence. Photos by Yuhang Cheng.

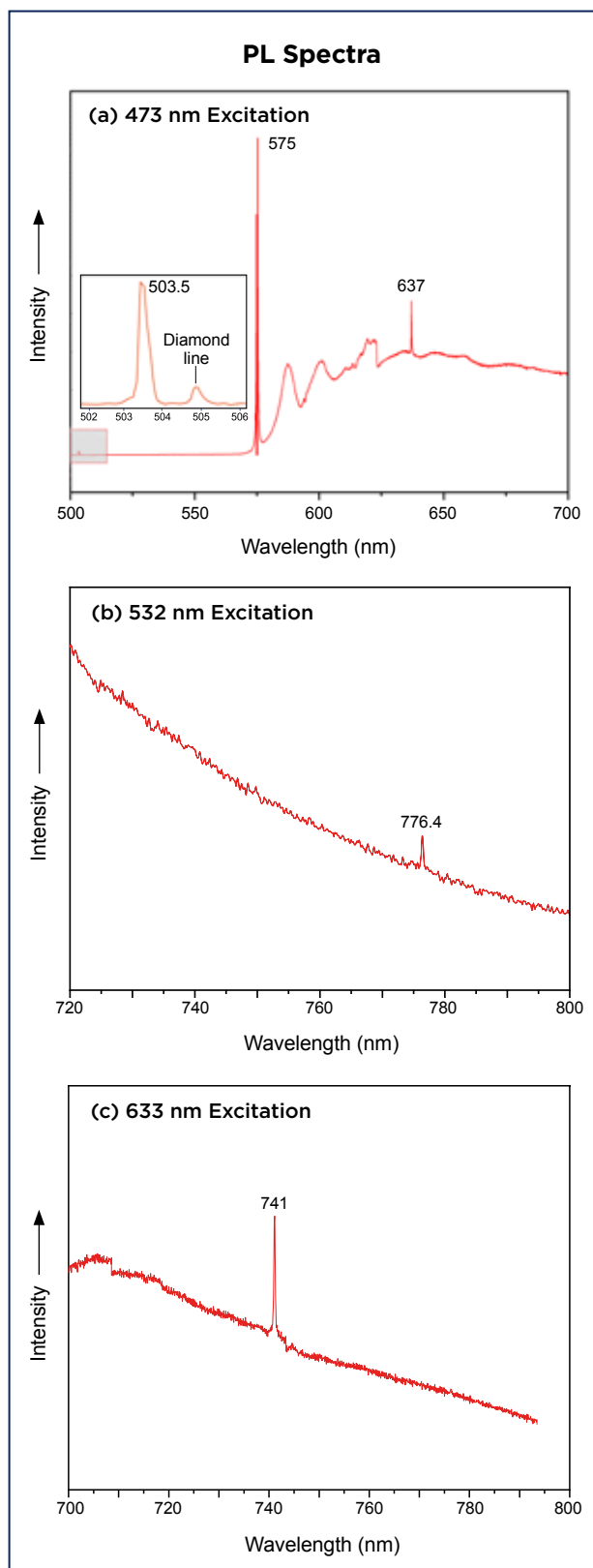


**Figure 34:** PL spectra of the synthetic diamond with (a) 473 nm, (b) 532 nm and (c) 633 nm laser excitation at liquid-nitrogen temperature indicate the presence of NV (575 and 637 nm), 3H (503.5 nm) and GR1 (741 nm) centres associated with irradiation and annealing, and a 776.4 nm peak possibly associated with a boron-vacancy defect—the last not seen previously in HPHT-grown synthetics.

The UV-Vis absorption spectrum showed a sharp peak at 595 nm, together with peaks at 575 and 637 nm that confirmed the presence of NV centres and indicated that the diamond had experienced irradiation and moderate-temperature annealing. Its pink colour is attributed mainly to strong absorption by these NV centres.

Photoluminescence spectroscopy with 473 and 633 nm laser excitation displayed features at 503.5 nm (3H) and 741 nm (GR1), respectively (Figure 34a, c), also indicating that the sample had been subjected to irradiation and annealing (D’Haenens-Johansson *et al.* 2014). In addition, 532 nm excitation produced a weak, distinct PL line at 776.4 nm (Figure 34b), possibly associated with the boron-vacancy defect (as seen previously in natural type IIb diamonds; Eaton-Magaña & Ardon 2016). This peak was observed only in the {111} growth sectors (i.e. those showing phosphorescence in the DiamondView).

Uncompensated boron is occasionally observed in some HPHT-grown diamonds, but to the authors’ knowledge the 776.4 nm PL peak has not been reported previously in HPHT-grown synthetics. This peak can be introduced by heating to 600°C, causing temperature-sensitive vacancies to become mobile within the diamond (Eaton-Magaña & Ardon 2016). Combined with the 503.5 and 741 nm features mentioned above, this suggests that the orangey pink HPHT synthetic diamond underwent post-growth treatment by an irradiation and annealing process. Further research is required to establish a definitive model of the defect that gives rise to the 776.4 nm PL peak.

Yuhan Cheng ([chengyh@ngtc.com.cn](mailto:chengyh@ngtc.com.cn)),  
Zhonghua Song, Yang Wang,  
Zhenping Lu and Di Pan  
NGTC, Guangzhou and Beijing, China

## References

- D’Haenens-Johansson, U.F.S., Moe, K.S., Johnson, P., Wong, S.Y., Lu, R. & Wang, W. 2014. Near-colorless HPHT synthetic diamonds from AOTC Group. *Gems & Gemology*, **50**(1), 30–45, <https://doi.org/10.5741/gems.50.1.30>.
- Eaton-Magaña, S. & Ardon, T. 2016. Temperature effects on luminescence centers in natural type IIb diamonds. *Diamond and Related Materials*, **69**, 86–95, <https://doi.org/10.1016/j.diamond.2016.07.002>.
- Johnson, P. 2010. Lab Notes: Intense purplish pink HPHT-grown/treated synthetic diamond. *Gems & Gemology*, **46**(4), 300–301.

## TREATMENTS

### An Unusual Tin Glass-filled Ruby

Heavily included corundum commonly undergoes glass filling to improve its appearance. Such treated material may show a dramatic difference in appearance before and after treatment. Lead glass is the most commonly used filler, although other additives such as Bi and Co have appeared in treated rubies and sapphires encountered on the market (e.g. Leelawatanasuk *et al.* 2013; Jia & Sit 2020).

Recently, a 0.95 ct ruby that had undergone an unusual filling treatment was submitted to Guild Gem Laboratories in Shenzhen, China (Figure 35). It showed saturated red colour and strong red luminescence to long-wave UV radiation (and it fluoresced weakly to short-wave UV). Microscopic observation revealed oriented rutile needles together with melted-looking platy inclusions (Figure 36a). In addition, a large amount of what appeared to be flux residues originating from the heating process was seen in the surface-reaching fissures. The sample's FTIR spectrum showed distinct bands at 3309 and 3232  $\text{cm}^{-1}$ , consistent with heated ruby (Vertriest & Saeseaw 2019). Based on these results, the stone seemed to have merely undergone traditional flux-assisted heat treatment.

Nevertheless, a small amount of glassy material seen near the surface aroused further attention (Figure 36b). Reflected lighting revealed areas along thin fissures with a lower lustre than the ruby host, consistent with the presence of a surface-reaching glass filler. Chemical analysis of the stone by energy-dispersive X-ray fluorescence (EDXRF) spectroscopy showed the presence of Cr (4490 ppmw), Fe (2110 ppmw), Ga (90 ppmw) and V



**Figure 35:** This 0.95 ct ruby proved to be Sn glass filled. Photo by Huixin Zhao.

(60 ppmw), as well as significant Sn (680 ppmw) but no Pb (Figure 37). Furthermore, high-definition X-radiography showed a heterogeneous structure that revealed the presence of a foreign material (Figure 38). EDXRF analysis combined with X-ray imaging confirmed the stone to be a Sn glass-filled ruby.

While traditional Pb glass-filled rubies commonly display obvious gas bubbles and orange/blue flash effects (e.g. McClure *et al.* 2006), these features were not seen in this Sn glass-filled sample. Thus, it was more difficult to identify, and gemmologists should be wary of this apparently new type of glass filling.

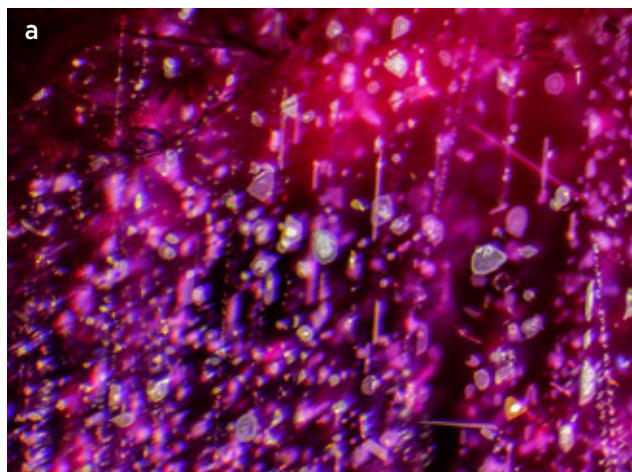


**Figure 36:** Microscopic examination of the treated ruby reveals (a) platy inclusions with a melted appearance and (b) glassy material near the surface of the stone (circled). Photomicrographs by Huixin Zhao; image widths (a) 2.3 mm and (b) 1.5 mm.



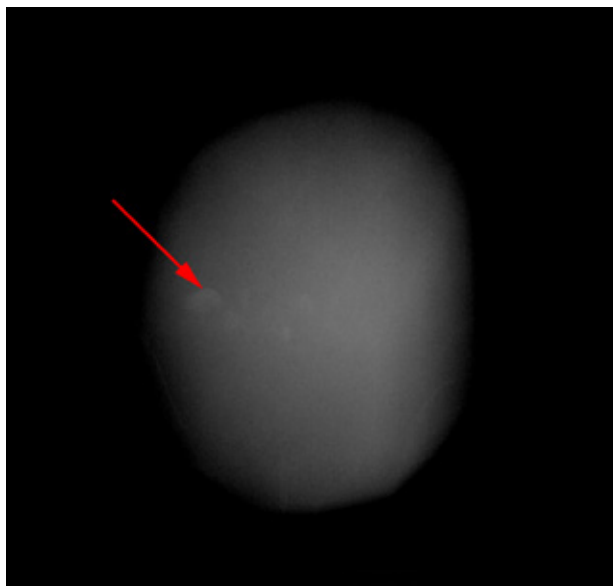
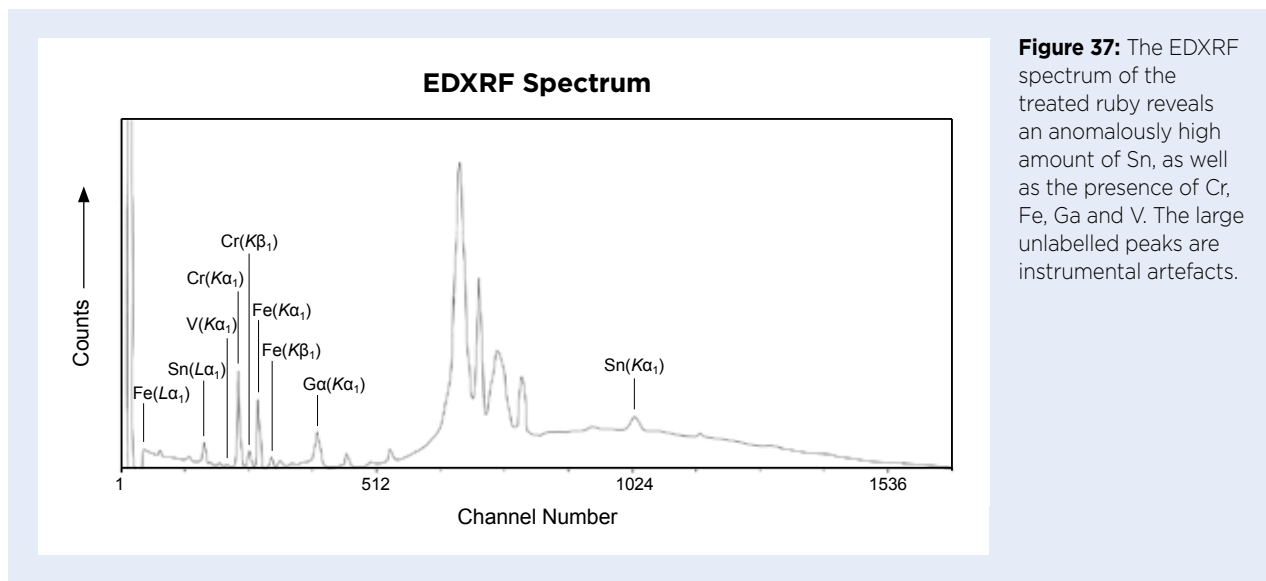


**Figure 38:** X-radiography of the 0.95 ct Sn glass-filled ruby reveals slightly lighter-appearing patchy areas (see arrow) corresponding to the location of the filler in surface-reaching fissures.

Xueying Sun, Yujie Gao ([peter.gao@guildgemlab.com](mailto:peter.gao@guildgemlab.com))  
and Tiantian Huang  
Guild Gem Laboratories  
Shenzhen, China

## References

- Jia, X. & Sit, M.M. 2020. Lab Notes: Bismuth glass-filled Burmese star ruby. *Gems & Gemology*, **56**(1), 139.
- Leelawatanasuk, T., Atitchat [sic], W., Pisutha-Arnond, V., Wattanakul [sic], P., Ounorn, P., Manorotkul, W. & Hughes, R.W. 2013. Cobalt-doped glass-filled sapphires: An update. *Australian Gemmologist*, **25**(1), 14–20.
- McClure, S.F., Smith, C.P., Wang, W. & Hall, M. 2006. Identification and durability of lead glass-filled rubies. *Gems & Gemology*, **42**(1), 22–36, <https://doi.org/10.5741/gems.42.1.22>.
- Vertriest, W. & Saeseaw, S. 2019. A decade of ruby from Mozambique: A review. *Gems & Gemology*, **55**(2), 162–183, <https://doi.org/10.5741/gems.55.2.162>.

## A New Reconstructed Turquoise Imitation Composed of Turquoise Powder with a PMMA (Acrylic) Binder

The authors recently encountered a light greenish blue, slightly flexible, thin plate (about 0.8 ct; 5 × 7 × 0.3 mm), which we initially suspected to be stabilised turquoise. According to the client who submitted it, the material was intended for use in high-end jewellery, although we do not know if the initial supplier intended it for a particular application or if it was developed for a specific purpose (i.e. for mechanical or stability reasons). Some of

its visual characteristics—in particular its homogeneity, lack of inclusions and glassy lustre (Figure 39)—suggested that it was not natural turquoise. Treatments of turquoise are well documented (e.g. Nassau 1994; Fritsch *et al.* 1999), and the use of organic compounds to stabilise such material has been extensively discussed in the literature (Moe *et al.* 2007; Han *et al.* 2015; Schwarzsinger & Schwarzsinger 2017). The major issues

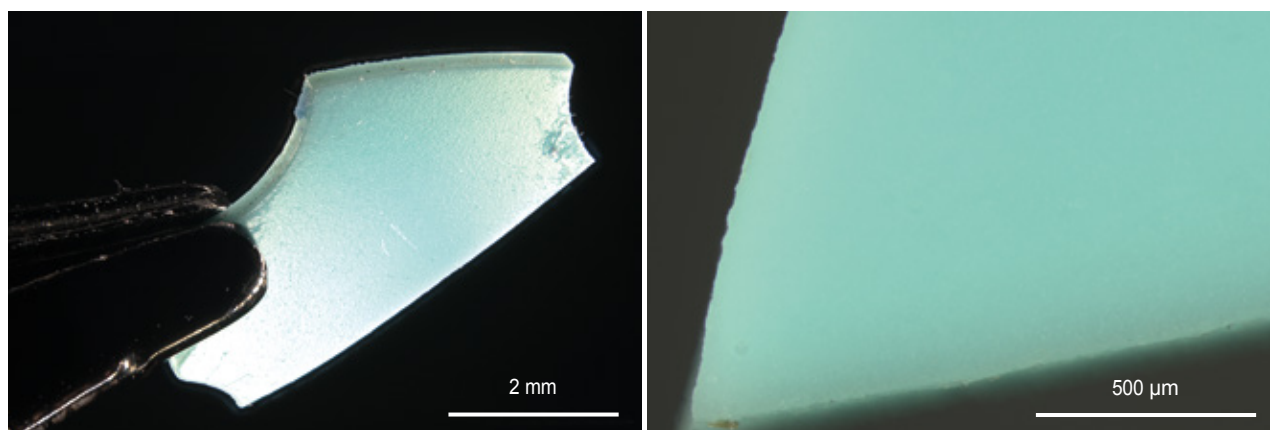


**Figure 39:** Microscopic examination of the turquoise-like specimen shows a glassy lustre (left) and extreme homogeneity, even at the highest available magnification (right). Photomicrographs by F. Blumentritt.

with turquoise are its low lustre and hardness (mainly due to high porosity) and its colour instability (Nassau 1994), which can be minimised by coating with epoxy resin or by injecting a plastic filler into the pores in a vacuum (to remove the air) or under pressure (to push in the filler; Moe *et al.* 2007).

In the present sample, fractures along the edges of the piece appeared relatively smooth compared to those typically seen on turquoise, and the absence of any colour concentrations around fractures excluded the possibility of dyeing (Fritsch *et al.* 1999). Further observations at the highest available magnification of our optical microscope ( $160\times$ ) did not help with determining the nature of the specimen due to its extreme homogeneity (again, see Figure 39). The sample was, unfortunately, not large enough to measure an accurate SG, although this measurement could have been useful for characterising the material, as organic compounds very often have a much lower SG than turquoise (2.6–2.8). The RI was recorded as about 1.55, which is lower than expected for untreated turquoise (about 1.62; Webster 1994).

Specular reflectance infrared spectroscopy showed features consistent with turquoise, along with some minor differences, which we attributed to possible impregnation treatment (Dontenville *et al.* 1985) or a surface coating. EDXRF chemical analysis revealed a composition matching that of turquoise, including the usual minor and trace elements, such as Zn, Sc and As (e.g. Khorassani & Abedini 1976; Fertelmes & Loendorf 2012).

The Raman spectrum (532 nm laser excitation, 10 mW) revealed turquoise signals, as well as the presence of an organic compound identifiable by sharp, intense features around  $3000\text{ cm}^{-1}$  ( $\text{CH}_2$  and  $\text{CH}_3$  vibration modes; Figure 40). These bands are similar to those recently observed in treated turquoise from Armenia (Štubňa & Andrášiová 2021). Among the large list of

possible compounds, we determined that the Raman features correspond best to the acrylic material known as *poly(methyl methacrylate)*, or PMMA (e.g. Plexiglas).

Scanning electron microscopy (SEM; using a JEOL 7600 instrument) was then conducted to determine whether the PMMA was used as a stabiliser for massive porous turquoise or as a binder for turquoise powder. The image in Figure 41 shows disordered tabular grains of turquoise that are up to several micrometres long. They are integrated into an organic matrix that represents at least 20% by volume (estimated visually) of the material. This demonstrates that the material consists of fine grains of turquoise embedded in a matrix of PMMA (as identified above by Raman spectroscopy).

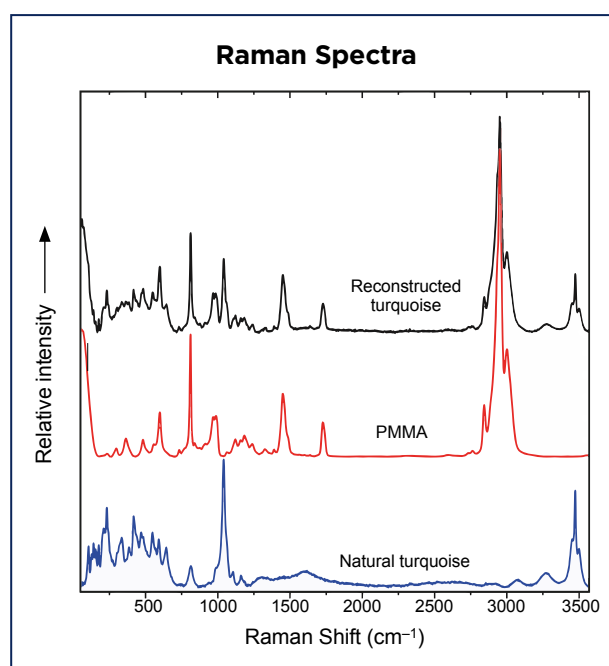


**Figure 40:** The Raman spectrum of the sample is consistent with a mixture of poly(methyl methacrylate), or PMMA, and natural turquoise.

This conclusion is supported by our other observations, such as the thin plate's homogeneity, glassy lustre and slight flexibility.

Assuming that the mixture of turquoise and PMMA is relatively homogeneous, then the amount of PMMA in such a mixture can be calculated from the sample's RI with the following equation:  $1.55 = 1.49x + 1.62(1-x)$  using, respectively, the RI values of 1.49 for PMMA (Speight 2005) and 1.62 for turquoise (Webster 1994). This yields a proportion of 54% PMMA. Although this value does not correlate well with the visual impression of the sample's surface as seen with the SEM (> 20% PMMA), a three-dimensional image of the volume would be needed to estimate it correctly, because the incident electron beam more easily penetrates PMMA than turquoise. Consequently, the presence of PMMA is not as well visualised when there is turquoise just below a PMMA layer that is not thick enough to prevent electrons from passing through it. However, this value reflects the covering of turquoise grains by PMMA at the surface of the plate and confirms the extensive use of organic binder in this material.

The similar practice of cementing together turquoise fragments with some sort of organic material has been mentioned occasionally in the literature (Lee & Webster 1960; Moe *et al.* 2007; Choudhary 2010). In those articles, the organic substance was defined as 'plastic', 'polymer' or 'epoxy resin' without being more specific. Hence, to the authors' knowledge, the use of PMMA to produce

reconstructed turquoise using natural stone powder has not been documented previously in the gemmological literature.

This new reconstructed turquoise imitation could be quite challenging for gemmological laboratories since, without SEM imaging, it could be easily confused with impregnated turquoise. At present, when PMMA is identified in turquoise by Raman spectroscopy, the authors recommend estimating the amount of filler from the RI and SG values, and calling it *reconstructed* in the case where it is estimated that there is more than 20% PMMA. If there is less than 20% PMMA, the material should be referred to as *stabilised* (while specifying that PMMA is used as the stabiliser). Simple tests with heat, fire or solvents might be helpful for laboratories or suppliers wishing to verify whether a sample is impregnated or reconstructed. However, such testing is (micro)destructive, and correlating the resulting reactions with the amount of filler present would need further study.

Dr Féodor Blumentritt

(feodor.blumentritt@ggtl-lab.org)<sup>1</sup>,

Dr Emmanuel Fritsch FGA<sup>2</sup>, Nicolas Stephant<sup>2</sup>,

Dr Stefanos Karampelas<sup>3</sup>, Aurélien Delaunay<sup>3</sup>,

Candice Caplan<sup>1</sup> and Franck Notari<sup>1</sup>

<sup>1</sup>GGTL Laboratories Switzerland, Geneva, Switzerland

<sup>2</sup>IMN-CNRS and University of Nantes, France

<sup>3</sup>Laboratoire Français de Gemmologie, Paris, France

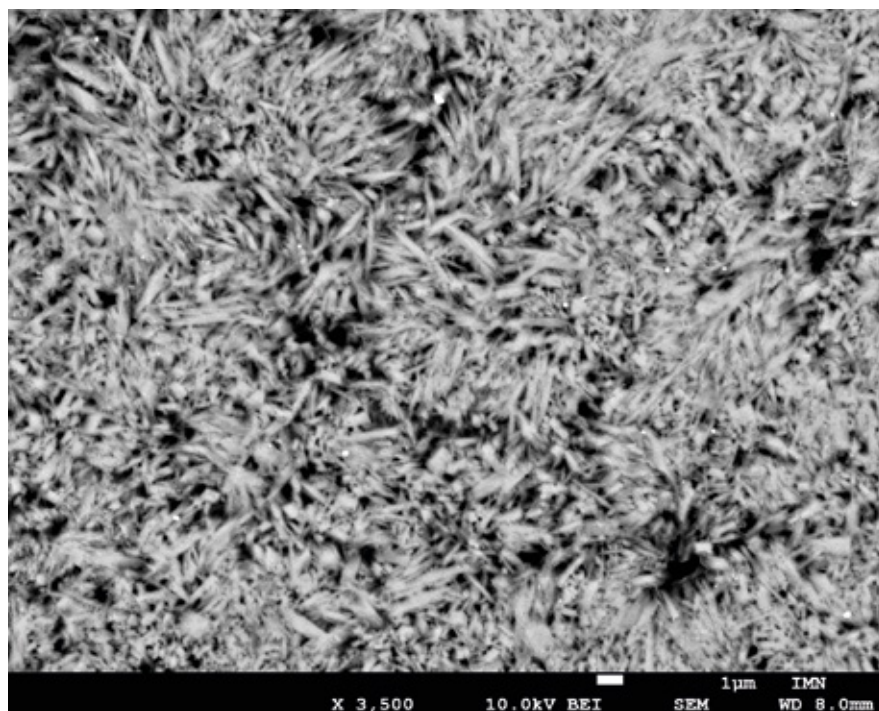


**Figure 41:** In this SEM image of the surface of the sample, use of a backscattered-electron detector, which reflects the chemical composition of the material, shows the global disorder of the turquoise grains (light tones) that are cemented together with organic matter (dark tones). Image by N. Stephant and E. Fritsch.



## References

- Choudhary, G. 2010. A new type of composite turquoise. *Gems & Gemology*, **46**(2), 106–113, <https://doi.org/10.5741/gems.46.2.106>.
- Dontenville, S., Calas, G. & Cervelle, B. 1985. Étude spectroscopique des turquoises naturelles et traitées. *Revue de Gemmologie A.F.G.*, No. 86, 8–10.
- Fertelmes, C.M. & Loendorf, C.R. 2012. *EDXRF Analysis of Disk Beads and Turquoise Artifacts from AZ U:9:90 (ASM), Maricopa County, Arizona*. Material Science Laboratory, Gila River Indian Community Cultural Resource Management Program, Sacaton, Arizona, USA, 25 pp.
- Fritsch, E., McClure, S.F., Ostrooumov, M., Andres, Y., Moses, T., Koivula, J.I. & Kammerling, R.C. 1999. The identification of Zachery-treated turquoise. *Gems & Gemology*, **35**(1), 4–16, <https://doi.org/10.5741/gems.35.1.4>.
- Han, W., Lu, T., Dai, H., Su, J. & Dai, H. 2015. Gem News International: Impregnated and dyed turquoise. *Gems & Gemology*, **51**(3), 343–345.
- Khorassani, A. & Abedini, M. 1976. A new study of turquoise from Iran. *Mineralogical Magazine*, **40**(314), 640–642, <https://doi.org/10.1180/minmag.1976.040.314.12>.
- Lee, H. & Webster, R. 1960. Imitation and treated turquoise. *Journal of Gemmology*, **7**(7), 249–269, <https://doi.org/10.15506/JoG.1960.7.7.249>.
- Moe, K.S., Moses, T.M. & Johnson, P. 2007. Polymer-impregnated turquoise. *Gems & Gemology*, **43**(2), 149–151, <https://doi.org/10.5741/gems.43.2.149>.
- Nassau, K. 1994. *Gemstone Enhancement: History, Science and State of the Art*, 2nd edn. Butterworth-Heinemann, Oxford, 272 pp.
- Schwarzinger, B. & Schwarzinger, C. 2017. Investigation of turquoise imitations and treatment with analytical pyrolysis and infrared spectroscopy. *Journal of Analytical and Applied Pyrolysis*, **125**, 24–31, <https://doi.org/10.1016/j.jaap.2017.05.002>.
- Speight, J.G. 2005. *Lange's Handbook of Chemistry*, 16th edn. McGraw-Hill Education, New York, New York, USA, 1,608 pp.
- Štubňa, J. & Andrášiová, A. 2021. Gem Notes: Turquoise from Armenia. *Journal of Gemmology*, **37**(5), 454–456, <https://doi.org/10.15506/JoG.2021.37.5.454>.
- Webster, R. 1994. *Gems: Their Sources, Descriptions and Identification*, 5th edn., revised by P.G. Read. Butterworth-Heinemann, Oxford, 1,026 pp.



# Gem-A

INSTRUMENTS






OVER 100  
PRODUCTS  
AVAILABLE

## Buy Gem-A Instruments online!

View the full collection at:  
**shop.gem-a.com**

GEM-A  
MEMBERS!

Log in to the Gem-A Instruments website and gain instant access to discounted rates.

**Username** is your Gem-A membership number.

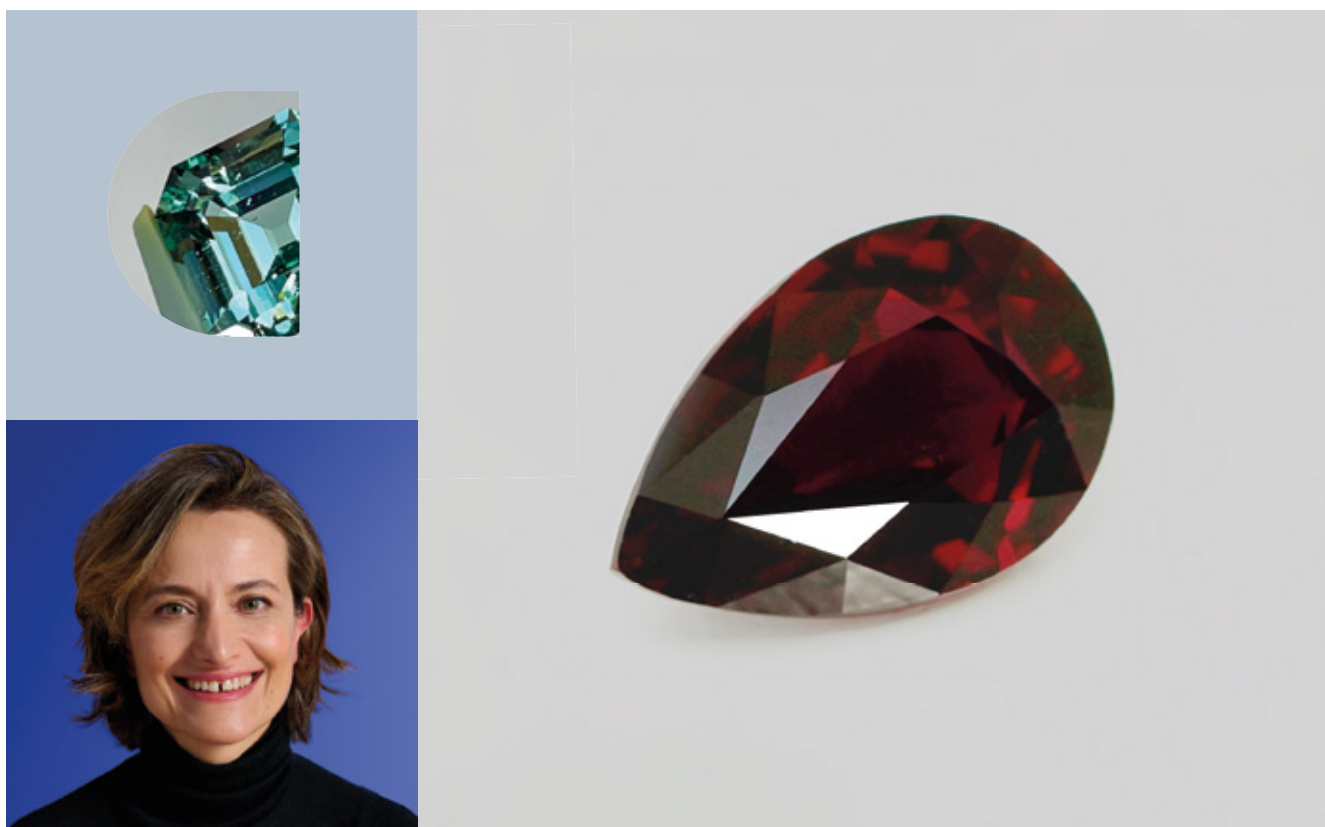
**Password** your surname with a capitalised first letter.

You must log in before adding products to your basket.

We recommend changing your password in the account settings.

# Bid on exceptional gemstones, **selected by** **Catawiki experts**

Every day, our in-house experts carefully select a wide range of gemstones from around the world for every collector.



Purificacion Aquino Garcia  
Expert Gemstones

Buy and sell on [catawiki.com](https://catawiki.com)



# The Imperial Crown of the Holy Roman Empire, Part I: Photoluminescence and Raman Spectroscopic Study of the Gemstones

Lutz Nasdala, Teresa Lamers, H. Albert Gilg, Chutimun Chanmuang N., Martina Griesser, Franz Kirchweger, Annalena Erlacher, Miriam Böhmler and Gerald Giester

**ABSTRACT:** The Imperial Crown of the Holy Roman Empire is not only a unique and outstanding symbol of European history, it is also one of the most significant works of Western goldsmiths' art from the High Middle Ages. However, little is known about the gem materials it contains. As part of an interdisciplinary research project led by the Kunsthistorisches Museum Vienna in Austria, the 172 gemstones in the crown were all conclusively identified for the first time using (non-destructive) photoluminescence and Raman spectroscopy. They include 71 blue sapphires, 50 garnets (22 almandines, 22 pyrope-almandines, five pyropes and one grossular), 20 emeralds, 13 amethysts, four chalcedonies and three spinels. In addition, 11 glass imitations of various colours were identified. Raman spectral details and inclusions in the garnets support their assignment to garnet types previously found to be used in antique and early medieval jewellery. The large red spinel in the centre of the crown's front plate is presumably part of the original crown and, thus, is one of the earliest-known spinels in a historic object, yet it yielded spectroscopic evidence of having been heated.

*The Journal of Gemmology*, 38(5), 2023, pp. 448–473, <https://doi.org/10.15506/JoG.2023.38.5.448>  
© 2023 Gem-A (The Gemmological Association of Great Britain)

From medieval times until 1792, the Imperial Crown (see Figure 1 and the cover of this issue) was used for the coronations of kings and emperors of the Holy Roman Empire. It is octagonal, with eight gold plates (heights between 11.9 and 14.9 cm) joined together by hinges to form the circlet. Affixed to the top of the crown is a removable single arch and cross that were added later (Fillitz 1953). A removable velvet biretta was added much later, and subsequently two iron bands were riveted to the inside walls of the circlet to stabilise its form.

The circlet includes four smaller picture plates with enamelled images (figurative representations from the Bible) surrounded by blue gems and pearls, and four larger

plates adorned by gemstones and pearls only. All the large stones in these eight plates are set atop openings in the gold sheet, facilitating transmitted-light illumination to brighten their colouration and overall appearance (Figure 2). In contrast, the settings in the arch and cross do not have such openings due to their double-sided construction.

The Imperial Crown contains a total of 172 gemstones in different kinds of settings on the circlet, arch and cross. These stones are mostly polished pebbles of oval to irregular shape, but some are distinctly shaped crystal fragments (i.e. green stones, identified as emeralds). A few gems with faceted shapes are considered to be later replacements.



**Figure 1:** The Imperial Crown of the Holy Roman Empire is shown here in a view towards the front right ('Maiestas') plate. The crown weighs 3,465 g, is 24.4 cm high and has a maximum diameter of 28.6 cm. Photo © KHM-Museumsverband (Christian Mendez); reproduced with permission.



The arrangement of the colourful stones together with 241 pearls (plus several hundred small pearls forming the letters on the arch) follows a complex concept that has already been studied in the context of medieval symbolism (Decker-Hauff 1955; Fillitz 1956). There are still many questions, however, concerning the nature of the stones themselves and their history with regard to the crown. Many adjustments, incidents of damage and repairs took place in the crown's long and eventful history, including some gem replacements (e.g. Figure 3). These are suspected in cases where the shape of the opening of the setting does not properly match the shape of the respective gemstone. On the other hand, the characteristics of some gemstones (such as old drill

holes, special cuts or intaglios) indicate an ancient provenance and reuse on the crown.

Apart from a few determinations of the large stones based on visual inspection, the gemstones in the Imperial Crown have never been studied and analysed completely. An article in the Austrian newspaper *Presse* (issued 19 June 1967) titled 'Edelsteintests in der Wiener Schatzkammer' (Gem tests in the Vienna Treasury) summarised an interview with Prof. Dr Hubert Scholler, at that time director of the Mineralogical and Petrological Department of the Natural History Museum Vienna, in which he mentioned future plans to study the gems in the Imperial Crown and other historic objects in the Kunsthistorisches Museum Vienna. However, it took ten





**Figure 2:** Illumination from the inside of the Imperial Crown's circlet (after removal of the arch and velvet biretta) reveals that its large stones are set atop openings in their gold plates. Thus, transmitted light makes the gems appear brighter. Photo © KHM-Museumsverband (Christian Mendez); reproduced with permission.

years until gem-related assessments of the crown were made by Prof. Dr Gero Kurat, Scholler's successor as director of the department. A sketch summarising his determinations of the large stones in the cross, front plate and nape plate is shown in Figure 4. This sketch was made by Dr Rudolf Distelberger, at that time curator of the Secular & Ecclesiastical Treasury (today the Imperial Treasury Vienna). The drawing notes a date of December 1977, but it is not known whether the examination, the sketch or both were made at that time. In the archive of the Kunsthistorisches Museum Vienna, there also exists a copy of a letter dated 20 December 1977 in which a former director of the department, Dr Manfred Leithe-Jasper, thanks Prof. Kurat, together with Dr Gerhard Niedermayr, for inspecting gemstones in the treasury.

There are a number of scientific studies of gemstones in regalia from the Late Middle Ages (1300–1500 CE),

such as the crowns of Saint Wenceslaus (Hyršl & Neumanova 1999) and Blanche of Lancaster (Schmetzer & Gilg 2020), but similar studies are scarce for regalia from the (earlier) High Middle Ages (1000–1300 CE; Bruni *et al.* 2021), such as the Imperial Crown described here. In 2022, a three-year interdisciplinary project 'Crown' ([www.projekt-reichskrone.at](http://www.projekt-reichskrone.at)) started at the Kunsthistorisches Museum Vienna. This project targets, at an advanced level, issues regarding the Imperial Crown's materials, manufacturing technology and state of preservation. It includes the application of numerous optical and analytical investigation methods, together with art-historical and historical studies such as the reassessment of written and pictorial sources, and evaluation of the crown's inscriptions. The project includes, among others, two analysis campaigns (April–July 2022 and several months in 2023). Note that conducting all the desired analyses in one extended campaign was impractical, as the removal of the crown—which is a key exhibit and tourist attraction—from its display needs to be strictly limited in time. The first campaign focused on the optical investigations of all parts of the crown with three-dimensional (3D) microscopic imaging and spectroscopic study of its gemstones, with the latter results reported here. The second campaign will comprise chemical analyses by X-ray fluorescence spectroscopy (micro-XRF and XRF mapping) of the enamel, pearls (with the aim of distinguishing freshwater vs saltwater origin) and selected gemstones.

## HISTORICAL BACKGROUND

The Imperial Crown and its history have been studied many times during the last 200 years, but essential questions are still open and under debate, including

**Figure 3:** This view from above the circlet's front plate (after removal of the adjoining cross) shows that the central large, perforated sapphire (stone A4; width about 2.6 cm) is most likely a later replacement that does not fit well in the cramped setting and is affixed with wire. Photo © KHM-Museumsverband (Herbert Reitschuler); reproduced with permission.



the time and place of its manufacture. For a long time, it was agreed that the circlet of eight golden plates was made before 980 CE, probably for the coronation of Otto I ('the Great') in 962 CE (Decker-Hauff 1955; Kugler 1986; Wolf 1995; Staats 2006). The front cross and the arch were accepted to be later additions from the first half of the eleventh century (Fillitz 1953). Since the 1990s, this dating has been questioned by archaeologists, who link the Imperial Crown's manufacture to the time of the Salian Conrad II (Schulze-Dörrlamm 1991), who ruled the Holy Roman Empire from 1024 to 1039. Historians have even argued that the crown should be assigned to the 1138–1152 reign of Conrad III (Schaller 1997). Proposals concerning its place of manufacture include the towns of Cologne and Essen in the lower

Rhine area, the Benedictine Abbey on the island of Reichenau in Lake Constance, and even goldsmiths' workshops outside present-day Germany, such as in Sicily, Lombardy or even Byzantium.

Medieval texts repeatedly mention the 'Orphan Stone' (from Latin *orphanus*), also referred to as *Pupilla* or *die Waise* (in Middle High German; often modified to *der Weise* in recent publications), as a one-of-a-kind specimen that was part of the Imperial Crown. It was perhaps the most famous gemstone of the Middle Ages in Germany (for a summary, see Buettner 2022 and Quenstedt 2022), heralded as the *aller fürsten leitesterner* ('guiding star to all princes') around 1200. The Orphan Stone was described as a pale reddish to vivid red ('carbuncle') gem that gleamed at night, mounted either

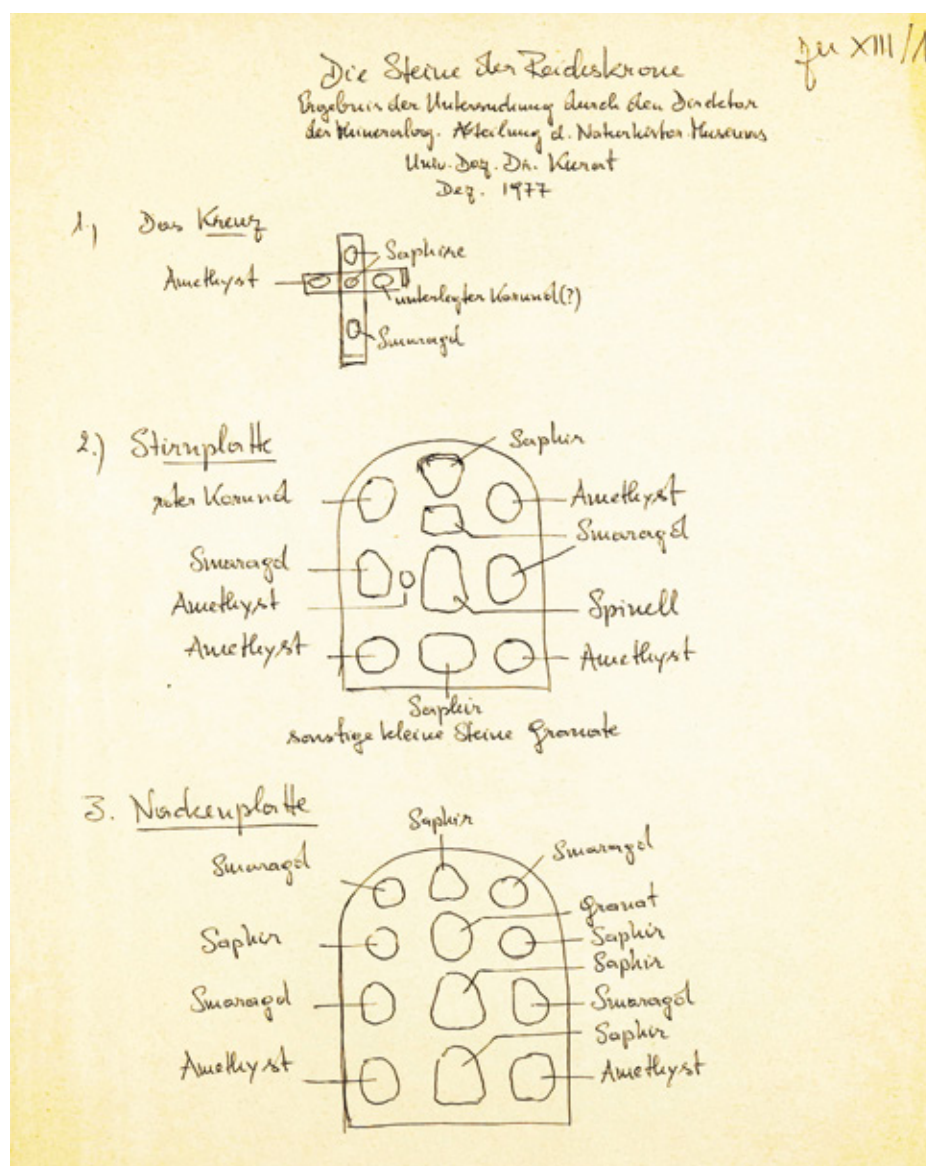


**Figure 4:** This sketch of the cross, front plate and nape plate notes the following (translated from German): 'The stones of the Imperial Crown. Result of the examination by the director of the Mineralogical Department of the Natural History Museum, University Lecturer Dr Kurat Dec. 1977.' All of these identifications were confirmed by the present study except for the right stone in the cross and the upper-left gem in the front plate (indicated in the sketch as *Korund*). © KHM-Museumsverband; reproduced with permission.





**Figure 5:** Detail from a circa 1600 copy of a 1511-13 painting by Albrecht Dürer (1471-1528) shows Charlemagne wearing the Imperial Crown of the Holy Roman Empire. The painting is anachronistic because the Imperial Crown was created at least one-and-a-half centuries after Charlemagne's reign (768–814). © KHM-Museumsverband, Picture Gallery, inv. no. 2771; reproduced with permission.

in the front plate or in the centre of the nape plate. All of these descriptions regarding the Orphan Stone were challenged recently, however, when medieval texts cited as references were declared to be purely fictional stories (Mentzel-Reuters 2004).

The Imperial Crown has had a long—and at times—eventful history. Its earlier times, especially, are rather poorly documented. Some information on its status in later times can be extracted from sixteenth- to eighteenth-century paintings and drawings (see, e.g., Figures 5 and 6). The crown was kept in many different places over the years (Kugler 1986). After 1424, it was deposited in the chapel of Heilig-Geist-Spital in Nuremberg, Germany, and only taken out for coronations, which were initially held in Aachen and later in Frankfurt am Main. Since 1800, the Imperial Crown has been kept in Vienna, except for 1938–1946 when it was brought to Nuremberg to be stored later on during World War II in the Historischer Kunstbunker (a tunnel complex under Nuremberg Castle). Since 1954, the Imperial Regalia—including the Imperial Crown—have been on display in the collection of secular and ecclesiastical treasures at the Hofburg Palace (now the Imperial Treasury Vienna).



**Figure 6:** This coloured copperplate print of the Imperial Crown of the Holy Roman Empire, by Johann Adam Delsenbach (1687-1765), was created around 1751 and released in 1790 as plate 1 of 'Wahre Abbildung der sämtlichen Reichskleinodien' (True representation of all imperial jewels). © KHM-Museumsverband, The Library, inv. no. 35.3261; reproduced with permission.

## MATERIALS AND METHODS

The Imperial Crown is an object of inestimable value. It was, therefore, necessary that all analyses be done on-site and be fully non-destructive, without any opportunity to detach the gems from the crown or otherwise manipulate them. Consequently, it was necessary to use a portable spectrometer system. Basic requirements included an easily positionable detector head and—because of the fairly complex surface shape of the crown—a sufficiently large free working distance.

For spectroscopy, the parts of the Imperial Crown to be analysed (eight-plate circlet, cross and arch) were separately placed onto a turntable (Figure 7), and their positions were manually adjusted by qualified museum conservators. Spectroscopists were forbidden to touch the objects. Options available to visually inspect the stones included hand-held UV and white-light LED lamps, and a 407 nm laser pointer (the last being particularly suitable to excite Cr-related luminescence in gems; see Zeug *et al.* 2022). Analyses were assisted by high-resolution images of stones obtained with a Hirox HRX-01 3D digital microscope. The spectroscopic analyses were carried out over the course of eight working days in May 2022.

Laser-induced photoluminescence (PL) and Raman spectra were obtained using a fibre-coupled WITec confocal Raman probe system with an alpha300 controller. The system featured a probe head equipped with an Olympus 20× objective (numerical aperture 0.25, free working distance 25 mm), a WITec UHTS 300

VIS ultra-high throughput spectrometer (focal length 300 mm) and a Peltier-cooled Andor Newton EMCCD (electron-multiplying charge-coupled device) detector. The system was operated using WITec's Suite Six software. Spectra were excited with the 457 nm emission of a diode laser (using a power of 0.05–8.5 mW at the sample surface for PL measurements depending on the emission intensity, and 8.5 mW for Raman measurements). The use of a green laser (532 nm excitation) was not considered, as it is well known that Raman spectra of several coloured stones (especially corundum) are strongly obscured by luminescence in the green range. For PL analyses, we used a diffraction grating with 600 grooves/mm, yielding an approximate spectral resolution in the range of 5 cm<sup>-1</sup> (red) to 4 cm<sup>-1</sup> (nearest IR). The Raman-scattered light was analysed by means of a diffraction grating with 1,800 grooves/mm, resulting in a spectral resolution of 3 cm<sup>-1</sup> (for blue light).

PL spectra were calibrated using lines of an Ar/Hg spectral lamp, and the accuracy of PL emissions in the red to near-infrared (NIR) range was better than  $\pm 0.03$  nm. All Raman spectra obtained included a small part of the anti-Stokes region, and the position of the Rayleigh line (Raman shift 0 cm<sup>-1</sup>) was used to check and adjust wavenumber calibration, resulting in an accuracy of Raman shifts better than  $\pm 0.5$  cm<sup>-1</sup>. After appropriate background correction, Raman spectra of spinels were fitted assuming asymmetric pseudo-Voigt shapes (Slotznick & Shim 2008). Fitted FWHM (full width at half band maximum) values were corrected for the artefact of experimental band broadening according to Váczi (2014).

To document and discuss the analytical results for the gemstones (Figure 8), we followed the internal sample labelling system of the Kunsthistorisches Museum

Vienna, which consists of combinations of letters and digits. The eight plates of the circlet are labelled A to H, counter-clockwise when seen from the top, beginning with A for the front plate. Thus, the left temporal plate is designated C, the nape plate is E, and so on (again, see Figure 8). The cross is designated K for the German *Kreuz* (cross). The two sides of the arch are designated BgCh and BgRo, which are derived from (1) the German *Bügel* (arch) and (2) the first two letters of the inscriptions formed by several hundred small pearls: on the arch's left side 'CHVONRADVS DEI GRATIA' and on the right side 'ROMANORV[M] IMPERATOR AVG[VSTVS]'. For the sample label of each gemstone, the following digit refers to consecutive horizontal numbering, from left to right, of both gemstones and large pearls on each single object, from top to bottom.

Reference materials consisted of the following: a clear, pinkish red gem spinel (Ratnapura, Sri Lanka), three almandines (from Garibpet and Rajmahal, India, and a Sasanian engraved gem), a Ca-poor pyrope-almandine (a Roman engraved gem from the Helmut Hansmann collection, Staatliche Antikensammlung München, inv. no. NI-15.046-473), a Ca-rich pyrope-almandine bead (from Anuradhapura, Sri Lanka; no. 23 in Schüssler *et al.* 2001), a grossular (Kamburupitiya, Sri Lanka) and two graphite samples (crystalline from Kahatagaha, Sri Lanka, and disordered from Saskatchewan, Canada). As one of the spinels in the crown showed spectroscopic evidence of heating, and to systematically document the effects of heat treatment on the PL and Raman spectra of gem spinel, two chips from our reference sample were placed in a platinum crucible and heated (in air) at a rate of 30°C per minute to 700°C and 1000°C, respectively. After two hours, the furnace was then switched

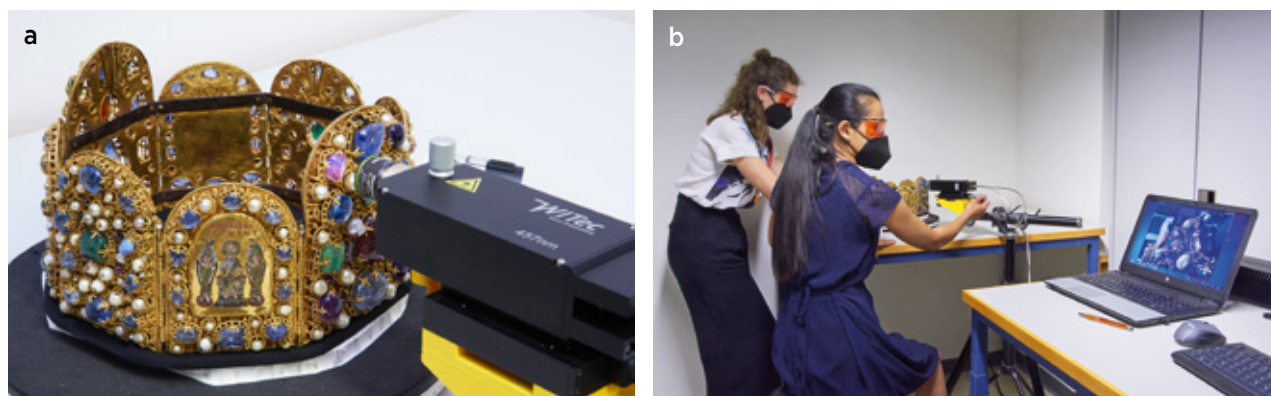


**Figure 7:** (a) The object (here the circlet after removal of the velvet biretta, arch and cross) was placed on a turntable in front of the position-adjustable probe head. Note the two inner, riveted iron strips that were mounted during an early modification phase of the crown to stabilise the octagon. (b) For Raman spectroscopy, the gem to be analysed was first roughly focused by minimising the laser spot seen in the video image, and then further focused by maximising the spectroscopic signal of interest. Shown here are authors CCN (right) and TL (left); they are wearing face coverings to protect the crown—especially its enamel figures—from the moisture of exhaled air. Photos © KHM-Museumsverband (Christian Mendez); reproduced with permission.

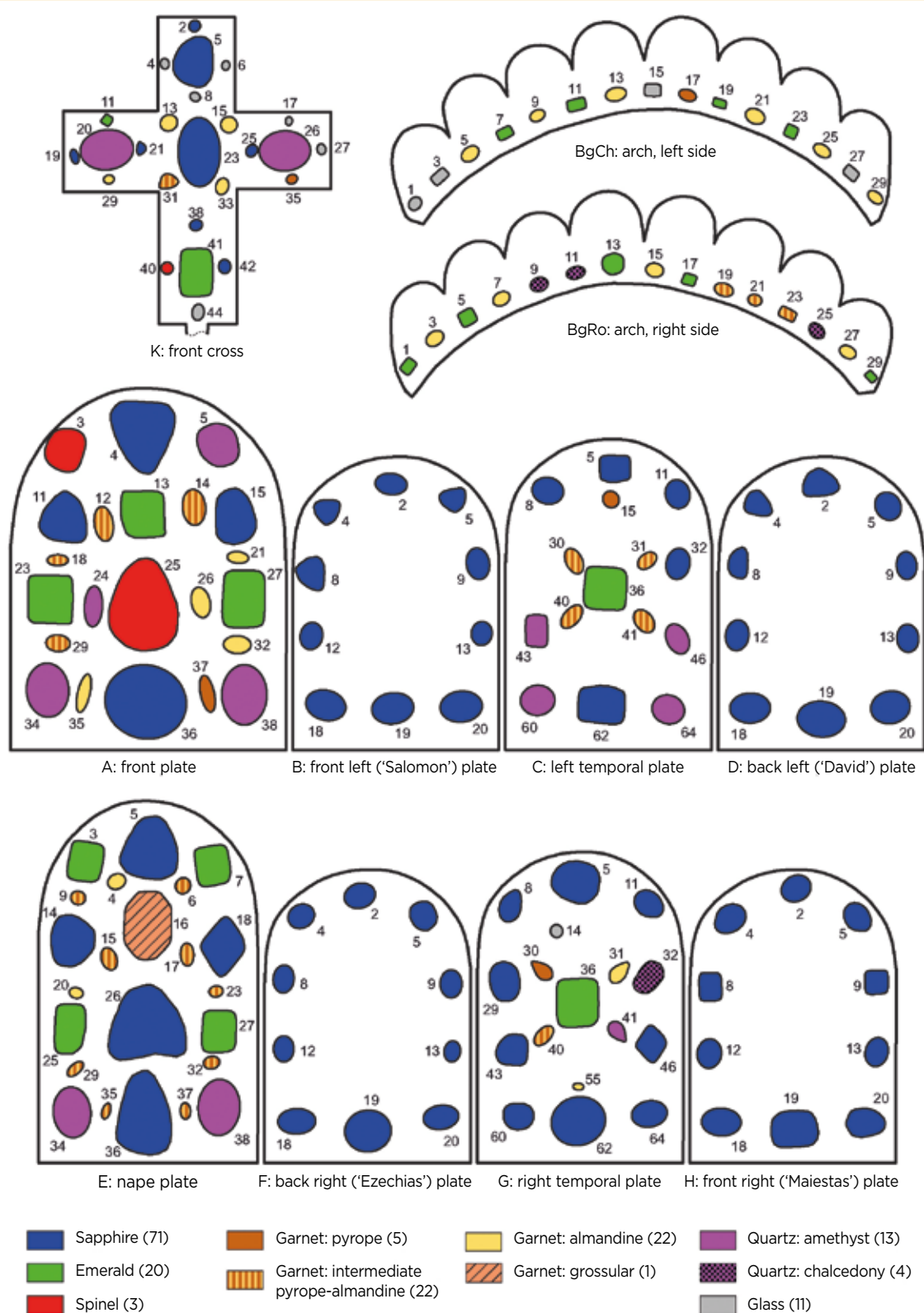


**Figure 8:** This drawing illustrates the distribution of the inorganic gem materials in the various components of the Imperial Crown, as identified in this study. For clarity and relevance to the present article, only inorganic gems are shown; pearls and enamelled areas are not indicated. The cross has been enlarged (by about 1.3×) relative to all other parts of the crown for clarity in labelling its many small stones. Sample numbers used throughout this article relate to the designations shown here.



off and each sample was allowed to cool down slowly (i.e. over several hours) in the closed furnace. To collect reference spectra, three spectrometers were used. Photoluminescence and Raman spectra with 473 nm excitation (0.42 and 17 mW, respectively) were obtained using a Horiba LabRAM HR Evolution system. With a diffraction grating of 1,800 grooves/mm in the beam path, the spectral resolution was in the range between  $1.2\text{ cm}^{-1}$  (for blue light) and  $0.6\text{ cm}^{-1}$  (NIR). Additional experimental details are described in Zeug *et al.* (2018). Raman spectra with 532 nm (14 mW) excitation were obtained using a Horiba XploRA Plus system equipped with a diffraction grating of 1,800 grooves/mm; for further details see Schmetzer *et al.* (2017). The garnet from Staatliche Antikensammlung München was analysed using a WITec alpha300 R Raman microscope with 532 nm (3.5 mW) excitation; more details are reported in Gilg and Gast (2012).

## RESULTS AND DISCUSSION

### Photoluminescence Analysis

More than half of the gemstones in the Imperial Crown yielded more-or-less intense PL in the red-to-NIR range of the electromagnetic spectrum. In many cases, the

emission was easily seen with the unaided eye, especially upon illumination with the 407 nm laser pointer (Figure 9). Detection and analysis of such strong spectroscopic signals enabled a relatively uncomplicated study of the stones. In particular, the identification of sapphires—as corundum is a relatively poor Raman scatterer—became quite straightforward: depending on the respective emission intensity, laser-induced PL had a count rate between 25 times (stone G5) and 200,000 times (stone F18) higher, compared to the count rate of the main Raman band. Analysing a suspected sapphire by maximising the signal intensity of the red PL emission was thus considerably easier than relying on the Raman signal. The same procedure was used for suspected emeralds and spinels.

A total of 94 gemstones in the Imperial Crown (71 sapphires, 20 emeralds and three spinels; Figures 10–12) were identified from their characteristic PL spectra (Figure 13). Emissions of all three gem minerals are mainly related to  $\text{Cr}^{3+}$  (even though contributions of other emission centres, such as  $\text{V}^{2+}$ , need to be considered; cf. Ollier *et al.* 2015). The obvious differences in emission characteristics among the three gem minerals are due to different effects of the crystal field surrounding the  $\text{Cr}^{3+}$  ions (for a summary, see Box B in Zeug *et al.* 2022).



**Figure 9:** A large, transparent sapphire in the bottom centre of the circlet's right temporal plate (stone G62; 2.1 cm long) shows (a) vivid blue colour in ambient room lighting, but (b) intense pinkish red emission from a 407 nm laser pointer. Photos © KHM-Museumsverband (Christian Mendez); reproduced with permission.

Corundum has a fairly strong crystal field, resulting in a comparably large energy difference between the  $^2E$  and  $^4T_2$  excited levels. Direct  $^4T_2 \rightarrow ^4A_2$  electronic relaxation does not occur at room temperature. Instead, excited electrons undergo fast intersystem crossing from the  $^4T_2$  to the split  $^2E$  level (Kisliuk & Moore 1967). The emission is therefore dominated by spin-forbidden  $^2E \rightarrow ^4A_2$  relaxation, observed as two narrow *R* lines (Nelson & Sturge 1965) at 14405 and 14436  $\text{cm}^{-1}$  (694.2 and 692.7 nm in Figure 13). Low-intensity PL features in the range 13500–15250  $\text{cm}^{-1}$  (about 740–655 nm) are caused by vibronic sidebands (couplings of main emissions with lattice vibrations; Rothamel *et al.* 1983). The narrow *N* lines at 14203 and 14267  $\text{cm}^{-1}$  (704.1 and 700.9 nm; analogues of *R* lines that are caused by closely spaced  $\text{Cr}^{3+}$  pairs; Powell *et al.* 1967) were not observed in our spectra. This is due to the generally low  $\text{Cr}^{3+}$  concentrations of the pale greyish blue (e.g. Figure 10a) to vivid blue (e.g. Figure 10b) sapphires. Emission patterns of all 71 sapphires were fairly similar, but with vast differences in absolute intensity, which might in first approximation be correlated to the Cr content in

each gem. However, no general correlation between sample colour and emission intensity was observed, which reconfirms that the intensity of blue sapphire colouration is independent of Cr content.

The emission spectrum of beryl (Figure 13), with its comparatively weak crystal field, is dominated by a broad hump in the range 11500–15500  $\text{cm}^{-1}$  (about 870–645 nm) that is assigned to spin-allowed  $^4T_2 \rightarrow ^4A_2$  electronic relaxation. This is superimposed by two low-intensity, quite broad *R* lines at 14615 and 14695  $\text{cm}^{-1}$  (684.2 and 680.5 nm) that are due to the spin-forbidden  $^2E \rightarrow ^4A_2$  electronic transition (Kisliuk & Moore 1967; Ollier *et al.* 2015) of  $\text{Cr}^{3+}$  and/or  $\text{V}^{2+}$ . In our beryl spectra, total PL intensity and relative intensity of the *R* lines correlated with sample colour (Figure 13) and, hence, presumably with chemical composition. Pale green emeralds (such as BgRo29) yielded low-intensity PL with relatively clear *R* lines, whereas in the higher-intensity emission spectra of vivid green stones (such as E25; Figure 11a) the *R* lines were poorly resolved (again, see Figure 13). For the latter, the main hump was shifted notably towards lower wavenumbers (from

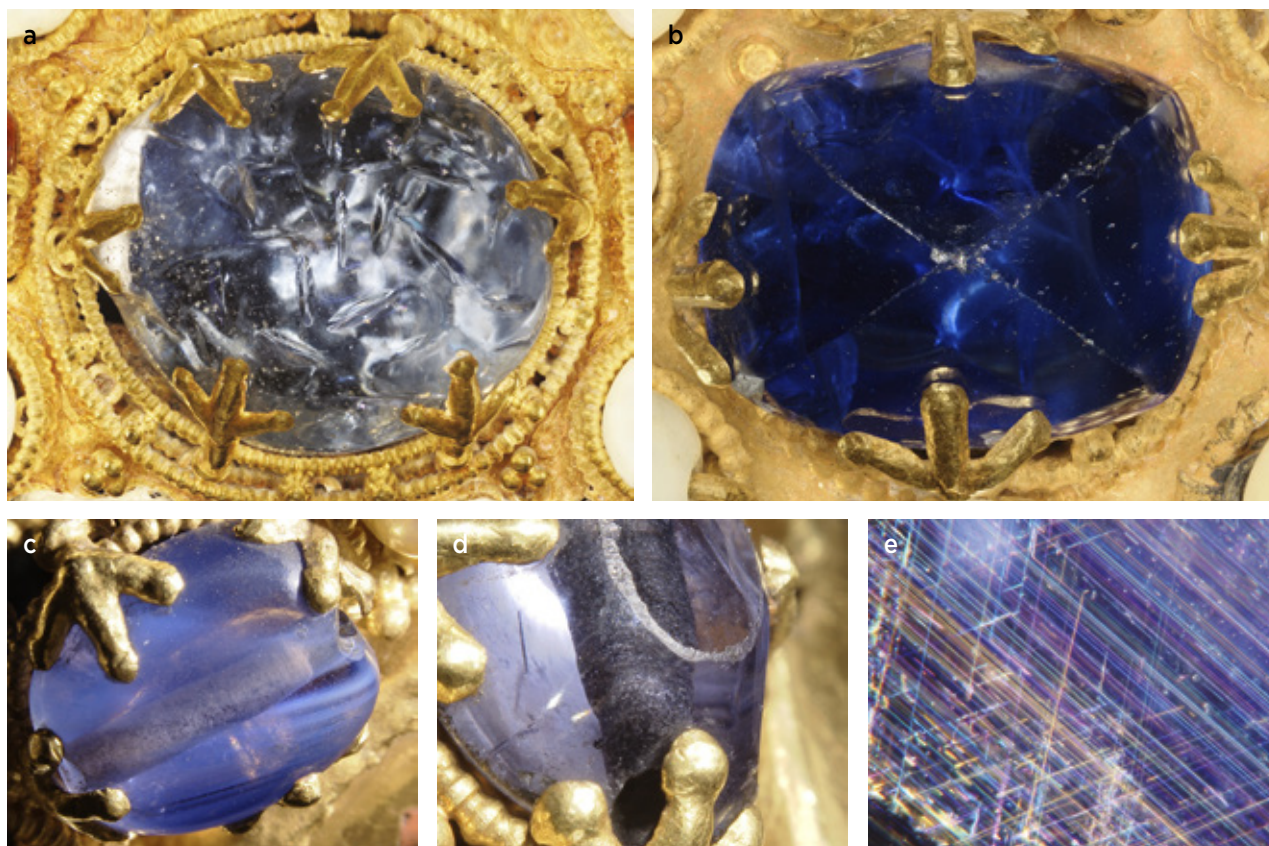


**Figure 10:** The sapphires in the crown range from (a) pale blue (stone A36, image width 4.0 cm) to (b) dark 'cornflower' blue (C62; image width 2.3 cm). (c) Many of the sapphires show growth zoning, as can be seen at lower right in this drilled cabochon (H4; image width 1.4 cm). (d) Drill-hole walls are, in some cases, coated with graphitic carbon (F8; image width 7.8 mm). (e) Oriented rutile needles such as these were seen in several of the sapphires (C5; image width 1.7 mm). Photos © KHM-Museumsverband (Herbert Reitschuler); reproduced with permission.



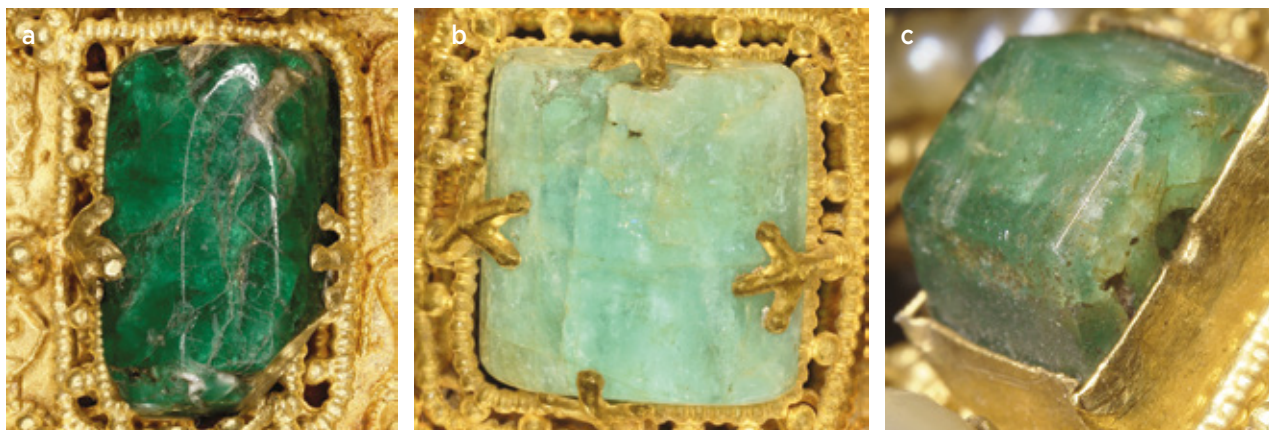


**Figure 11:** Emeralds in the crown range from (a) vivid green (stone E25; image width 1.9 cm) to (b) pale green (A23, image width 2.3 cm). (c) Some of the emeralds are only lightly polished and still exhibit a natural hexagonal prismatic crystal shape (BgCh23; image width 6.9 mm). Photos © KHM-Museumsverband (Herbert Reitschuler); reproduced with permission.

about 13750 to 13500  $\text{cm}^{-1}$ , or about 727 to 741 nm), which could indicate an increased contribution of the  $^4T_2 \rightarrow ^4A_2$  electronic transition of  $V^{2+}$  (Ollier *et al.* 2015).

Similar to corundum, Mg-Al spinel has a rather high crystal-field strength, and the emission is therefore controlled by the spin-forbidden  $^2E \rightarrow ^4A_2$  electronic transition. However, compared to sapphire and emerald, the PL pattern of gem spinel is much more complex (Figure 13). For a summary description of the emissions, see Brik *et al.* (2016) and references therein. In addition to the *R* line near 14590  $\text{cm}^{-1}$  (685.4 nm), there are several *N* lines, which are assigned to either  $\text{Cr}^{3+}$  pairs or cation perturbations in the host ('structure-dependent' *N* lines; Mikenda & Preisinger 1981). Both *R* and *N* lines have fairly strong vibrational couplings (Mohler & White 1995), generally referred to as phonon sidebands. All aforementioned spectral components sum up to a typical fingerprint pattern of emission features (again, see Figure 13) that enables straightforward

spinel identification. The integral emission intensities in the red range obtained from the violet-to-pinkish red spinels A25 and A3 (Figure 12a, b) were similar, whereas reddish orange spinel K40 (Figure 12c) emitted about four times as much red light under comparable experimental conditions (laser power and measurement time).

### Raman Analysis: General Results

Our identifications of all sapphires (for a reference spectrum, see Porto & Krishnan 1967), emeralds (Hagemann *et al.* 1990) and spinels (White & DeAngelis 1967) were confirmed by their Raman spectra (not shown). However, many Raman spectra were obscured by more-or-less intense background luminescence. This was especially the case for the vivid green emeralds (A13, A27, E25 and G36), which generated such strong background signals that it was impossible to obtain Raman spectra in the O-H stretching region (although the elevated background did not prevent mineral



**Figure 12:** There are only three spinels in the crown: two large specimens (a) A25 (image width 3.6 cm) and (b) A3 (image width 2.0 cm) mounted in the front plate, and (c) a small stone of rather low quality (K40; image width 4.7 mm) in the cross. Photos © KHM-Museumsverband (Herbert Reitschuler); reproduced with permission.

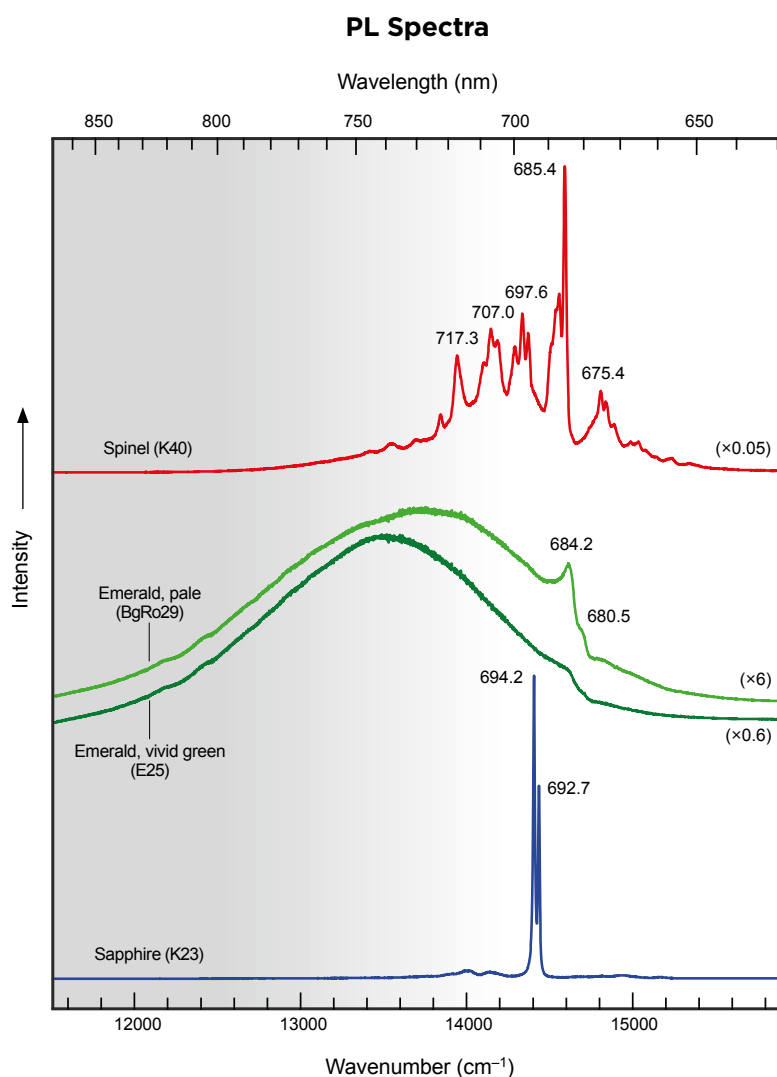


**Figure 13:** Representative PL spectra (457 nm excitation) are shown for three Cr-containing gem minerals in the Imperial Crown: sapphire, emerald (pale and vividly coloured examples) and spinel. The spectra are offset vertically for clarity, and the emission intensity of the spectrum of stone K23 (one of the lowest-PL sapphires in this study) was adjusted for clarity and comparison. The NIR spectral range not visible to the human eye is shaded grey.

identification in the Raman shift range of 100–1200  $\text{cm}^{-1}$ ). Water bands could only be identified in some of the low-luminescence, pale-coloured emeralds (such as C36 and E7). Here, the O–H stretching range (again, not shown) is dominated by a symmetric band at 3597  $\text{cm}^{-1}$ , which is assigned to ‘type II water’ (Huong *et al.* 2010); that is, water molecules adjacent to alkali ions in structural channels. Consequently, these pale emeralds originated from alkali-rich ‘schist type’ deposits.

The remaining 78 stones in the crown were identified only from their Raman spectra. They included 11 glass, 17 quartz and 50 garnet specimens.

The glass gems in the Imperial Crown (e.g. Figure 14) were presumably selected by goldsmiths according to colour, to imitate more valuable gems. Colours span the wide range from vivid green (K4, BgCh3, BgCh15 and BgCh27), pale green (K17), deep bluish green (K6) and

greenish blue (K8); vivid blue (K27 and K44); and red (G14) to dark brownish red (BgCh1). Obtaining Raman spectra from the glass specimens was challenging. Glass has a much lower Raman-scattering intensity than most crystalline gem materials, and the poor signal was typically overlain by weak-to-strong background phenomena (in some cases including intense luminescence of material underlying the stones in the settings). Adjusting the probe head position in order to maximise the low-intensity Raman signal was, therefore, tedious and time-consuming. Even though the identity of the glasses had been suspected from bubble-like inclusions observed with the optical microscope, it was desirable to provide positive spectroscopic evidence of their identity. All these stones yielded spectra (not shown) dominated by a broad double band or plateau at 950–1100  $\text{cm}^{-1}$  (several stretching modes) and a broad band at 550–620



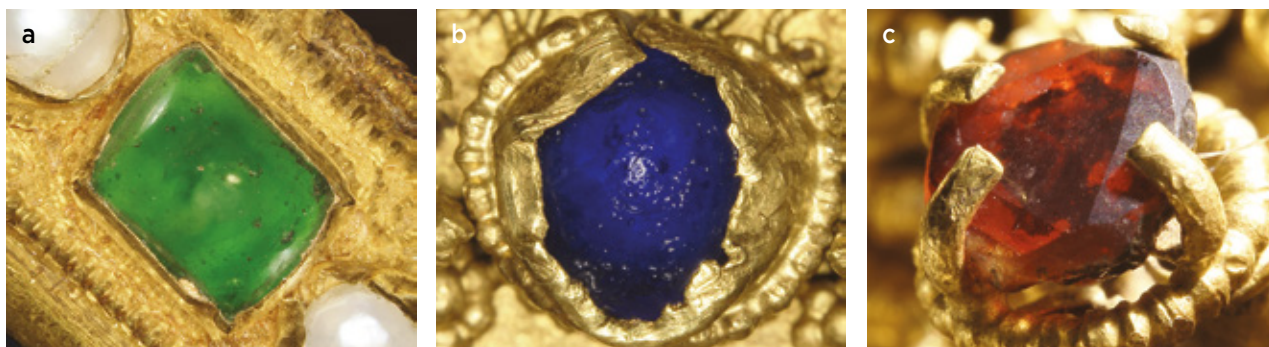


**Figure 14:** Three of the 11 glass gems in the crown are shown here: (a) BgCh27 (image width 1.2 cm), (b) K44 (image width 7.7 mm) and (c) G14 (image width 6.4 mm). Photos © KHM-Museumsverband (Herbert Reitschuler); reproduced with permission.

$\text{cm}^{-1}$  (bending), which characterises them as silicate glasses (Colomban 2003; Colomban *et al.* 2006; Neuville 2006).

Quartz samples consisted of 13 amethysts of diverse transparencies and hues, and four chalcedonies (e.g. Figure 15). Raman spectra of amethysts K26 and C60 were obscured by a flat background that increased towards higher Raman shifts; the background intensity depended quite strongly on the focused sample point.

This phenomenon is rather unusual for macro-crystalline amethyst, and we attribute it to luminescence arising from foreign material (such as tissue, foil or glue) underlying the stones. The occasional presence of such material is supported by the observation that stone K26 resembled rose quartz or carnelian with white-light LED illumination from the front, but when illuminated from the side it appeared pale lilac. Its pink-to-brownish

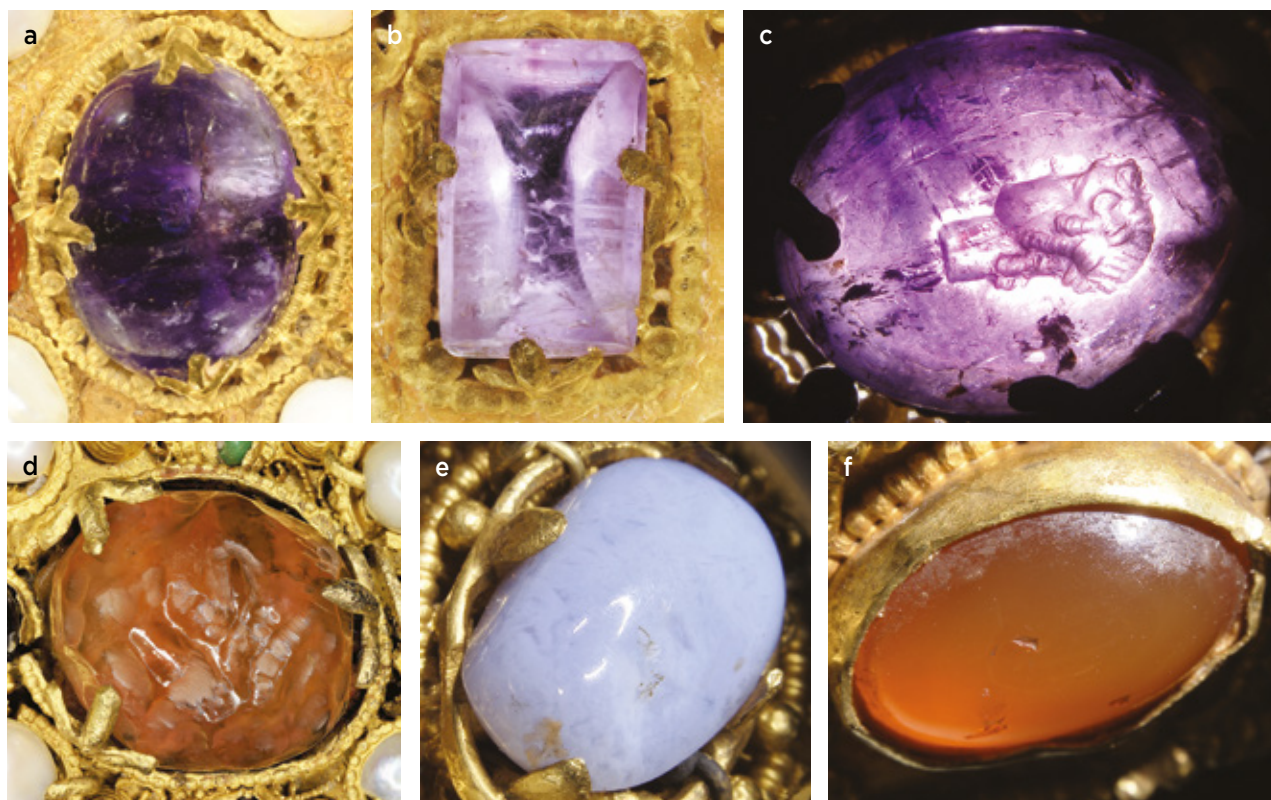


**Figure 15:** Quartz-family gems in the crown consist of amethyst and chalcedony. Most of the amethysts are (a) cabochons (stone A38; image width 2.4 cm) or (b) have a rectangular shape (C43; image width 1.2 cm). (c) Amethyst C64 at the lower left corner of the left temporal plate, seen here in transmitted light, consists of an intaglio showing the head of Apollon (image width 1.4 cm). (d) In spite of its appearance, stone K26 is not carnelian or rose quartz but rather very pale amethyst with a colour appearance that comes from an underlying reddish substance (image width 1.9 cm). (e) This pale bluish, milky chalcedony (G32; image width 1.2 cm) has a non-fitting prong setting in an apparent 'sapphire place' in the right temporal plate, which suggests it is a replacement. The three other chalcedonies are bezel-set in the arch's right side; two are pale greenish grey and (f) one has carnelian colour (BgRol1; image width 9.4 mm). Photos © KHM-Museumsverband (Herbert Reitschuler); reproduced with permission.

colouration seemed to come from a waxy reddish substance behind the stone. (For the assignments of quartz bands, see Etchepare *et al.* 1974.)

The chalcedonies were orange (carnelian BgRo11), milky white (G32) and an almost emerald-like pale greenish grey (BgRo9 and BgRo25). Their spectra (not shown) were all somewhat affected by background signal. In Raman spectra, fibrous chalcedony is distinguished from macro-crystalline quartz by an additional band at 502–503  $\text{cm}^{-1}$  that is assigned to a combination of the main band of moganite (a monoclinic  $\text{SiO}_2$  polymorph commonly occurring in chalcedony) and chemically bound water forming silanol ( $\text{SiOH}$ ) groups (Schmidt *et al.* 2014).

Although the main objective of our first analytical campaign was the unequivocal identification of all inorganic gem materials in the crown, a few attempts were made to identify large, near-surface inclusions and accompanying phases, mainly based on high-resolution images of individual stones. Several of the sapphires had been used in other jewellery before being set in the Imperial Crown, as indicated by drill holes. One such hole in a sapphire contained a black substance covering its inner wall (Figure 10d), which was found to be strongly disordered graphitic carbon (Figure 16a; cf. Beyssac & Lazzeri 2012).

Whitish to pale grey inclusions in the emeralds were identified as apatite (Klee 1970) and Mg and Ca-Mg carbonate (Rividi *et al.* 2010). The two carbonate spectra (not shown) differed especially in the low-energy range comprising translational (around 200  $\text{cm}^{-1}$ ) and librational (around 300  $\text{cm}^{-1}$ ) external cation-carbonate vibrations.

Another interesting finding was a fairly strong band pattern in the Raman spectrum of the pale green glass K17 (Figure 16b). A similar pattern (although of lower intensity) was also detected in the dark bluish green glass K6. This spectrum matches the Raman pattern of a pigment known as ‘lead tin yellow type II’ (cubic  $\text{PbSn}_{1-x}\text{Si}_x\text{O}_3$ ; Šefců *et al.* 2015), although another pigment called ‘Naples yellow’ (cubic  $\text{Pb}_2\text{Sb}_2\text{O}_7$ ; Bell *et al.* 1997; Antušková *et al.* 2022) cannot be excluded at this time.

### Raman Analysis: Garnets

In discussing Raman spectra of garnets, we use the band numbering system (from I to XVI) of Pinet and Smith (1994). For band assignments, see Hofmeister and Chopelas (1991) and Kolesov and Geiger (1998). For possible provenance assignments of garnets, the A–G cluster system of Then-Obłuska *et al.* (2021) is used here. Cluster assignments are based on chemical composition, which in turn influences Raman spectral characteristics

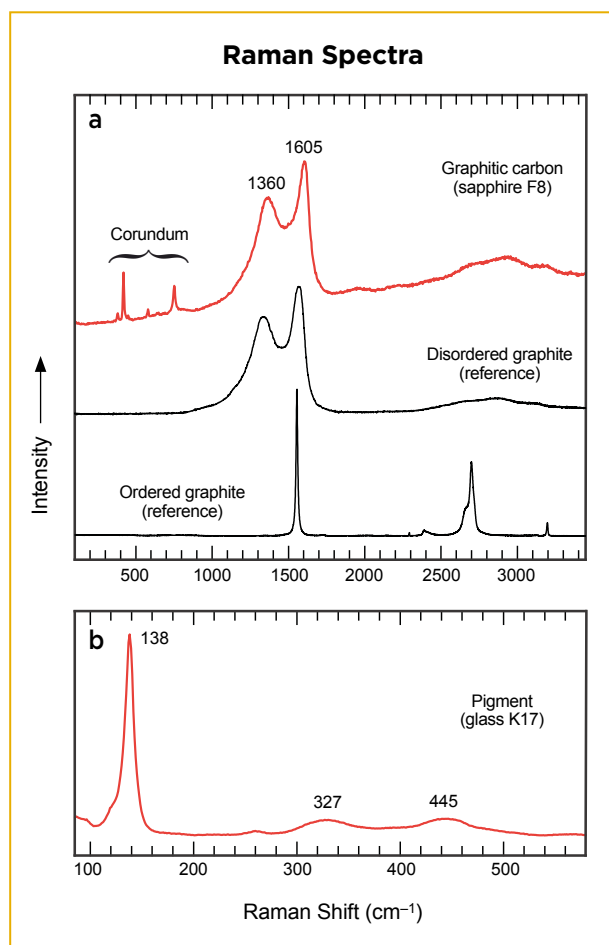


**Figure 16:** Selected Raman spectra (457 nm excitation) are shown for (a) a black substance in the borehole of sapphire F8, which consists of disordered  $\text{sp}^2$  (graphitic) carbon (reference spectra were obtained with 473 nm excitation), and (b) the pigment in the pale whitish green glass K17, which is assigned to ‘lead tin yellow type II’.

and observed inclusion assemblages. Abbreviations of mineral names are from Whitney and Evans (2010).

Among the garnets in the Imperial Crown, 49 were members of the binary pyrope-almandine system,  $(\text{Mg}, \text{Fe}^{2+})_3\text{Al}_2(\text{SiO}_4)_3$  (no spessartine was found), and only one was grossular,  $\text{Ca}_3\text{Al}_2(\text{SiO}_4)_3$  (Figure 17). The 49 Mg-Fe garnets showed some variations in colour, Raman spectra and inclusions. Most of them were vivid red to reddish brown to dark brownish red (such as C40; Figure 17a), with only a few having lighter colouration (such as brownish yellow A14 or pink E32; Figure 17b). Most of the Raman spectra of Mg-Fe garnets (45 out of 49) could be classified into seven distinct categories: four types of almandine (Alm 1 to Alm 4), two types of intermediate pyrope-almandine (Prp-Alm 1 and Prp-Alm 2) and one type of pyrope (Prp; see Figure 18 and Table I). These different garnet types also showed distinct inclusion characteristics (Figures 19 and 20; Table II). The Raman



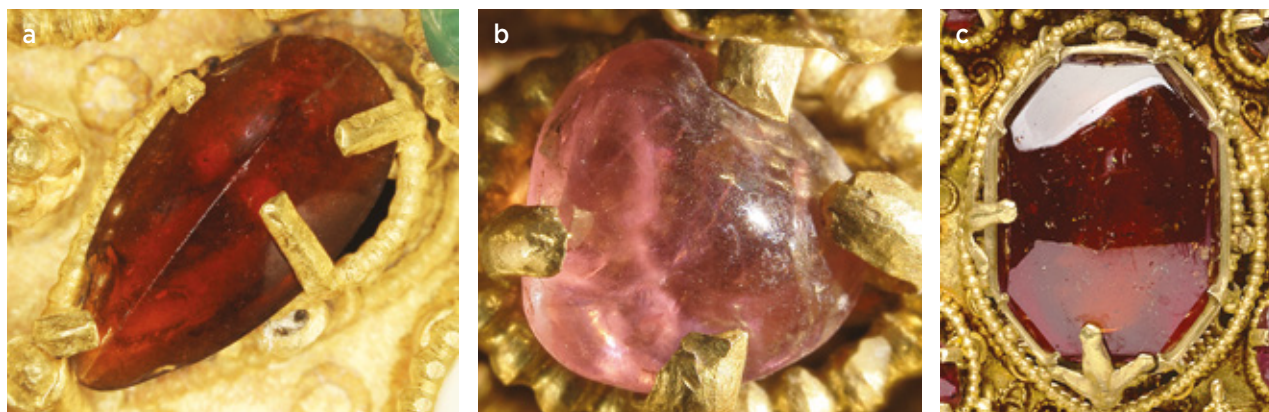


**Figure 17:** Almost all garnets in the crown belong to the pyrope-almandine series. Most commonly they are (a) vivid red to reddish brown (C40; image width 11.8 mm), but (b) a few show lighter colour (E32; image width 6 mm). (c) A single garnet in the crown, in the centre of the nape plate, is grossular—a large, well-polished stone of octagonal shape (E16, image width 3.2 cm). Photos © KHM-Museumsverband (Herbert Reitschuler); reproduced with permission.

band positions and observed inclusion characteristics of these types match those of garnets used in jewellery from the Hellenistic period to late antiquity (e.g. Rösch *et al.* 1997; Schüssler *et al.* 2001; Calligaro *et al.* 2002; Gilg *et al.* 2010; Gilg & Gast 2012; Thoresen & Schmetzer 2013; Gilg & Gast 2016; Schmetzer *et al.* 2017; Gilg *et al.* 2018; Kos *et al.* 2020; Then-Obłuska *et al.* 2021). Only four garnets (A14, C31, BgRo19 and BgRo21) yielded Raman band positions located between these seven types, and hence have intermediate chemical compositions.

The positions of the Raman bands in the various garnet types are summarised in Table II. Low Raman shifts of band V ( $F_{2g}$  mode related to  $SiO_4$  bending) below  $636\text{ cm}^{-1}$  and of band XII ( $A_{1g}$  mode related to rotations) below  $349\text{ cm}^{-1}$  are indicative of almandine-rich garnets, while values above  $639$  and  $355\text{ cm}^{-1}$ , respectively, characterise pyrope-rich compositions (Pinet & Smith 1994). Both bands are barely affected by additional spessartine (Mn) and grossular (Ca) components. By contrast, the spectral positions of band IV ( $F_{2g}$  mode related to Si–O stretching) and the intense band II ( $A_{1g}$  mode related to Si–O stretching) are both strongly shifted to lower wavenumbers by increasing grossular content. For these two bands, moderate spessartine and pyrope components in almandine-rich garnets have minimal effects. For instance, moderate spessartine contents of  $<15\text{ mol. \%}$ —corresponding to less than  $6.5\text{ wt. \% MnO}$ —influence these Raman bands for almandine by less than  $1\text{ cm}^{-1}$ .

Orange-red almandine A35, the only representative of type Alm 1, showed significantly lower values for bands II and IV ( $913$  and  $857\text{ cm}^{-1}$ ) than the other three almandine types Alm 2 to Alm 4 (Table II), suggesting a significantly higher Ca content. This garnet *also* showed a weak shoulder in the  $830\text{ cm}^{-1}$  region that has been

attributed to elevated Ti contents (Gilg & Gast 2016). It had no visible solid inclusions, only a single partially healed fracture (Figure 19a). The Raman spectral features of A35 (Figure 18a) match those of Ca-rich almandine in Roman engraved gemstones (cluster Z of Gilg & Gast 2012, recently renamed cluster F by Then-Obłuska *et al.* 2021). Cluster F garnets are orange-red, Ca-rich ( $4.7\text{--}7.7\text{ wt. \% CaO}$ ), Mg-poor ( $<3\text{ wt. \% MgO}$ ) and have moderate  $TiO_2$  contents of  $0.03\text{--}0.12\text{ wt. \%}$  (Gartzke 2004; Gilg & Gast 2012; Thoresen & Schmetzer 2013). They typically have partially healed fractures (Figure 19b) with secondary fluid inclusions, and only very rarely contain solid inclusions such as zircon or opaque phases (Gilg & Gast 2012; Thoresen & Schmetzer 2013, their group 4). Ca-rich almandine garnets of cluster F have so far only been described from objects dating from the third century BCE to the first century CE (Thoresen & Schmetzer 2013), and are absent from garnet cloisonné jewellery from late antiquity (e.g. Calligaro *et al.* 2002; Gilg *et al.* 2010). In addition, the shape of almandine A35 resembles curved garnets used in Heracles knots in diadems of the Hellenistic period (see figure 1 in Thoresen & Schmetzer 2013). The chemical composition of cluster F garnets is similar to those of the gem almandine from deposits mined in the nineteenth century in Zillertal, Austria, but cluster F stones lack the solid inclusions that characterise Austrian garnets (Leute 2000; Gilg & Gast 2012; Gilg & Hyršl 2014). The origin(s) of cluster F garnets is/are as yet unknown.

Three almandines (A21, G31 and K33) belong to type Alm 2. They had similarly low Raman shifts of band V compared to Alm 1, likewise inferring low Mg contents. Low Ca values are indicated by the spectral positions of bands II and IV (Table II). There are well-distinguishable bands XI at  $370\text{--}371\text{ cm}^{-1}$  and XIII at



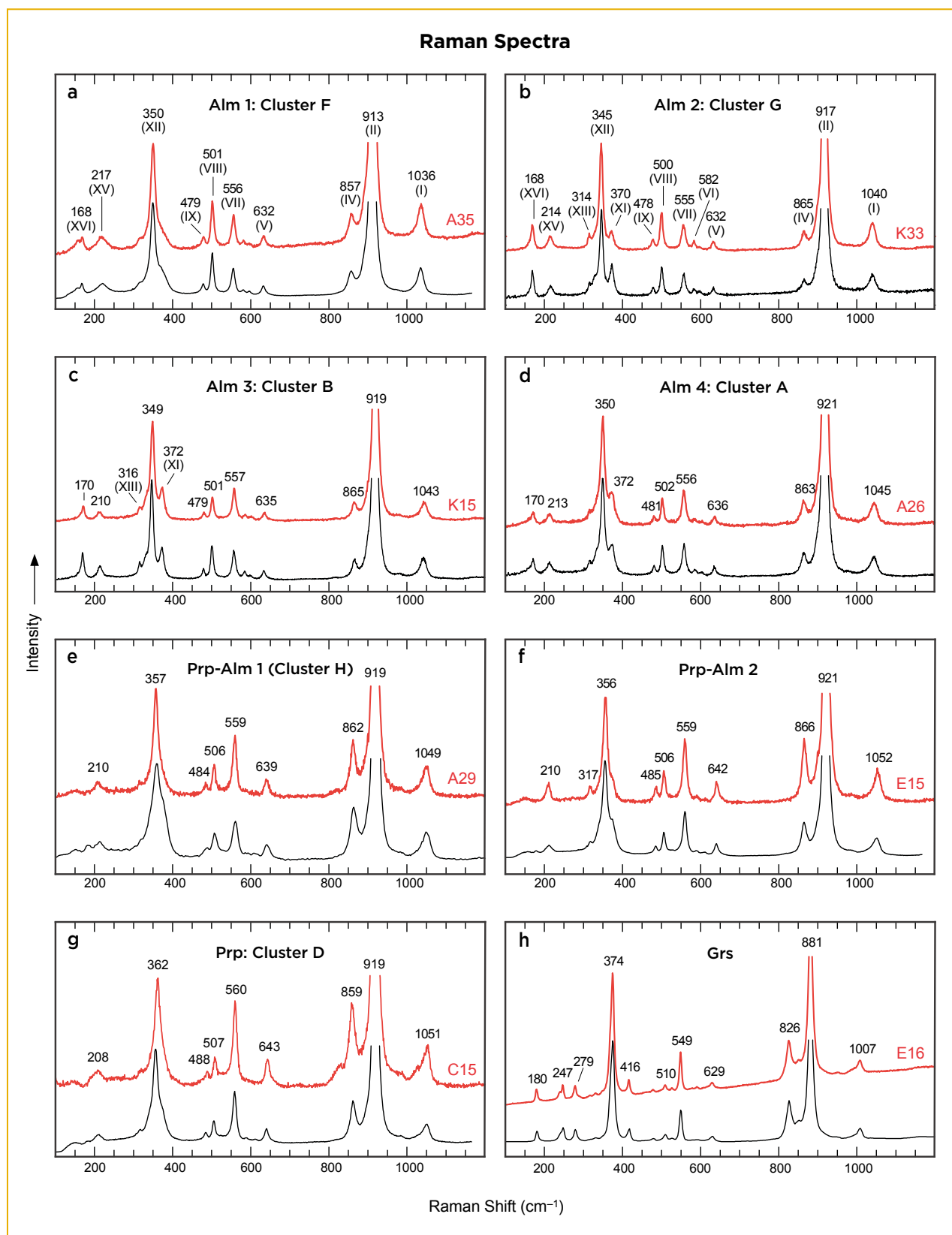


**Figure 18:** Representative Raman spectra of the different types of garnets in the crown (red traces) are compared to reference spectra (black traces) that were obtained from the following: (a) a Roman engraved gem (sample SL637 from Gilg & Gast 2012); (b) a cluster G almandine from the Garibpet deposit, Telangana State, India; (c) an almandine from Rajmahal, India; (d) a Sasanian engraved almandine; (e) a Ca-rich almandine-rich pyrope from Anuradhapura, Sri Lanka (i.e. 'cluster H', a designation that is still unpublished); (f) a low-Ca pyrope (Roman engraved gem); (g) a cluster D pyrope (Roman engraved gem; spectrum SL630 from Gilg & Gast 2012); and (h) a hessonite from Kamburupitiya, Sri Lanka. Spectra are offset vertically for clarity.

314–315  $\text{cm}^{-1}$  (Figure 18b). These zoned garnet crystals had an inclusion-rich core with opaque and transparent long-prismatic crystals surrounded by abundant fibrous needles at the boundary with an inclusion-poor rim (Figure 19c). Their Raman spectra and inclusion characteristics match those of garnets from the Garibpet deposit, Telangana State, India (Figures 18b and 19d; Schmetzer *et al.* 2017). Garnets from this deposit are represented by (1) those used for bead production at Arikamedu, Tamil Nadu, India (Schmetzer *et al.* 2017), (2) beads recovered from Angkor Borei in Cambodia (Carter *et al.* 2021), (3) garnets in Hellenistic jewellery from northern Greece (Gartzke 2004) and (4) an Early Byzantine engraved gem (Gilg *et al.* 2018). This well-characterised garnet type was used from the second century BCE to the first millennium CE, and was termed cluster G by Then-Obłuska *et al.* (2021).

Garnets of types Alm 3 and Alm 4 were the most common almandine types in the Imperial Crown (14 and four gemstones, respectively). Their Raman band positions were widely overlapping, indicating similarly Ca-poor chemical compositions (Table II). Their spectra were differentiated only by slightly higher positions of bands XII and I ( $\text{F}_{2g}$  mode related to Si–O stretching) for Alm 3 (Figure 18c, d). This suggests a slightly higher pyrope content for Alm 4 (Pinet & Smith 1994). The inclusion assemblages of Alm 3 and Alm 4, however, were quite distinct. Alm 3 garnets were often inclusion-poor, but occasionally they had anhedral elongated slightly greenish inclusions up to 1 mm, small zircons with tension cracks (Figure 19e, f) and tiny spherical black inclusions with brownish radiation haloes (not shown), while Alm 4 garnets (cluster A) had a well-developed three-dimensional network of rutile needles, and opaque as well as rounded transparent inclusions (Figure 19g, h).

The inclusion assemblages and Raman band positions of Alm 3 and Alm 4 are identical to those observed for the two most prominent garnet varieties used in cloisonné jewellery of the Early Middle Ages: type I and type II of Calligaro *et al.* (2002), and cluster B and cluster A (Gilg *et al.* 2010, 2018; Kos *et al.* 2020), respectively. The almandines of cluster B appeared for the first time during the fifth century CE (Calligaro *et al.* 2002; Bugoi *et al.* 2016), while cluster A garnets have been known since

**Table I:** Assignment of the 50 garnets in the Imperial Crown.

Location	Sample	Assignment <sup>a</sup>	Cluster
Front plate	A12	Prp-Alm 1 (high Ca)	(H) <sup>b</sup>
	A14	Prp-Alm	
	A18	Prp-Alm 2 (low Ca)	
	A21	Alm 2	G
	A26	Alm 4	A
	A29	Prp-Alm 1 (high Ca)	(H)
	A32	Alm 3	B
	A35	Alm 1	F
	A37	Prp	D
Left temporal plate	C15	Prp	D
	C30	Prp-Alm 2 (low Ca)	
	C31	Prp-Alm	
	C40	Prp-Alm 1 (high Ca)	(H)
	C41	Prp-Alm 2 (low Ca)	
Nape plate	E4	Alm 3	B
	E6	Prp-Alm 1 (high Ca)	(H)
	E9	Prp-Alm 1 (high Ca)	(H)
	E15	Prp-Alm 2 (low Ca)	
	E16	Grs	
	E17	Prp-Alm 2 (low Ca)	
	E20	Alm 4	A
	E23	Prp-Alm 1 (high Ca)	(H)
	E29	Prp-Alm 1 (high Ca)	(H)
	E32	Prp-Alm 2 (low Ca)	
	E35	Prp-Alm 1 (high Ca)	(H)
	E37	Prp-Alm 1 (high Ca)	(H)
Right temporal plate	G30	Prp	D
	G31	Alm 2	G
	G40	Prp-Alm 2 (low Ca)	
	G55	Alm 4	A
Cross	K13	Alm 4	A
	K15	Alm 3	B
	K29	Alm 3	B
	K31	Prp-Alm 1 (high Ca)	(H)
	K33	Alm 2	G
	K35	Prp	D
Arch, left side	BgCh5	Alm 3	B
	BgCh9	Alm 3	B
	BgCh13	Alm 3	B
	BgCh17	Prp	D
	BgCh21	Alm 3	B
	BgCh25	Alm 3	B
	BgCh29	Alm 3	B
Arch, right side	BgRo3	Alm 3	B
	BgRo7	Alm 3	B
	BgRo15	Alm 3	B
	BgRo19	Prp-Alm	
	BgRo21	Prp-Alm	
	BgRo23	Prp-Alm 2 (low Ca)	
	BgRo27	Alm 3	B

<sup>a</sup> Abbreviations of mineral names (Alm = almandine, Grs = grossular and Prp = pyrope) are according to Whitney and Evans (2010).

<sup>b</sup> Cluster H is hitherto still unpublished (Gilg *et al.*, in preparation), and is therefore shown in parentheses.

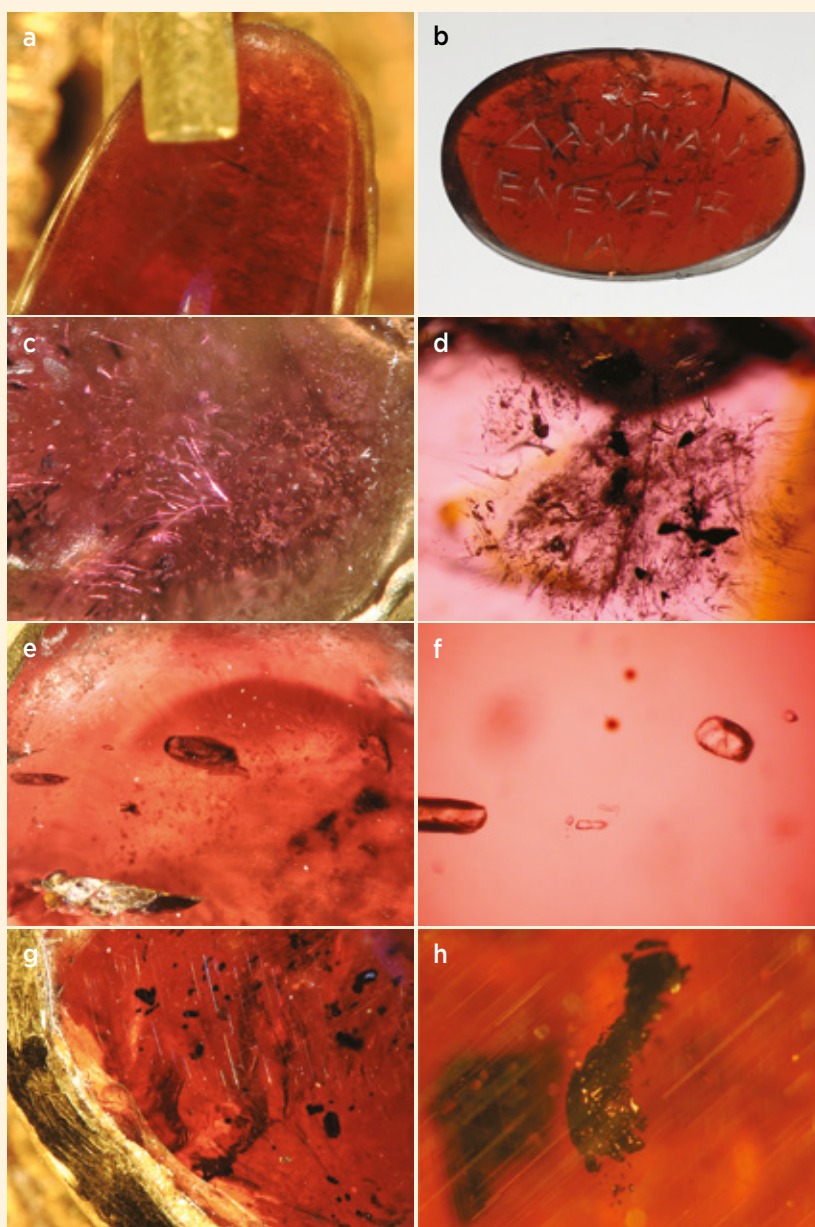


**Figure 19:** Inclusions in almandines of the crown are shown with comparison samples. (Note that inclusion minerals were identified by Raman spectroscopy only in the comparison samples.) Partially healed fractures, but no mineral inclusions, are present in (a) stone A35 (image width 5.3 mm) and in (b) a comparison almandine (cluster F; Roman engraved gem from Staatliche Antikensammlung München, inv. no. NI 15.046-101; 1.84 cm tall). Sillimanite fibres and inclusion zoning are present in (c) K33 (image width 2.3 mm) and in (d) a comparison almandine from Garibpet (image width 3.2 mm). Apatite inclusions can be seen in (e) K33 (image width 2.9 mm) and in (f) a cluster B almandine from Nordendorf, Germany, the latter also with tiny uraninite inclusions (image width 75  $\mu$ m). Rutile needles and ilmenite are present in (g) A26 (image width 1 mm) and in (h) a cluster A almandine from Unterhaching, Germany (image width 1.3 mm). Photomicrographs a, c, e and g © KHM-Museumsverband (Herbert Reitschuler); reproduced with permission. Photomicrographs b, d and f by H. A. Gilg, and h by Norbert Hommrichhausen.

the Hellenistic period (Gartzke 2004; Gilg & Gast 2012; Thoresen & Schmetzer 2013). Garnets with chemical compositions similar to both of these types were found in a reliquary crown from Namur, Belgium, dated from the early thirteenth century (Bruni *et al.* 2021), and also in fourteenth century jewellery in Germany (Greiff 2010). Inclusion observations supporting the attribution to the garnet types, however, were not reported in these studies. Cluster B garnets were very probably sourced from the Rajmahal District, Rajasthan, India, while the provenance of cluster A garnets is still unclear (Gilg *et al.* 2019).

Two types of intermediate pyrope-almandine (Prp-Alm 1 and Prp-Alm 2) could be distinguished on the basis

of their Raman band positions. The overlapping values of their bands V and XII suggest that they have similar Mg contents that are higher than that of the four Alm types. Low Raman shifts of bands II and IV of Prp-Alm 1 indicate higher Ca content than for Ca-poor Prp-Alm 2 (Figure 18e, f; Table II). The Raman band positions of Prp-Alm 1 are identical to those of garnet beads and rough stones excavated from archaeological sites dating to the first millennium CE in Sri Lanka (Rösch *et al.* 1997; Schüssler *et al.* 2001) and a third- to fourth-century CE ring stone in the James Loeb collection (SL630 in Gilg & Gast 2012). Their Ca-rich (3.9–6.1 wt.% CaO) compositions, with pyrope and almandine contents varying between about 30 and 55 mol.% (Rösch *et al.* 1997;



**Table II:** Raman shifts of main bands, inclusions and cluster assignment for 45 of the 49 Mg-Fe garnets in the Imperial Crown.

Garnet type	Alm 1	Alm 2	Alm 3	Alm 4	Prp-Alm 1	Prp-Alm 2	Prp
No. samples	1	3	13	5	10	8	5
Raman shifts (cm <sup>-1</sup> )							
Band I	1036	1039-1040	1040-1043	1044-1045	1049-1052	1051-1055	1049-1051
Band II	913	916-917	917-919	917-919	918-919	921-924	917-919
Band IV	857	864-865	864-866	863-866	861-862	865-867	859-860
Band 830*	Shoulder	—	—	—	—	—	Shoulder
Band V	632	631-633	632-635	633-636	639-641	640-643	641-643
Band VII	556	555	556-558	556-558	557-559	559-561	559-560
Band VIII	501	498-500	500-502	501-502	506-507	505-508	506-508
Band IX	479	476-478	478-480	479-481	484-485	485-487	487-488
Band XI	Shoulder	370-371	370-372	370-372	Shoulder	373-375	Shoulder
Band XII	350	344-345	345-347	348-349	356-357	355-357	358-362
Band XIII	Shoulder	314-315	314-317	315-316	Shoulder	317-318	Shoulder
Band XV	217	214	210-214	210-216	209-210	209-210	208-210
Band XVI	168	167-168	168-170	169-171	—	—	—
Colour	Orange-red	Red to violet	Brownish red to pink	Orange-red to brownish red	Red to dark red	Red to violet/pink	Orange-red to dark red
Inclusions	No solid inclusions; healed fractures	Zoned: inclusion-rich core with ilmenite, prismatic apatite and sillimanite bundles at boundary to inclusion-poor rim	Inclusion-poor: anhedral apatite, uraninite, zircon	Inclusion-rich: rutile needles, ilmenite, quartz, sillimanite, zircon	Inclusion-rich: oriented short needles and short prismatic crystals ('dashes and dots')	Inclusion-rich: oriented needles and short prismatic crystals ('dashes and dots'), clusters of roundish apatite	No inclusions
Garnet cluster	F	G	B	A	(H)	—	D

\* This band has remained unnamed (Pinet & Smith 1994).

Schüssler *et al.* 2001; Gilg & Gast 2012), mark a narrow area within the large field of un-clustered garnet compositions in cloisonné jewellery (Gilg *et al.* 2010), or type III of Calligaro *et al.* (2002). Abundant equant to needle-shaped mineral inclusions ('dashes and dots'), with preferred orientations forming a loose three-dimensional network, are found in both Prp-Alm 1 garnet and in Sri Lankan garnet beads (Figure 20a, b). The same oriented equant to needle-shaped mineral inclusions and rarely clusters of rounded transparent crystals (Figure 20c, d) were observed in the Ca-poor Prp-Alm 2 garnets.

The five orange-red inclusion-free pyropes (type Prp, e.g. Figure 20e) were characterised by the lowest positions of band IV (859–860 cm<sup>-1</sup>), the highest Raman shifts of

band XII (358–362 cm<sup>-1</sup>) and a significant shoulder in the 830 cm<sup>-1</sup> region, indicating a Ca-, Mg- and Ti-rich composition (see Table II and Figure 18g). The Raman spectra of these five pyropes match those of the orange-red inclusion-free (e.g. Figure 20f) Cr-poor, Ti-rich pyropes of cluster D (Gilg & Gast 2012, 2016; Then-Obłuska *et al.* 2021), but are distinct from the red-to-violet Cr- and Ti-rich and more Mg-rich Bohemian pyropes (Gilg & Hyršl 2014; Gilg & Gast 2016). Cluster D pyropes have been used since the Hellenistic period and form phenocrysts in alkaline basaltic rocks. Such a geological provenance can be inferred for type Prp in the present study, as all known occurrences have overlapping chemical compositions. Potential sources in antiquity and the medieval

period are Monte Suímo in Portugal, alluvial deposits in Jos and the Biu plateau in northern Nigeria, Mount Carmel in Israel and Elie Ness in Scotland (Then-Obłuska *et al.* 2021).

Interestingly, the only grossular in the crown (the large octagonal, vivid orange to brownish red stone E16 on the nape plate; Figure 17c) is not original but was a replacement. The original stone was lost after a treasurer pressed the pillowed crown firmly to his body while riding to the royal quarters, and in 1764 the empty setting was filled with an assumed-to-be ‘jacinth’ (Klaar 1986) from a necklace. In 1977, based only on visual inspection, Prof. Kurat of the Natural History Museum Vienna correctly recognised that this stone could not

be a zircon and identified it as a red garnet (see Figure 5). The very low Raman shifts of bands II and IV (826 and 881  $\text{cm}^{-1}$ ; Figure 18h) are very close to the respective end-member values of grossular (Kolesov & Geiger 1998). The assignment to ‘hessonite’ is supported by the common presence of transparent rounded inclusions (probably apatite and/or calcite; Figure 20g, h), the stone’s orange-brown colour and its ‘oily’ diaphaneity (Mathavan *et al.* 2000).

### The Enigma of Spinel A25

Natural Mg-Al spinel of gem quality typically yields PL and Raman fingerprint patterns analogous to those of stone K40 (Figures 12c and 13). Such spectra were also

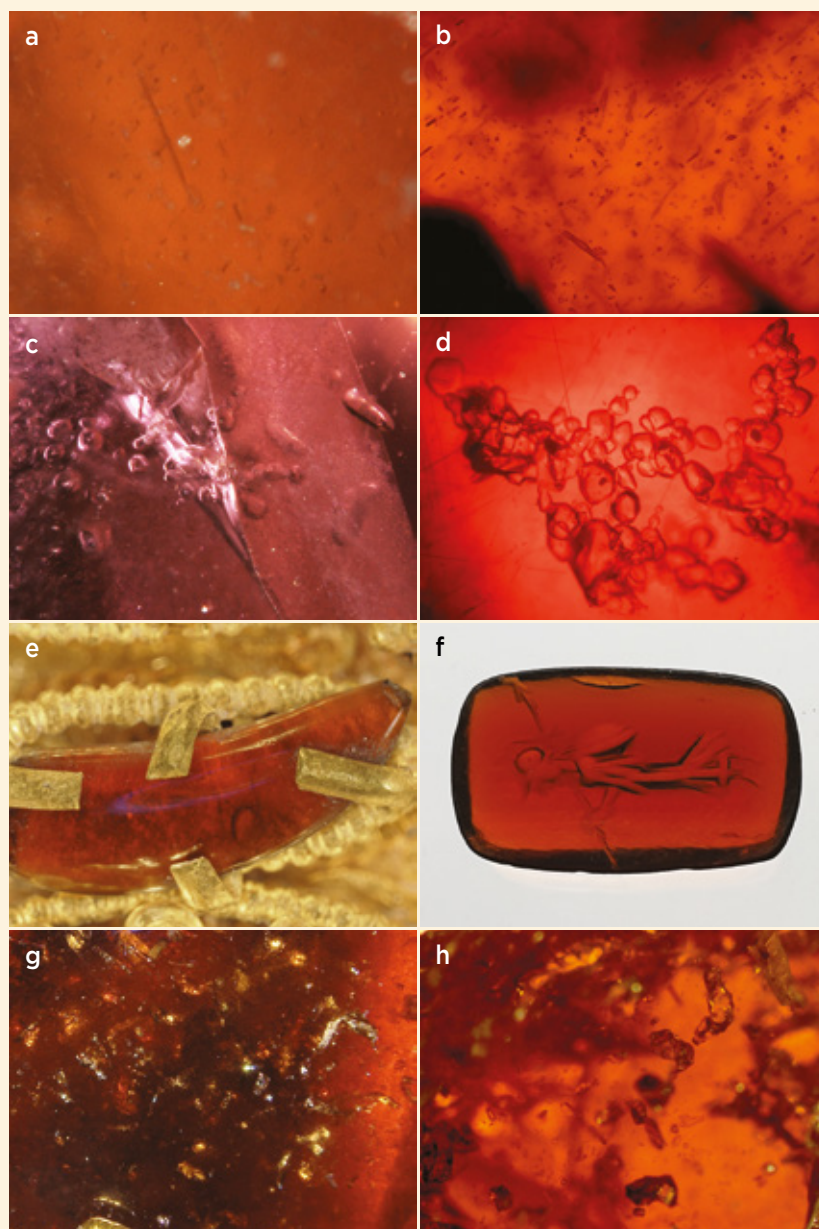


**Figure 20:** Inclusions in other garnet types of the crown are shown with comparison samples. (Note that inclusion minerals were identified by Raman spectroscopy only in the comparison samples.) Equant to needle-shaped mineral inclusions (‘dashes and dots’) are present in both (a) pyrope-almandine A29 (image width 0.9 mm) and (b) a comparison Ca-rich pyrope-almandine from Anuradhapura, Sri Lanka (image width 1.3 mm). Agglomerations of roundish apatite are present in (c) pyrope-almandine A29 (image width 2 mm) and (d) a comparison Hellenistic engraved Ca-poor, almandine-rich pyrope (Staatliche Antikensammlung München, inv. no. NI 15.046-473; image width 1.3 mm). (e) Pyrope A37, most likely an antique reused stone, does not show any visible inclusions (image width 1.2 cm). (f) Analogously, this cluster D pyrope (a Roman engraved gem from Staatliche Antikensammlung München, inv. no. NI 15.046-069; 1.3 cm long) appears inclusion-free. (g) Grossular E16 shows numerous elongated, rounded inclusions (image width 8.9 mm). (h) Large apatite inclusions with a similar appearance are seen in a grossular (hessonite) from Kamburupitiya, Sri Lanka (image width 5.1 mm). Photomicrographs a, c, e and g © KHM-Museumsverband (Herbert Reitschuler); reproduced with permission. Photomicrographs b, d, f and h by H. A. Gilg.

obtained from stone A3 (Figure 12b), whereas sample A25 (Figure 12a) yielded clearly different spectral characteristics.

Emission lines in the PL spectrum of A25 were significantly broader, and the rather complex fine structure of the emission was not present (Figure 21). Such ‘blurred’ PL patterns have, to the best of our knowledge, only been obtained thus far from heat-treated natural gem spinel (Smith 2012; Peretti *et al.* 2015; Widmer *et al.* 2015), or from high-temperature synthetic (i.e. melt-grown) spinel that typically has a somewhat non-stoichiometric chemical composition (Mohler & White 1995; Dereń *et al.* 1996; Peretti *et al.* 2015). As the setting of spinel A25 in the crown seems to be original, and since gem-quality synthetic red spinel was available only in recent times (e.g. Muhlmeister *et al.* 1993), it appears impossible that A25 could be a synthetic spinel. Therefore, the broadened PL spectrum points to a heated natural stone.

Similarly, the Raman band pattern of A25 was broadened, with clear asymmetry of the main 407–408  $\text{cm}^{-1}$   $E_g$  band towards the low-energy side (Figure 22). Such Raman spectra are typical for heated natural gem spinel (Van Minh & Yang 2004; Slotznick & Shim 2008; Widmer *et al.* 2015). This is supported by the presence of an additional band near 724  $\text{cm}^{-1}$  in the Raman spectrum, which is not, or with only very low intensity, present in the spectra of non-heat-treated natural Mg-Al spinel. This band has been assigned to structural disorder caused by heat-induced cation inversion, which may cause ‘normal’ spinel to shift towards ‘inverse’ spinel<sup>1</sup> (Cynn *et al.* 1992; Slotznick & Shim 2008; Ma *et al.* 2022). Widmer *et al.* (2015) found that heating of spinel for 72 hours to 700°C, followed by slow cooling, did not result in any measurable Raman spectral changes. Correspondingly, Liu *et al.* (2022) did not find significant spectral changes after heating for two hours up to 750°C; they obtained a broadened emission spectrum corresponding to that of spinel A25 only after heating at 1000°C. Spectra obtained from our own heat treatment experiments (Figures 21 and 22) confirm these

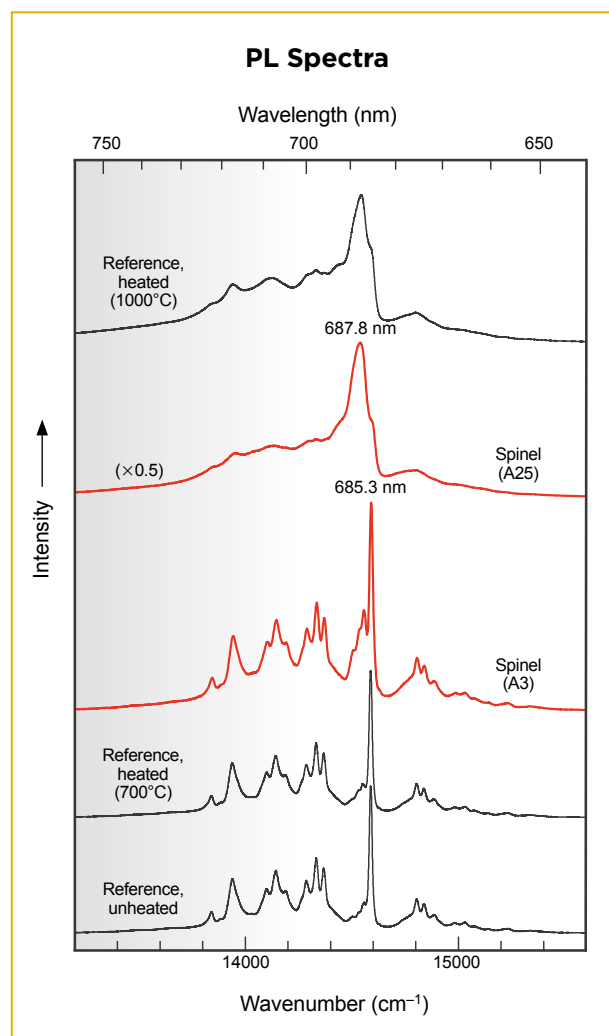


**Figure 21:** Laser-induced PL spectra (457 nm excitation) are shown for ‘normal’ spinel A3 and significantly ‘inverse’ spinel A25, in comparison with reference spectra (473 nm excitation) for a gem spinel from Ratnapura, Sri Lanka (unheated and heated to 700°C and 1000°C). For spinel A25, note the low degree of emission fine-structure, consistent with the reference spinel that was heated to 1000°C. The spectral range not visible to the human eye is shaded grey. Spectra are offset vertically for clarity.

results: spinel A25 must have experienced heating up to well above 700°C, perhaps close to 1000°C.

It therefore appears that red stone A25 is a natural

<sup>1</sup> The term ‘normal’ refers to a so-called normal cation occupation in the spinel structure (that is, four-coordinated divalent cations and six-coordinated trivalent cations). Natural Mg-Al spinel typically has (close to) ‘normal’ cation occupation, whereas other members of the spinel supergroup (Bosi *et al.* 2019), such as magnetite, are ‘inverse’ (that is, divalent cations occupy a six-coordinated site and half of the trivalent cations occupy a four-coordinated site). Heating of predominantly ‘normal’ Mg-Al spinel to above 700–800°C, especially (but not necessarily) when followed by more-or-less rapid cooling, causes irreversible structural perturbation by significantly increasing the degree of cation inversion to well above 20% (Van Minh & Yang 2004; Slotznick & Shim 2008; Ma *et al.* 2022), according to the following:



where  $i$  = a parameter describing the degree of proportionately inverse cation occupation (Wood *et al.* 1986).



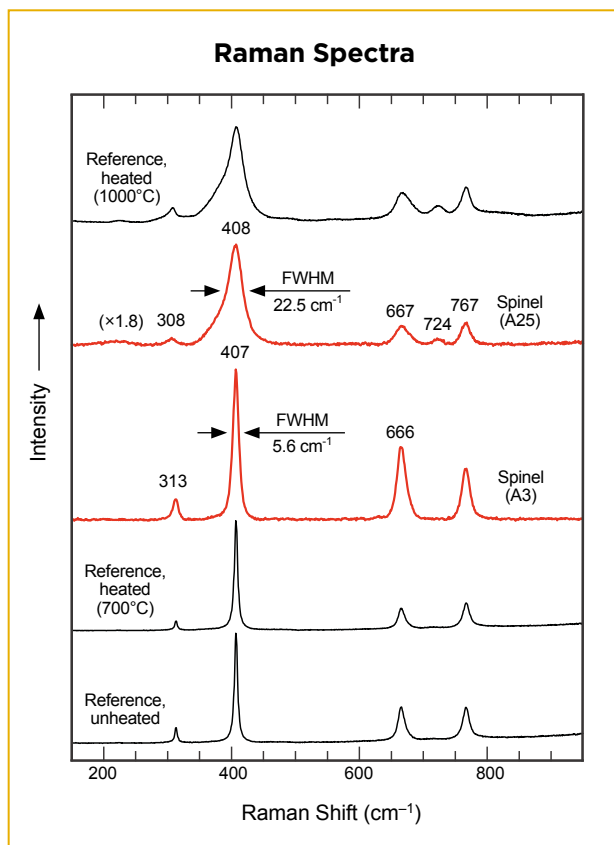


**Figure 22:** Raman spectra (457 nm excitation) are shown for the same samples as in Figure 21. For spinel A25, note the asymmetry and broad width of the main Raman band; analogous spectral changes of the reference spinel were achieved only after heating to well above 700°C. Quoted FWHM values are corrected for experimental band broadening. Spectra are offset vertically for clarity.

spinel that was heated before being set into the Imperial Crown. At the time the Imperial Crown was manufactured, the most common gem enhancements were dyeing, oiling, coating and foiling (Nassau 1984; Karampelas *et al.* 2020), but there have been a number of reports of very early heating of gems. For example, heating of microcrystalline silica was done as early as the Pre-Pottery Neolithic period to make it easier to shape beads and to enhance the colour of carnelian (Coşkunsu 2008; Groman-Yaroslavski & Bar-Yosef Mayer 2015)—techniques brought to perfection by the Indus Valley civilisation during the Bronze Age (Roux 2000; Possehl 2002). Heat treatments to improve colour and transparency of hard red, blue and yellow gemstones (termed *yaqut* in Arabic) have been mentioned frequently in Arabic mineralogical texts since the ninth century CE (e.g. Ruska 1912; Said 1989; Huda 1998; Troupeau 1998; Content 2016). It has generally been assumed that *yaqut* refers to gem corundum (ruby and sapphire), but this term might have also included

spinel, as red *yaqut* weighing more than 200 ct have been described (Qaddumi 1996; Content 2016). Consequently, it needs to be taken into consideration that, as early as more than 1,000 years ago, spinel A25 could have been subjected to intentional heating for colour or clarity enhancement.

The possibility that the stone was accidentally exposed to fire before being set in the crown also needs to be considered. It has been known for a long time that accidental heating can affect gem properties. Köhler (1877) reported an early example: after the house of a miner burned down in 1757, 50 kg of previously wine-yellow Schneckenstein topaz turned colourless. Heating of spinel A25 in the course of experimental, traditional or religious practices (such as to prove imperishable durability or the like) could be another possibility. Two drill holes, one at the upper end and one on the bottom side of A25, lead to the presumption that this spinel had already been mounted in another object before its placement in the Imperial Crown. A link between this former usage and the ascertained heating of the stone is also worth considering. Overall, spinel A25 is most remarkable because, to our knowledge, it represents one of the earliest uses of this mineral as a gemstone, as well as the earliest known heat-treatment of this gem material. Pink spinels first appeared in European and Asian jewellery in the thirteenth century (Content 2016; Bruni *et al.* 2021; Ogden 2021), slowly replacing dark garnets, but they became more common in the fourteenth century (e.g. Hyršl & Neumanova 1999; Schmetzer & Gilg 2020). This largest red gemstone in the crown was, therefore, a unique new gem material at that time with respect to transparency and size, and might have initiated the myth of the ‘Orphan Stone’.

## CONCLUSION

One general limiting factor in analysing gemstones in archaeological and art-historical specimens is that, in many cases, objects cannot be taken to a laboratory; instead, analytical devices need to be brought to the objects. This includes immovable items such as sculptures and wall tessellations, as well as objects with enormous historical and/or monetary value, or those where a critical state of preservation does not allow transportation.

Many successful spectroscopic studies have been conducted on-site using small, portable systems. Most of these units, however, have the drawback that only limited (and in some cases fixed, pre-set) spectral ranges can be detected. In our case, it was most beneficial to have

a research-grade spectrometer available that allowed us to analyse the full spectral range of interest (that is, from the blue to NIR region), because both laser-induced PL (cf. Tsai & D'Haenens-Johansson 2021) and Raman spectra could be obtained and interpreted. Apart from the information gained, the use of PL proved advantageous simply because electronic emissions, compared to Raman-scattered light, are often several orders of magnitude higher in intensity and, hence, much more easily detected. Another advantage of the spectrometer used in this study, compared to small gem-testing Raman devices, was its reasonable spectral resolution. The latter helps resolve closely adjacent spectroscopic signals and evaluate band shapes.

All 172 gemstones in the Imperial Crown of the Holy Roman Empire were successfully identified (again, see Figure 8). Apart from some unexpected results—such as for stones A3 (pink spinel) and K26 (pale amethyst underlain by a reddish substance) that were initially assumed to be

corundum—the previous assignments of most large stones were confirmed. Most of the small gems in the crown have, to the best of our knowledge, never been appropriately studied or identified before.

Beyond the identification of gem minerals in the crown, further interpretation—such as the comprehensive characterisation of the glass gems (chemical composition, degree of deterioration and possible origin)—remains speculative and requires additional analytical work. Moreover, chemical analysis of the enamel, pearls and selected gems in the crown will be the focus of our forthcoming second measurement campaign, and we plan to publish the results in a future issue of *The Journal*. These studies are part of an ongoing project that aims to capture and analyse as many details as possible concerning the Imperial Crown's materials, manufacturing techniques and history, with the objective of providing a profound basis for further research and interpretations pertaining to this crown.

## REFERENCES

- Anušková, V., Šefců, R., Šulcová, P., Dohnalová, Ž., Luxová, J., Bajoux Kmoníčková, M., Turková, I. & Kotrlý, M. 2022. Spectroscopic characterisation of Naples yellow variations in paintings from the turn of the 20th century. *Journal of Raman Spectroscopy*, **22**, article 6470, <https://doi.org/10.1002/jrs.6470>.
- Bell, I.M., Clark, R.J.H. & Gibbs, P.J. 1997. Raman spectroscopic library of natural and synthetic pigments (pre- ~ 1850 AD). *Spectrochimica Acta Part A: Molecular and Biomolecular Spectroscopy*, **53**(12), 2159–2179, [https://doi.org/10.1016/s1386-1425\(97\)00140-6](https://doi.org/10.1016/s1386-1425(97)00140-6).
- Beysac, O. & Lazzeri, M. 2012. Application of Raman spectroscopy to the study of graphitic carbons in the earth sciences. In: Dubessy, J., Caumon, M.-C. & Rull, F. (eds) *Raman Spectroscopy Applied to Earth Sciences and Cultural Heritage*. European Mineralogical Union and the Mineralogical Society of Great Britain & Ireland, Twickenham, 415–454, <https://doi.org/10.1180/EMU-notes.12.12>.
- Bosi, F., Biagioni, C. & Pasero, M. 2019. Nomenclature and classification of the spinel supergroup. *European Journal of Mineralogy*, **31**(1), 183–192, <https://doi.org/10.1127/ejm/2019/0031-2788>.
- Brik, M.G., Papan, J., Jovanović, D.J. & Dramićanin, M.D. 2016. Luminescence of Cr<sup>3+</sup> ions in ZnAl<sub>2</sub>O<sub>4</sub> and MgAl<sub>2</sub>O<sub>4</sub> spinels: Correlation between experimental spectroscopic studies and crystal field calculations. *Journal of Luminescence*, **177**, 145–151, <https://doi.org/10.1016/j.jlumin.2016.04.043>.
- Bruni, Y., Hatert, F., George, P., Cambier, H. & Strivay, D. 2021. A gemmological study of the reliquary crown of Namur, Belgium. *European Journal of Mineralogy*, **33**(2), 221–232, <https://doi.org/10.5194/ejm-33-221-2021>.
- Buettner, B. 2022. *The Mineral and the Visual: Precious Stones in Medieval Secular Culture*. Pennsylvania State University Press, University Park, Pennsylvania, USA, 272 pp.
- Bugoi, R., Oanță-Marghitu, R. & Calligaro, T. 2016. IBA investigations of loose garnets from Pietroasa, Apahida and Cluj-Someșeni treasures (5th century AD). *Nuclear Instruments and Methods in Physics Research Section B: Beam Interactions with Materials and Atoms*, **371**, 401–406, <https://doi.org/10.1016/j.nimb.2015.09.038>.
- Calligaro, T., Colinart, S., Poirot, J.-P. & Sudres, C. 2002. Combined external-beam PIXE and  $\mu$ -Raman characterisation of garnets used in Merovingian jewellery. *Nuclear Instruments and Methods in Physics Research Section B: Beam Interactions with Materials and Atoms*, **189**(1–4), 320–327, [https://doi.org/10.1016/s0168-583x\(01\)01078-3](https://doi.org/10.1016/s0168-583x(01)01078-3).
- Carter, A.K., Dussubieux, L., Stark, M.T. & Gilg, H.A. 2021. Angkor Borei and protohistoric trade networks: A view from the glass and stone bead assemblage. *Asian Perspectives*, **60**(1), 32–70, <https://doi.org/10.1353/asi.2020.0036>.
- Colomban, P. 2003. Polymerization degree and Raman identification of ancient glasses used for jewelry, ceramic enamels and mosaics. *Journal of Non-Crystalline Solids*, **323**(1–3), 180–187, [https://doi.org/10.1016/s0022-3093\(03\)00303-x](https://doi.org/10.1016/s0022-3093(03)00303-x).

- Colomban, P., Etcheverry, M.-P., Asquier, M., Bounichou, M. & Tournié, A. 2006. Raman identification of ancient stained glasses and their degree of deterioration. *Journal of Raman Spectroscopy*, **37**(5), 614–626, <https://doi.org/10.1002/jrs.1495>.
- Content, D.J. 2016. *Ruby, Sapphire & Spinel: An Archaeological, Textual and Cultural Study*. Brepols Publishers, Turnhout, Belgium, 452 pp.
- Coşkunsu, G. 2008. Hole-making tools of Mezraa Teleilat with special attention to micro-borers and cylindrical polished drills and bead production. *Neo-Lithics*, **1**(8), 25–36, [https://www.exorient.org/repository/NEO-LITHICS/NEO-LITHICS\\_2008\\_1.pdf](https://www.exorient.org/repository/NEO-LITHICS/NEO-LITHICS_2008_1.pdf).
- Cynn, H., Sharma, S.K., Cooney, T.F. & Nicol, M. 1992. High-temperature Raman investigation of order-disorder behavior in the  $\text{MgAl}_2\text{O}_4$  spinel. *Physical Review B*, **45**(1), 500–502, <https://doi.org/10.1103/PhysRevB.45.500>.
- Decker-Hauff, H. 1955. Die “Reichskrone” angefertigt für Kaiser Otto I. In: Schramm, P.E. (ed) *Herrschaftszeichen und Statussymbolik. Beiträge zu ihrer Geschichte vom dritten bis zum sechzehnten Jahrhundert. Monumenta Germaniae Historica*. Anton Hierseman Verlag, Stuttgart, Germany, **13**(II), 560–637.
- Dereñ, P.J., Malinowski, M. & Stręk, W. 1996. Site selection spectroscopy of  $\text{Cr}^{3+}$  in  $\text{MgAl}_2\text{O}_4$  green spinel. *Journal of Luminescence*, **68**(2–4), 91–103, [https://doi.org/10.1016/0022-2313\(96\)00020-8](https://doi.org/10.1016/0022-2313(96)00020-8).
- Etchepare, J., Merian, M. & Smetankine, L. 1974. Vibrational normal modes of  $\text{SiO}_2$ . I.  $\alpha$  and  $\beta$  quartz. *Journal of Chemical Physics*, **60**(5), 1873–1876, <https://doi.org/10.1063/1.1681287>.
- Fillitz, H. 1953. Studien zur römischen Reichskrone. *Jahrbuch der Kunsthistorischen Sammlungen in Wien*, **50**(14), 23–52.
- Fillitz, H. 1956. Die Edelsteinordnung auf der Reichskrone und ihre Beziehung zur Spätantike. *Österreichische Zeitschrift für Kunst und Denkmalpflege*, **10**, 38–45.
- Gartzke, E. 2004. *Methoden zur materialkundlichen Untersuchung antiker Schmuckstücke*. Master's thesis, University of Würzburg, Germany, 196 pp.
- Gilg, H.A. & Gast, N. 2012. Naturwissenschaftliche Untersuchungen an Granatgemmen der Sammlung James Loeb. In: Weiss, C. & Knauss, F.S. (eds) *Die Gemmen der Sammlung James Loeb*. Kunstverlag Josef Fink, Lindenberg im Allgäu, Germany, 48–57, 62–63.
- Gilg, H.A. & Gast, N. 2016. Determination of titanium content in pyrope by Raman spectroscopy. *Journal of Raman Spectroscopy*, **47**(4), 486–491, <https://doi.org/10.1002/jrs.4838>.
- Gilg, H.A. & Hyršl, J. 2014. Garnet deposits in Europe. In: Toussaint, J. (ed) *Rouges et Noirs: Rubis, Grenat, Onyx, Obsidienne et Autres Minéraux Rouges et Noirs dans l'Art et l'Archéologie*. Société Archéologique de Namur, Namur, France, 144–173.
- Gilg, H.A., Gast, N. & Calligaro, T. 2010. Vom Karfunkelstein. In: Wamser, L. (ed) *Karfunkelstein und Seide: neue Schätze aus Bayerns Frühzeit*. F. Pustet, Regensburg, Germany, 87–100.
- Gilg, H.A., Schmetzer, K. & Schüssler, U. 2018. An Early Byzantine engraved almandine from the Garibpet deposit, Telangana State, India: Evidence for garnet trade along the ancient Maritime Silk Road. *Gems & Gemology*, **54**(2), 149–165, <https://doi.org/10.5741/gems.54.2.149>.
- Gilg, H.A., Schüssler, U., Krause, J. & Schulz, B. 2019. The use of phosphate inclusions in origin determination of ancient and medieval red garnets. *36th International Gemmological Conference*, Nantes, France, 27–31 August, 41–43.
- Greiff, S. 2010. Zur Herkunft der roten Granate an Schmuckobjekten des Erfurter Schatzfundes. In: Ostritz, S. (ed) *Die mittelalterliche jüdische Kultur in Erfurt. Band 2. Der Schatzfund: Analysen – Herstellungstechniken – Rekonstruktionen*. Thüringisches Landesamt für Denkmalpflege und Archäologie, Weimar, Germany, 482–487.
- Groman-Yaroslavski, I. & Bar-Yosef Mayer, D.E. 2015. Lapidary technology revealed by functional analysis of carnelian beads from the early Neolithic site of Nahal Hemar Cave, southern Levant. *Journal of Archaeological Science*, **58**, 77–88, <https://doi.org/10.1016/j.jas.2015.03.030>.
- Hagemann, H., Lucken, A., Bill, H., Gysler-Sanz, J. & Stalder, H.A. 1990. Polarized Raman spectra of beryl and bazzite. *Physics and Chemistry of Minerals*, **17**(5), 395–401, <https://doi.org/10.1007/bf00212207>.
- Hofmeister, A.M. & Chopelas, A. 1991. Vibrational spectroscopy of end-member silicate garnets. *Physics and Chemistry of Minerals*, **17**(6), 503–526, <https://doi.org/10.1007/bf00202230>.
- Huda, S.N.A. (transl.) 1998. *Arab Roots of Gemology: Ahmad ibn Yusuf Al Tifaschi's 'Best Thoughts on the Best of Stones'*. Scarecrow Press Inc., Lanham, Maryland, USA and London, 271 pp.
- Huong, L.T.-T., Häger, T. & Hofmeister, W. 2010. Confocal micro-Raman spectroscopy: A powerful tool to identify natural and synthetic emeralds. *Gems & Gemology*, **46**(1), 36–41, <https://doi.org/10.5741/gems.46.1.36>.
- Hyršl, J. & Neumanova, P. 1999. Eine neue gemmologische Untersuchung der Sankt Wenzelskrone in Prag. *Gemmologie: Zeitschrift der Deutschen Gemmologischen Gesellschaft*, **48**(1), 29–36.
- Karampelas, S., Kiefert, L., Bersani, D. & Vandenabeele, P. 2020. Gem treatments, synthetics and imitations. In: *Gems and Gemmology*. Springer, Cham, Switzerland, 67–90, [https://doi.org/10.1007/978-3-030-35449-7\\_4](https://doi.org/10.1007/978-3-030-35449-7_4).
- Kisliuk, P. & Moore, C.A. 1967. Radiation from the  $^4\text{T}_2$  state of  $\text{Cr}^{3+}$  in ruby and emerald. *Physical Review*, **160**(2), 307–312, <https://doi.org/10.1103/PhysRev.160.307>.



- Klaar, K.-E. 1986. Sicherung und Pflege der Reichskleinodien in Nürnberg. In: Schuhmann, G. (ed) *Nürnberg – Kaiser und Reich*. Ausstellungskataloge der staatlichen Archive Bayerns, Neustadt an der Aisch, Germany, **20**, 71–79.
- Klee, W.E. 1970. The vibrational spectra of the phosphate ions in fluorapatite. *Zeitschrift für Kristallographie*, **131**(1–6), 95–102, <https://doi.org/10.1524/zkri.1970.131.1-6.95>.
- Köhler, E. 1877. Ein Beitrag zur Geschichte des Topasfels Schneckenstein. In: Usbeck, O. (ed) *Mittheilungen des Vogtländischen Vereins für allgemeine und spezielle Naturkunde in Reichenbach i.V.*, Vol. 3, 29–38.
- Kolesov, B.A. & Geiger, C.A. 1998. Raman spectra of silicate garnets. *Physics and Chemistry of Minerals*, **25**(2), 142–151, <https://doi.org/10.1007/s002690050097>.
- Kos, S., Dolenec, M., Lux, J. & Dolenec, S. 2020. Raman microspectroscopy of garnets from S-fibulae from the archaeological site Lajh (Slovenia). *Minerals*, **10**(4), <https://doi.org/10.3390/min10040325>.
- Kugler, G.J. 1986. *Die Reichskrone*. Herold-Verlag, Vienna, Austria, 158 pp.
- Leute, M.A. 2000. *Mineralogische Charakterisierung der Radentheiner und Zillertaler Schmuckgranate, Österreich*. Unpublished Diploma thesis, University of Vienna, Austria, 129 pp.
- Liu, Y., Qi, L., Schwarz, D. & Zhou, Z. 2022. Color mechanism and spectroscopic thermal variation of pink spinel reportedly from Kuh-i-Lal, Tajikistan. *Gems & Gemology*, **58**(3), 338–353, <https://doi.org/10.5741/gems.58.3.338>.
- Ma, Y., Bao, X., Sui, Z., Zhao, X. & Liu, X. 2022. Quantifying Mg–Al cation distribution in  $\text{MgAl}_2\text{O}_4$ -spinel using Raman spectroscopy: An experimental calibration. *Solid Earth Sciences*, **7**(1), 60–71, <https://doi.org/10.1016/j.sesci.2021.09.002>.
- Mathavan, V., Kalubandara, S.T. & Fernando, G.W.A.R. 2000. Occurrences of two new types of gem deposits in the Okkampitiya gem field, Sri Lanka. *Journal of Gemmology*, **27**(2), 65–72, <https://doi.org/10.15506/JoG.2000.27.2.65>.
- Mentzel-Reuters, A. 2004. Die goldene Krone: Entwicklungslinien mittelalterlicher Herrschaftssymbolik. *Deutsches Archiv für Erforschung des Mittelalters*, **60**, 135–182, <https://www.mgh-bibliothek.de/dokumente/a/a123901.pdf>.
- Mikenda, W. & Preisinger, A. 1981. N-lines in the luminescence spectra of  $\text{Cr}^{3+}$ -doped spinels: (II) Origins of N-lines. *Journal of Luminescence*, **26**(1–2), 67–83, [https://doi.org/10.1016/0022-2313\(81\)90170-8](https://doi.org/10.1016/0022-2313(81)90170-8).
- Mohler, R.L. & White, W.B. 1995. Influence of structural order on the luminescence of oxide spinels:  $\text{Cr}^{3+}$ -activated spinels. *Journal of the Electrochemical Society*, **142**(11), 3923–3927, <https://doi.org/10.1149/1.2048435>.
- Muhlmeister, S., Koivula, J.I., Kammerling, R.C., Smith, C.P., Fritsch, E. & Shigley, J.E. 1993. Flux-grown synthetic red and blue spinels from Russia. *Gems & Gemology*, **29**(2), 81–98, <https://doi.org/10.5741/gems.29.2.81>.
- Nassau, K. 1984. The early history of gemstone treatments. *Gems & Gemology*, **20**(1), 22–33, <https://doi.org/10.5741/gems.20.1.22>.
- Nelson, D.F. & Sturge, M.D. 1965. Relation between absorption and emission in the region of the R lines of ruby. *Physical Review*, **137**(4A), A1117–A1130, <https://doi.org/10.1103/PhysRev.137.A1117>.
- Neuvill, D.R. 2006. Viscosity, structure and mixing in (Ca, Na) silicate melts. *Chemical Geology*, **229**(1–3), 28–41, <https://doi.org/10.1016/j.chemgeo.2006.01.008>.
- Ogden, J.M. 2021. Gem knowledge in the thirteenth century: The St Albans jewels. *Journal of Gemmology*, **37**(8), 816–834, <https://doi.org/10.15506/JoG.2021.37.8.816>.
- Ollier, N., Fuchs, Y., Cavani, O., Horn, A.H. & Rossano, S. 2015. Influence of impurities on  $\text{Cr}^{3+}$  luminescence properties in Brazilian emerald and alexandrite. *European Journal of Mineralogy*, **27**(6), 783–792, <https://doi.org/10.1127/ejm/2015/0027-2484>.
- Peretti, A., Tun, N.L. & Armbruster, T. 2015. Heat-treatment of spinels. *Contributions to Gemology*, No. 11, 269–278, <https://www.gemresearch.ch/assets/documents/publication-articles/2015-05-spinel-heat-treatment-1.pdf>.
- Pinet, M. & Smith, D.C. 1994. La microspectrométrie Raman des grenats  $\text{X}_3\text{Y}_2\text{Z}_3\text{O}_{12}$ : II. La série alumineuse naturelle pyrope-almandine-spessartite. *Schweizerische Mineralogische und Petrographische Mitteilungen*, **74**(2), 161–179, <https://doi.org/10.5169/seals-56339>.
- Porto, S.P.S. & Krishnan, R.S. 1967. Raman effect of corundum. *Journal of Chemical Physics*, **47**(3), 1009–1012, <https://doi.org/10.1063/1.1711980>.
- Possehl, G.L. 2002. *The Indus Civilization: A Contemporary Perspective*. Rowman Altamira Press, Walnut Creek, California, USA, 276 pp.
- Powell, R.C., DiBartolo, B., Birang, B. & Naiman, C.S. 1967. Fluorescence studies of energy transfer between single and pair  $\text{Cr}^{3+}$  systems in  $\text{Al}_2\text{O}_3$ . *Physical Review*, **155**(2), 296–308, <https://doi.org/10.1103/PhysRev.155.296>.
- Qaddumi, G.H. (transl.) 1996. *Book of Gifts and Rarities (Kitāb al-Hadāyā wa al-Tuḥaf)*. Harvard University Press, Cambridge, Massachusetts, USA, 551 pp.
- Quenstedt, F. 2022. *Der Waise: Transkulturelle Verflechtungen eines mittelalterlichen Kronjuwels*.

- Logbuch Wissensgeschichte des SFB Episteme in Bewegung, Freie Universität Berlin, Germany, <https://www.logbuch-wissensgeschichte.de/2390/der-waise>, accessed 26 September 2022.
- Rividi, N., van Zuilen, M., Philippot, P., Ménez, B., Godard, G. & Poidatz, E. 2010. Calibration of carbonate composition using micro-Raman analysis: Application to planetary surface exploration. *Astrobiology*, **10**(3), 293–309, <https://doi.org/10.1089/ast.2009.0388>.
- Rösch, C., Hock, R., Schüssler, U., Yule, P. & Hannibal, A. 1997. Electron microprobe analysis and X-ray diffraction methods in archaeometry: Investigations on ancient beads from the Sultanate of Oman and from Sri Lanka. *European Journal of Mineralogy*, **9**(4), 763–783, <https://doi.org/10.1127/ejm/9/4/0763>.
- Rothamel, U., Heber, J. & Grill, W. 1983. Vibronic sidebands in ruby. *Zeitschrift für Physik B Condensed Matter*, **50**(4), 297–304, <https://doi.org/10.1007/bf01470041>.
- Roux, V. 2000. *Cornaline de l'Inde: Des Pratiques Techniques de Cambay aux Techno-systèmes de l'Indus*. Éditions de la Maison des Sciences de l'Homme, Paris, France, 558 pp., <https://doi.org/10.4000/books.editionsmsmh.8706>.
- Ruska, J. 1912. *Das Steinbuch des Aristoteles*. Carl Winter's Universitätsbuchhandlung, Heidelberg, Germany, vii + 208 pp., <https://archive.org/details/dassteinbuchdesa00aris>.
- Said, H.M. (transl.) 1989. *Kitāb al-Jamāhir fī Ma'rifat al-Jawāhir (The Book Most Comprehensive in Knowledge on Precious Stones: Al-Beruni's Book on Mineralogy)*. Pakistan Hijra Council, Islamabad, Pakistan, xxix + 355 pp.
- Schaller, H.M. 1997. Die Wiener Reichskrone – entstanden unter König Konrad III. In: Becker, H.-J. (ed) *Die Reichskleinodien. Herrschaftszeichen des Heiligen Römischen Reiches*. Schriften zur staufischen Geschichte und Kunst, Göppingen, Germany, **16**, 58–105.
- Schmetzer, K. & Gilg, H.A. 2020. The late 14th-century royal crown of Blanche of Lancaster—History and gem materials. *Journal of Gemmology*, **37**(1), 26–64, <https://doi.org/10.15506/JoG.2020.37.1.26>.
- Schmetzer, K., Gilg, H.A., Schüssler, U., Panjekar, J., Calligaro, T. & Périn, P. 2017. The linkage between garnets found in India at the Arikamedu archaeological site and their source at the Garibpet deposit. *Journal of Gemmology*, **35**(7), 598–627, <https://doi.org/10.15506/JoG.2017.35.7.598>.
- Schmidt, P., Bellot-Gurlet, L., Leá, V. & Sciau, P. 2014. Moganite detection in silica rocks using Raman and infrared spectroscopy. *European Journal of Mineralogy*, **25**(5), 797–805, <https://doi.org/10.1127/0935-1221/2013/0025-2274>.
- Schulze-Dörrlamm, M. 1991. *Die Kaiserkrone Konrads II. (1024 - 1039). Eine archäologische Untersuchung zu Alter und Herkunft der Reichskrone*. Thorbecke Verlag, Sigmaringen, Germany, 145 pp.
- Schüssler, U., Rösch, C. & Hock, R. 2001. Beads from ancient Sri Lanka – First results of a systematic material analysis. In: Weisshaar, H.J., Roth, H. & Wijeyapala, W. (eds) *Ancient Ruhuna. Sri Lankan-German Archaeological Project in the Southern Province*, Vol. 1. Verlag Philipp von Zabern, Mainz am Rhein, Germany, 227–242.
- Šefců, R., Chlumská, Š. & Hostašová, A. 2015. An investigation of the lead tin yellows type I and II and their use in Bohemian panel paintings from the Gothic period. *Heritage Science*, **3**(1), article 16, <https://doi.org/10.1186/s40494-015-0045-2>.
- Slotznick, S.P. & Shim, S.H. 2008. In situ Raman spectroscopy measurements of MgAl<sub>2</sub>O<sub>4</sub> spinel up to 1400 °C. *American Mineralogist*, **93**(2–3), 470–476, <https://doi.org/10.2138/am.2008.2687>.
- Smith, C.P. 2012. Spinel and its treatments: A current status report. *InColor*, No. 19, 50–54, <http://www.incolormagazine.com/books/pcpz/#p=50>.
- Staats, R. 2006. *Die Reichskrone: Geschichte und Bedeutung eines europäischen Symbols*. Steve-Holger Ludwig, Kiel, Germany, 125 pp.
- Then-Obluska, J., Gilg, H.A., Schüssler, U. & Wagner, B. 2021. Western connections of northeast Africa: The garnet evidence from late antique Nubia, Sudan. *Archaeometry*, **63**(2), 227–246, <https://doi.org/10.1111/arcm.12607>.
- Thoresen, L. & Schmetzer, K. 2013. Greek, Etruscan and Roman garnets in the antiquities collection of the J. Paul Getty Museum. *Journal of Gemmology*, **33**(7), 201–222, <https://doi.org/10.15506/JoG.2013.33.7.201>.
- Troupeau, G. 1998. Le premier traité arabe de minéralogie: Le livre de Yūḥannā Ibn Māsawayh sur les pierres précieuses. *Annales Islamologiques*, **32**(6), 219–238, <https://www.ifao.egnet.net/anisl/32/12>.
- Tsai, T.-H. & D'Haenens-Johansson, U.F.S. 2021. Rapid gemstone screening and identification using fluorescence spectroscopy. *Applied Optics*, **60**(12), 3412–3421, <https://doi.org/10.1364/ao.419885>.
- Váczi, T. 2014. A new, simple approximation for the deconvolution of instrumental broadening in spectroscopic band profiles. *Applied Spectroscopy*, **68**(11), 1274–1278, <https://doi.org/10.1366/13-07275>.
- Van Minh, N. & Yang, I.-S. 2004. A Raman study of cation-disorder transition temperature of natural MgAl<sub>2</sub>O<sub>4</sub> spinel. *Vibrational Spectroscopy*, **35**(1–2), 93–96, <https://doi.org/10.1016/j.vibspec.2003.12.013>.

- White, W.B. & DeAngelis, B.A. 1967. Interpretation of the vibrational spectra of spinels. *Spectrochimica Acta Part A: Molecular Spectroscopy*, **23**(4), 985–995, [https://doi.org/10.1016/0584-8539\(67\)80023-0](https://doi.org/10.1016/0584-8539(67)80023-0).
- Whitney, D.L. & Evans, B.W. 2010. Abbreviations for names of rock-forming minerals. *American Mineralogist*, **95**(1), 185–187, <https://doi.org/10.2138/am.2010.3371>.
- Widmer, R., Malsy, A.-K. & Armbruster, T. 2015. Effects of heat treatment on red gemstone spinel: Single-crystal X-ray, Raman, and photoluminescence study. *Physics and Chemistry of Minerals*, **42**(4), 251–260, <https://doi.org/10.1007/s00269-014-0716-7>.
- Wolf, G.G. 1995. *Die Wiener Reichskrone*. Skira, Milan, Italy, 203 pp.
- Wood, B.J., Kirkpatrick, R.J. & Montez, B. 1986. Order-disorder phenomena in  $\text{MgAl}_2\text{O}_4$  spinel. *American Mineralogist*, **71**(7–8), 999–1006.
- Zeug, M., Nasdala, L., Wanthanachaisaeng, B., Balmer, W.A., Corfu, F. & Wildner, M. 2018. Blue zircon from Ratanakiri, Cambodia. *Journal of Gemmology*, **36**(2), 112–132, <https://doi.org/10.15506/JoG.2018.36.2.112>.
- Zeug, M., Nasdala, L., Chanmuang N, C. & Hauzenberger, C. 2022. Gem topaz from the Schneckenstein Crag, Saxony, Germany: Mineralogical characterization and luminescence. *Gems & Gemmology*, **58**(1), 2–17, <https://doi.org/10.5741/gems.58.1.2>.

### The Authors

**Prof. Dr Lutz Nasdala\***,  
**Dr Chutimun Chanmuang N.**,  
**Annalena Erlacher and Prof. Dr Gerald Giester**  
 Institut für Mineralogie und Kristallographie,  
 Universität Wien, Josef-Holaubek-Platz 2,  
 1090 Vienna, Austria  
 \*Email: lutz.nasdala@univie.ac.at

**Teresa Lamers, Dr Martina Griesser**  
**and Dr Franz Kirchweiger**  
 Kunsthistorisches Museum Vienna, Burgring 5,  
 1010 Vienna, Austria

**Prof. Dr H. Albert Gilg**  
 TUM School of Engineering and Design,  
 Technische Universität München, Arcisstr. 21,  
 80333 Munich, Germany

**Dr Miriam Böhmmler**  
 WITec Wissenschaftliche Instrumente und  
 Technologie GmbH, Lise-Meitner-Straße 6,  
 89081 Ulm, Germany

### Acknowledgements

Roman Schuckert and Erich Polacek (both from Universität Wien) are thanked for customising the Raman probe head and video camera to a tripod, including 3D printing of an adaptor plate. Dr Alexey Loparev (WITec GmbH, Ulm), Thomas Rosen and Wolfgang Zirbs (both from Universität Wien) provided software help. We are very much indebted to Helene Hanzler for her manifold help

in the Imperial Treasury Vienna, Herbert Reitschuler for operating the digital microscope and taking the photographs that were used as a working basis and for presentation herein, Christian Mendez for many additional photographs and Sabine Stanek (all from Kunsthistorisches Museum Vienna) for assisting with the PL and Raman measurements. Sincere thanks to WITec Wissenschaftliche Instrumente und Technologie GmbH for loaning a spectrometer system, and to Kunsthistorisches Museum Vienna for the permission to use photographs and reproductions of documents herein. Author HAG is most grateful to the Staatliche Antikensammlung München and the Archäologische Staatssammlung (Munich, Germany) for the possibility to investigate garnets in their collections, and to Norbert Hommrichhausen (experimenta – The Science Center, Heilbronn, Germany) for help with Raman analysis and taking photographs of inclusions in reference garnets. We thank Prof. Dr Emmanuel Fritsch, Dr Stefanos Karamelas, Dr Radka Šefců and Dr Hao Wang for discussions and hints to literature. The constructive reviews of three anonymous experts and editorial help of Damon Strom are gratefully acknowledged. Author TL is recipient of a DOC fellowship of the Austrian Academy of Sciences at the Institute of Conservation and Restoration, University of Applied Arts Vienna. Research project ‘Crown’ is funded by Ernst von Siemens Kunststiftung and Rudolf August Oetker-Stiftung. Additional funding is supplied by the Federal Ministry for Arts, Culture, the Civil Service and Sport (BMKOES), Republic of Austria.

**Gem-A Members and Gem-A registered students receive 5% discount on books and 10% discount on instruments from Gem-A Instruments**

Contact [instruments@gem-a.com](mailto:instruments@gem-a.com) or visit our website for a catalogue





**Figure 1:** These gem-quality Co-bearing blue spinels (3–12 ct) come from a new deposit in the Lukande area of Tanzania. Composite photo by M. S. Krzemnicki.

# Cobalt-bearing Blue Spinel from Lukande, near Mahenge, Tanzania

Michael S. Krzemnicki, Alex Leuenberger and Walter A. Balmer

**ABSTRACT:** In September 2021, a new deposit of Co-bearing blue spinel was discovered in the Lukande area, south of Mahenge in central Tanzania. We analysed 44 faceted spinels from this source, ranging from Co-dominated blue to Fe-dominated (greyish) blue. Interestingly, nearly all of these spinels showed characteristic inclusion features, consisting predominantly of oriented rhombic lamellae (inferred to be högbomite), as well as oriented short needles and particles. In addition, trace-element analyses revealed two types of spinel from this new deposit: attractive blue stones that showed an average Co concentration of 32 ppm (designated type I), and darker material with distinctly higher Co (averaging 200 ppm; designated type II). The latter showed a beautiful blue colour only when cut into melee-sized stones (i.e. about 2 mm diameter). Based on their trace-element composition, stones from this new deposit near Lukande can be separated from Co-bearing spinels from Vietnam, Sri Lanka and Pakistan. U-Pb dating of surface-reaching zircon inclusions indicates the Tanzanian spinels formed during a late stage of the East African Orogeny, possibly overprinted by the Kuunga-Malagasy orogeny (about 500–570 million years ago).

*The Journal of Gemmology*, **38**(5), 2023, pp. 474–493, <https://doi.org/10.15506/JoG.2023.38.5.474>  
© 2023 Gem-A (The Gemmological Association of Great Britain)

**G**em-quality spinel ( $\text{MgAl}_2\text{O}_4$ ) from Tanzania has been well known in the trade for many decades. However, until recently, fine blue Co-bearing spinel (e.g. Figure 1) was quite rare from this country. Gem-quality Tanzanian spinel was described from the Umba Valley (near the Kenyan border), and later from the Uluguru Mountains near

Morogoro in the central part of the country. These spinels were mostly red to pink and purple (Bank *et al.* 1989; Hänni & Schmetzer 1991; Schmetzer & Berger 1992). Occasionally, blue spinel from the Morogoro Region has been mentioned in the literature (Schmetzer & Berger 1992) and, later, was found together with other gem varieties in alluvial deposits at Tunduru in

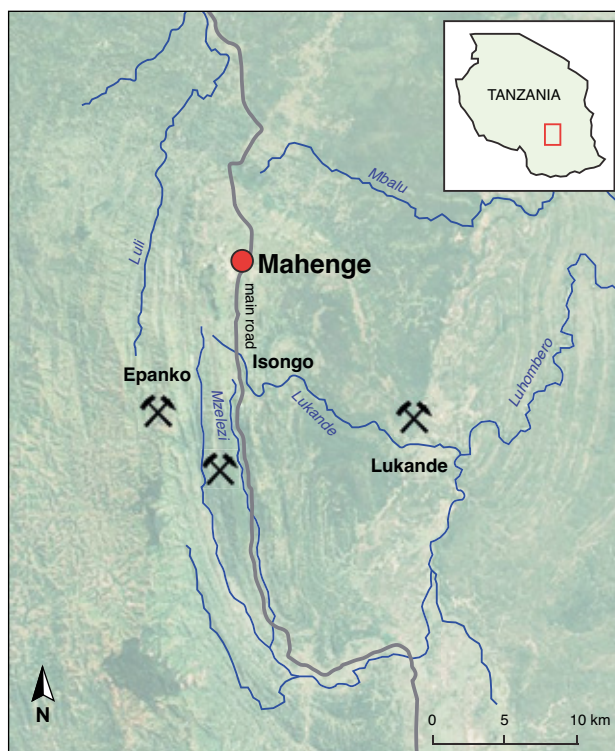


**Figure 2:** The locations of the spinel deposits at Epanko, Isongo and Lukande in the Mahenge area of central Tanzania are shown on this map (slightly adapted from Hendy *et al.* 2018 and combined with a background image from Google Earth).

southern Tanzania (Henn & Milisenda 1997; Schaub 2004; D'Ippolito *et al.* 2015; Sokolov *et al.* 2019).

Since the 1990s, spinel (together with ruby) has also been found in the Mahenge Mountains near the township of Mahenge in south-central Tanzania (Figure 2), but in rather limited quantities (Koivula *et al.* 1993; Quinn & Laurs 2004; Kukharuk & Manna 2019). This dramatically changed in August 2007 with the discovery of several giant (up to 54 kg) pinkish red crystals at Epanko (or Ipanko), located several kilometres south-west of Mahenge (Weinberg 2007; Pardieu & Hughes 2008). Several gemstones of exceptional quality and size (10–50 ct) were cut from this material, placing these Tanzanian spinels among the most sought-after gems in the international trade. During a visit to the Epanko spinel deposits in October 2009, two of the authors (WAB and MSK) also visited small artisanal mining sites for purple and greyish violet Fe-rich spinels about 5 km south of Isongo village near Mahenge.

To the authors' knowledge, until recently, Co-bearing blue spinel from Tanzania was known only from Tunduru, where a very few vivid blue stones have been mined. However, in September 2021, a new deposit of Co-bearing blue spinel was discovered near Lukande, which is located about 15 km south-east of Mahenge.

The attractive colouration and availability of relatively large sizes (again, see Figure 1) have generated significant interest in this spinel in the gem trade (Branstrator 2022; Krzemnicki 2022; Stephan *et al.* 2022). In this article, we describe this new material and its gemmological characteristics.

## LOCATION AND MINING

The new deposit of Co-bearing blue spinel is located near Lukande village (8°48'40.0" S, 36°50'00.0" E; Figure 2), which is a 45-minute drive on a dirt road from Mahenge. The mining area is situated in a valley with farmland, near a site where rubies were dug in the 1990s (i.e. at the 'Simba' mine). The spinel occurs in an eluvial layer buried approximately 1–8 m below the surface, together with other minerals of little commercial value (mostly ruby and pink sapphire of low quality). Artisanal miners use simple tools such as shovels to remove the overburden (dark-coloured soil; Figure 3). The spinels are also mined from heavily weathered marble, which has partially decomposed into soil (Figure 4). The miners load the gem-bearing material into bags, which are carried on bicycles to a nearby stream, where washing is done using sieves (Figure 5). Larger-sized stones are found in big blocks of unweathered marble, which miners break using hammers.

One of the authors (AL) visited the mining area in January 2022, when about 3,000 people were working there. About 300–500 of them were reportedly from Mahenge, but most came from elsewhere in Tanzania and even neighbouring countries such as Mozambique, Kenya and Burundi. In response to the initial mining rush, local government supervisors divided the area into small mining plots of about 6 × 10 m, which the



**Figure 3:** Artisanal miners search for blue spinel in a series of pits near Lukande. Photo by A. Leuenberger.





**Figure 4:** A pile of soil from weathered marble will be taken to a nearby stream for washing Co-bearing spinel. Marble boulders are also visible in this pit. Photo by A. Leuenberger.

artisanal miners could work after paying a fee equivalent to USD10 to compensate the landowners. Access to the mines by foreigners and gem dealers is generally restricted; only local brokers can buy stones from the miners (Figure 6), and they must present the gems to government officials at the mining office in Mahenge. The brokers are then required to pay a royalty upon selling the rough material to local dealers and foreign buyers.

According to information gathered during author AL's visit to the area in January 2022, most miners are unable to cover their mining expenses, partly because the spinels are commonly included and tend to have an undesirable greyish purple, greyish blue or greenish blue colouration. The production of attractive facetable blue-coloured Co-bearing spinel from this deposit is

rather small, and as of March 2022 only several hundred rough stones had been found that could yield clean blue gemstones up to 3 ct (e.g. Figure 7). Faceted stones of fine quality over 5 ct are rare. Of the approximately 50 blue spinels from this deposit analysed so far by SSEF, only a few exceptional stones weighed 10+ ct.

The miners also find some very dark to nearly black rough spinel (e.g. bottom left in Figure 7). Since faceting this material in typical gem sizes would yield over-dark stones, it is cut into small gems (usually calibrated melee sizes) to reveal a beautiful Co-related blue colour (Figure 8).

Most of the blue spinels from this new deposit first came to the Sri Lankan market, and subsequently they have been popular with Chinese buyers working in Bangkok, Thailand. A small number of these faceted spinels were offered at the February 2022 Tucson shows, mostly in 2–3 ct sizes. So far in 2023, the authors estimate that a few hundred of these blue spinels have been shown at various trade shows. The majority weighed 1.5–3.5 ct, while larger sizes up to 7 ct were uncommon and good-quality stones exceeding 10 ct were rare.

## GEOLOGY

Similar to other marble-related spinel and ruby deposits in East Africa, the Co-bearing spinel deposit near Lukande is related to the Neoproterozoic East African Orogeny (EAO). This large-scale mountain-building event occurred when parts of East and West Gondwana collided about 640–580 million years (Ma) ago, and eventually led to the formation of large, high-grade metamorphic complexes in today's East Africa (i.e. the



**Figure 5:** Spinel miners use sieves to wash gem-bearing gravel in a local stream. Photo by A. Leuenberger.





**Figure 6:** An artisanal miner (**a**) shows a small selection of blue spinel fragments, which represent one week's production by a group of five miners. (**b**) A close-up of the same parcel is shown here. The miners sell the rough material to brokers, who then must pay a royalty to government officials at the mining office in Mahenge, before it can be offered to local dealers and foreign buyers. Photos by A. Leuenberger.

Mozambique Metamorphic Belt; Stern 1994; Meert 2003; Fritz *et al.* 2005; Hauzenberger *et al.* 2007 and references therein). Rocks of the EAO include two granulitic terrains in Tanzania: the Western and Eastern Granulites. The Eastern Granulites, which host the spinel deposits near the municipalities of both Morogoro and Mahenge, consist of a migmatitic basement of juvenile crustal and meta-igneous rocks which are overlain by



**Figure 7:** These Co-bearing spinels (about 1–4 g each) from the Lukande area were offered for sale by a local gem broker in Arusha, Tanzania. They were collected over four weeks during the most intense mining period in November 2022. The very dark stones at bottom-left can be cut into melee-size stones to reveal their blue colour (see Figure 8). Photo by A. Leuenberger.

a cover sequence of metamorphosed sedimentary units containing gem-bearing marble units (Möller *et al.* 2000; Fritz *et al.* 2005; Hauzenberger *et al.* 2007 and references therein). The initial sedimentation of the metacarbonate cover sequence took place in close proximity to the hinterland, most probably during the early Neoproterozoic. A lagoon or lacustrine sediment basin on the passive continental margin of former East Gondwana seems to be a plausible geological setting (Balmer *et al.* 2017).

During the EAO, a high-grade metamorphic event (amphibolite-to-granulite facies conditions) led to the formation of the gem deposits within the cover sequence of the Eastern Granulites. These include the ruby and spinel occurrences in the Mahenge Mountains and Uluguru Mountains. Finally, the gem-bearing marbles of



**Figure 8:** Five small calibrated spinels (from left to right: SPTan-2\_1 to SPTan-2\_5; each approximately 2 mm diameter; total weight 0.17 ct), reportedly cut from very dark rough from the same mining area near Lukande, were examined for this study. Photo by Alice Chalain, SSEF.

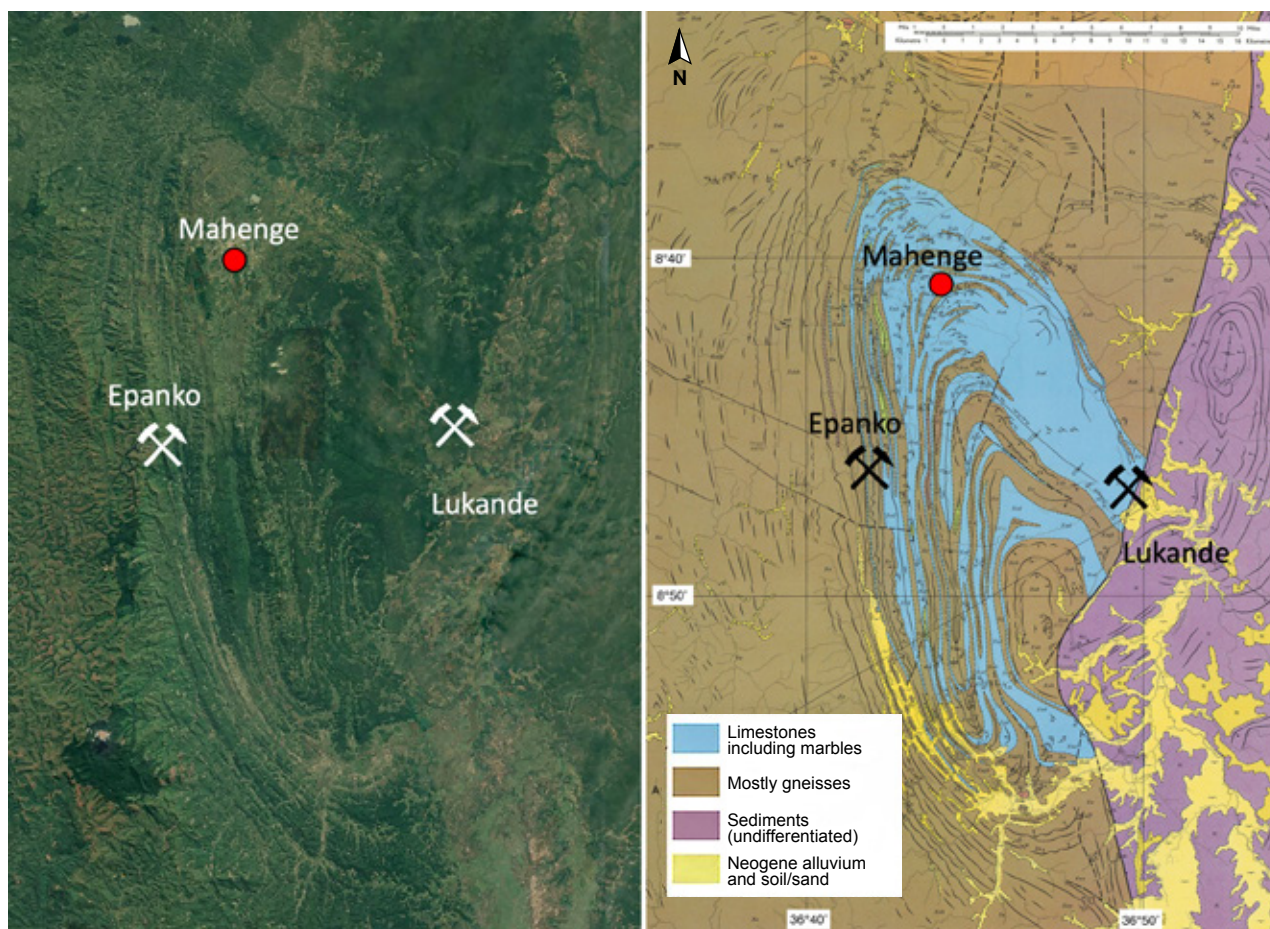


**Figure 9:** Both a satellite image (from Google Earth) and geological map (from Birch & Stephenson 1962) of the Mahenge Mountains show the folded nappe structure that covers an area about 35 km long and about 20 km wide. Pink-to-red spinel is mined at Epanko, and the new deposit of Co-bearing blue spinel is located near Lukande.

the Morogoro Region were affected by greenschist-facies metamorphism, which is linked to the Kuunga-Malagasy orogen (about 500–570 Ma), a late-stage episode of the EAO (Balmer 2011; Fritz *et al.* 2013; Balmer *et al.* 2017). Structurally, the gem-bearing marbles form regional nappes (thrust sheets) overlaying the granulitic basement gneisses (Figure 9). These nappes were thrust onto the basement in a north-western direction. The nappe structures are cross-cut in their root zones by a major fault with a mostly north-eastern-trending strike (Birch & Stephenson 1962; Sampson & Wright 1964; Schlüter 1997; Rossetti *et al.* 2008; Fritz *et al.* 2009; Balmer *et al.* 2017). The Co-bearing spinel deposit near Lukande is located in the root zone of the local nappe structure in the Mahenge Mountains.

Since the host rock at Lukande is strongly weathered, a detailed petrographic characterisation (e.g. marble or calc-silicate-rich metacarbonate) has not been possible. Still, what was observed on site by author AL appears to relate well to other marble-hosted spinel deposits in the Mahenge Mountains (examined previously by

author WAB; see Balmer *et al.* 2017), as well as at additional localities where Co-bearing spinel is found as an accessory mineral in marble or other metacarbonates, such as in Vietnam (Chauviré *et al.* 2015), Canada (Belley & Groat 2019), Tajikistan (Schwarz *et al.* 2022) and Pakistan (Schollenbruch *et al.* 2021).

## MATERIALS AND METHODS

The Lukande spinels analysed for this study were kindly provided by several reliable gem dealers (e.g. in Arusha, Tanzania). They mainly consisted of 39 faceted stones ranging from 2.07 to 11.25 ct, most of which had an attractive blue colour and fine clarity (e.g. Figures 1 and 10). The study sample also included five calibrated melee-sized vivid blue spinels (total weight 0.17 ct; Figure 8) that were cut from very dark rough material reportedly found in the same area (S. Jaquith, pers. comm. 2023). Based on differences in the colour and trace-element composition (as reported below) for these two groups, we separated them into two categories,



with the main ones designated type I (sample numbers starting with SPTan-1) and the melee stones as type II (SPTan-2); all of them are listed in Table I.

The samples were characterised with standard gemmological instruments (i.e. refractometer, hydrostatic balance, and long- and short-wave UV lamps), except for the type II spinels, for which RI and SG values were not determined due to their small size. Internal features in all stones were examined with a System Eickhorst Gemmaster microscope with Zeiss optics.

Ultraviolet-visible-near infrared (UV-Vis-NIR) absorption spectroscopy was performed on all type I samples and one type II spinel using a Cary 500 spectrophotometer in unpolarised mode (290–900 nm range with 1 nm resolution).

For inclusion identification and photoluminescence (PL) spectroscopy, we used a Renishaw inVia Raman microscope with an argon laser (514 nm emission). Raman analyses of inclusions in selected samples were done with  $20\times$  or  $50\times$  magnification, using a spectral resolution of  $1.6\text{ cm}^{-1}$  in the range of  $150\text{--}1400\text{ cm}^{-1}$  Raman shift (or  $150\text{--}1800\text{ cm}^{-1}$  for zircon) with a 10 s counting time. To increase the signal-to-noise ratio, spectra were accumulated 3–10 times depending on the quality of the signal. For PL spectroscopy, only a single scan was measured in the 600–800 nm range.

Chemical analyses were performed by energy-dispersive X-ray fluorescence (EDXRF) spectroscopy with a Thermo Quant’X instrument using our in-house-developed spinel setup with excitation energies ranging from 4 to 25 kV. All type I samples were analysed, but not the type II spinels due to their small size. In addition, trace- and ultra-trace-element analyses were carried out on 17 type I samples (specified in Table I) and all five type II spinels with our GemTOF system (laser ablation inductively coupled plasma time-of-flight mass spectrometry; LA-ICP-TOF-MS) using a 193 nm ArF excimer laser with a fluence of  $5.6\text{ J/cm}^2$ . For each sample, we analysed three to four spots (usually on the girdle) that were each  $100\text{ }\mu\text{m}$  diameter. Reference glass NIST SRM 610 was used as the external standard and the theoretical (stoichiometric) Al concentration of spinel as the internal standard. By using a time-of-flight (TOF) system, we were able to record nearly all elements in the periodic table simultaneously at ultra-high speed and high sensitivity. The limit of detection of our TOF-MS setup ranges from single-digit-ppb for heavy elements to low-ppm for light elements. The error bars (uncertainty) for each data point in the LA-ICP-MS plots were calculated using the transient signal and found to be commonly about 1–2%—distinctly smaller than the

data points in the logarithmic diagrams presented in this article. The same instrumentation was used for the radiometric dating of a total of four surface-reaching zircon inclusions in two of the spinel samples (SPTan-1\_3 and SPTan-1\_13). More detailed information about this highly versatile system, and the analytical settings used for the chemical analyses and radiometric dating, can be found in Wang *et al.* (2016), Phyo *et al.* (2020) and Wang and Krzemnicki (2021).

## RESULTS

### Gemmological Properties

The samples showed an attractive blue colour, ranging from blue to slightly greyish blue to greenish blue, often with vivid blue internal reflections. In addition, many of the stones showed high clarity, even in large sizes (e.g. Figure 10).

The type I spinels had an RI ranging from 1.712 to 1.718 and an SG of 3.59 to 3.62, consistent with the expected values for Mg-Al spinel. Although the RI and SG values of the five type II melee samples could not be measured with acceptable accuracy, we would expect them to be slightly higher due to their trace-element composition (see below). Most of the investigated spinels showed a weak greenish reaction when exposed to long-wave UV radiation, but were inert to short-wave UV.

### Microscopic Features

All of the samples contained some inclusions. Regularly arranged rhombic (to slightly irregular) lamellae oriented parallel to the octahedral crystal directions were among the most prominent features (see also Table I). They often showed intriguing iridescence colours when rotated under a light source (Figure 11). They



**Figure 10:** This 7.48 ct Co-bearing spinel (SPTan-1\_31) from the Lukande area was cut from one of the larger pieces of rough in Figure 7. Photo by Luc Phan, SSEF.



**Table I:** Tanzanian Co-bearing spinel samples characterised in this study.









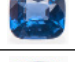



































Photo	Sample	Weight (ct)	Shape	RI	SG	Microscopy (main features)	GemTOF	PL band at 640 nm
	SPTan-1_1	3.13	Cushion	1.715	3.61	Högbomite lamellae, apatite, zircon	Yes	Distinct
	SPTan-1_2	10.68	Oval	1.718	3.62	Högbomite lamellae, etc. <sup>a</sup>	Yes	Distinct
	SPTan-1_3 <sup>b</sup>	10.62	Cushion	1.716	3.60	Högbomite lamellae, zircon, apatite, mica	Yes	Moderate
	SPTan-1_4	8.67	Oval	1.714	3.61	Högbomite lamellae, etc.	Yes	Distinct
	SPTan-1_5	6.78	Cushion	1.714	3.59	Högbomite lamellae, etc.	Yes	Distinct
	SPTan-1_6	3.55	Cushion	1.715	3.60	Högbomite lamellae, apatite	Yes	Distinct
	SPTan-1_7	2.77	Cushion	1.712	3.60	Particles, zircon	Yes	Moderate
	SPTan-1_8	2.64	Oval	1.714	3.60	Högbomite lamellae, etc.	Yes	Distinct
	SPTan-1_9	2.52	Cushion	1.714	3.62	Högbomite lamellae, etc.	Yes	Distinct
	SPTan-1_10	2.30	Cushion	1.714	3.61	Högbomite lamellae, etc.	Yes	Moderate
	SPTan-1_11	2.28	Cushion	1.712	3.59	Högbomite lamellae, etc.	Yes	Distinct
	SPTan-1_12	2.11	Cushion	1.716	3.62	Högbomite lamellae, etc.	Yes	Weak
	SPTan-1_13 <sup>c</sup>	2.07	Cushion	1.715	3.60	Högbomite lamellae, zircon	Yes	Distinct
	SPTan-1_14	4.46	Cushion	1.715	3.62	Dispersed particles	No	Distinct
	SPTan-1_15	3.31	Oval	1.715	3.61	Högbomite lamellae, etc.	No	None
	SPTan-1_16	4.09	Cushion	1.718	3.61	Dispersed particles	Yes	Distinct
	SPTan-1_17	4.01	Cushion	1.717	3.62	Högbomite lamellae, etc.	No	Distinct
	SPTan-1_18	5.86	Cushion	1.716	3.60	Högbomite lamellae, etc.	No	Moderate
	SPTan-1_19	4.65	Octagonal	1.715	3.60	Högbomite lamellae, etc.	No	Moderate
	SPTan-1_20	4.23	Cushion	1.716	3.60	Högbomite lamellae, etc.	No	Distinct
	SPTan-1_21	3.75	Cushion	1.718	3.61	Högbomite lamellae, etc.	No	Moderate
	SPTan-1_22	5.15	Cushion	1.718	3.62	Högbomite lamellae, etc.	No	Moderate
	SPTan-1_23	5.18	Cushion	1.717	3.62	Högbomite lamellae, etc.	Yes	None
	SPTan-1_24	4.94	Cushion	1.716	3.59	Milkiness	Yes	Moderate

Table I: (continued)

Photo	Sample	Weight (ct)	Shape	RI	SG	Microscopy (main features)	GemTOF	PL band at 640 nm
	SPTan-1_25	4.11	Cushion	1.716	3.62	Högbomite lamellae, etc.	Yes	Distinct
	SPTan-1_26	6.14	Cushion	1.716	3.59	Högbomite lamellae, etc.	No	Distinct
	SPTan-1_27	10.14	Cushion	1.716	3.61	Högbomite lamellae, etc.	No	Distinct
	SPTan-1_28	4.98	Cushion	1.716	3.62	Högbomite lamellae, etc.	No	Distinct
	SPTan-1_29	10.31	Cushion	1.716	3.60	Högbomite lamellae, etc.	No	Distinct
	SPTan-1_30	7.12	Cushion	1.715	3.61	Högbomite lamellae, etc.	No	Moderate
	SPTan-1_31	7.48	Oval	1.715	3.61	Högbomite lamellae, etc.	No	Distinct
	SPTan-1_32	10.07	Cushion	1.714	3.59	Högbomite lamellae, etc.	No	Distinct
	SPTan-1_33	3.54	Heart-shaped	1.717	3.62	Högbomite lamellae, etc.	No	Moderate
	SPTan-1_34	6.66	Cushion	1.717	3.62	Lines of particles, etc.	No	Distinct
	SPTan-1_35	11.25	Cushion	1.715	3.61	Högbomite lamellae, etc.	No	None
	SPTan-1_36	5.52	Oval	1.716	3.60	Högbomite lamellae, etc.	No	nd
	SPTan-1_37	7.13	Cushion	1.717	3.61	Högbomite lamellae, etc.	No	Moderate
	SPTan-1_38	7.09	Cushion	1.718	3.61	Högbomite lamellae, etc.	No	nd
	SPTan-1_39	3.10	Cushion	1.717	3.59	Högbomite lamellae, etc.	No	nd
	SPTan-2_1	0.035	Round	nd	nd	Högbomite lamellae, etc.	Yes	None
	SPTan-2_2	0.038	Round	nd	nd	Högbomite lamellae, etc.	Yes	Moderate
	SPTan-2_3	0.034	Round	nd	nd	Högbomite lamellae, etc.	Yes	Strong
	SPTan-2_4	0.035	Round	nd	nd	Högbomite lamellae, etc.	Yes	Strong
	SPTan-2_5	0.031	Round	nd	nd	Högbomite lamellae, etc.	Yes	Very strong

<sup>a</sup> Abbreviations: nd = not determined; etc. = one or more of the following: dispersed fine particles, needles, zones of turbidity, octahedral negative crystals, fissures and partially healed fissures.

<sup>b</sup> U-Pb age dating of two zircon inclusions yielded an age of  $508 \pm 48$  million years.

<sup>c</sup> U-Pb age dating of two zircon inclusions yielded an age of  $501 \pm 29$  million years.

were first described by Schmetzer and Berger (1992) in reddish to purple spinel from Morogoro, Tanzania, and identified as högbomite,  $(\text{Mg,Fe})_2(\text{Al,Ti})_5\text{O}_{10}$ . Such inclusions have also been documented in Co-bearing

spinel from Pakistan (Schollenbruch *et al.* 2021), and recently were reported in material from this new deposit in Tanzania (Krzemnicki 2022; Stephan *et al.* 2022).

Our samples occasionally contained various solid

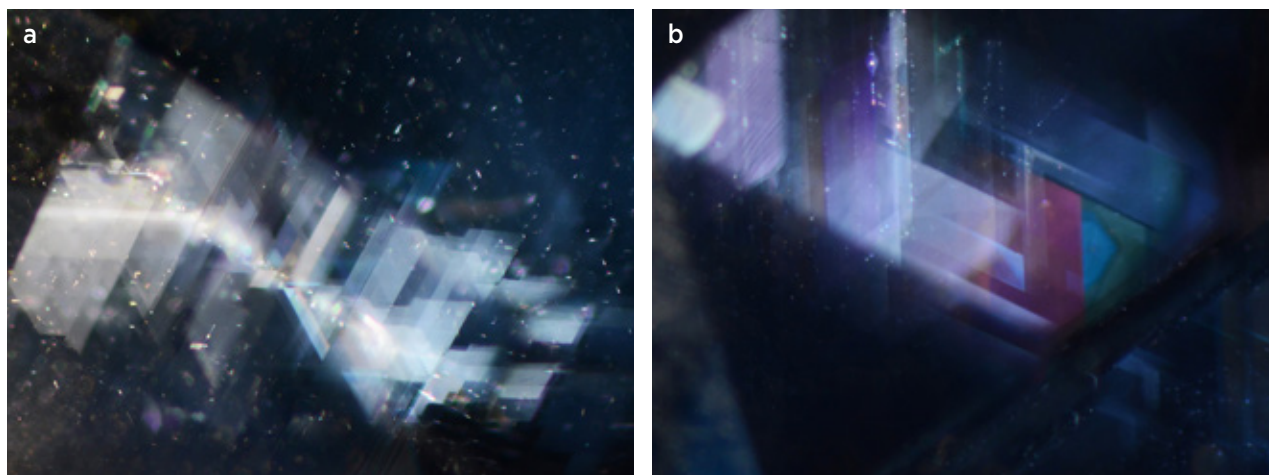


**Figure 11:** (a) Oriented lamellae in Lukande spinel are inferred to consist of högbomite (magnified 40×). (b) They display iridescence at certain orientations (magnification 70×). Photomicrographs by M. S. Krzemnicki, in darkfield illumination.

inclusions—rounded apatite, phlogopite and zircon—mostly as small clusters (Figure 12). The identity of these three inclusion minerals was confirmed by Raman spectroscopy (Figure 13). The main Raman peak in the zircon spectrum,  $\nu_3(\text{SiO}_4)$  at about  $1007\text{ cm}^{-1}$ , showed some broadening (FWHM  $11.43\text{ cm}^{-1}$ ) due to incipient metamictisation (Nasdala *et al.* 1995).

In addition, we commonly observed oriented needle-like inclusions, similar to those reported in blue spinels from Sri Lanka and Vietnam (Shigley & Stockton 1984; Smith *et al.* 2008), and some samples contained zones of milky turbidity caused by minute particles (Figure 14). Also seen were partially healed fissures and octahedral negative crystals, often surrounded by oriented, dotted, discoid structures, resembling to those commonly observed in spinel (e.g. Shigley & Stockton 1984).

### UV-Vis-NIR Absorption Spectroscopy

Figure 15 shows UV-Vis-NIR absorption spectra for three samples representing the spectral variation observed in

blue spinel from the Lukande deposit. Band attribution is according to D'Ippolito *et al.* (2015, and references therein), and a brief background on blue spinel colouration is presented in Box A. In general, all the spectra reveal a strong UV-edge absorption due to Fe, and a series of partially overlapping Co and Fe bands in the visible range. The top spectrum in Figure 15 of a greyish-greenish blue sample is dominated by Fe-related absorption bands and has only a limited contribution by Co. The other two spectra (from purer blue samples) exhibit stronger Co-related absorption bands in the visible range. The Co-Fe-related spectral variations of these selected samples is also reflected in their blue to vivid blue colouration. Apart from the presence of Co, the total amount of Fe (which affects the UV absorption edge via  $\text{O}^{2-}\text{-Fe}^{2+}$  ligand-metal charge transfer), as well as octahedrally coordinated  $\text{Fe}^{2+}$  and  $\text{Fe}^{3+}$  (resulting in an intervalence charge transfer via  $\text{Fe}^{2+}\text{-Fe}^{3+}$ ), both have a major effect on colour, causing the indigo blue colouration to shift to a distinctly more greenish blue (again, see Figure 15).

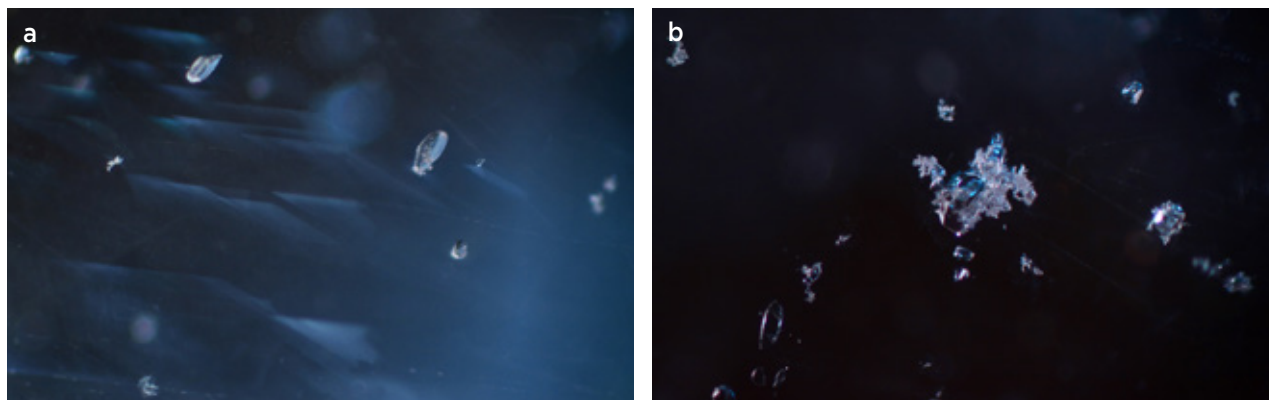


**Figure 12:** These inclusions in Lukande spinel consist of (a) dispersed apatite crystals and (b) a zircon cluster. Photomicrographs by M. S. Krzemnicki; magnified 50×.



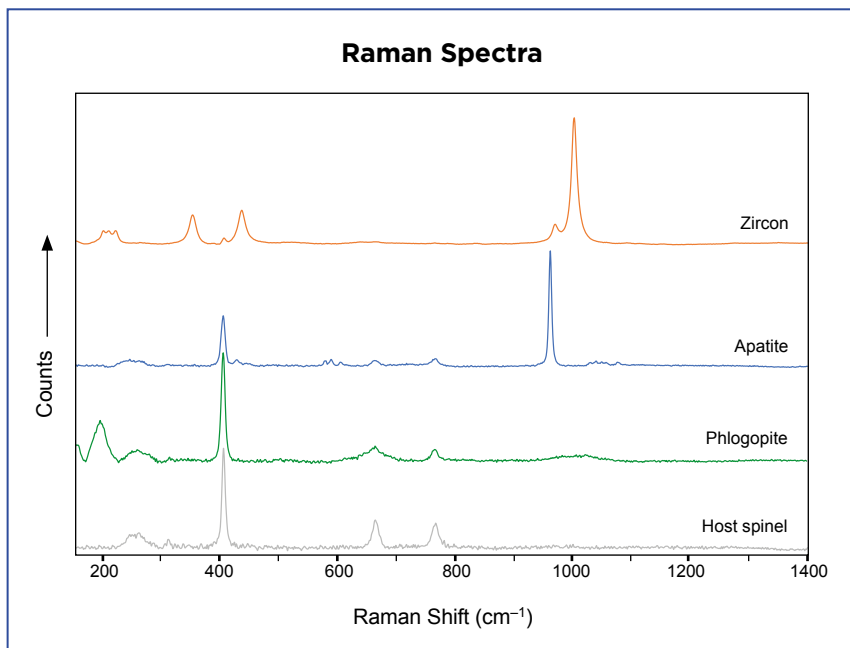


**Figure 13:** Raman spectra of solid inclusions in the studied spinels from Lukande confirm the presence of zircon, apatite and phlogopite. All spectra were baseline-corrected and are offset vertically for clarity. The zircon peak at about 1007  $\text{cm}^{-1}$  shows some broadening due to incipient metamictisation. Peaks from the host spinel (bottom trace) are present to varying degrees in the inclusion spectra.

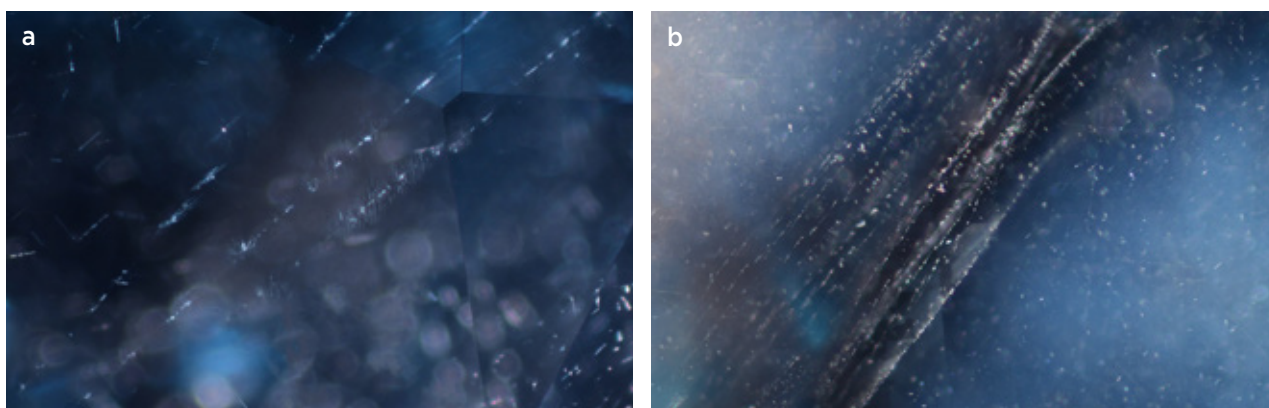


**Figure 14:** Also present in the Lukande spinels are (a) oriented needles and (b) milky turbidity. Photomicrographs by M. S. Krzemnicki; magnified 40 $\times$ .

#### Box A: Blue Spinel Colouration

The colour of spinel and, specifically, of Co-bearing blue spinel, has been investigated quite extensively in the literature (e.g. Gaffney 1973; Shigley & Stockton 1984; Schmetzer *et al.* 1989; Hålenius *et al.* 2002; Taran *et al.* 2005, 2009; Bosi *et al.* 2012; Hanser 2013; Fregola *et al.* 2014; Chauviré *et al.* 2015; D'Ippolito *et al.* 2015; Andreozzi *et al.* 2018). Usually, spinel colouration is due to a combination of transition metals—for blue spinel mainly Fe and Co (if present), and in some purplish blue stones also Cr (Schollenbruch *et al.* 2021). Shigley & Stockton (1984) were the first to attribute Co in addition to Fe as an important chromophore in natural blue spinel.

The hue and saturation of the blue colour is not only related to the concentration of the chromophores Fe and Co, but also to the valence state of iron ( $\text{Fe}^{2+}$  or  $\text{Fe}^{3+}$ ) and their distribution on the two crystallographic sites in the spinel structure.<sup>1</sup> Notably, very low traces of Co have a strong effect on the blue colour of spinel when present as tetrahedrally coordinated  $\text{Co}^{2+}$  (Marfunin 1979; Schmetzer *et al.* 1989; D'Ippolito *et al.* 2015; Andreozzi *et al.* 2018). Often the amount of Co is so low that it is near the detection limit of EDXRF spectroscopy, which is the technique commonly used to analyse the chemical composition of gem materials in gemmological laboratories.

<sup>1</sup> Designated  $\text{AB}_2\text{O}_4$ , with A referring to bivalent ions that are generally at the tetrahedrally coordinated T-site (e.g.  $^{\text{T}}\text{Mg}^{2+}$ ,  $^{\text{T}}\text{Fe}^{2+}$  and  $^{\text{T}}\text{Co}^{2+}$ ), and B indicating trivalent ions that are typically at the octahedrally coordinated M-site (e.g.  $^{\text{M}}\text{Al}^{3+}$ ,  $^{\text{M}}\text{Fe}^{3+}$  and  $^{\text{M}}\text{Cr}^{3+}$ ).

## UV-Vis-NIR Spectra

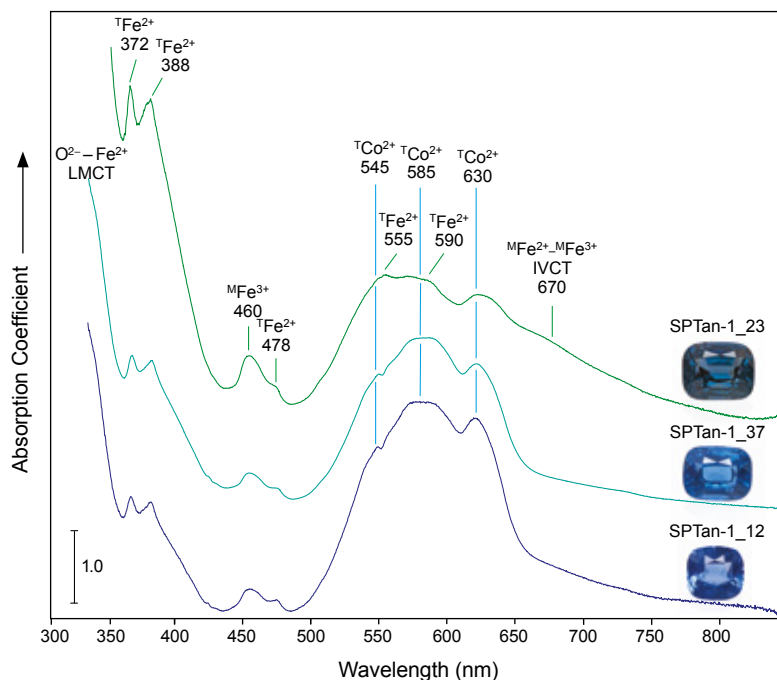


**Figure 15:** The UV-Vis-NIR absorption spectra of Co-bearing blue spinels from Lukande range from Fe dominated (SPTan-1\_23) to Co dominated (SPTan-1\_37 and SPTan-1\_12). The three spectra have been offset vertically for clarity and corrected for path length (absorption coefficient). Abbreviations: LMCT = ligand-metal charge transfer and IVCT = intervalence charge transfer.

## PL Spectra

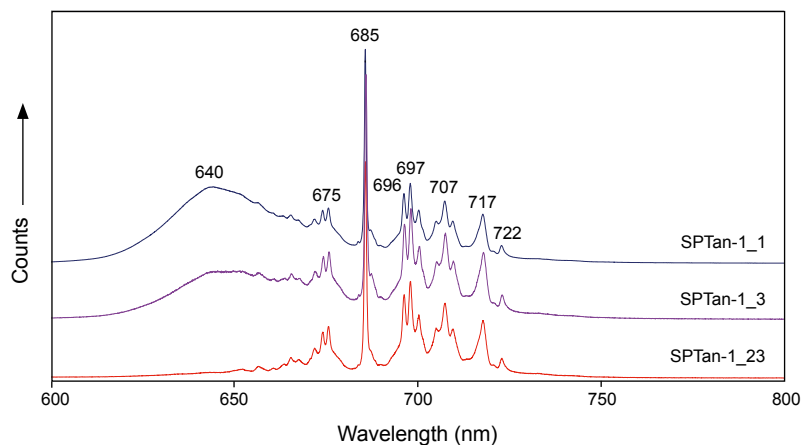


**Figure 16:** Photoluminescence spectra with 514 nm laser excitation of three representative Co-bearing blue spinels from the Lukande area show a series of PL peaks related to octahedrally coordinated  $\text{Cr}^{3+}$  and, to a variable extent, a broad band at about 640 nm assumed to be related to octahedrally coordinated  $\text{Mn}^{2+}$ . The spectra have been offset vertically for clarity.

### Photoluminescence Spectroscopy

The PL spectra of the Lukande spinels show a series of emission lines (a so-called organ-pipe spectrum; Figure 16) related to the presence of traces of  $\text{Cr}^{3+}$  replacing  $\text{Al}^{3+}$  on the octahedrally coordinated site of the spinel structure. The position and shape (i.e. FWHM) of these emission lines confirm that the samples are natural and have not been heated (Saeseaw *et al.* 2009; Smith 2012; Widmer *et al.* 2014).

In addition, most but not all of the investigated

spinel display a broad emission band at about 640 nm (see Table I). In the literature, a similar broad band has been attributed either to tetrahedrally coordinated  $\text{Co}^{2+}$  (Abritta & Blak 1991; Kuleshov *et al.* 1993; Chauviré *et al.* 2015) or to octahedrally coordinated Mn (Gaft *et al.* 2015; Khaidukov *et al.* 2020). From our trace-element data, an attribution to Co is not evident, as some of the samples with little or no emission also have higher Co concentrations than those with a distinct 640 nm band, even if we take into account that some  $\text{Co}^{2+}$  could be

located on the octahedrally coordinated site. An attribution to Mn is more likely, as the three spectra in Figure 16 correlate with increasing Mn concentration (from bottom to top) from about 100 ppm to about 250 ppm. In addition, most of our samples displayed weak greenish luminescence when exposed to long-wave UV radiation. This luminescence results from an emission band at about 514 nm attributed to tetrahedrally coordinated  $\text{Mn}^{2+}$  in the spinel structure (Yu & Lin 1996; Cornu *et al.* 2015; Khaidukov *et al.* 2020). However, other factors (e.g. quenching by Fe) may also play a role in the presence or absence of the 640 nm band.

### Chemical Analysis

**EDXRF Spectroscopy.** EDXRF chemical analyses of the type I study spinels reveal a very uniform chemical composition (see Table II), with a low standard deviation for most elements. The only element showing larger variations is zinc ( $\text{Zn}^{2+}$ ), which commonly replaces magnesium ( $\text{Mg}^{2+}$ ) at the tetrahedral site. This can be seen in a plot of MgO vs ZnO (Figure 17a), which shows a fairly good negative correlation for these two elements.

The Fe concentration in the investigated spinels is quite constant at about 1.2 wt. %  $\text{Fe}_2\text{O}_3$  and shows no evident negative correlation with Mg (Figure 17b). This indicates that most Fe is present as octahedrally coordinated  $\text{Fe}^{3+}$ , with only minor amounts as  $\text{Fe}^{2+}$  in tetrahedral coordination. Nevertheless, the latter plays a major role in the colouring of these blue spinels, in addition to tetrahedrally coordinated  $\text{Co}^{2+}$  (see Figure 15).

Although considerably affecting the colour (and absorption spectra) of these spinels, Co was found to be present only at or below the detection limit (about 50 ppm)

**Table II:** EDXRF analyses of 39 type I Co-bearing blue spinels from Lukande, Tanzania.\*

Oxide (wt.%)	Range	Average	Std. Dev.
MgO	27.80–29.42	28.60	0.34
$\text{Al}_2\text{O}_3$	68.76–69.93	69.47	0.27
$\text{TiO}_2$	0.006–0.013	0.010	0.002
$\text{V}_2\text{O}_3$	bdl–0.015	0.008	0.003
$\text{Cr}_2\text{O}_3$	bdl–0.007	0.004	0.002
MnO	0.034–0.063	0.053	0.006
$\text{Fe}_2\text{O}_3$	1.06–1.84	1.24	0.18
$\text{Co}_2\text{O}_3$	bdl–0.001	0.001	0.000
NiO	0.011–0.024	0.015	0.003
ZnO	0.152–1.403	0.544	0.338
$\text{Ga}_2\text{O}_3$	0.014–0.060	0.033	0.013

\* Abbreviations: bdl = below detection limit; Std. Dev. = Standard Deviation.

of the EDXRF system using our analytical setup. As mentioned above, this is common for gem-quality Co-bearing spinel, and traces of this element are best quantified by mass spectrometry (LA-ICP-MS).

Although Ni is commonly present as a trace element in Co-bearing spinels, the Ni concentrations indicated by EDXRF appear too high (analytical error assumed), as shown by comparison with our LA-ICP-MS data.

**LA-ICP-TOF-MS Analysis.** Table III summarises the trace-element data for the 22 Lukande samples analysed for this study, in comparison with data for Co-bearing

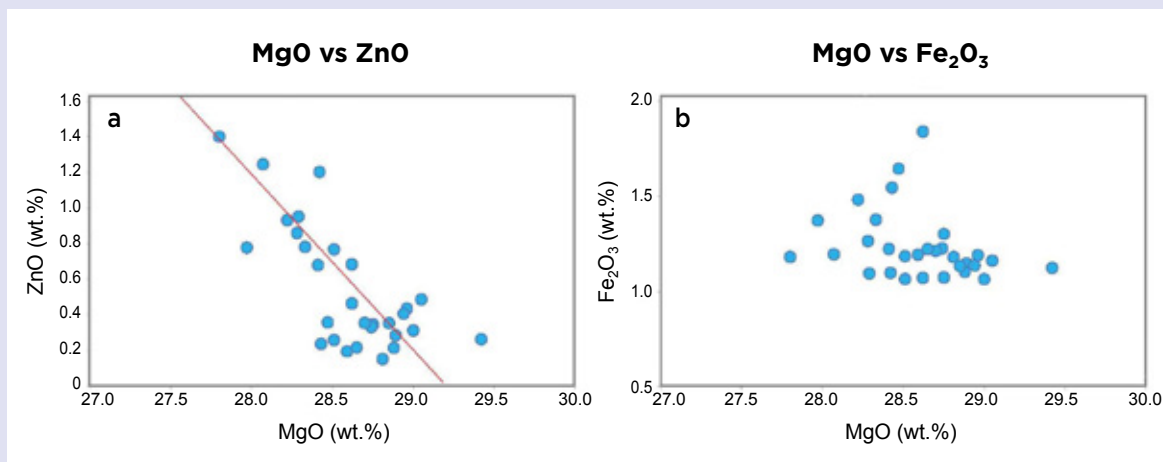


**Figure 17:** Plots of EDXRF data for the type I Co-bearing spinels show (a) a fairly good negative correlation for MgO and ZnO (red line:  $r = -1$ ), and (b) no such correlation for MgO and  $\text{Fe}_2\text{O}_3$ .



**Table III:** Trace-element data for Co-bearing blue spinels from various localities.\*

Element (ppmw)	Tanzania, type I (n = 68)			Tanzania, type II (n = 15)		
	Range	Avg.	Std. Dev.	Range	Avg.	Std. Dev.
Li	80.43–318.3	235.0	59.87	102.2–182.9	128.6	29.32
Be	13.82–34.99	20.89	5.02	4.44–12.79	8.75	2.47
Ti	13.33–206.6	36.42	22.17	12.93–75.15	32.67	17.27
V	29.86–78.05	40.78	11.15	58.85–127.8	99.79	23.59
Cr	4.56–129.5	16.17	27.69	7.99–57.15	36.21	15.21
Mn	128.6–293.8	247.0	32.42	44.85–93.32	64.78	16.49
Fe	7242–12850	8940	1474	9295–13960	11800	1890
Co	15.93–48.22	31.74	7.76	88.30–315.0	199.5	86.84
Ni	30.39–58.57	39.77	7.87	80.16–201.8	136.1	44.62
Zn	1007–11540	3855	2854	22370–115890	59493	36194
Ga	81.60–329.7	170.3	73.79	107.0–286.9	166.3	64.23

\* Data for Tanzanian, Sri Lankan and Vietnamese samples were obtained at SSEF by LA-ICP-TOF-MS, and data for Pakistani samples were obtained at Gübelin Gem Lab by LA-ICP-MS (courtesy of K. Schollenbruch). Abbreviations: bdl = below detection limit; n = number of points analysed.

blue spinels from Sri Lanka and Vietnam (from the SSEF research database), as well as Pakistan (data obtained from Gübelin Gem Lab). The full trace-element analyses of our Lukande samples are available in *The Journal’s* online data depository.

As mentioned above, the Lukande Co-bearing spinels were separated into two categories: type I which shows medium to medium-strong blue colour and can be cut into larger stones (Figure 1), and type II which, as rough fragments, are very dark blue and only display an attractive blue colour when cut into melee sizes of about 2 mm in diameter (Figure 8). These two types not only differ in colour, but also in their trace-element concentrations (see Table III and Figure 18). Type II spinels show, on average, less Mn (about 65 ppm vs about 250 ppm in type I), but distinctly more Co (about 200 ppm vs about 30 ppm in type I) and Ni (about 135 ppm vs about 40 ppm in type I) than the spinels of type I. Iron varies within a limited and similar range in both spinel types. The most obvious difference, however, is the enrichment of Zn (gahnite component) in the type II spinels (up to 115,890 ppmw or 14 wt. % ZnO). Although Zn and other trace elements (e.g. chromophores such as Fe and Co) vary considerably from sample to sample (e.g. from 1,000 to 100,000 ppm Zn), multiple analyses of a single stone show a relatively constant chemical composition (see data in *The Journal’s* data depository). This sample homogeneity also applies to spinel from many other origins. This also explains why gem-quality spinels are generally of homogeneous

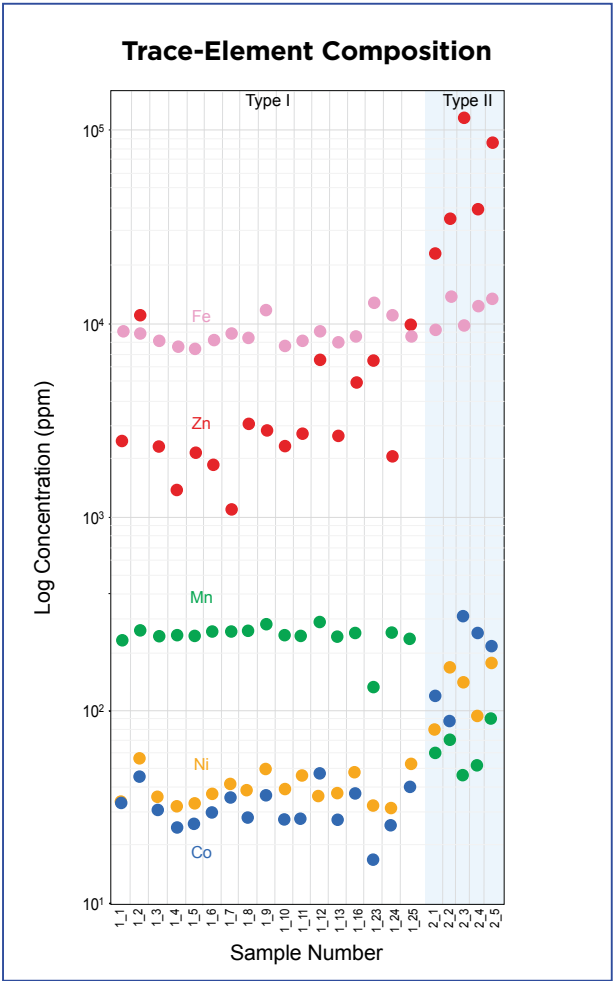


**Figure 18:** The concentrations of selected trace elements (Fe, Zn, Mn, Ni and Co) are shown for both type I and type II Co-bearing spinels from the Lukande area. Notably, the type I spinels contain much less Zn, Ni and Co—and more Mn—than the type II spinels.

Table III: (continued)

Sri Lanka (n = 20)			Vietnam (n = 33)			Pakistan (n = 103)		
Range	Avg.	Std. Dev.	Range	Avg.	Std. Dev.	Range	Avg.	Std. Dev.
12.32–185.8	95.58	57.71	42.70–859.9	294.5	229.8	7.90–561.2	268.0	149.6
3.97–101.8	46.26	32.35	9.82–72.79	20.17	18.84	11.83–78.04	33.95	14.62
bdl–81.62	20.09	28.44	bdl–8.10	2.04	2.30	3.01–1102	117.4	171.9
11.65–86.09	34.06	24.18	2.10–25.61	8.15	7.63	49.56–917.8	190.2	159.7
0.296–20.85	6.84	8.22	0.96–76.66	13.38	25.70	108.2–4947	1142	946.3
26.51–619.9	272.4	223.9	49.14–289.1	120.4	78.66	32.48–192.6	85.48	45.85
5523–23560	15310	6039	3758–21980	14030	6030	10110–47170	20820	10140
17.33–109.9	54.23	29.80	10.82–71.94	39.95	17.84	62.36–420.5	226.6	97.45
2.86–359.2	110.5	129.3	3.63–43.98	25.08	13.10	19.61–335.6	157.8	94.05
33.64–3531	1229	1100	252.7–4141	1547	1415	1611–7522	2945	1375
108.6–200.3	151.6	35.11	79.56–628.4	193.1	171.8	68.49–258.2	130.7	53.50

colour and only rarely show colour zoning (DuToit 2012; Buathong & Narudeesombat 2020), in contrast to corundum, in which chemical and colour zoning are very common.

### U-Pb Radiometric Dating

U-Pb dating of all four surface-reaching zircon inclusions analysed in two of the type 1 spinels yielded an

approximate age of 500 Ma (e.g. Figure 19). This is well in line with radiometric ages for zircon inclusions in rubies and sapphires from East Africa, Sri Lanka and Madagascar (Link 2015; Elmaleh *et al.* 2019; Krzemnicki *et al.* 2019) and can be linked to mineralisation during a late stage of the East African Orogeny (650–500 Ma). These inclusion analyses showed no mixed ages due to accidental ablation of an old detrital zircon core. We thus assume that the calculated U-Pb ages represent the formation age not only of the zircon but also of the spinel during the East African Orogeny, although complex internal zoning of zircon (e.g. an older detrital core) cannot be fully excluded.

## DISCUSSION

The new deposit in the Lukande area in Tanzania has produced a number of attractive blue spinels since September 2021. Our study of a selection of these stones reveals that they all contain traces of Co in various amounts, which has an impact not only on their colour but also on their commercial value. Various criteria have been used to assess whether a stone can be properly termed *Co-spinel* in the gem trade. The first and most strict example is limiting the term only to those spinels that show a vibrant, saturated blue colour resulting from the presence of Co. This excludes lighter blue spinels (e.g. from Vietnam), even though their colour is basically only due to traces of cobalt.

Another approach is to use concentrations of colouring elements, mainly cobalt and iron (e.g. >40–60 ppm Co in ‘low-Fe’ spinels; Peretti *et al.* 2015) or Co/Fe

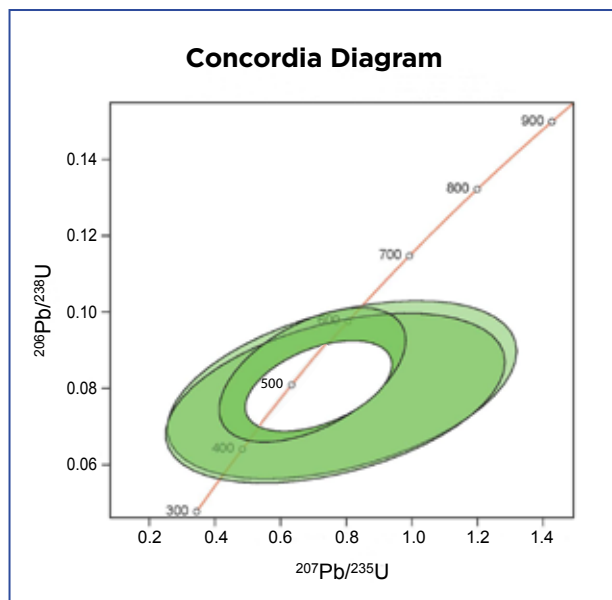


**Figure 19:** This Concordia diagram for zircon inclusions in a Co-bearing spinel from the Lukande area (SPTan-1\_13) reveals an average ( $n = 3$ ) U-Pb age of  $501.1 \pm 29.1$  Ma. The ‘concordia line’ in the centre of the plot shows the U-Pb ratios for a closed system in which all the Pb originates from U decay (i.e. undisturbed by later events such as metamorphism). Figure by H. A. O. Wang, SSEF.

(and Co/Cr) ratios (Sokolov *et al.* 2019; Schollenbruch *et al.* 2021). These approaches have some limitations, as they are based mainly on concentrations, and do not take into account the influence of iron on the absorption spectrum depending on its valence state ( $\text{Fe}^{2+}$  and  $\text{Fe}^{3+}$ ) and site occupancy (octahedrally and tetrahedrally coordinated). Another drawback is that, in most cases, this approach requires LA-ICP-MS analysis, as Co usually cannot be detected by EDXRF.

The concept used by most gemmological laboratories is to rely mainly on the visible-range spectrum—which has to be dominated by cobalt absorption bands—in combination with the observed colour. This concept interprets the term *Co-spinel* as a gem varietal name (similar to corundum varieties such as sapphire, ruby or padparadscha), accepting a certain range of colour hues and saturations, as long as the above-mentioned criteria are met.

Our UV-Vis-NIR spectral analyses have clearly shown that this new Tanzanian source produces spinels gradually ranging from blue stones with an absorption spectrum dominated by Co (Figure 15: sample SPTan-1\_12) to greyish-greenish blue material with Fe absorption dominating over the Co bands (Figure 15: sample SPTan-1\_23; see also Chauviré *et al.* 2015). In this latter sample, the main absorption is greatest at 555 nm ( $^{\text{T}}\text{Fe}^{2+}$ ), with a distinct shoulder at about 670 nm ( $^{\text{M}}\text{Fe}^{2+} - ^{\text{M}}\text{Fe}^{3+}$  IVCT) and strong Fe peaks in the UV range ( $^{\text{T}}\text{Fe}^{2+}$  and  $\text{O}^{2-} - \text{Fe}^{2+}$  LMCT). In the other two spectra in Figure 15, Co-related bands predominate in the visible range. This is also evident from the trace-element data

(see Figure 18 and Table III), which reveal a distinctly lower concentration of Co but higher Fe in the greyish-greenish blue spinel sample. As such, in our opinion not all blue spinels from this new deposit should be called *Co-spinel*, although all of them contain traces of Co to some extent.

Interestingly, Co-bearing spinels from this new source, but also from other origins, contain similar traces of Ni, as both of these elements are geochemically related. Nickel, commonly also present as  $\text{Ni}^{2+}$ , is assumed to replace tetrahedrally coordinated  $\text{Mg}^{2+}$ . Such  $^{\text{T}}\text{Ni}^{2+}$  also results in a blue colour, but with a slightly more greenish hue (similar to ‘Swiss blue’ irradiated topaz) and lower saturation (Hanser 2013).

In a previous study on blue spinels, a Verneuil synthetic doped with Ni was investigated and compared to Co-spinel from Vietnam and also to synthetic Co-spinels (Hanser 2013). The spectrum of the Ni-doped sample showed two main absorption-band systems, the first in the UV centred at 377 nm, and the second a broad system centred at about 595 nm (Figure 20a). Interestingly, Co absorption is much stronger than Ni. This is evident in Figure 20b, which compares two Verneuil synthetic spinels, one doped with Ni (about 1100 ppm) and the other with Co (330 ppm). Consequently, we would not expect to see Ni-related absorption features in our natural spinel samples, even more so because Fe-related bands strongly overlap the positions of the Ni bands.

The geographic origin determination of spinel and, specifically, of Co-spinel, has become more important

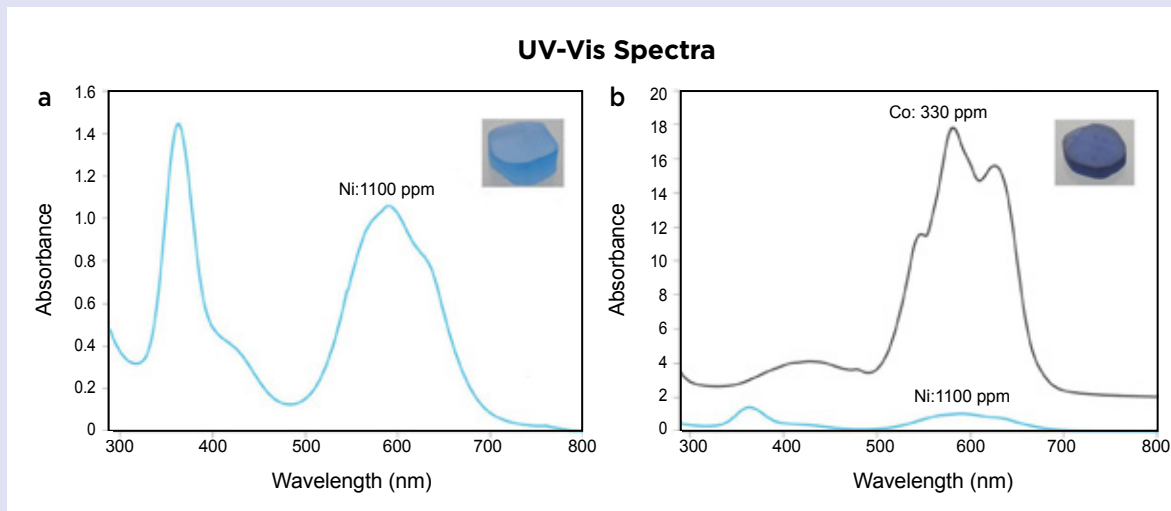


**Figure 20:** UV-Vis absorption spectra are shown for (a) a blue Ni-doped Verneuil synthetic spinel and (b) a blue Co-doped synthetic spinel. In the latter diagram, it is apparent that the absorbance of Co is much stronger than that of Ni, even though the Ni content is about 4× the concentration of Co in these samples. The spectrum from (a) has been added for comparison, and the two spectra have been offset vertically for clarity. Adapted from Hanser (2013).



for the trade in recent years. As mentioned above, our study has shown that Co-bearing spinel from Tanzania often shows characteristic inclusion features (högbomite lamellae), which could help gemmologists with origin determination.

In addition, trace elements are commonly used for the origin determination of coloured stones, including spinels. Figure 21 shows four different scatterplots (based on the data in Table III) comparing Ni, Mn, Fe and Ti with Co concentrations in Co-bearing spinels from Tanzania, Sri Lanka, Vietnam and Pakistan. Generally, Tanzanian type I spinels are quite uniform and can be separated from those of Pakistan by lower Co, Ni and Fe, as well as higher Mn. Tanzanian type I spinels can be further distinguished from those of Sri Lanka and Vietnam by different Ti contents. Sri Lankan samples seem to be very non-uniform. Plotting Co vs Ni (Figure 21a) reveals a general positive correlation for these elements ( $r = \text{approximately } 1$ ) in

slightly separate but overlapping fields for each locality, except for the Sri Lankan samples, which do not follow this general trend. By contrast, the Co vs Mn plot (Figure 21b) shows a slight negative correlation for these two transition elements. In a plot of Co vs Fe (Figure 21c), the Tanzanian type I spinel can be separated from a Pakistan origin by their lower Co and Fe contents. However, they show considerable overlap with Co and Fe for analysed samples from Vietnam and Sri Lanka.

Interestingly, the Tanzanian type I spinels in all four plots form a restricted and well-defined group. The scatterplots thus confirm that the analysed samples are chemically quite homogeneous, indeed much more so than gem-quality Co-bearing spinel from other origins, as seen also from the rather low standard-deviation values in Table III. In contrast to this, Tanzanian type II spinels plot in a much wider range, best fitting with Co-spinels from Pakistan.

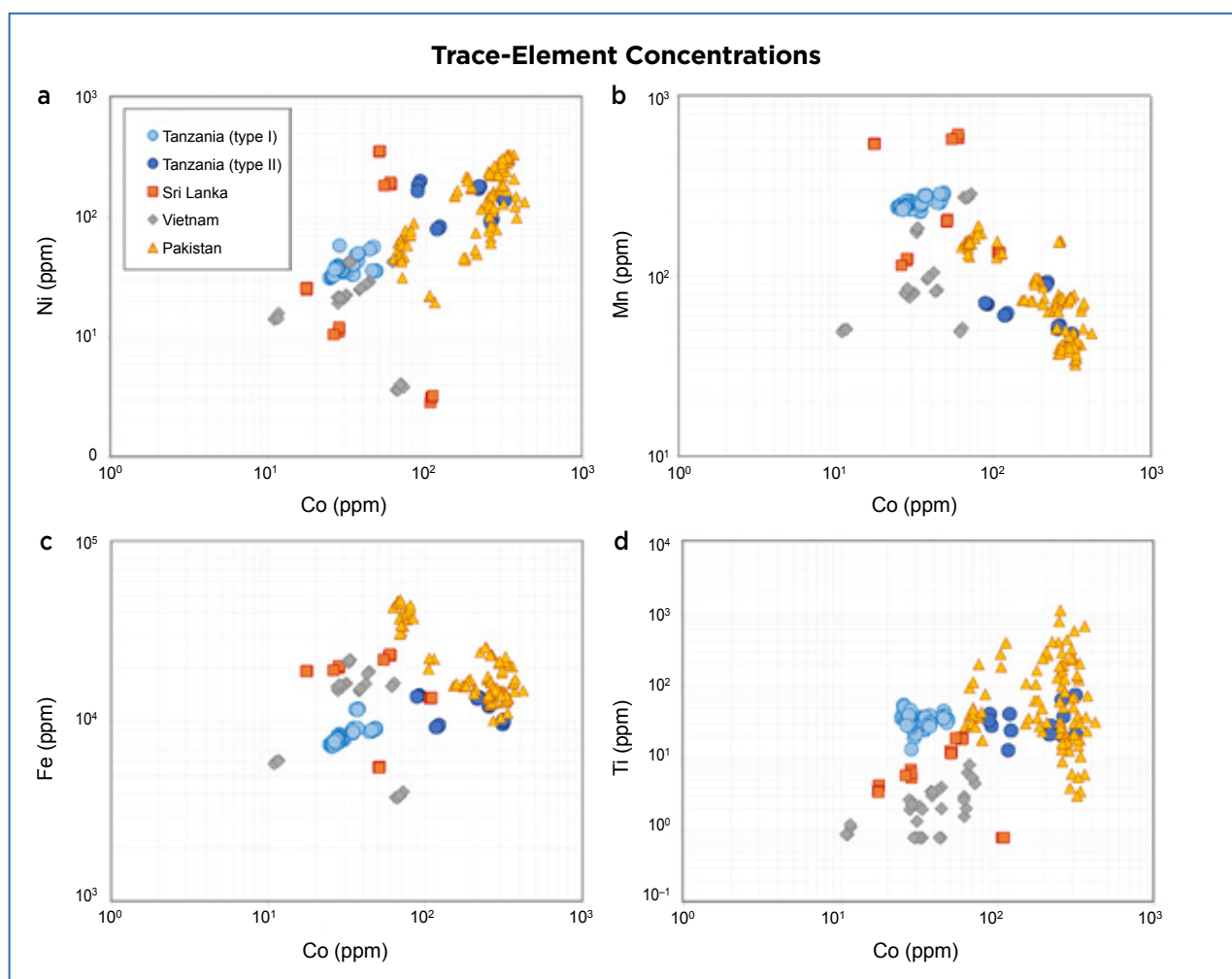


**Figure 21:** Trace-element plots are shown for Co-bearing spinel from Tanzania together with samples from Vietnam, Sri Lanka and Pakistan for: (a) Co vs Ni, (b) Co vs Mn, (c) Co vs Fe and (d) Co vs Ti. Error bars were calculated but found to be smaller than the data spots.

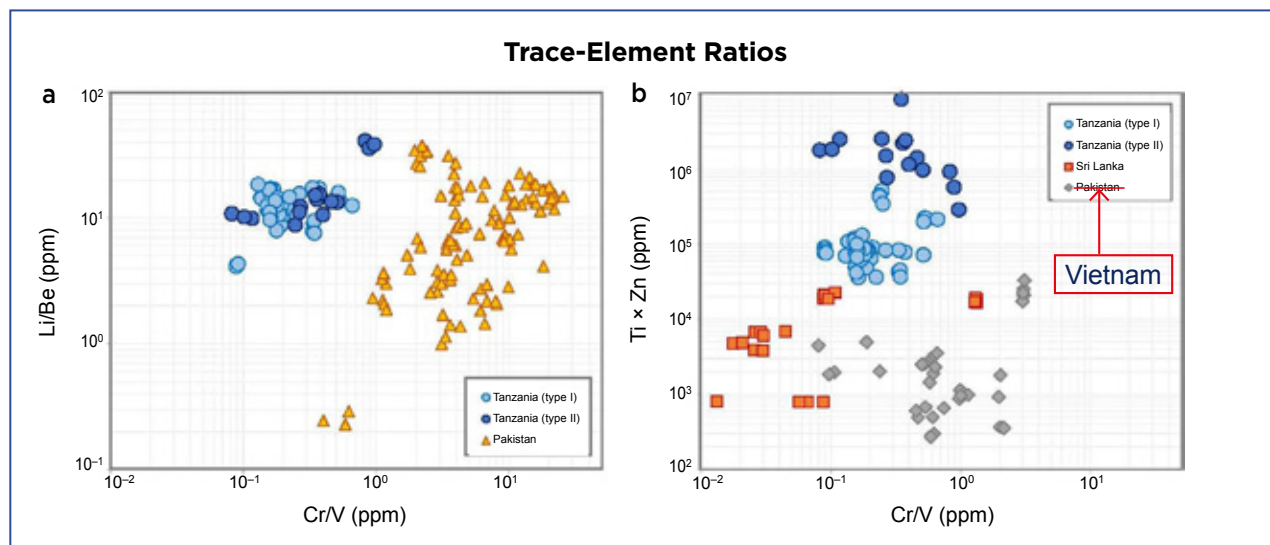


**Figure 22:** Plots of trace-element ratios are helpful for separating Tanzanian Co-bearing spinels from those of (a) Pakistan using Cr/V vs Li/Be, and (b) Vietnam and Sri Lanka using Cr/V vs Ti × Zn. Error bars were calculated but found to be smaller than the data spots.

Another approach to separating Co-bearing blue spinel from different origins is by using concentration-ratio plots (Figure 22). The analysed samples from Tanzania (types

I and II) can be well separated from Co-spinels from Pakistan by plotting Cr/V versus Li/Be (Figure 22a). Sri Lankan and Vietnamese samples overlap in this plot and therefore are not shown. However, by also using a plot of Cr/V versus Ti × Zn (Figure 22b), stones from Tanzania (types I and II) can be well separated from Vietnamese and Sri Lankan blue spinel.



**Figure 23:** This platinum ring features a 2.69 ct Tanzanian Co-bearing blue spinel that is set with smaller grey-to-blue spinels (2 ct total weight). Courtesy of Mary van der Aa Fine Jewels; stones faceted by Tucson Todd's Gems (Tucson, Arizona, USA).

## CONCLUSIONS

A new deposit of Co-bearing blue spinel is associated with weathered marble in the Lukande area about 15 km south-east of Mahenge in central Tanzania. The stones first reached the market in September 2021, and they vary from attractive blue Co-spinel to greyish blue material dominated by Fe-related absorption bands in the visible spectral range. Some stones attain relatively large sizes, weighing up to 10 + ct, making this deposit an important newcomer to the global gem trade. The beauty of these Co-bearing blue spinels from Tanzania is the driving force for their desirability in jewellery (e.g. Figure 23).

The geological context, combined with field observations and U-Pb dating, indicate the formation of the deposit near Lukande is linked to late-stage metamorphic events of the EAO. This is well in line with other marble-hosted gem deposits in central Tanzania (i.e. ruby and spinel deposits in the Uluguru and Mahenge mountains). These new Co-bearing blue spinels from Tanzania can be separated from Co-spinels from Vietnam, Sri Lanka and Pakistan based on their characteristic inclusion features and trace-element patterns.

## REFERENCES

- Abritta, T. & Blak, F.H. 1991. Luminescence study of  $\text{ZnGa}_2\text{O}_4$ :  $\text{Co}^{2+}$ . *Journal of Luminescence*, **48–49**(Part 2), 558–560, [https://doi.org/10.1016/0022-2313\(91\)90192-x](https://doi.org/10.1016/0022-2313(91)90192-x).
- Andreozzi, G.B., D'Ippolito, V., Skogby, H., Hålenius, U. & Bosi, F. 2018. Color mechanisms in spinel: A multi-analytical investigation of natural crystals with a wide range of coloration. *Physics and Chemistry of Minerals*, **46**(4), 343–360, <https://doi.org/10.1007/s00269-018-1007-5>.
- Balmer, W.A. 2011. *Petrology, geochemistry, and gemmological characterisation of marble-hosted ruby deposits of the Morogoro Region, Tanzania*. PhD thesis, Chulalongkorn University, Bangkok, Thailand, 185 pp.
- Balmer, W.A., Hauzenberger, C.A., Fritz, H. & Sutthirath, C. 2017. Marble-hosted ruby deposits of the Morogoro Region, Tanzania. *Journal of African Earth Sciences*, **134**, 626–643, <https://doi.org/10.1016/j.jafrearsci.2017.07.026>.
- Bank, H., Henn, U. & Petsch, E. 1989. Spinnelle aus dem Umba-Tal, Tanzania. *Gemmologie: Zeitschrift der Deutschen Gemmologischen Gesellschaft*, **38**, 166–168.
- Belley, P.M. & Groat, L.A. 2019. Metacarbonate-hosted spinel on Baffin Island, Nunavut, Canada: Insights into the origin of gem spinel and cobalt-blue spinel. *Canadian Mineralogist*, **57**(2), 147–200, <https://doi.org/10.3749/canmin.1800060>.
- Birch, R.L. & Stephenson, E.A. 1962. *Geological Map Series of Tanganyika, Quarter Degree Sheet 251*. Directorate of Overseas Surveys, London.
- Bosi, F., Hålenius, U., D'Ippolito, V. & Andreozzi, G.B. 2012. Blue spinel crystals in the  $\text{MgAl}_2\text{O}_4$ - $\text{CoAl}_2\text{O}_4$  series: Part II. Cation ordering over short-range and long-range scales. *American Mineralogist*, **97**(11–12), 1834–1840, <https://doi.org/10.2138/am.2012.4139>.
- Branstrator, B. 2022. A new source in Tanzania is producing cobalt-blue spinel. *National Jeweler*, <https://nationaljeweler.com/articles/10908-a-new-source-in-tanzania-is-producing-cobalt-blue-spinel>, 17 May, accessed 28 February 2023.
- Buathong, A. & Narudeesombat, N. 2020. Gem Notes: A rare bicoloured spinel. *Journal of Gemmology*, **37**(3), 250–252, <https://doi.org/10.15506/JoG.2020.37.3.250>.
- Chauviré, B., Rondeau, B., Fritsch, E., Ressigeac, P. & Devidal, J.-L. 2015. Blue spinel from the Luc Yen District of Vietnam. *Gems & Gemology*, **51**(1), 2–17, <https://doi.org/10.5741/gems.51.1.2>.
- Cornu, L., Gaudon, M., Ilin, E., Aymonier, C., Veber, P., Garcia, A., Kahn, M., Champouret, Y. *et al.* 2015. Luminescence of sensitive materials: Towards new optical sensing. *Oxide-based Materials and Devices VI*, San Francisco, California, USA, 7–12 February, <https://doi.org/10.1117/12.2076948>.
- D'Ippolito, V., Andreozzi, G.B., Hålenius, U., Skogby, H., Hametner, K. & Günther, D. 2015. Color mechanisms in spinel: Cobalt and iron interplay for the blue color. *Physics and Chemistry of Minerals*, **42**(6), 431–439, <https://doi.org/10.1007/s00269-015-0734-0>.
- DuToit, G. 2012. Lab Notes: Bicolored spinel. *Gems & Gemology*, **48**(4), 304.
- Elmaleh, E., Schmidt, S.T., Karampelas, S., Link, K., Kiefert, L., Sussenberger, A. & Paul, A. 2019. U-Pb ages of zircon inclusions in sapphires from Ratnapura and Balangoda (Sri Lanka) and implications for geographic origin. *Gems & Gemology*, **55**(1), 18–28, <https://doi.org/10.5741/gems.55.1.18>.
- Fregola, R.A., Skogby, H., Bosi, F., D'Ippolito, V., Andreozzi, G.B. & Hålenius, U. 2014. Optical absorption spectroscopy study of the causes for color variations in natural Fe-bearing gahnite: Insights from iron valency and site distribution data. *American Mineralogist*, **99**(11–12), 2187–2195, <https://doi.org/10.2138/am-2014-4962>.
- Fritz, H., Tenczer, V., Hauzenberger, C.A., Wallbrecher, E., Hoinkes, G., Muhongo, S. & Mogessie, A. 2005. Central Tanzanian tectonic map: A step forward to decipher Proterozoic structural events in the East African Orogen. *Tectonics*, **24**(6), article TC6013, <https://doi.org/10.1029/2005tc001796>.
- Fritz, H., Tenczer, V., Hauzenberger, C., Wallbrecher, E. & Muhongo, S. 2009. Hot granulite nappes – Tectonic styles and thermal evolution of the Proterozoic granulite belts in East Africa. *Tectonophysics*, **477**(3–4), 160–173, <https://doi.org/10.1016/j.tecto.2009.01.021>.
- Fritz, H., Abdelsalam, M., Ali, K.A., Bingen, B., Collins, A.S., Fowler, A.R., Ghebreab, W., Hauzenberger, C.A. *et al.* 2013. Orogen styles in the East African Orogen: A review of the Neoproterozoic to Cambrian tectonic evolution. *Journal of African Earth Sciences*, **86**, 65–106, <https://doi.org/10.1016/j.jafrearsci.2013.06.004>.
- Gaffney, E.S. 1973. Spectra of tetrahedral  $\text{Fe}^{2+}$  in  $\text{MgAl}_2\text{O}_4$ . *Physical Review B*, **8**(7), 3484–3486, <https://doi.org/10.1103/PhysRevB.8.3484>.
- Gaft, M., Reisfeld, R. & Panczer, G. 2015. *Modern Luminescence Spectroscopy of Minerals and Materials*. Springer-Verlag, Berlin, Germany, 356 pp., <https://doi.org/10.1007/978-3-319-24765-6>.
- Hålenius, U., Skogby, H. & Andreozzi, G.B. 2002. Influence of cation distribution on the optical absorption spectra of  $\text{Fe}^{3+}$ -bearing spinel s.s.-hercynite crystals: Evidence for electron transitions in  $^{\text{VI}}\text{Fe}^{2+}$ - $^{\text{VI}}\text{Fe}^{3+}$  clusters. *Physics and Chemistry of Minerals*, **29**(5), 319–330, <https://doi.org/10.1007/s00269-002-0240-z>.



- Hänni, H.A. & Schmetzer, K. 1991. New rubies from the Morogoro area, Tanzania. *Gems & Gemology*, **27**(3), 156–167, <https://doi.org/10.5741/gems.27.3.156>.
- Hanser, C.S. 2013. *Blue spinel from Luc Yen, Vietnam: A spectroscopic study*. Bachelor's thesis, University of Freiburg, Freiburg im Breisgau, Germany, 52 pp.
- Hauzenberger, C.A., Sommer, H., Fritz, H., Bauernhofer, A., Kröner, A., Hoinkes, G., Wallbrecher, E. & Thöni, M. 2007. SHRIMP U–Pb zircon and Sm–Nd garnet ages from the granulite-facies basement of SE Kenya: Evidence for Neoproterozoic polycyclic assembly of the Mozambique Belt. *Journal of the Geological Society*, **164**(1), 189–201, <https://doi.org/10.1144/0016-76492005-081>.
- Hendy, A., Krüger, A., Pfarr, K., De Witte, J., Kibweja, A., Mwingira, U., Dujardin, J.-C., Post, R. *et al.* 2018. The blackfly vectors and transmission of *Onchocerca volvulus* in Mahenge, south eastern Tanzania. *Acta Tropica*, **181**, 50–59, <https://doi.org/10.1016/j.actatropica.2018.01.009>.
- Henn, U. & Milisenda, C.C. 1997. Neue Edelsteinvorkommen in Tansania: die Region Tunduru-Songea. *Gemmologie: Zeitschrift der Deutschen Gemmologischen Gesellschaft*, **46**(1), 29–43.
- Khaidukov, N.M., Brekhovskikh, M.N., Kirikova, N.Y., Kondratyuk, V.A. & Makhov, V.N. 2020. Luminescence properties of spinels doped with manganese ions. *Russian Journal of Inorganic Chemistry*, **65**(8), 1135–1141, <https://doi.org/10.1134/s0036023620080069>.
- Koivula, J.I., Kammerling, R.C. & Fritsch, E. 1993. Gem News: Ruby mining near Mahenge, Tanzania. *Gems & Gemology*, **29**(2), 136.
- Krzemnicki, M.S. 2022. SSEF conducts analysis of cobalt-blue spinel from a newly reported source in Tanzania. Swiss Gemmological Institute SSEF, 2 pp., <https://tinyurl.com/2p92wxjp>, 16 May, accessed 28 February 2023.
- Krzemnicki, M.S., Wang, H.A.O. & Phyo, M.M. 2019. Age dating applied as a testing procedure to gemstones and biogenic gem materials. *36th International Gemmological Conference*, Nantes, France, 28–31 August, 48–50, <https://tinyurl.com/52x8xrdb>.
- Kukharuk, M. & Manna, C. 2019. The spinels of Mahenge, Tanzania. *InColor*, No. 43, 54–58, <http://www.incolormagazine.com/books/robz/#p=54>.
- Kuleshov, N.V., Mikhailov, V.P., Scherbitsky, V.G., Prokoshin, P.V. & Yumashev, K.V. 1993. Absorption and luminescence of tetrahedral  $\text{Co}^{2+}$  ion in  $\text{MgAl}_2\text{O}_4$ . *Journal of Luminescence*, **55**(5–6), 265–269, [https://doi.org/10.1016/0022-2313\(93\)90021-e](https://doi.org/10.1016/0022-2313(93)90021-e).
- Link, K. 2015. Age determination of zircon inclusions in faceted sapphires. *Journal of Gemmology*, **34**(8), 692–700, <https://doi.org/10.15506/JoG.2015.34.8.692>.
- Marfunin, A.S. 1979. *Physics of Minerals and Inorganic Materials*. Springer-Verlag, Berlin, Germany, xii + 342 pp.
- Meert, J.G. 2003. A synopsis of events related to the assembly of eastern Gondwana. *Tectonophysics*, **362**(1–4), 1–40, [https://doi.org/10.1016/s0040-1951\(02\)00629-7](https://doi.org/10.1016/s0040-1951(02)00629-7).
- Möller, A., Mezger, K. & Schenk, V. 2000. U–Pb dating of metamorphic minerals: Pan-African metamorphism and prolonged slow cooling of high pressure granulites in Tanzania, East Africa. *Precambrian Research*, **104**(3–4), 123–146, [https://doi.org/10.1016/s0301-9268\(00\)00086-3](https://doi.org/10.1016/s0301-9268(00)00086-3).
- Nasdala, L., Irmer, G. & Wolf, D. 1995. The degree of metamictization in zircon: A Raman spectroscopic study. *European Journal of Mineralogy*, **7**(3), 471–478, <https://doi.org/10.1127/ejm/7/3/0471>.
- Pardieu, V. & Hughes, R.W. 2008. Spinel: Resurrection of a classic. *InColor*, No. 8, 10–18, <http://www.incolormagazine.com/books/gibu/#p=10>.
- Peretti, A., Günther, D. & Haris, M.T.M. 2015. GRS Alert: New spinel treatment discovered involving heat and cobalt-diffusion. GRS Gemresearch Swisslab, 4 pp., <https://tinyurl.com/2kdau95s>, 22 May, accessed 28 February 2023.
- Phyo, M.M., Wang, H.A.O., Guillon, M., Berger, A., Franz, L., Balmer, W.A. & Krzemnicki, M.S. 2020. U–Pb dating of zircon and zirconolite inclusions in marble-hosted gem-quality ruby and spinel from Mogok, Myanmar. *Minerals*, **10**(2), article 195, <https://doi.org/10.3390/min10020195>.
- Quinn, E.P. & Laurs, B.M. 2004. Gem News: Pink to pink-orange spinel from Tanzania. *Gems & Gemology*, **40**(1), 71–72.
- Rossetti, F., Cozzupoli, D. & Phillips, D. 2008. Compressional reworking of the East African Orogen in the Uluguru Mountains of eastern Tanzania at c. 550 Ma: Implications for the final assembly of Gondwana. *Terra Nova*, **20**(1), 59–67, <https://doi.org/10.1111/j.1365-3121.2007.00787.x>.
- Saeseaw, S., Wang, W., Scarratt, K., Emmett, J.L. & Douthit, T.R. 2009. Distinguishing heated spinels from unheated natural spinels and from synthetic spinels: A short review of on-going research. Gemological Institute of America, 13 pp., <https://www.gia.edu/doc/Heated-spinel-Identification-at-April-02-2009.pdf>, 2 April, accessed 28 February 2023.
- Sampson, D.N. & Wright, A.E. 1964. *The Geology of the Uluguru Mountains*. Government Printer, Dar es Salaam, Tanzania, 69 pp.
- Schaub, P. 2004. *Spektrometrische Untersuchungen an Al-Spinellen*. Master's thesis, University of Basel, Switzerland, 275 pp.

- Schlüter, T. 1997. *Geology of East Africa*. Gebrüder Borntraeger, Berlin, Germany, xii + 484 pp.
- Schmetzer, K. & Berger, A. 1992. Lamellar inclusions in spinels from Morogoro area, Tanzania. *Journal of Gemmology*, **23**(2), 93–94, <https://doi.org/10.15506/JoG.1992.23.2.93>.
- Schmetzer, K., Haxel, C. & Amthauer, G. 1989. Colour of natural spinels, gahnospinel and gahnites. *Neues Jahrbuch für Mineralogie, Abhandlungen*, **160**(2), 159–180.
- Schollenbruch, K., Malsy, A.-K., Bosshard, V. & Blauwet, D. 2021. Cobalt-blue spinel from northern Pakistan. *Journal of Gemmology*, **37**(7), 726–737, <https://doi.org/10.15506/JoG.2021.37.7.726>.
- Schwarz, D., Liu, Y., Zhou, Z., Lomthong, P. & Rozet, T. 2022. Spinel from the Pamir Mountains in Tajikistan. *Journal of Gemmology*, **38**(2), 138–154, <https://doi.org/10.15506/JoG.2022.38.2.138>.
- Shigley, J.E. & Stockton, C.M. 1984. ‘Cobalt-blue’ gem spinels. *Gems & Gemology*, **20**(1), 34–41, <https://doi.org/10.5741/gems.20.1.34>.
- Smith, C.P., Beesley, C.R., Quinn Darenius, E., Mayerson, W.M. 2008. A closer look at Vietnamese spinel. *InColor*, No. 43, 31–34, <http://www.incolormagazine.com/books/kvfr/#p=10>.
- Smith, C.P. 2012. Spinel and its treatments: A current status report. *InColor*, No. 19, 50–54, <http://www.incolormagazine.com/books/pcpz/#p=50>.
- Sokolov, P., Kuksa, K., Marakhovskaya, O. & Gussiås, G.A. 2019. In search of cobalt blue spinel in Vietnam. *InColor*, No. 43, 60–65, <http://www.incolormagazine.com/books/robz/#p=60>.
- Stephan, T., Henn, U. & Muller, S. 2022. Neue Funde von kobalthaltigem Spinell bei Mahenge, Tansania. *Gemmologie: Zeitschrift der Deutschen Gemmologischen Gesellschaft*, **71**(3/4), 57–64.
- Stern, R.J. 1994. Arc assembly and continental collision in the Neoproterozoic East African Orogen: Implications for the consolidation of Gondwanaland. *Annual Review of Earth and Planetary Sciences*, **22**(1), 319–351, <https://doi.org/10.1146/annurev.ea.22.050194.001535>.
- Taran, M.N., Koch-Müller, M. & Langer, K. 2005. Electronic absorption spectroscopy of natural ( $\text{Fe}^{2+}$ ,  $\text{Fe}^{3+}$ )-bearing spinels of spinel s.s.-hercynite and gahnite-hercynite solid solutions at different temperatures and high-pressures. *Physics and Chemistry of Minerals*, **32**(3), 175–188, <https://doi.org/10.1007/s00269-005-0461-z>.
- Taran, M.N., Koch-Müller, M. & Feenstra, A. 2009. Optical spectroscopic study of tetrahedrally coordinated  $\text{Co}^{2+}$  in natural spinel and staurolite at different temperatures and pressures. *American Mineralogist*, **94**(11–12), 1647–1652, <https://doi.org/10.2138/am.2009.3247>.
- Wang, H.A.O. & Krzemnicki, M.S. 2021. Multi-element analysis of minerals using laser ablation inductively coupled plasma time of flight mass spectrometry and geochemical data visualization using t-distributed stochastic neighbor embedding: Case study on emeralds. *Journal of Analytical Atomic Spectrometry*, **36**(3), 518–527, <https://doi.org/10.1039/d0ja00484g>.
- Wang, H.A.O., Krzemnicki, M.S., Chalain, J.-P., Lefèvre, P., Zhou, W. & Cartier, L. 2016. Simultaneous high sensitivity trace-element and isotopic analysis of gemstones using laser ablation inductively coupled plasma time-of-flight mass spectrometry. *Journal of Gemmology*, **35**(3), 212–223, <https://doi.org/10.15506/JoG.2016.35.3.212>.
- Weinberg, D. 2007. Giant red spinel crystal discovered in East Africa. Multicolour Gems Ltd, <https://www.multicolour.com/spinel/giant-red-spinel-crystal-discovered-in-east-africa.html>, 5 October, accessed 28 February 2023.
- Widmer, R., Malsy, A.-K. & Armbruster, T. 2014. Effects of heat treatment on red gemstone spinel: Single-crystal X-ray, Raman, and photoluminescence study. *Physics and Chemistry of Minerals*, **42**(4), 251–260, <https://doi.org/10.1007/s00269-014-0716-7>.
- Yu, C.F. & Lin, P. 1996. Manganese-activated luminescence in  $\text{ZnGa}_2\text{O}_4$ . *Journal of Applied Physics*, **79**(9), 7191–7197, <https://doi.org/10.1063/1.361435>.

### The Authors

**Dr Michael S. Krzemnicki**<sup>FGA1,2,\*</sup>,  
**Alex Leuenberger**<sup>3</sup> and **Dr Walter A. Balmer**<sup>1</sup>

<sup>1</sup> Swiss Gemmological Institute SSEF,  
Aeschengraben 26, 4051 Basel, Switzerland

<sup>2</sup> Department of Environmental Sciences,  
Mineralogy and Petrology, University of Basel,  
Bernoullistrasse 32, 4056 Basel, Switzerland

<sup>3</sup> ALine GmbH, Bernstrasse 264,  
3627 Heimberg, Switzerland

\* Email: michael.krzemnicki@ssef.ch

### Acknowledgements

The authors thank the following gem traders for information and samples: Salim Almas (Arusha, Tanzania), Mark Saul (Swala Gem Traders Ltd, Arusha), Steve Jaquith (G.E.O. International Co. Ltd, Bangkok) and Wez Barber (Mahenge Gems Pte. Ltd, Singapore). Furthermore, we thank Dr Klaus Schollenbruch (Gübelin Gem Lab, Lucerne, Switzerland) for kindly providing LA-ICP-MS data of Co-bearing spinel from Pakistan. And finally, we thank the following people for data acquisition and processing at the Swiss Gemmological Institute SSEF: Dr H. A. O. Wang, Dr Markus Wälle, Judith Braun, Susanne Büche, Hannah Amsler and all other colleagues at SSEF for fruitful discussions.

# Nephrite Jade from Washington State, USA, Including a New Variety Showing Optical Phenomena

Jean-Pierre Jutras, Cara Williams, Bear Williams and George R. Rossman

**ABSTRACT:** In 2018, a new type of nephrite jade was recognised from the DJ project in Washington State (USA) that exhibits subtle-to-strong directional colour variations when viewed at different orientations. Its colouration ranges from green to blue in light-to-dark tones, and its mineralogical and gemmological properties are consistent with nephrite jade from other localities. The optical phenomenon is related to pleochroism resulting from the internal structure of the tremolite fibres constituting the nephrite. These fibres show high-angle to orthogonal cross-felting, often with variations in chemical composition, and appear to result from more than one generation of formation. The presence of sheen (caused by the scattering of light from fibrous tremolite domains) is sometimes seen in addition to the pleochroic optical effect. This phenomenal material has the toughness required to be cut into cabochons or carved without any stabilising treatment, thus possessing workability that qualifies it as a new and unique variety of nephrite jade. Three other nephrite types—classified here as Ornamental, Carving and Gem—additionally occur at the DJ project, and are also described in this article.

*The Journal of Gemmology*, 38(5), 2023, pp. 494–511, <https://doi.org/10.15506/JoG.2023.38.5.494>

© 2023 Gem-A (The Gemmological Association of Great Britain)

Nephrite jade is prized for its attractive appearance as well as its toughness, both of which contribute to its desirability in jewellery and *objets d'art*. A new type of nephrite jade with a unique optical phenomenon was recently identified from Jade Leader Corp.'s DJ project, located in Washington State, USA. Unlike most nephrite jades, which typically show fine-grained texture and a fairly even colouration, this new material has coarser texture and exhibits subtle-to-strong directional colour variations when properly cut or carved (Figure 1).

Although several nephrite varieties have been defined from the DJ occurrence, only one type exhibits the optical phenomenon. The unusual appearance of this nephrite was first noticed in 2018 by author J-PJ, but it took him until mid-2022 to develop the proper cutting protocols to best reveal the phenomenon. The range of colour and translucency shown by the material was initially explored in an early test suite comprising 10 stones totalling nearly

400 carats (2.7–164.95 ct each) that were cut by author J-PJ. Since then, this nephrite has been cut into a wide variety of cabochons and carvings.

Regarding the two internationally recognised jade varieties—*nephrite* (amphibole-dominant) and *jadeite* (pyroxene-dominant)—all the materials described in this article are nephrite, consistent with most previous analyses of jade materials from Washington (e.g. Ream 2022). The new phenomenal nephrite is distinct from the 'cat's-eye jade' or 'chatoyant jade' that was recently documented from Washington (Hogarth 2019, 2022). For such chatoyancy to be displayed, the tremolite or actinolite fibres must have optically continuous areas of parallel alignment, which means the material lacks the interlocking or felted texture that is necessary for the material to properly be called *nephrite jade* (LMHC 2011; Barnes 2022). Therefore, Hogarth (2022) indicated that GIA's laboratory would refer to the chatoyant material mentioned above as 'cat's-eye actinolite' (or, 'cat's-eye





**Figure 1:** Four views are shown of a marquis-shape nephrite cabochon (17.1 × 7.4 mm) during a 90° counterclockwise rotation under a fixed light source. It exhibits multiple domains showing strong colour variations depending on the viewing angle. Composite image taken from a video by J.-P. Jutras.

tremolite', depending on the dominant mineral composition), rather than 'cat's-eye nephrite'.

This article examines the four different types of nephrite jade from the DJ occurrence and focuses on the phenomenal type in particular. The history, geology and exploration of the jade deposit are described, and samples of each nephrite type are characterised mineralogically and gemmologically. Finally, the cause of the optical effect in the phenomenal nephrite is explained.

## LOCATION AND ACCESS

The DJ project consists of a group of contiguous lode-mining claims covering roughly 350 acres of land with multiple nephrite showings in north-western Washington State, USA (Figure 2). Specific information on the location of the deposit is not provided here to prevent unauthorised visitation and collection of material from the claims.

The project is readily accessible by paved and gravel (U.S. Forest Service) roads, within 20–30 minutes from the nearest community with services such as food, fuel and field supplies. Access to the property to conduct exploration and extraction activities is typically possible from April to November, with slight annual variations depending on winter snow loads. The project is located on public lands, and regulated activities are administered jointly by the Bureau of Land Management and the U.S. Forest Service.

## HISTORY AND NEPHRITE VARIETIES

Nephrite was used prehistorically in Washington State, with one of the earliest mentions of such artefacts made around 1900 by archaeologist Harlan Smith of the American Museum of Natural History (Leaming & Hudson 2005). In modern times, hobbyists have collected jade and other ornamental stones over the past several decades

from various localities in the USA's Pacific Northwest (Ream 1974, 2022), but only limited organised mining has taken place. Commercial nephrite production in Washington has historically lagged behind that of neighbouring British Columbia, Canada, where annual jade production has sometimes exceeded 500 tons (Ward 2015). By comparison, the Washington Gem Jade and Mining Company, which was one of the larger operations for lapidary materials in the 1970s (Ream 1974), had a total production estimated at some 50 tons (Leaming 1995). Recently, a small group has been marketing cat's-eye actinolite from Washington (Hogarth 2019, 2022).

The initial discovery of the nephrite deposit that is the subject of the present article was reportedly made by Lucky Case and Fred Krapsicher in the early 1970s (L. Ream, pers. comm. 2018). They noted a pod of nephrite of unreported quality hosted by heavily serpentinised ultramafic rocks that was exposed in a road cut, which

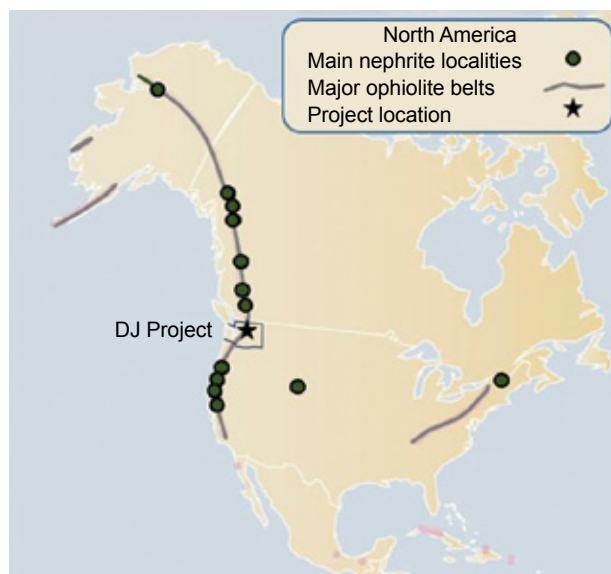


**Figure 2:** The general location of the DJ project in Washington State is shown in the context of other North American nephrite jade localities. Modified from an illustration by G. Harlow in Hughes (2022).



**Figure 3:** The first jade pendant (7.5 cm long) cut and polished by author J-PJ from the DJ project shows the good quality and high lustre of some of the nephrite from this deposit. Photo by J.-P. Jutras (the lower image is a reflection).

led them to stake mineral claims. These claims were repeatedly sold, expired and re-staked with little formal exploration or development work until some new owners re-staked the showing and, starting in 2014, began more systematic prospecting in the area.

Author J-PJ first visited the deposit in July 2015, with the consent of the then-owner of the claims, as part of a general nephrite research project. Samples collected at one of the main outcrops were cut to reveal a fine-grained, highly translucent bluish green nephrite. It showed an unusually high polish lustre (e.g. Figure 3) for North American nephrite

jade other than the material from Wyoming, USA.

In 2017, author J-PJ co-founded Jade Leader Corp., a Canadian-listed public company with a mandate to explore for and develop nephrite occurrences in the continental USA. Jade Leader first optioned and then purchased the above-mentioned Washington claims, now referred to as the DJ project, in 2018. The company then began exploration work to better define the various nephrite types present, determine the appropriate cutting protocols and evaluate the commercial potential of the jade occurrences. The previous property owners estimated that roughly 2 tonnes of various types of nephrite were mined from 2014 to 2018, with the largest single block weighing approximately 550 kg (D. Smith, pers. comm. 2022). This material was largely collected for the previous owner's lapidary hobby use and did not enter the market in any significant commercial sense. Exploration work since 2018 has included mapping, trenching, core drilling, geophysical surveys and nephrite characterisation studies done in-house by Jade Leader and also in conjunction with the University of Arizona (Tucson, Arizona, USA).

DJ project nephrite has been classified by author J-PJ into four major types according to its visual characteristics and likely potential uses: (1) *Ornamental*, (2) *Carving*, (3) *Gem* and (4) *Phenomenal* (see Figures 4 and 5). These categories are further described below in the Results and Discussion section.

Unusual botryoidal nephrite material has also been found at a few of the DJ project's jade occurrences, but it is not listed here as a specific category due to its rarity. Long-fibre tremolite, likely capable of exhibiting chatoyancy if cut *en cabochon*, has also been noted in some areas.

The new Phenomenal-type nephrite (Figures 1 and 4d) that is the main subject of this article was first presented publicly at the Canadian Gemmological Association conference in October 2022.

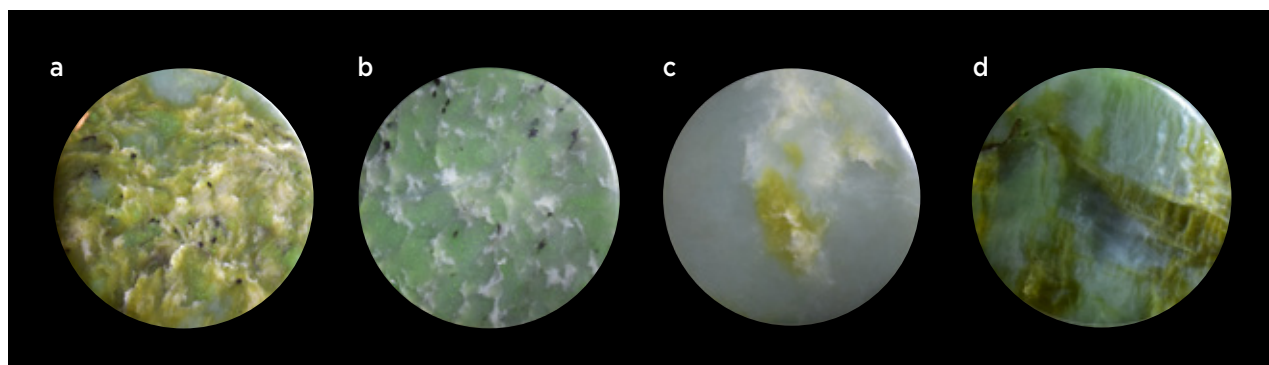


**Figure 4:** The four types of nephrite jade from the DJ project are represented by these cut and polished reference discs: (a) Ornamental (50 mm in diameter), (b) Carving (55.7 mm in diameter), (c) Gem (50 mm in diameter) and (d) Phenomenal (36.6 × 36.1 mm). Composite photo by J.-P. Jutras.

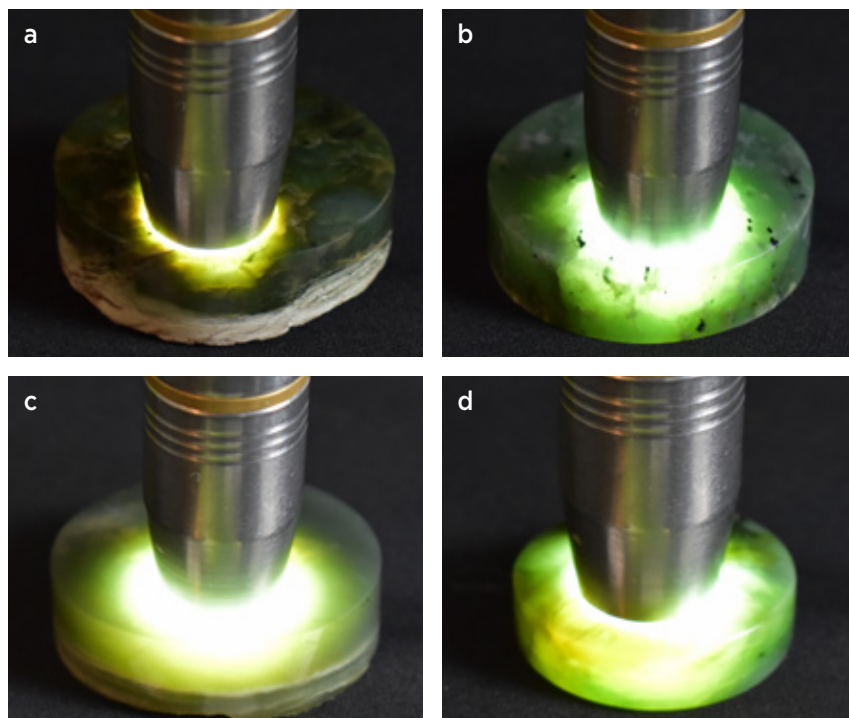


**Figure 5:** The same set of reference discs as in Figure 4 show variations in translucency and light transmission depending on the composition and texture of the nephrite. Sometimes referred to as the ‘jade carver’s torch test’, the stone is illuminated by placing it in contact with a high-intensity torch to evaluate its texture and translucency, as well as the presence of fractures. Photos by J.-P. Jutras.

## GEOLOGY

The DJ project is situated within a subduction zone-parallel coastal belt of thrust and accreted ophiolitic rocks containing varying amounts of mafic/ultramafic units and associated serpentinites. These belts are known to host nephrite jade intermittently from Alaska to California (again, see Figure 2), and are well documented on the Canadian side of the border (Leaming 1978) and in California (Blankenship 2022).

The nephrite occurrence discussed here lies along the Devil’s Mountain Fault where it cuts the Helena-Haystack melange (Tabor *et al.* 2002). Specific lithological units in this area include schistose metavolcanic rocks, phyllite, amphibolite and biotite-hornblende tonalite embedded in a serpentinite matrix. The nephrite is spatially related to serpentinite, similar in many respects to the Canadian counterparts described by Leaming (1978).

Tabor *et al.* (2002) reported formation ages of 141–150 million years for amphibolite units near the project site, and interpreted the Helena-Haystack melange as a thrust unit that was emplaced between 90 and 40 million years ago. No work has yet been performed to specifically define the age of nephrite genesis or the specific event related to its formation.

To date, three separate *in-situ* nephrite occurrences or ‘lodes’ have been recognised on the surface at the DJ project, all associated with a poorly exposed serpentinite unit. The nephrite forms veins, pods and elongated lenses

extending over tens of metres at the sheared boundaries between more resistive units (e.g. rodingite, a metasomatic calc-silicate rock) and ductile serpentinite (Figure 6). The continuity between the individual discrete nephrite occurrences cannot yet be ascertained due to lack of exposure in the forested areas between the lodes.

The Phenomenal-type nephrite has been recognised within surface outcrops over some 40 m of strike length and was intercepted in core drilling at depths up to 30 m. This nephrite type is therefore present throughout the larger nephrite-bearing system and is not simply a localised anomaly. The largest block containing this type of nephrite recovered during test sampling weighed 37.4 kg and measured 47 × 34 × 19 cm.

## EXPLORATION AND MINING

Since 2018, exploration sampling (including core drilling; Figure 7) and limited jade production has been conducted for material characterisation and test-marketing purposes. As the nephrite system crops out locally, extraction to date has been accomplished with the use of tools such as diamond saws, jackhammers and wedges (e.g. Figure 8). There is a very high contrast in competency between the variably fractured or foliated host rocks (rodingite and serpentinite; Ream 2022), which are relatively structurally weak, and the massive nephrite. This simplifies extraction and sorting of the target nephrite materials. A short video of an October 2022 pilot-scale nephrite extraction programme at the





**Figure 6:** The mode of occurrence of nephrite at the DJ project is exemplified by this tabular, steeply dipping vein that occurs at a sheared contact between serpentinite and rodingite. The vein varies from 0.6 to 1 m thick at the surface (see the hammer for scale). The same nephrite vein was intersected by drill core 30 m down-dip below the surface of the trench, where it had expanded to 5.2 m wide. Photo by J.-P. Jutras.

DJ project can be viewed at <https://www.youtube.com/watch?v=uI9V032p6Jo>, and some of the resulting rough and polished production is visible at [www.jadeleader.shop](http://www.jadeleader.shop). In the future, extraction could involve typical quarrying techniques with mechanised equipment.

Most nephrite blocks have an alteration rind that must be sliced away to assess their quality and type. However, no other crushing or sorting equipment requiring a significant surface disturbance is necessary, nor is the use of water or the creation of tailings piles.

## MATERIALS AND METHODS

An initial study of nephrite materials from the DJ project was conducted in conjunction with the University of Arizona in 2018 with the objective of confirming the mineralogical composition and textures, in order for the samples to be properly classified as nephrite jade.

Specimens representing all four nephrite types were selected by author J-PJ and sent to Quality Thin Sections (also in Tucson), and seven of the resulting polished thin sections were supplied to Drs Hexiong Yang and Robert T. Downs at the University of Arizona for both microscopic characterisation (including mineral-phase identification) and chemical analyses. The latter were performed using a Cameca SX-100 electron probe micro-analyser (EPMA) in wavelength-dispersive mode with an accelerating voltage of 15 kV, a beam current of 20 nA and a beam diameter of < 1 µm. A total of 74 points were analysed of the main amphibole constituent of the thin sections, as well as 35 points for accessory mineral phases. Backscattered electron (BSE) images were obtained (using the same instrument) of some of the areas analysed.

More recently, in 2021–2022, several nephrite samples from the DJ project underwent gemmological characterisation, inclusion identification with Raman analysis, visible-near infrared (Vis-NIR) spectroscopy and chemical analysis by energy-dispersive X-ray fluorescence (EDXRF) spectroscopy. Gemmological properties were obtained at Stone Group Labs by authors BW and CW on six samples (3.58–87.90 ct; Figure 9), which consisted of two partially polished rough pieces and four



**Figure 7:** A small, hydraulic, track-mounted core-drilling rig was used in November 2018 to test the continuity and variation at depth of the nephrite bodies at the DJ project. Photo by J.-P. Jutras.

cabochons representative of the two potentially most commercially important nephrite types (Phenomenal and Gem). RIs were measured on a standard gemmological refractometer and SG values were determined hydrostatically. The samples were observed with a Chelsea Colour Filter, and also under standard long- and short-wave UV lamps. A gemmological microscope was used to examine the nephrite texture. In addition, author J-PJ examined polished samples of the Gem-type nephrite with a polariscope to confirm that it acts as a polycrystalline (aggregate) material.

Raman spectroscopy was performed at the California Institute of Technology (Pasadena, California, USA) by author GRR to identify inclusions commonly present in the Carving-type nephrite, as well as to analyse the main amphibole phase of the jade. The analyses were done on two discs that were cut from a single nephrite slab (Figure 10), using a Renishaw inVia system operating with a 514 nm laser and a 50× objective lens with about 1.5 mW power on the samples. Typically 3–10 spectra were averaged from each analysis point to improve the signal-to-noise ratio. Mineral identification was accomplished by comparison to reference spectra in the RRUFF database (<https://rruff.info>).

Vis-NIR spectroscopy was also performed by author GRR on a polished slice of nephrite (1.53 mm thick) cut from one of the discs mentioned above, using a custom-built microscope spectrometer for the 380–1000 nm range that employs a silicon photodiode array detector, and a Thermo-Nicolet iS50 Fourier-transform infrared (FTIR) spectrometer for the 1000–2500 nm range equipped with an InGaAs detector and a silica beam splitter.

The bulk chemical compositions of the nephrite and its host rocks were investigated using portable EDXRF analysis by Dr Shane Ebert (Prince George, British Columbia, Canada). The samples consisted of four slabs representing the different nephrite types, and two host-rock slabs of rodingite and serpen-



**Figure 8:** A portable diamond saw is used to extract masses of nephrite, shown here during initial sampling in October 2017. Photo by J.-P. Jutras.

tinite. An enclosed workstation housed an Olympus Innov-X Delta-series unit equipped with an X-ray tube (operated at 40 kV and 4 W) and an Rh anode excitation source. Samples were analysed using the factory-set ‘mining plus’ analysis mode utilising two beams, each with a run time of 30 s. This configuration allows measurement of Mg, Al, Si, K, Ca, Fe, Cr and several additional trace elements. The sample window was 9 mm wide, which is the minimum area that can be sampled during analysis (therefore, sample heterogeneity may influence the results in some cases). Precision and accuracy for each analytical session were monitored with a factory calibration disc, reference standards and an SiO<sub>2</sub> blank, and through multiple duplicate analyses. EDXRF analysis was also performed on the disc of Phenomenal-type nephrite supplied to Stone Group Labs using an Amptek X123-SDD spectrometer.



**Figure 9:** A suite of polished rough and cut nephrite from the DJ project was used for gemmological characterisation. It includes both Gem-type nephrite (a polished block weighing 15.5 g and a 19.5 × 14 mm oval cabochon) and Phenomenal-type material (a disc measuring 36.5 × 35.5 mm, a polished rough piece weighing 5.8 g, a 17.1 × 7.4 mm marquise-shape cabochon and a 23.5 × 7.8 mm pear-shape cabochon). Photo by J.-P. Jutras.



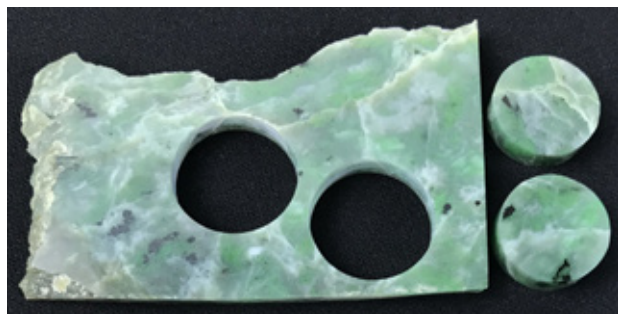


**Figure 10:** Two discs (each 19.3 mm in diameter) were cut and polished for inclusion studies from an 8 × 5 cm slab of Carving-type nephrite. Photo by J.-P. Jutras.

## RESULTS AND DISCUSSION

Table I provides representative EPMA analyses of minerals in the four types of DJ project nephrite. Figures 11–14 show images of each of the nephrite types, including photos of selected polished samples, thin-section photomicrographs and BSE images. The mineral species labelled in the BSE images include a main Fe-poor tremolite phase, a more Fe-rich tremolite phase, and the accessory minerals diopside and chlorite.

### Mineral Composition and Texture

Tremolite formed the main mineral constituent of all four nephrite types. Some of the tremolite in the Phenomenal type was more Fe-rich. Diopside, chlorite and chromite were identified as accessory minerals in the Ornamental- and Carving-type nephrites. Minor barite and Fe-Cu oxides were also noted in the Ornamental type. In addition, the Carving-type samples contained a Ca-Si-Cr-bearing phase that could not be identified by EPMA analysis.

The EPMA data showed that the main (Fe-poor) tremolite phase had an average composition of  $\text{Ca}_{1.96}\text{Na}_{0.01}\text{K}_{0.01}(\text{Mg}_{4.51}\text{Fe}^{2+}_{0.44}\text{Al}_{0.03}\text{Mn}_{0.01})\text{Si}_8\text{O}_{22}(\text{OH})_2$ , whereas the more Fe-rich tremolite phase in the Phenomenal-type nephrite showed an average composition of  $(\text{Ca}_{1.99}\text{K}_{0.01})_{2.00}(\text{Mg}_{4.08}\text{Fe}_{0.82}\text{Mn}_{0.05})_{4.95}\text{Si}_{8.02}\text{O}_{22}(\text{OH})_2$ . Some of the latter analyses verged into the actinolite field, as per the International Mineralogical Association's 1997 definition of actinolite and as outlined in Hawthorne *et al.* (2012).

The Ornamental-type nephrite (Figure 11) generally tends to be coarser grained and has a darker, more yellowish green appearance than the other categories.

**Table I:** Representative EPMA analyses of various minerals in nephrite from the DJ project.\*

Mineral	Tremolite (Fe-poor)				Tremolite (Fe-rich)	Diopside		Chlorite	
Nephrite type	Orn	Carving	Gem	Phen	Phen	Carving		Orn	Carving
Sample, point	DJ-O, 35/1	DJ-GJ, 72/1	DJ-G, 108/1	DJ-C, 21/1	DJ-C, 18/1	DJ-GJ, 77/1	DJ-GJ, 69/1	DJ-O, 40/1	DJ-GJ, 68/1
Figure/label	11d/MTr	12d/MTr	13d/MTr	14d/MTr	14d/FeTr	12d/Dio	12d/Dio	11d/Chl	12d/Chl
Oxide (wt.%)									
SiO <sub>2</sub>	57.49	58.25	58.65	58.61	57.22	54.91	54.17	31.89	37.00
TiO <sub>2</sub>	nd	0.01	nd	nd	nd	nd	0.01	nd	nd
Al <sub>2</sub> O <sub>3</sub>	0.42	0.24	0.06	0.18	0.07	1.15	0.74	15.26	12.26
Cr <sub>2</sub> O <sub>3</sub>	0.06	0.05	nd	0.03	0.01	0.07	0.01	1.12	1.11
FeO	4.95	3.26	3.32	4.04	7.23	2.51	4.13	9.86	5.83
MnO	0.08	0.04	0.16	0.10	0.43	0.08	0.31	0.05	0.03
MgO	21.57	22.20	22.47	21.80	19.54	16.36	15.33	26.74	30.06
CaO	12.90	13.38	13.23	13.15	13.12	24.88	25.14	0.17	1.23
Na <sub>2</sub> O	0.04	0.08	0.05	0.07	0.04	0.65	0.30	nd	nd
K <sub>2</sub> O	0.02	0.09	0.07	0.05	0.05	nd	nd	nd	0.02
Total	97.53	97.59	98.02	98.02	97.70	100.61	100.16	85.09	87.53

\*Data from Yang & Downs (2018). Abbreviations: nd = not detected, Orn = Ornamental and Phen = Phenomenal.



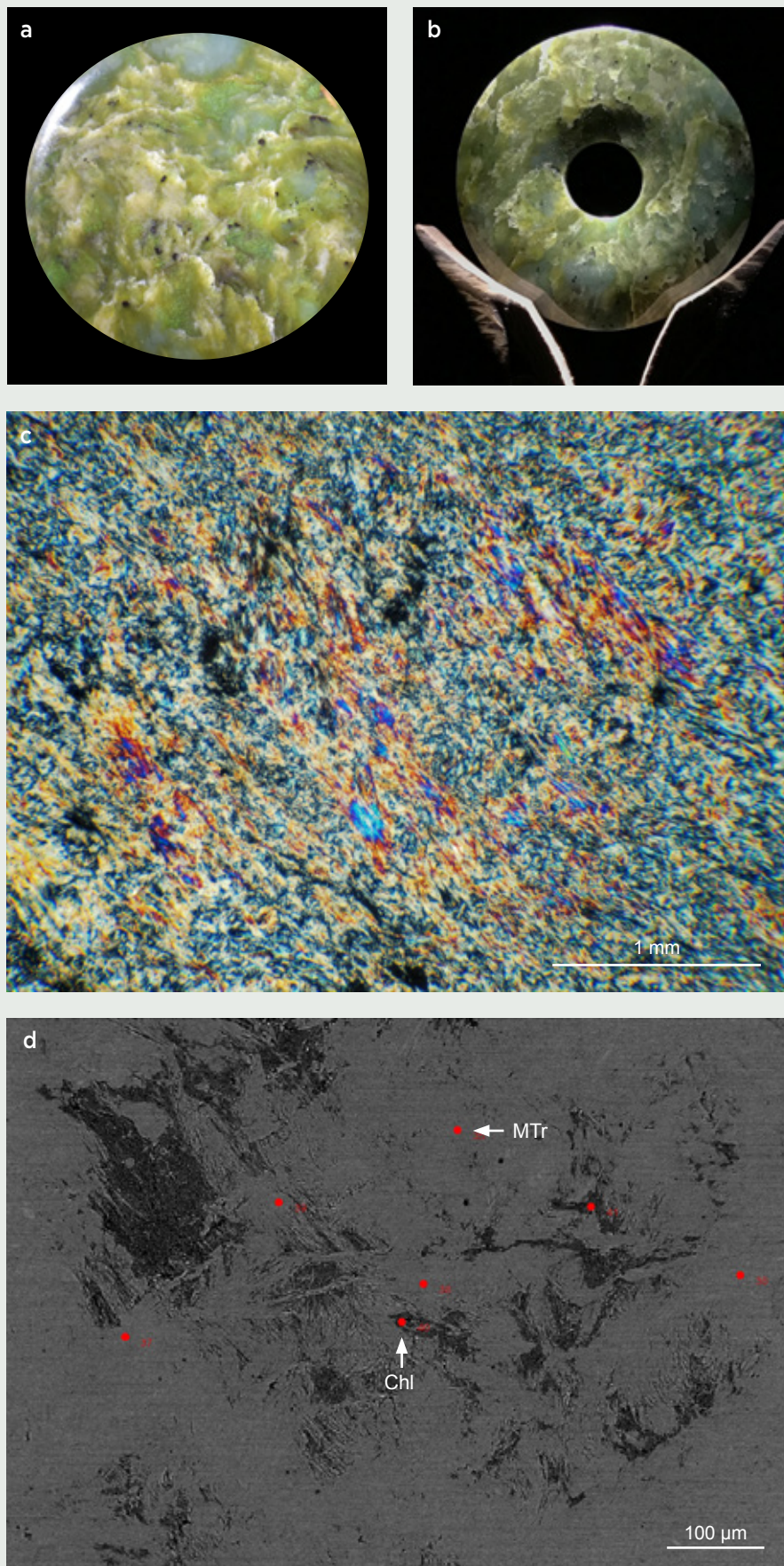


**Figure 11:** Ornamental-type nephrite is illustrated here by **(a)** a polished disc measuring 50 mm in diameter; **(b)** a carved *bi* disc of 75 mm diameter; **(c)** a petrographic thin section, viewed with crossed polarisers, showing the grain size and mostly random orientation of the constituent felted tremolite; and **(d)** a BSE image, with red dots showing the locations of EPMA analyses. Abbreviations: MTr = Main (Fe-poor) tremolite phase and Chl = chlorite. Photos a and b by J.-P. Jutras; images c and d courtesy of the University of Arizona.

It also has a weak incipient foliation that slightly diminishes its competency. It was found to contain more abundant chlorite and other accessory minerals (i.e. pyrite, chalcopyrite and goethite). Although this nephrite type is attractive and similar to much of the jade production from neighbouring British Columbia, the DJ Ornamental-type nephrite appears better suited for architectural, ornamental or carving works than for jewellery use.

The Carving-type nephrite (Figure 12) is a marbled white and green stone, with local diopside veining and conspicuous dark grains of goethite. It tends to have a brighter appearance than the Ornamental type, and is suitable for carvings, beads, bangles, pendants and earrings.

The Gem-type nephrite (Figure 13) is very fine grained (constituent tremolite grain size is generally less than 0.1 mm) and strongly monomineralic with few accessory minerals, resulting in fairly uniform pale green to bluish green colouration as cut stones. It is translucent and shows a high (vitreous) polish lustre, and is therefore appropriate for use in fine jewellery.

The Phenomenal-type nephrite (Figure 14) displays subtle-to-strong directional colour variations when viewed in different orientations, ranging from green to blue in light-to-dark tones. Although it is difficult to capture the optical behaviour in static images, videos of several rotating samples can be viewed at [https://www.youtube.com/watch?v=r9qtYM4\\_2Fg&t=99s](https://www.youtube.com/watch?v=r9qtYM4_2Fg&t=99s). The dominant tremolite fibres are noticeably coarser (3–4+ mm long) than in the other nephrite types, and are commonly oriented directionally with kinked banding, as shown by the presence of bent fibres and cross-fibre growth (again, see Figure 14). It is well suited for beads, carvings and fine jewellery (e.g. in rings, brooches and pendants), as well as mineral specimens for collectors.

### **Gemmological Properties and Raman Analysis**

RI values ranged from 1.613 to 1.617, and SG varied from 2.98 to 2.99. No reactions were noted with the Chelsea filter or with UV radiation. Examination of the Phenomenal-type nephrite with a gemmological microscope showed sharp-to-diffuse colour boundaries (Figure 15). The overall colour appearance in overhead fluorescent lighting was noticeably more bluish (with more obvious sheen) as compared to a yellower and more translucent appearance in incandescent transmitted light. Testing of a cabochon of Gem-type nephrite with a polariscope showed the typical bright appearance for an aggregate polycrystalline material.

Several bright green inclusions (Figure 16) exposed on the surface of the Carving-type nephrite were identified as andradite by Raman spectroscopy. Such inclusions are also sometimes present in the other nephrite types. In addition, Carving-type nephrite commonly contains minute, metallic-appearing inclusions, which were provisionally identified (poor Raman spectral quality) as pyrite. In the same sample, Raman analysis of the main constituent amphibole provided a good match with tremolite in the RRUFF database.

### **Vis-NIR Spectroscopy**

Vis-NIR transmission spectroscopy (Figure 17) showed a sharp absorption feature near 1400 nm, which is the first overtone of the stretching vibration of the OH<sup>-</sup> group (Mustard 1992). A weaker sharp feature near 950 nm is the second overtone of the OH<sup>-</sup> group. An absorption band near 1920 nm results from a combination of stretching and bending motions of molecular water.

The Fe<sup>2+</sup> in nephrite can occupy different sites in the crystal structure. Fe<sup>2+</sup> in the octahedrally coordinated sites has two broad absorption bands near 930 and 1150 nm. Fe<sup>2+</sup> in the distorted M4 site has a broad absorption near 1030 nm (Goldman & Rossman, 1977). The combination of these bands gives rise to the broad absorption in the 850–1250 nm region seen in Figure 17. There is a hint of a weak absorption feature at about 445 nm, and this is the region where andradite (which was identified in the sample by Raman spectroscopy) has its strongest Fe<sup>3+</sup> absorption feature. Because of the green colour of the nephrite (again, see Figure 10), one might expect that the least absorption in the visible region would be in the 500–600 nm region. However, due to the scattering of light (which increases at shorter wavelengths) by numerous grain boundaries, there is an overall rise in absorption towards the lower-wavelength side of Figure 17 for light passing through the sample.

### **EDXRF Analysis**

Major-element bulk compositions obtained by portable EDXRF spectroscopy of the various DJ nephrite types and their host rocks are presented in Table II. All four nephrite sub-types showed essentially the same major-element chemical composition.

EDXRF analyses obtained by Stone Group Labs on near-colourless and darker green portions of the disc of Phenomenal-type nephrite in Figure 9 showed that both areas had a similar composition, except the darker green nephrite contained greater amounts of Cr and Ni (Figure 18).



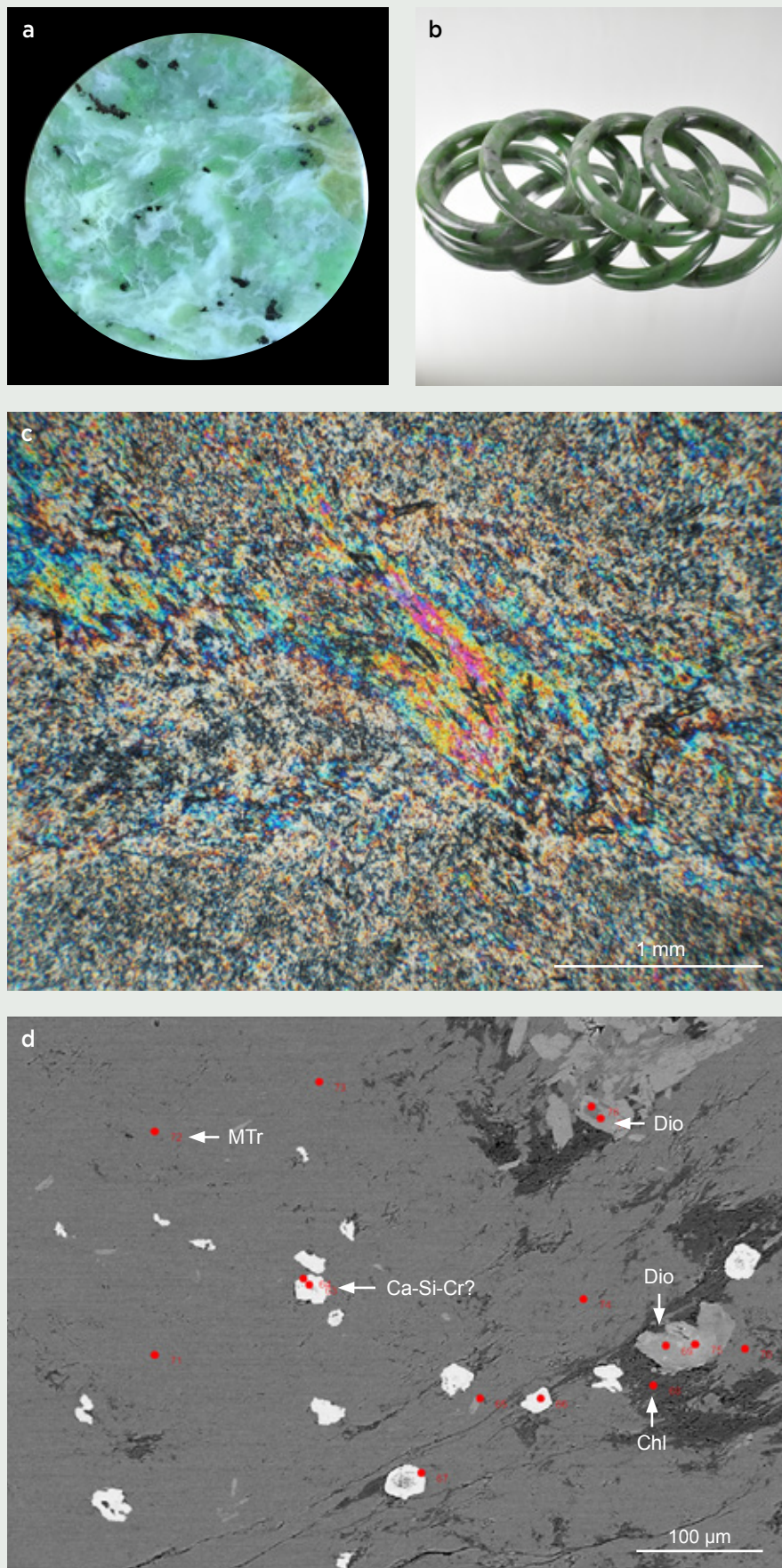


**Figure 12:** Carving-type nephrite is illustrated here by **(a)** a polished disc measuring 55.7 mm in diameter; **(b)** a set of four bangles with an average diameter of about 70 mm; **(c)** a petrographic thin section, viewed with crossed polarisers, showing the grain size and random orientation of the constituent felted tremolite; and **(d)** a BSE image with red dots showing the locations of EPMA analyses. Abbreviations: Ca-Si-Cr? = unidentified phase, Chl = chlorite, Dio = diopside and MTr = Main (Fe-poor) tremolite phase. Photos a and b by J.-P. Jutras; images c and d courtesy of the University of Arizona.



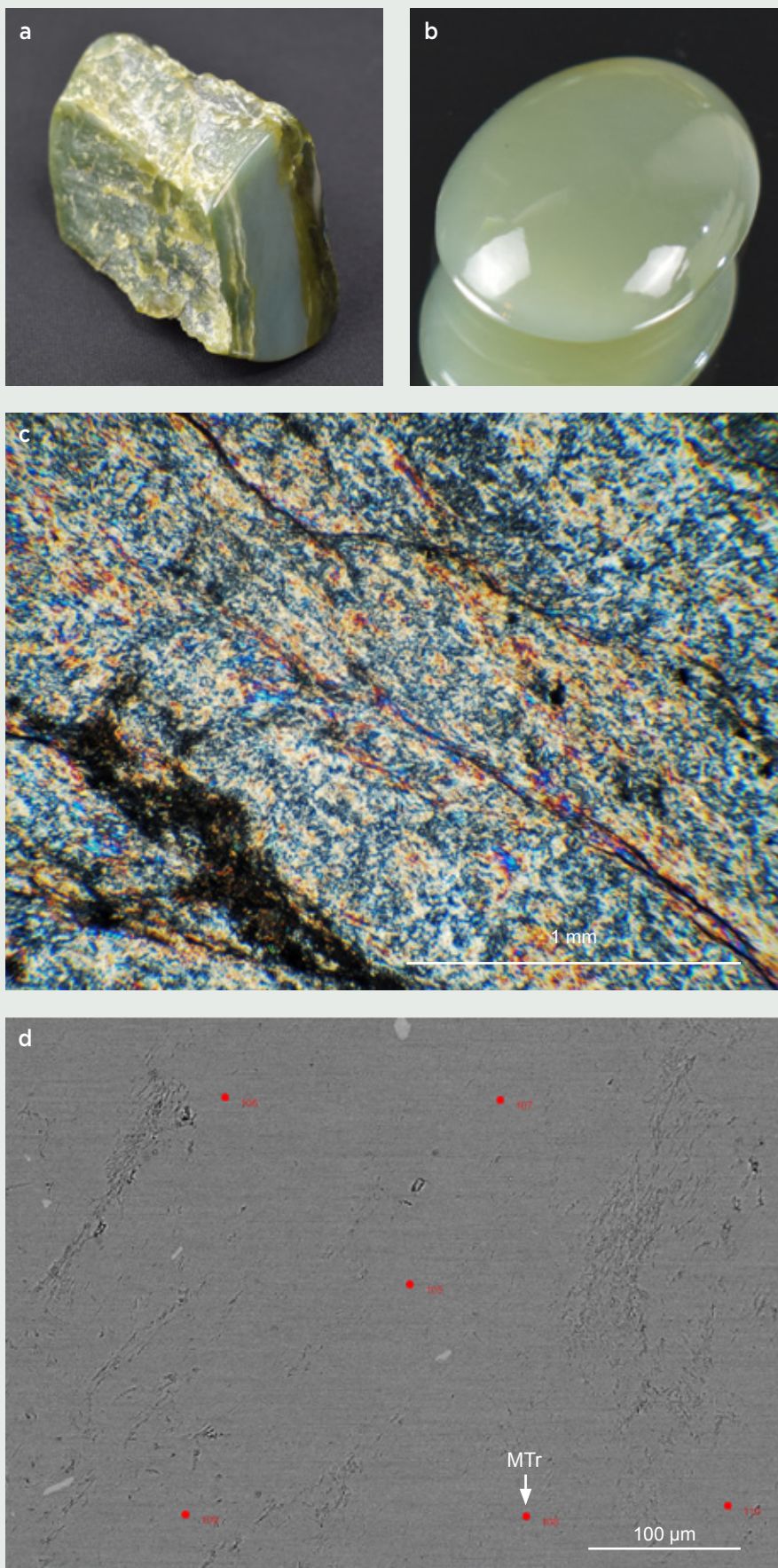


**Figure 13:** Gem-type nephrite is illustrated here by (a) a partially polished rough sample (312.7 g) that shows a central vein which is finer-grained, massive and lighter in colour that is cutting through coarser-grained, darker nephrite; (b) an oval cabochon measuring 19.5 × 14 mm; (c) a petrographic thin section, viewed with crossed polarisers, showing the grain size and random orientation of the constituent felted tremolite; and (d) a BSE image with red dots showing the locations of EPMA analyses. Abbreviation: MTr = main (Fe-poor) tremolite phase. Photos a and b by J.-P. Jutras; images c and d courtesy of the University of Arizona.



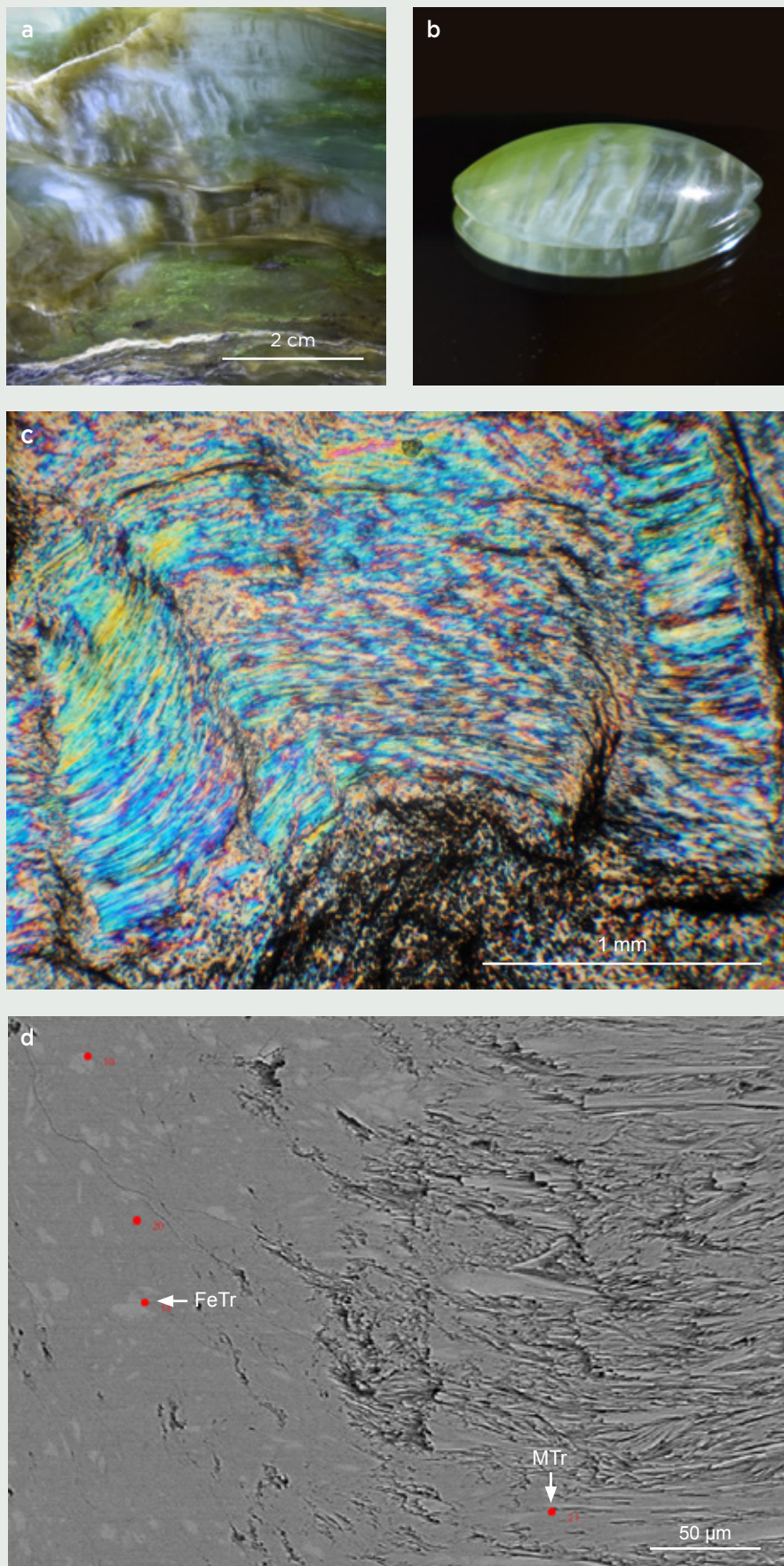


**Figure 14:** Phenomenal-type nephrite is illustrated here by **(a)** a polished slab that shows tremolite fibres elongated in two main directions; **(b)** a marquise-shape cabochon measuring 17.1 × 7.4 mm that displays colour banding; **(c)** a petrographic thin section, viewed with crossed polarisers, showing the relatively large grain size and elongated fibres of tremolite with kinked banding; and **(d)** a BSE image with red dots indicating locations of EPMA analyses. Both Fe-poor tremolite (MTr) and more Fe-rich tremolite (FeTr) phases are present. Photos a and b by J.-P. Jutras; images c and d courtesy of the University of Arizona.

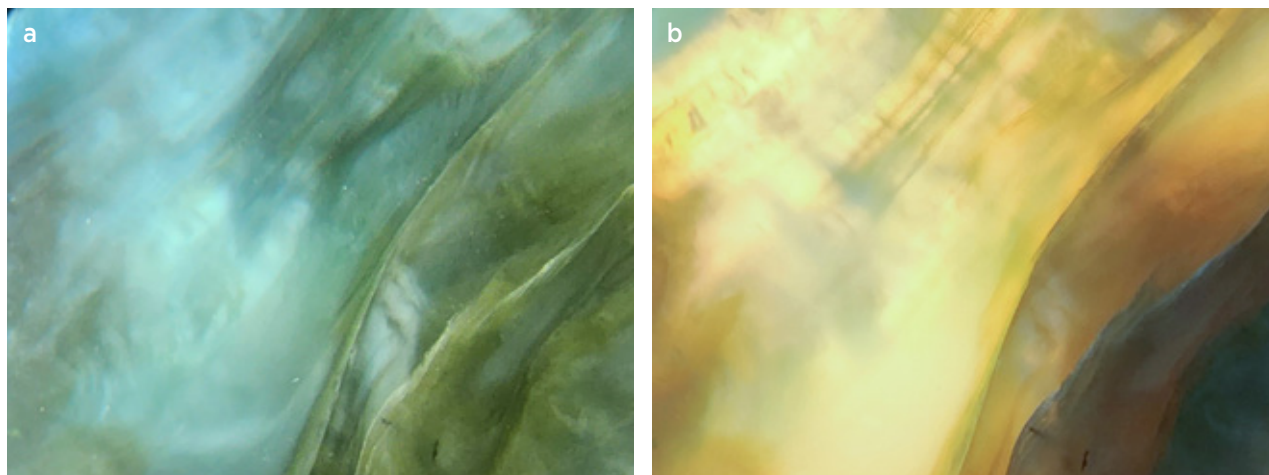


**Figure 15:** A microscopic view of Phenomenal-type nephrite (disc in Figure 9) is shown with (a) overhead fluorescent lighting at a 45° angle above the sample and (b) incandescent transmitted lighting. Note the sharp-to-diffuse colour boundaries. Photomicrographs by B. Williams; image width 0.75 mm.

### *Cause of the Optical Phenomenon*

The cause of the optical phenomenon seen in some of the DJ nephrite is best illustrated via textural comparison with other nephrite types from this deposit, as all of them are otherwise essentially indistinguishable on the basis of their mineralogy and bulk chemical composition (Yang & Downs 2018; Tables I and II). Insights obtained through examination of rough and polished samples, as well as thin-section observation and BSE imagery, show the presence of more than one generation of tremolite fibres in the Phenomenal type, as exhibited by high-angle to orthogonal cross-felting and local variations in chemical composition (i.e. low-Fe and high-Fe tremolite). This is shown in Figure 14, as well as in Figure 19, where the longer-fibre, coarser-

crystalline tremolite is labelled T1. The generally finer, orthogonally cross-cutting set of fibres is labelled T2, and these fibres are particularly evident on broken surfaces that display a splintery to hackly texture (Figure 19c).

Field evidence suggests that this type of fibre ‘felting’ is a consequence of nephrite formation in a changing deformation regime. The initial stages of tremolite fibre growth, replacing an unknown protolith within the serpentinite melange, occurred in a ductile environment, as illustrated by nephrite fold forms (e.g. Figure 20). Tension gashes that formed during this folding hosted the later generation of cross-cutting tremolite fibre growth. Areas of nephrite that experienced more extreme deformation tend to form elongated, typically sinuous pods and lenses with cross-fibre structure

**Figure 16:** The Carving-type nephrite commonly contains clusters of bright green inclusions that were identified as andradite by Raman spectroscopy. Also present are minute, bright, reflective inclusions that are possibly pyrite. Photomicrograph by J.-P. Jutras in reflected light; image width 6 mm.

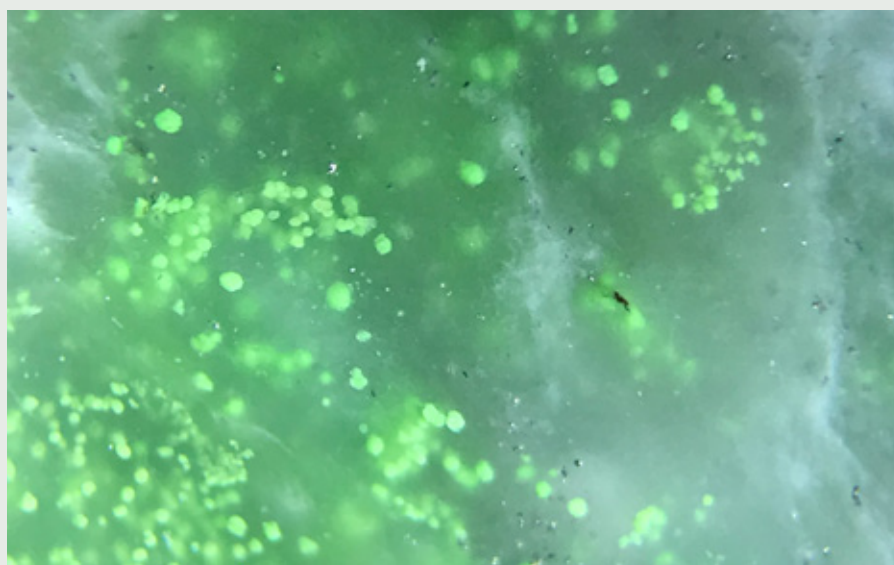




**Figure 17:** The Vis-NIR transmission spectrum of the nephrite shows main features due to the OH<sup>-</sup> group (sharp lines at 1400 and 950 nm), molecular water (1920 nm) and Fe<sup>2+</sup> (850-1250 nm). The features above 2250 nm arise from a combination of metal-oxygen bond stretching and OH<sup>-</sup>-group stretching vibrations.

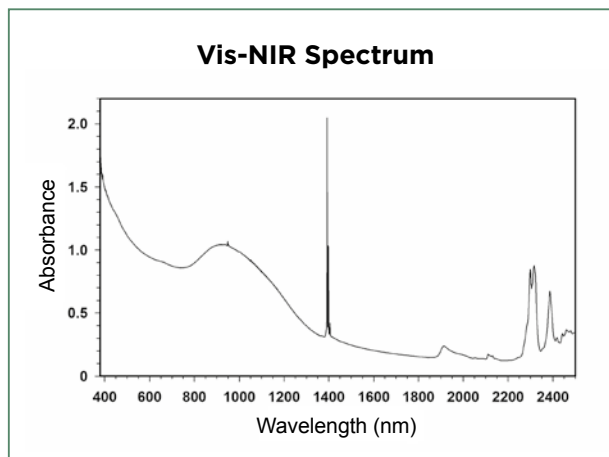


(Figure 21) that often exhibits the optical phenomenon.

At the macroscopic scale, when enough of the T1 or T2 fibres bundle in any one direction, they can be seen to exhibit subtle to strikingly different pleochroic colours along the main tremolite crystallographic *c*-axis (long) direction and perpendicularly along the *a*- and *b*-axis directions (Figure 22). This has been observed by author J-PJ for both generations (T1 and T2) of fibre directions, and is seen in

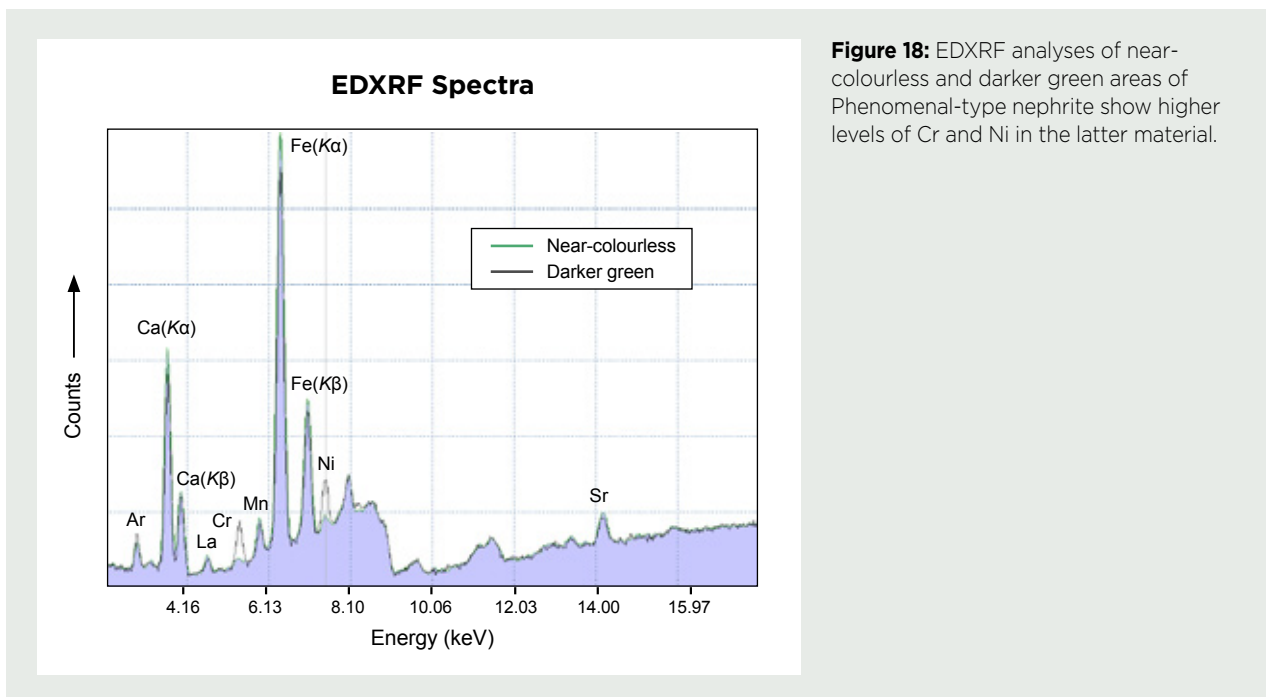


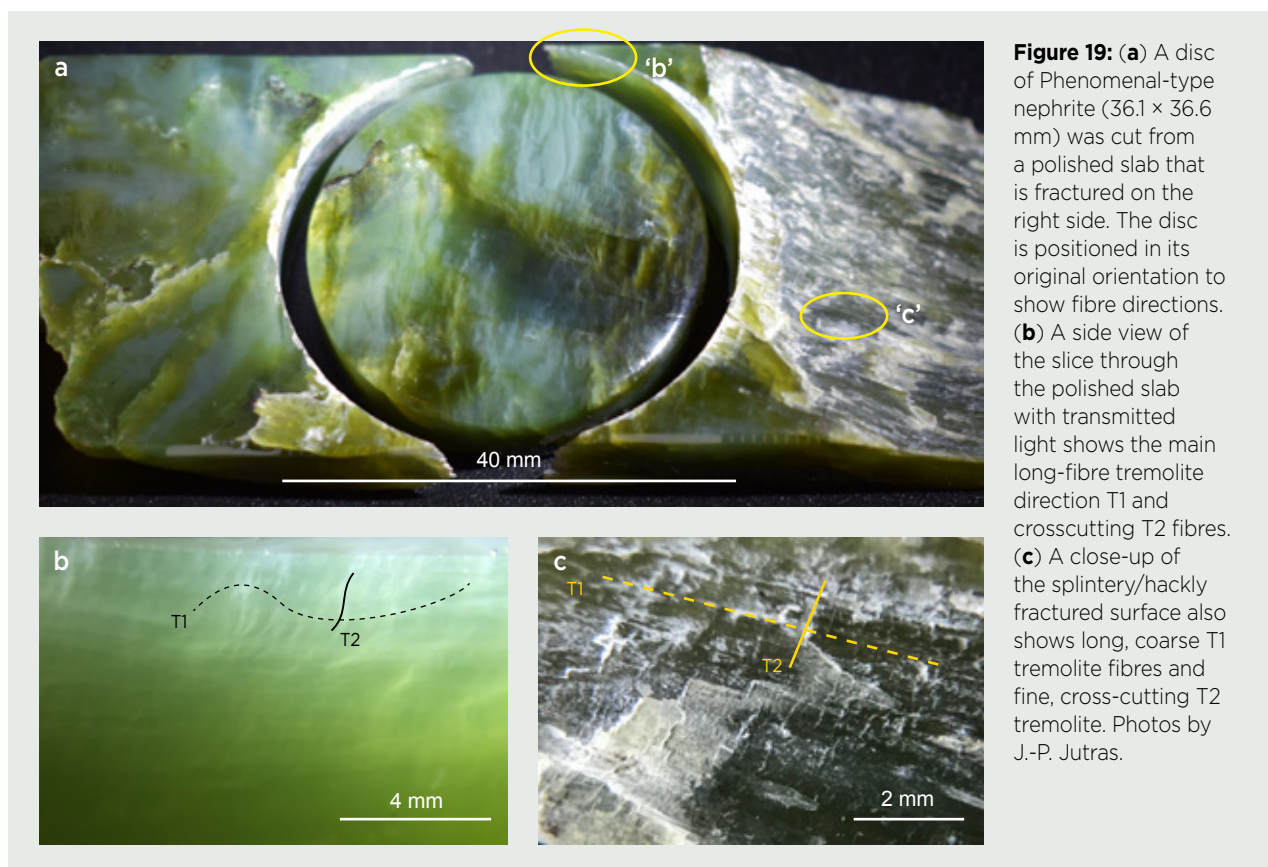
**Figure 18:** EDXRF analyses of near-colourless and darker green areas of Phenomenal-type nephrite show higher levels of Cr and Ni in the latter material.

**Table II:** Semi-quantitative major-element composition by portable EDXRF spectroscopy of nephrite and associated host rocks from the DJ project.<sup>a</sup>

Element (%)	Nephrite				Host Rocks	
	Ornamental	Carving	Gem	Phenomenal	Rodingite	Serpentinite
Ca	10.77	10.98	10.65	10.75	7.33	0.10
Mg	11.26	10.17	9.93	10.63	9.86	20.71
Si	24.5	23.84	23.57	24.28	22.03	21.86
Fe	3.38	2.60	3.08	3.34	4.37	5.57
Others <sup>b</sup>	49.26	51.98	52.38	50.68	53.72	49.03

<sup>a</sup> Data represent single analyses of the Ornamental and Gem types, and an average of three analyses of the Carving type and four analyses of the Phenomenal type.

<sup>b</sup> Components reported by the instrument as being outside the detection range (e.g. light elements).



both lighter- and darker-coloured domains within single stones, excluding the possibility that the optical phenomenon is only controlled by the presence of the more Fe-rich tremolite phase. The range of colours along and across various generations of fibres varies from light to dark green, yellowish green, bluish green, pale blue and locally almost colourless. Although pleochroism is not an optical effect normally associated with nephrite, trichroism has been recognised in well-crystallised forms of tremolite (e.g. colourless, light yellow-green and light green), consistent with its monoclinic crystal structure (Zwaan & Hawthorne 2015; Zwaan *et al.* 2018). The generally high translucency of the jade exhibiting the pleochroic optical effect can also facilitate the appearance of sheen caused by internal light scattering from the different generations of fibrous tremolite domains. When present, the sheen effect can contribute to the brightness seen in certain areas of a sample, but it is separate from the pleochroic effect.

In cut and polished material, the maximum perception of the phenomenal effect is achieved by orienting the cut surface of the stone parallel to the main T1 *c*-axis direction (to maximise lighter T1 *a*- and *b*-axis colours), and as perpendicular as possible to the T2 *c*-axis direction for maximum contrast (Figure 23).

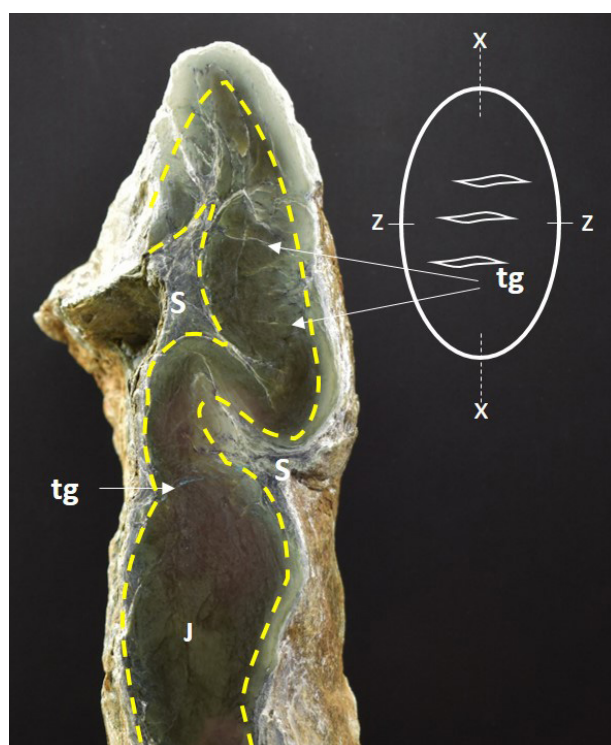


**Figure 20:** A sawn slab shows ptygmatic folds within nephrite jade (J) that is hosted by sheared serpentinite (S). The interpreted stress ellipsoid shows the axis of maximum compression (z) and the main extension direction (x) which is associated with tension gashes (tg). The sample is 33 cm tall and has a maximum width of 8 cm. Photo by J.-P. Jutras.



**Figure 21:** (a) This elongate nephrite pod (31 cm long) was extracted from sheared serpentinite host rock. Its weathered natural surface is likely due to interaction with near-surface groundwater, leading to the formation of a soft alteration rind hiding the stone's true texture and colour. (b) The same piece is shown after slicing and polishing, revealing that it consists of Phenomenal-type nephrite. The width of the upper polished surface is 8 cm. Photos by J.-P. Jutras.

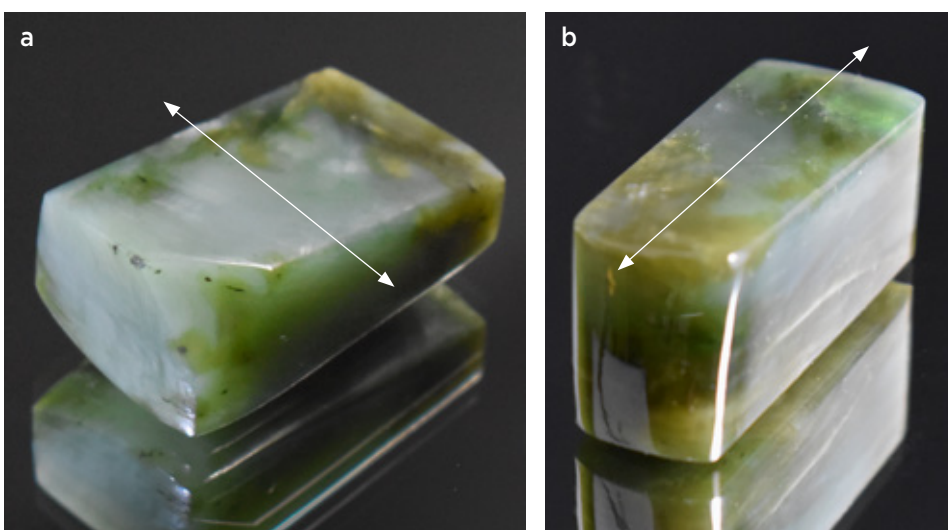


**Figure 22:** (a) A polished block (40 × 17 × 16 mm) of Phenomenal-type nephrite was cut to highlight the darker colour seen along the main fibre *c*-axis direction, which in this case is dark green. The *a*- and *b*-axis directions exhibit much paler colouration. (b) Similar colouration is shown by another polished block of Phenomenal-type nephrite (39.5 × 23 × 15.5 mm). Arrows indicate the main T1 fibre *c*-axis direction. Photos by J.-P. Jutras.

## CONCLUSIONS

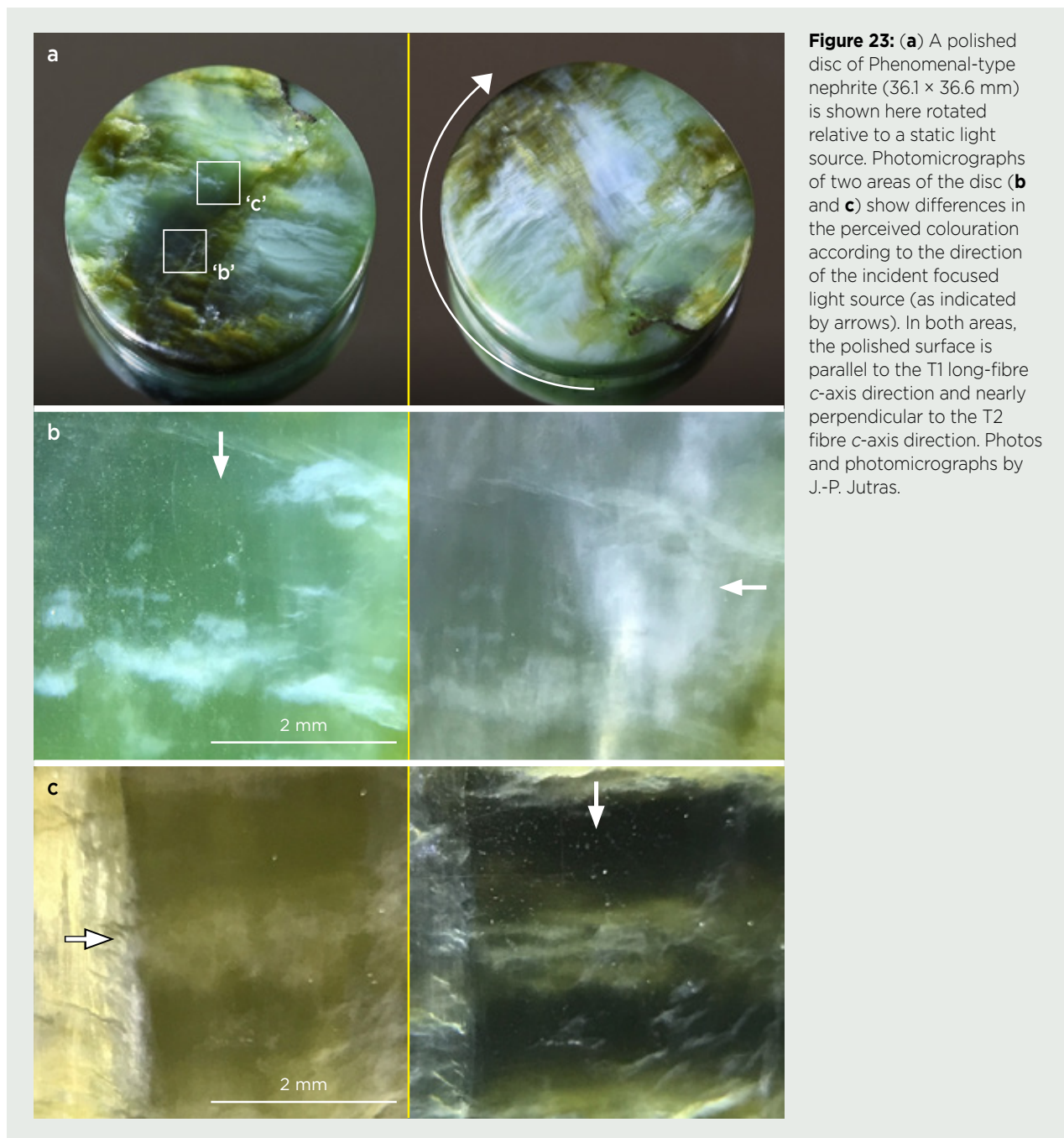
Nephrite jade from Washington State is an attractive gem material that takes a high polish (e.g. Figure 24) and exhibits a variety of appearances. In general, the gemmological and mineralogical properties of this jade are consistent with previous reports on nephrite from various world localities (Leaming 1978; Harlow *et al.* 2014; Barnes 2018; Hughes 2022).

Of the four different types of nephrite identified at the DJ project, one of them displays an optical phenomenon consisting of subtle-to-strong directional colour variations when viewed at different

orientations. This effect is shown by highly translucent samples containing more than one generation of interwoven-fibre growth in macroscopically continuous domains. The optical effect is interpreted to result from tremolite's pleochroism, which can be seen as the stone is rotated and the orientation of the dominant *c*-axis direction of the fibre bundles changes relative to the viewer. Internal light reflections within the fibrous tremolite domains can also occur, but this is expressed as sheen and not an apparent change of the perceived colour.

The full extent of the lode occurrence hosting the Phenomenal-type nephrite has not been





determined. Exploration work, including trenching and exploratory core drilling performed to date, allows for a target estimate of 5,900–6,800 tonnes of nephrite (inclusive of all types) in the DJ claim area tested. The future development of this occurrence will depend on market demand. While surface production work can continue to take place at a minimally intrusive small scale under the current permitting regime, a full operation plan compliant with all applicable environmental and social regulations would be required to obtain additional permits to scale up and potentially expand future operations.



**Figure 24:** This carved seashell (shown with an accompanying bead) of Phenomenal-type nephrite was done as a test of the new material's structural integrity. The carving is 5 cm long and is by jade sculptor Shane Hauser. Photo by J.-P. Jutras.

## REFERENCES

- Barnes, G.L. 2018. Understanding Chinese jade in a world context. *Journal of the British Academy*, **6**, 1–63, <https://doi.org/10.5871/jba/006.001>.
- Barnes, G.L. 2022. True jades, false friends. In: *Tectonic Archaeology: Subduction Zone Geology in Japan and its Archaeological Implications*. Archaeopress, Oxford, 338–372, <https://doi.org/10.2307/j.ctv35n89zf>.
- Blankenship, D. 2022. Chapter 11: North to Alaska, USA jade. In: Hughes, R.W. (ed) *Jade: A Gemologist's Guide*. Lotus Publishing, Bangkok, Thailand and RWH Publishing, Boulder, Colorado, USA, 195–219.
- Goldman, D.S. & Rossman, G.R. 1977. The identification of Fe<sup>2+</sup> in the M(4) site of calcic amphiboles. *American Mineralogist*, **62**(3–4), 205–216.
- Harlow, G.E., Sorensen, S.S., Sisson, V.B. & Shi, G. 2014. The geology of jade deposits. In: Groat, L.A. (ed) *The Geology of Gem Deposits*. Mineralogical Association of Canada Short Course Series Vol. 44, Québec City, Québec, Canada, 205–374.
- Hawthorne, F.C., Oberti, R., Harlow, G.E., Maresch, W.V., Martin, R.F., Schumacher, J.C. & Welch, M.D. 2012. Nomenclature of the amphibole supergroup. *American Mineralogist*, **97**(11–12), 2031–2048, <https://doi.org/10.2138/am.2012.4276>.
- Hogarth, E. 2019. Gem News International: Cat's-eye nephrite jade from Washington State. *Gems & Gemology*, **55**(1), 124–125.
- Hogarth, E. 2022. Gem News International: Washington jade update. *Gems & Gemology*, **58**(1), 92–93.
- Hughes, R.W. (ed) 2022. *Jade: A Gemologist's Guide*. Lotus Publishing, Bangkok, Thailand and RWH Publishing, Boulder, Colorado, USA, 534 pp.
- Leaming, S.F. 1978. *Jade in Canada*. Geological Survey of Canada Paper 78-19, Geological Survey of Canada, Ottawa, Canada, 59 pp.
- Leaming, S.F. 1995. Chapter 13: Jade in North America. In: Keverne, R. (ed) *Jade*. Lorenz Books, London, 296–315.
- Leaming, S.F. & Hudson, R.D. 2005. *Jade Fever: Hunting the Stone of Heaven*. Heritage House Publishing Co., Surrey, British Columbia, Canada, 191 pp.
- LMHC 2011. *Information Sheet #11: Jade and Related Minerals*. Laboratory Manual Harmonisation Committee, 2 pp.
- Mustard, J.F. 1992. Chemical analysis of actinolite from reflectance spectra. *American Mineralogist*, **77**(3–4), 345–358.
- Ream, L.R. 1974. Washington gem jade. *Lapidary Journal*, **28**(4), 708–711.
- Ream, L.R. 2022. *Nephrite Jade of Washington and Associated Gem Rocks: Their Origin, Occurrence and Identification*. LR Ream Publishing, Coeur d'Alene, Idaho, USA, 130 pp.
- Tabor, R.W., Booth, D.B., Vance, J.A. & Ford, A.B. 2002. *Geologic Map of the Sauk River 30- by 60-Minute Quadrangle, Washington*. U.S. Geological Survey Geologic Investigation Series I-2592, U.S. Geological Survey, Denver, Colorado, USA, 67 pp. pamphlet and two map sheets, <https://doi.org/10.3133/i2592>.
- Ward, F.C. 2015. *Jade*, 3rd edn. Gem Book Publishers, Malibu, California, USA, 64 pp.
- Yang, H. & Downs, R.T. 2018. A Short Report of the Analysis on Four Jade Samples from JP Jutras. University of Arizona, Tucson, Arizona, USA, unpublished report, 2 pp.
- Zwaan, J.C. & Hawthorne, F.C. 2015. Gem Notes: Tremolite from Mwajanga, Tanzania. *Journal of Gemmology*, **34**(7), 569–571.
- Zwaan, J.C., Hawthorne, F.C. & Day, M. 2018. Gem Notes: Cat's-eye tremolite from Badakhshan, Afghanistan. *Journal of Gemmology*, **36**(1), 14–15.

## The Authors

## Jean-Pierre Jutras

Jade Leader Corp.  
Calgary, Alberta, Canada  
Email: [jp@gold.ca](mailto:jp@gold.ca)

## Bear Williams FGA and Cara Williams FGA

Stone Group Labs, PO Box 104504,  
Jefferson City, Missouri 65110-4504, USA

## Dr George R. Rossman

Division of Geological and Planetary Sciences,  
California Institute of Technology, Pasadena,  
CA 91125-2500, USA

## Acknowledgements

Author J-PJ would like to acknowledge Jade Leader Corp. and its shareholders for the financial support invested in the nephrite exploration and research presented here. Also, thanks to both Dr Shane Ebert and Dr Peter K. Megaw (IMDEX Inc., Tucson, Arizona) for early reviews of the article. Lanny Ream (LRReam, Coeur d'Alene, Idaho, USA) was instrumental in sharing the oral history of the occurrence, as one of the most recognised scholars and historians on Washington jade. Finally, author J-PJ is grateful to David Smith, United States operations manager for Jade Leader, both for his knowledge of historical production from the claim area and for his continued involvement with the project as a fantastic field operator and logistician.

# Copper Minerals in Chalcedony from Obi Island, Indonesia

Joel Ivey and Brendan M. Laurs

**ABSTRACT:** Obi Island is a small, remote Indonesian island located in the Molucca Sea that is endowed with a variety of mineral resources. Since 2019, artisanal miners have produced colourful specimens containing various copper minerals in chalcedony from altered andesite breccia near the village of Sesepe in the north-eastern part of the island. The specimens are sawn open to reveal the copper mineralisation, and sold into the lapidary and collector market. Locals call this material *batu kawat*, meaning ‘wire rock’. Silica-rich areas of the deposit provide semi-transparent masses of chalcedony that are speckled with blue chrysocolla and shiny blebs of native copper (e.g. ‘confetti chrysocolla’). The combination of interesting textures and attractive colouration make these ornamental materials popular with collectors and lapidaries.

*The Journal of Gemmology*, 38(5), 2023, pp. 512–521, <https://doi.org/10.15506/JoG.2023.38.5.512>

© 2023 Gem-A (The Gemmological Association of Great Britain)

During the past few years, Indonesia has emerged as a source of various attractive gem materials containing copper minerals, including native-copper-bearing opal and silicified wood from West Java (Laurs 2018, 2022). In addition, fine-quality chrysocolla chalcedony (or ‘gem silica’) has been mined for the past two decades in the Bacan Archipelago of Indonesia’s North Maluku Province (Einfalt & Sujatmiko 2006). Recently, another locality in this province—Obi Island—has become a source of colourful specimens of various copper minerals that are commonly included within chalcedony (e.g. Figure 1).

Obi Island is located in a remote part of eastern Indonesia, which has been much studied for its diverse and unique flora and fauna. The complex geology of the island gives rise to several mineral occurrences that have been the focus of exploitation by small-scale miners from the Indonesian archipelago, as well as by foreign companies. On the western side of the island, Fe-Ni-Co deposits in saprolitic soil are being commercially exploited by a Chinese consortium near the village of Kawasi. The northern portion of the island hosts locally high-grade gold deposits and several alluvial gold occurrences, although the foreign company that was awarded

a mining concession was unable to work there due to resistance from small-scale miners. A site in north-eastern Obi Island is the focus of artisanal diggings for the copper minerals that are the subject of this article.



**Figure 1:** These cut and polished tablets of chalcedony from Obi Island, Indonesia, contain inclusions of chrysocolla and native copper. Such material is commonly referred to as ‘confetti chrysocolla’. They weigh 97.83 ct (top), 82.34 ct (left) and 79.14 ct total weight for the matched pair (bottom right). Photo by Mia Dixon, Pala International, Fallbrook, California, USA.



These are hosted by andesitic breccia, and include native copper associated with copper-bearing minerals such as chrysocolla and malachite, which are commonly encased in chalcedony (e.g. Figure 2). Known locally as *batu kawat* (wire rock), these specimens are eagerly sought after by lapidaries and collectors.

This article describes the location, history, geology, mining and types of this colourful material being exploited by artisanal miners from the mountainous volcanic terrain of Obi Island.

## LOCATION AND ACCESS

The Obi Island group is part of the Maluku Islands, which are situated in North Maluku Province in the eastern portion of the Indonesian archipelago (Figure 3). The Obi Island group consists of 42 islands, which lie just south of Halmahera Island in the Molucca Sea. Obi Island (Figure 4), the largest of the group, measures  $84 \times 42$  km and is often referred to as Obi Major.

Travel to Obi Island starts in Indonesia's capital city, Jakarta, with a flight to Ternate (in North Maluku Province) that takes about four hours. Next, an ocean ferry sails for eight hours to Bacan Island, followed by 12 hours on a smaller ferry to the terminal on the northern side of Obi Island at Laiwui (see Figure 4). A local boat then shuttles passengers to the village of Kelo on the north-east side of the island. The route from Kelo to the mining area is 14.7 km long, via a motorbike path to Sesepe village and then along the Mangga Dua River to the final drop-off point, followed by a five-hour jungle hike to the digging area. The deposit is located at coordinates  $1^{\circ}32'25.2''$  S,  $127^{\circ}57'4.4''$  E (Djasmin, pers. comm. 2022).

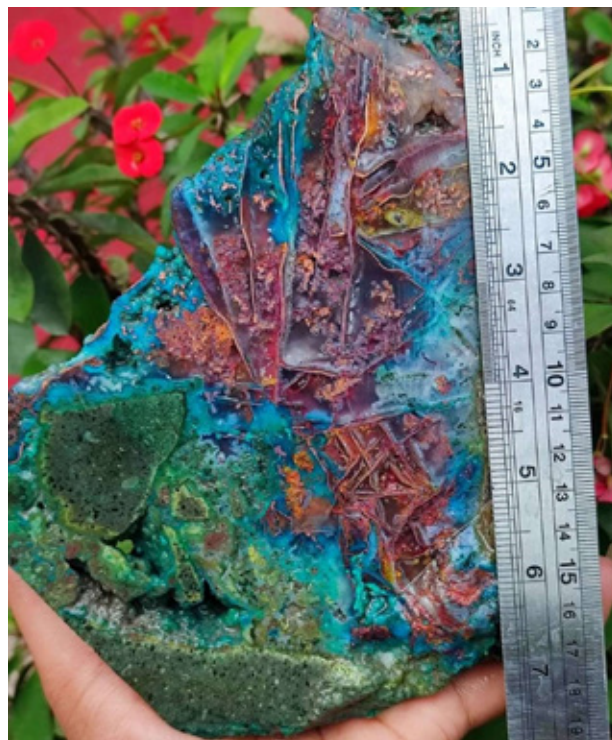


**Figure 2:** This sawn slab shows fragments of the chlorite-altered andesite breccia host rock (lower left) with vuggy leached areas filled by native copper, chrysocolla and chalcedony. Photo courtesy of Dan Norquist.

## HISTORY

At the beginning of the 20th century, Dutch explorers identified anomalous nickel enrichment in saprolitic soils near what is now the village of Kawasi on the western end of Obi Island (Figure 4; van der Ent *et al.* 2013). Nearly a century later, in the 1990s, a Japanese consortium (INDECO) evaluated the resource and



**Figure 3:** This map of Indonesia shows the locations of the Obi Island group, Halmahera Island and Bacan Island. Adapted from map provided by Wikimedia Commons.



**Figure 4:** The locations of the mineral deposits near the villages of Kawasi, Anggai and Sesepe are indicated on this satellite image of the Obi Island group. Image modified from [www.wikiloc.com](http://www.wikiloc.com).

defined 51 million tons at 1.5% of ferro-nickel and 19.6 million tons of 2.2% nickel in the soils (van Leeuwen 2018). Ferry access to the island, and the importation of miners to explore and exploit the nickel deposits, facilitated the artisanal exploitation of the nearby gold and copper deposits.

In 1992–1995, Obi Island was explored by PT Obi Minerals, a joint venture between BHP Minerals Pacific Inc. and state mining group PT Aneka Tambang (Antam). A regional stream-sediment sampling programme was conducted, and geochemical analysis of the samples identified anomalous gold just inland from the village of Anggai, as well as copper to the south-west of Sesepe (again, see Figure 4). The company conducted further exploration and drilling on the Anggai gold property, and reported a possible resource of 6.8 million tons with an ore grade of 2.35 g/ton gold in quartz veins (Prihatmoko & Nugroho 1998). Follow-up work on the copper anomaly south-west of Sesepe identified volcanic rock (monomict andesite breccia) containing chalcedony, chrysocolla, malachite and native copper. Further testing was done in a 174-m-long trench that yielded 0.64% copper (Prihatmoko & Nugroho 1998). Geologists concluded the style of mineralisation represented a limited occurrence, and since the company was looking for a much larger copper deposit, they did no further work here. This is the same area that local villagers are digging today to produce the gem and ornamental materials described in this article.

In 2010, Indonesian President Susilo Bambang Yudhoyono gave then-U.S. President Barak Obama a ring containing chrysocolla chalcedony (similar to Figure 5;

Anonymous 2015) from the Bacan Archipelago, located 100 km north-north-west of Obi Island. A mining rush ensued there (specifically on Kasiruta Island), and large amounts of the chrysocolla chalcedony were cut into cabochons in workshops throughout Indonesia. On websites such as eBay, Etsy, GemRock, Facebook and Instagram, any unemployed miner or villager with a smartphone and a PayPal account suddenly had a market and source of income. This stimulated additional

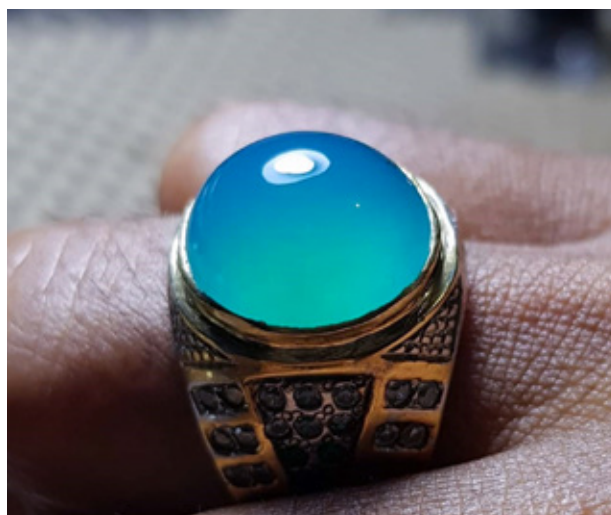


**Figure 5:** A cabochon of chrysocolla chalcedony from the Bacan Archipelago is shown here in a ring similar to one presented to former U.S. President Barak Obama by Indonesian President Susilo Bambang Yudhoyono. The discoverers of the deposit attempted to keep its location a secret by calling the material *batu bacan* (for Bacan Island), although it was found on nearby Kasiruta Island. Discovered in the 1990s, *batu bacan* has become increasingly popular and expensive. Photo courtesy of Yusef Sulaeman.



exploration for gems and ornamental stones in the region.

Author JI first noted rough copper-bearing material from Obi Island arriving in the West Java town of Sukabumi in 2019, when Indonesian friends with lapidary workshops there posted photos of the specimens on social media. One of the first groups to mine the deposit near Sesepe was organised by a dealer named Djasmin (whom author JI had known for 21 years) together with his son. Djasmin reported that his team first started digging there in 2016, but after one month they found only 10 kg of material, so it was difficult to imagine making a profit. Several more groups that attempted to mine the area came to the same conclusion before they eventually found good-quality material in 2019.

## GEOLOGY

The geology of Obi Island is summarised in Figure 6, which is based on the detailed fieldwork and interpretation of Augustiyanto (1995). The region is located between two splays of the Sorong Fault Zone, and has been displaced and rotated over time. The south-western and north-western portions of Obi Island are underlain by Paleozoic high-grade metamorphic basement rocks

with local granitic intrusions. The protoliths of the metamorphic rocks were probably derived from erosion of the Australian continent and deposited onto the Philippine Sea Plate prior to migration of the terrain along the Sorong Fault Zone (Augustiyanto 1995).

Overlying the basement are younger Cretaceous mafic to ultramafic ophiolitic rocks. These are exposed mainly in the north, west and south-west parts of the island, and are considered basement there. Weathering of these rocks has concentrated Fe, Ni and Co into economically important mineral deposits in saprolitic soils on the western side of the island.

Overlying the ophiolitic rocks are Tertiary volcanics and sediments, which are the products of periodic subduction-related arc volcanism during the Oligocene, Miocene and Pliocene epochs (i.e. from about 33.9 to 2.6 million years ago; Augustiyanto 1995). From oldest to youngest, these are represented by the Guyuti, Woi and Anggai formations.

The Woi Formation hosts the Cu-mineralised rocks near Sesepe. It consists of andesite and basalt lava flows, volcanic breccia (pyroclastics) and tuff, as well as sandstone and siltstone, with a combined thickness of up to 1,000 m. Augustiyanto (1995) interpreted the

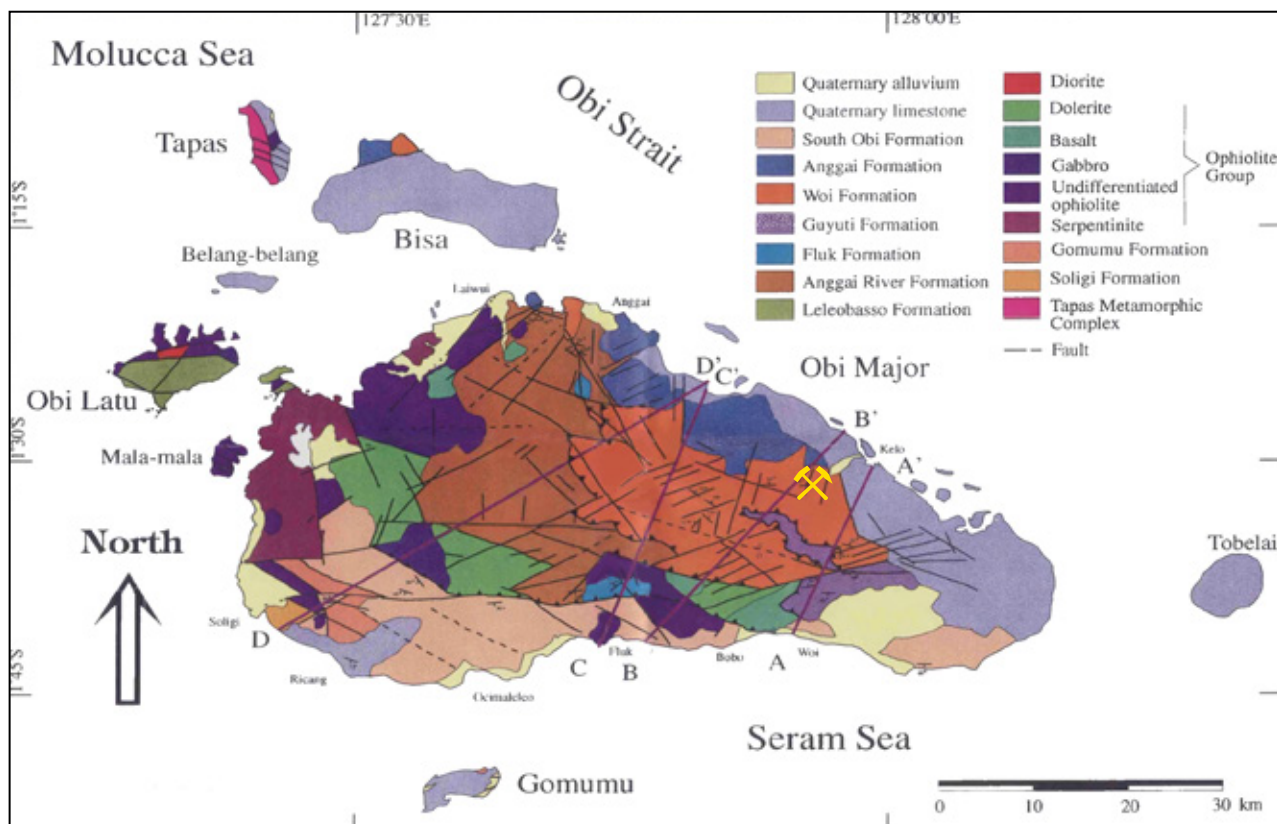


**Figure 6:** A geologic map of the Obi Islands shows the location of the Woi Formation, which hosts the Cu-mineralised rocks that are the subject of this article (yellow mine symbol). Splays of the Sorong Fault Zone lie outside the map area to the north and south of Obi Island, and are oriented in a direction trending approximately east-west. Modified from figure 2.1 of Augustiyanto (1995).



sequence as a series of mid-Miocene to early Pliocene strata deposited on land or in a shallow marine environment. Although the Woi Formation rocks analysed during the surveys in the 1990s were andesite and basaltic volcanics typical of island-arc subduction zones, chemical analysis of samples from the Kelo and Sesepe areas were notably higher in Si and K (see figure 5.24 in Augustiyanto 1995), suggesting a different volcanic source. In author JJ's opinion, this unique rock chemistry and the subsequent mixing with oxygenated groundwater were instrumental in the formation of the copper mineral assemblage.

Prihatmoko and Nugroho (1998) indicated that the copper deposit near Sesepe is hosted by andesitic breccia, which they interpreted as a volcanic debris flow or a collapse breccia. According to Prihatmoko and Nugroho (1998), the copper minerals—mainly chrysocolla, malachite and native copper—are typically associated with low-temperature quartz (chalcedony and opal) and smectite-zeolite alteration. These authors speculated that the mineralisation could have resulted from leaching of an underlying copper sulphide body by low-temperature hydrothermal fluid, or from leaching of andesitic host rocks (that were originally rich in copper) during the cooling of the volcanic rocks.

It should be noted that Augustiyanto (1995) concluded the Woi Formation is the age- and lithological-equivalent of the Kaputusan (or Keputusan) Formation on Bacan and Kasiruta islands to the north. These rocks host the chrysocolla chalcedony deposit mentioned above, as well as the Kaputusan porphyry copper deposit (with resources of 254,000 tons of Cu and 19 tons of Au; van Leeuwen 2018, pp. 63–64).

## MINING AND PRODUCTION

According to Djasmin (pers. comm. 2022), as of October 2022, about 35–40 miners were active at the site, many of whom migrated there from the Anggai goldfields. The miners live in tarpaulin tents along the Sesepe stream (Figure 7a), and tarps cover the active diggings on the hillside above (Figure 7b). More than 20 pits and tunnels penetrate into the steep, east-facing slopes located about 1,300 m from the miners' camp. Most of the current diggings are concentrated in a zone measuring 100 × 30 m.

Typically, each digging hole is worked in shifts by four or five miners. A typical adit is less than 1 m wide and nearly 2 m tall, and is dug by hammer and chisel. The adits follow a string of veinlets and stockworks of oxidised blue or green copper minerals. The tunnels typically extend up to 10 m into the mountainside before the weathered zone diminishes and the rock becomes too hard to exploit by hand. The less-oxidised, highly silicified rocks at depth are particularly difficult to dig with hand tools and are also poorer in copper-oxide mineralisation.

Since most of the buyers are from the lapidary industry, any rock that is hard enough to hold together and exhibits the blue or green colouration indicative of chrysocolla or malachite is sought after by the miners (e.g. Figure 8). Most of the digging takes place in chlorite-altered andesite breccia, and the miners can often tell from the density of the material whether it will reveal native copper and associated minerals when it is sawn open (Figure 9). The miners also recover specimens of chrysocolla from weathered pockets and solution cavities in the breccia.



**Figure 7:** (a) The miners' camp is located on Sesepe stream. From the camp to the mining area is a travel distance of about 1,300 m (and an 800 m elevation gain). (b) Tarps cover the entrances to adits and pits on the hillside where the copper-bearing specimens are mined. Photos by Djasmin.





**Figure 8:** This specimen (approximately 15 cm tall) consists of native copper sheets coated with chrysocolla in a vuggy web pattern, bounded on the top and bottom by andesite breccia. Photo by Dace Irwan.



**Figure 9:** Local miners mainly search for material usable for lapidary purposes, and thus look for heavier, solid pieces infiltrated by silica and also containing a colourful mixture of native copper and chrysocolla with few voids, as shown by this sawn example (approximately 19 × 16 cm). Photo courtesy of Dade Dialami.

The extracted stones are washed in the nearby stream and taken down the steep hillsides in heavy polybags. From Kelo, they are loaded into small boats and then taken by ferry to Ternate, where some are sawn open and others are sent to West Java to be sorted and processed. Well-formed specimens constitute a very minor portion of the ornamental rock recovered, as the diggers have little experience protecting the delicate pieces from damage during mining and transport.

Author JI estimates that around 1.5 tonnes of ornamental rock have been extracted by the artisanal miners. Specimens containing native copper comprise only 20–25% of the production (again, see Figure 9), and most of the rest is what they call ‘copper web’, in which oxidised copper minerals form chrysocolla- and malachite-cemented boxwork textures (Djasmin, pers. comm. 2022). Particularly appreciated by both collectors and lapidary enthusiasts are arborescent native copper dendrites hosted by chrysocolla (Figure 10). Recently, the miners encountered some crystalline native copper-rich aggregates within the andesite breccia (Figure 11).

In general, the rocks with the highest degree of weathering and hydrous copper oxide minerals are the most colourful, exhibiting the blues and greens of chrysocolla and malachite. They are found in shallow



**Figure 10:** Native copper blebs and dendritic wires permeate a sawn slab of pervasively silicified chrysocolla (approximately 8 × 6 cm). Photo by Yusef Sulaeman.



surface diggings, and the miners report that the deeper they dig, the less ‘colour’ they find, with the specimens consisting mainly of chalcedony and native copper. Among the most distinctive are masses of semi-transparent chalcedony containing blebs of native copper together with flecks or wavy masses of greenish blue chrysocolla (i.e. ‘confetti chrysocolla’; Figures 1 and 12a). In addition, rare pieces display attractive aggregates of tiny copper crystals (Figure 12b), which in some cases resemble exploding fireworks (Figure 12c).

## MINERAL ASSEMBLAGE

The minerals in five samples from the Obi Island copper deposit were identified by Dr George R. Rossman (California Institute of Technology, Pasadena, California, USA) using Raman spectroscopy: three hand specimens that were provided by James Walker and two cabochons that were donated to Gem-A by Yianni Melas and Avant Chordia (e.g. Figure 13). Raman spectra were obtained with a Renishaw inVia system using a 514 nm laser and a 50 × objective lens with about 1.5 mW power on the sample. Mineral identification was accomplished by comparison to reference spectra in the RRUFF database (<https://rruff.info>).

The analyses confirmed the presence of greenish blue to bluish green chrysocolla, green malachite and deep red cuprite (rarely appearing yellow in one specimen). These formed together with native copper in a colourless matrix consisting of quartz (chalcedony) and rarely a white zeolite that provided the best Raman spectral matches with mordenite and epistilbite in the RRUFF database. In addition, Raman analysis of



**Figure 11:** This sawn specimen (approximately 18 × 15 cm) contains a native-copper-rich crystalline aggregate in brecciated andesite. Infiltration by late-stage chalcedonic silica prevented alteration of the copper by meteoric waters and subsequent weathering. Photo by Yusef Sulaeman.

black-appearing areas of the cabochons showed a mixture of quartz and poorly crystallised graphite.

The presence of chrysocolla, malachite, native copper and cuprite is consistent with the results reported by Renfro (2022).

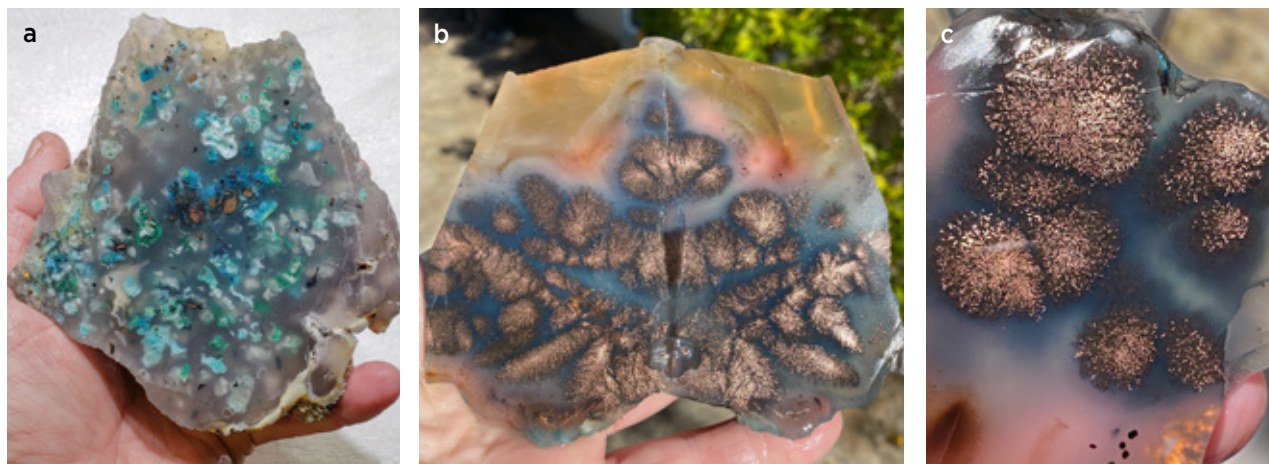


**Figure 12:** (a) This sawn slab (10 × 12 cm) consists mainly of colourless chalcedony which hosts small masses of native copper and blue chrysocolla. (b) Chalcedony-rich specimens also rarely contain fine-grained aggregates of native copper (sawn pair measuring about 14 cm wide total), which (c) can form patterns reminiscent of exploding fireworks (image width 8 cm). Photo credits: (a) courtesy of Horizon Mineral Lapidary, photo by Joe Jelks; (b) and (c) courtesy of Bud Standley.





**Figure 13:** These cabochons (up to 45 × 30 mm) from the Obi Island deposit show various textures and mineral associations, including native copper, chrysocolla, cuprite and malachite, with local black areas of matrix that proved to consist of poorly crystallised graphite in quartz. Raman analysis of the mineral phases was done on the upper-left and lower-right specimens. Gift of Yianni Melas and Avant Chordia; photo by Jeff Scovil.

## LAPIDARY USES

Stone cutters have created polished slices for display and cabochons for jewellery use, sometimes incorporating small vugs and natural edges into their pieces. The popularity of these pieces has been noted by Indonesian lapidaries on Facebook and Instagram, and they have begun to incorporate the textures and colours into their own creations (e.g. Figure 14). The diversity of patterns lends the material to cutting a variety of unconventional shapes.

Although most of the assemblages are quite durable once they have been cut, resins such as Bond Optic are used by some lapidaries to stabilise the material and to

fill small pits in the surface for a better polish (Joe Jelks, pers. comm. 2022; see Figure 15a). However, pieces consisting of mostly chalcedony (see Figures 1 and 15b) do not require such stabilisation.

## FORMATION CONDITIONS AND CONCLUSION

Copper mineralisation on Obi Island is not only responsible for attractive specimens (e.g. Figure 16), but is also interesting from an economic geology standpoint. Indeed, the amount of native copper and associated minerals produced from this deposit over the past few years has caught global attention. The theory proposed

**Figure 14:** Stonecutters in Indonesia created (a) this matched pair of cabochons (15 × 35 mm each), which consists of a patterned assemblage of native copper and chrysocolla in chalcedony, and (b) this free-form piece (30 × 55 mm) containing native copper sheets with chrysocolla- and chalcedony-filled vugs lined with drusy quartz. Photos by (a) Rika Djasmin and (b) Yusef Sulaeman.



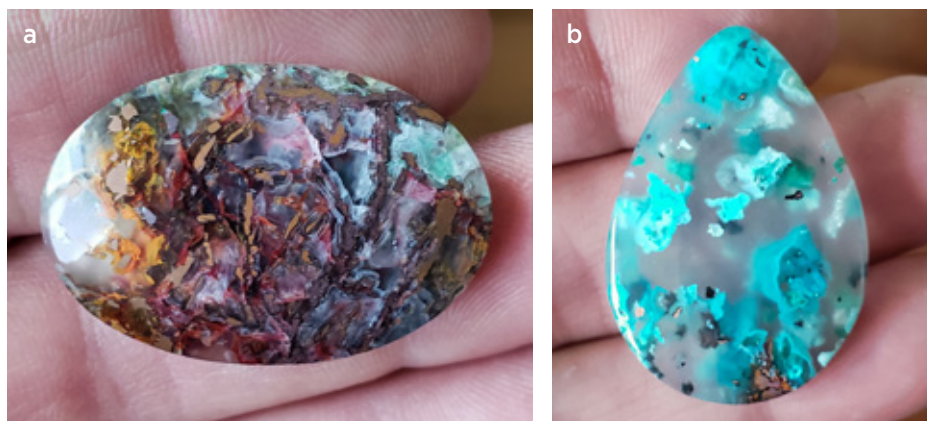


**Figure 15:** (a) This Obi Island cabochon (40 × 23 mm) has been resin-impregnated to fill tiny pits on its surface and facilitate a high polish. (b) The chalcedony-rich ‘confetti’ material from this locality, such as this cabochon (27 × 38 mm), is typically not treated in any way. Courtesy of Horizon Mineral Lapidary; photos by Joe Jelks.

by BHP and Aneka Tambang geologists in the 1990s explaining the copper anomaly as related to hydrothermal fluids leaching copper from cooling volcanic host rocks is unlikely due to the scale of copper enrichment there.

Author JI proposes that the large amount of copper (and silica) deposited in veins and breccias within andesite that experienced low-temperature (propylitic) alteration is related to a later volcanic event. The ascent of associated hypogene fluids could leach copper from sulphides in a buried porphyry deposit at depth. As these fluids rose to the surface, they could mix with descending oxygenated meteoric waters, causing oxidation of sulphides and depositing native copper and copper-bearing minerals in chalcedony. Specimens from the deposit commonly exhibit chrysocolla and malachite

around vein and breccia boundaries and fractures, which probably formed in a near-surface mixing zone. The flecks of chrysocolla in chalcedony may have originated during outflow of the fluids in a hot-spring environment near the surface.

Interestingly, a similar style of mineralisation has been drill-sampled and documented at the Kaputusan porphyry copper deposit, which is hosted by a volcanic suite of the same age on Bacan Island to the north of Obi Island. Kaputusan was discovered in the 1990s, and although the copper mineralisation proved uneconomic, local artisanal diggers continue to mine high-quality chrysocolla chalcedony there.

In the future, the more easily accessed near-surface portion of the Obi Island deposit will eventually be mined out, and the diggers will then migrate elsewhere. Meanwhile, the production of these interesting and colourful specimens for collectors and lapidaries should continue for at least the next few years.



**Figure 16:** This cabochon (30 × 40 mm) from Obi Island was cut in a West Java lapidary workshop and displays intricate patterns of native copper and chrysocolla in chalcedony. Photo by Rika Djasmin.

## REFERENCES

- Agustiyo, D.A. 1995. *The geology and tectonic evolution of the Obi region, eastern Indonesia*. MPhil thesis, University College London, 245 pp. (see pp. 111, 219–220 and 229–230), <https://discovery.ucl.ac.uk/id/eprint/10101177>.
- Anonymous 2015. Batu Bacan SBY untuk Obama, berjasa besar populerkan batu akik [SBY’s Batu Bacan for Obama, great service for popularising agate]. *Ekonomi*, <https://tinyurl.com/p2xer7pk>, 13 June, accessed 23 February 2023.
- Einfalt, H.C. & Sujatmiko, H. 2006. Chrysocolla quartz from the Bacan Archipelago, South Halmahera Regency, North Maluku Province, Indonesia. *Journal of Gemmology*, **30**(3), 155–168, <https://doi.org/10.15506/JoG.2006.30.3.155>.
- Laurs, B.M. 2018. Gem Notes: Copper-bearing opal from West Java, Indonesia. *Journal of Gemmology*, **36**(1), 10–11.

Laurs, B.M. 2022. Gem Notes: Copper-bearing silicified wood from Indonesia. *Journal of Gemmology*, **38**(4), 321–322.

Prihatmoko, S. & Nugroho, F.E. 1998. Tertiary volcanic and intrusive rocks in Obi Islands, Maluku, Indonesia, and related hydrothermal mineralizations. *Prosiding Pertemuan Ilmiah Tahunan XXVII*, Yogyakarta, Indonesia, 8–9 December, 1–29–1–45.

Renfro, N. 2022. G&G Micro-World: Copper “confetti” inclusions in chalcedony. *Gems & Gemology*, **58**(4), 490–491.

van der Ent, A., Baker, A.J.M., van Balgooy, M.M.J. & Tjoa, A. 2013. Ultramafic nickel laterites in Indonesia (Sulawesi, Halmahera): Mining, nickel hyperaccumulators and opportunities for phytomining. *Journal of Geochemical Exploration*, **128**, 72–79, <https://doi.org/10.1016/j.gexplo.2013.01.009>.

van Leeuwen, T. 2018. *25 Years of Mineral Exploration and Discovery in Indonesia*. Masyarakat Geologi Indonesia, Jakarta Selatan, Indonesia, 319 pp. (see pp. 62–63, 101–102 and 146).

### The Authors

#### Joel Ivey

Geologist, [www.IndoAgate.com](http://www.IndoAgate.com),  
Bangkok, Thailand  
Email: [jaivey@attglobal.net](mailto:jaivey@attglobal.net)

#### Brendan M. Laurs FGA

Gem-A, 1106 2nd St. #317, Encinitas,  
California 92024, USA

### Acknowledgements

The authors thank those who made it possible to document this remote mining activity during a difficult period while the world was locked down during the COVID-19 pandemic. Djasmin (who, like most in Java, goes by only one name),

Dace Irwan, Yusef Sulaeman, Dade Dialami, Dan Norquist and Rika Djasmin were instrumental in providing photographs, information and performing the legwork. Specimens for research were kindly donated by James Walker (Ikon Mining & Exploration, Fallbrook, California, USA) and by Greek gem explorer Yianni Melas and stone dealer Avant Chordia (Guman Impex Pvt Ltd, Jaipur, India). Dr George R. Rossman (California Institute of Technology, Pasadena, California, USA) is thanked for performing Raman analyses to confirm the identity of minerals present in those samples. Thanks also to Joe Jelks (Horizon Mineral Lapidary, Lewes, Delaware, USA) and Bud Standley (Poway, California, USA) for supplying information and photos.

## Gem-A: over **110 years of experience** in gemmology education

Our FGA and DGA Members are located around the world – join them by studying with Gem-A

**STUDY  
IN ONE  
OF THREE  
WAYS**

At Gem-A HQ  
London



Worldwide at one  
of our ATC's



Online with  
practical lab classes  
in your area



**Find out more by contacting: [education@gem-a.com](mailto:education@gem-a.com)**

*Creating gemmologists since 1908*





# Conferences

## AGA TUCSON CONFERENCE

The 2023 Accredited Gemologists Association (AGA) Conference in Tucson, Arizona, USA, took place on 1 February and was attended by 136 people from 11 countries. The event was moderated by AGA president **Teri Brossmer** (Gem Appraisals Unlimited LLC, Glendora, California, USA) and featured six presentations.

The conference was opened by **Teri Brossmer**, and then AGA Diamond Sponsor **Art Samuels** (EstateBuyers.com, Miami, Florida, USA) gave some remarks on various topics related to diamonds.

The first presenter was **Meg Berry** (Megagem, Fallbrook, California), who described how she evaluates gem rough for her carvings, cabochons and faceted stones. For pleochroic gem materials, it is important to first find the direction that will display the best colouration (i.e. using a polariscope and dichroscope), and then decide on the shape of the piece. For carvings, she sometimes performs initial faceting to optimise the optics of the piece and then proceeds to complete the carving. For faceted stones, she prefers to cut the table facet first, then attach the table to the dop in order to cut the pavilion (shaping it from girdle to culet), and finally cut the crown.

**Bill Larson** (Pala International, Fallbrook) chronicled the history and mining of gem tourmaline in Pala, San Diego County, California. He focused on four mines: the Stewart Lithia, Pala Chief, Tourmaline Queen and Tourmaline King. In November 1971, his company made a particularly important discovery at the Queen mine, where they found a large cavity containing 37 crystal specimens of ‘blue-cap’ tourmaline (rubellite with distinctive shiny blue terminations), some of which were world class. More recently (since January 2022), extensive tunnelling at the King mine by another group has produced some attractive crystals and gem rough (see *The Journal*, Vol. 38, No. 3, 2022, pp. 221–222).

The conference then shifted to a live-stream interview with well-known gemmologist **Alan Hodgkinson** at his home in Scotland (Figure 1). This Q&A session was moderated by **Dr Çiğdem Lüle** (Kybele LLC, Buffalo Grove, Illinois, USA) and **Stuart Robertson** (Gemworld International Inc., Glenview, Illinois), who also took questions from the audience. Hodgkinson emphasised

the importance of education, and also observed that it is possible to learn more while sharing your gem knowledge with others.

Next, the AGA board members for 2023–2026 were introduced. These include executive officers **Teri Brossmer**, **Dr Çiğdem Lüle**, **Heidi Harders**, **Adam Ostrow** and **Stuart Robertson**, as well as governors **Gina D’Onofrio**, **Donna Hawrelko**, **Antoinette Matlins**, **Alberto Scarani**, **Gary Roskin** and **Martin Fuller**.

The afternoon session was kicked off by **Robert Weldon** (Gemological Institute of America, Carlsbad, California), who covered digital photography of gemstones and jewellery. In addition to reviewing camera types and the best settings for gem photography, he explained the intricacies of proper lighting for a variety of situations, as well as the use of digital ‘photo-stacking’ software to maximise the depth of field. As a general rule, he suggested using a simple background for a complex subject, and ensuring that there is some tonal contrast between the background and subject.

**Gary Roskin** (*Roskin Gem News Report*, Exton, Pennsylvania, USA) explored the international gem trade-show business. He explained the evolution of various shows, including those in Denver (Colorado, USA) and Tucson, as well as JA New York (USA), Baselworld and GemGenève (both in Switzerland). He predicted that to be successful in the future, shows will need to take a hybrid approach, utilising technology such as live-streaming, webinars, virtual events and simultaneous translation, as well as an online marketplace.

**Dr Clemens Schwarzing** (Johannes Kepler University Linz, Austria; Figure 2) explored the colouration, chemical composition and cutting of tanzanite and fancy-colour zoisite. Vanadium is responsible for blue, manganese for pink, and titanium for yellow to greenish colouration, but the mechanism associated with Ti is unknown. Because the yellow component is removed by heat treatment to 400–550°C, such stones will always appear dichroic rather than trichroic, although naturally heated tanzanite can also show this appearance.

Simultaneous afternoon breakout sessions were hosted by **Sarah Caldwell Steele** on Whitby jet, **Richard**



**Figure 1:** Dr Çiğdem Lüle and Stuart Robertson conduct a live-stream interview with Alan Hodgkinson. In addition to asking some prepared questions, they took queries from the audience. Photo by B. M. Laurs.



**Figure 2:** Dr Clemens Schwarzingler explains the relationship among colour, chemical composition and cutting in tanzanite and fancy-colour zoisite. Photo by B. M. Laurs.



**Figure 3:** Previous Bonanno Award winners who attended this year's AGA Gala include (from left to right) Stuart Robertson, Thom Underwood, Robert Weldon, Richard Drucker, Dr Jim Shigley, Antoinette Matlins, Gary Roskin (2022 awardee), Shane McClure, Donna Hawrelko, Richard Hughes, Dr Çiğdem Lüle, Mikko Åström, John Koivula and Alberto Scarani. Photo by B. M. Laurs.

**W. Hughes** on jade identification, and **Kerry Gregory** on how to quickly and efficiently separate the more valuable items recovered from scrapped jewellery.

The AGA Gala took place that evening, and approximately 170 people attended. **Gary Roskin** was honoured

as the recipient of the 2022 Antonio C. Bonanno Award for Excellence in Gemology, and several previous Bonanno Award winners were also present at this year's gala (Figure 3).

*Brendan M. Laurs FGA*

# Gem-A Notices

## MESSAGE FROM GEM-A CEO ALAN HART



I hope you have had a good start to the year. It has certainly been a busy and exciting start for Gem-A. Firstly, I would like to thank you for renewing your Gem-A Membership, and I hope you continue enjoying the many benefits

of being a Gem-A Member as part of our diverse and global gemmology community. I was excited to read this current issue of *The Journal*, and I am sure you will enjoy it too, with feature articles on the historic Imperial Crown of the Holy Roman Empire, an exciting new find of Co-bearing spinel from Tanzania, a new variety of nephrite jade from Washington State (USA), and a beautiful and diverse suite of copper minerals in chalcedony from Indonesia.

Following the success of the Gem-A Conference last year, I am very pleased to announce that we are planning to again host an in-person event this year. The conference will take place Sunday, 5 November 2023, at etc.venues County Hall in central London. In addition, tours and workshops will be available on Monday,

6 November, and a Graduation Ceremony for our students will also take place on the evening of 6 November. I look forward to catching up with our very knowledgeable and passionate Members—and our students—at this important educational and networking event.

With travel restrictions being eased around the world, I attended the Tucson gem and mineral shows in February this year, and it was wonderful to see many industry friends and colleagues. We were delighted to once again deliver the Gem-A bash, this year in collaboration with the Accredited Gemologists Association and the Canadian Gemmological Association. I would personally like to thank 100% Natural Ltd (New York, USA) for their sponsorship of the event.

Also in February, many of our students took the Gem-A Foundation and Diploma examinations. We all know the amount of hard work and commitment that goes into successfully completing the Gem-A examinations. My best wishes to all students who took their exams in February and are awaiting their results.

As always, I would like to acknowledge and thank our Members for their ongoing support. Here's to seeing old faces—and meeting new ones—in the months to come!

## MEMBERSHIP RENEWAL

We thank our valued Members for renewing their Gem-A Membership. Benefits include the use of your post-nominals, access to eight publication issues a year—including the prestigious *Journal of Gemmology* and insightful *Gems&Jewellery*—and a discount on all Gem-A events, as well as Gem-A instruments and equipment. You may also access your Membership logo from the Members' area of the Gem-A website, and have your name listed in the online FGA/DGA register. If you require assistance with your membership, please email [membership@gem-a.com](mailto:membership@gem-a.com).

### Gem-A Membership





## GIFTS TO THE ASSOCIATION

Gem-A is most grateful to the following for their generous donations that will support continued research and teaching:

**Andrew Hyde**, UK, for donating a Rayner refractometer that belonged to his late mother Sylva Hyde (nee Warnes) FGA. It was awarded to his mother as the winner of the Rayner Prize for her Diploma examinations in 1949.

**Joe Jelks**, Horizon Mineral Lapidary, USA, for donating several sawn pieces of chalcedony containing copper-mineral inclusions from Obi Island, Indonesia.

**Jean-Pierre (JP) Jutras**, Jade Leader, Canada, for donating two polished pieces of nephrite jade and two polished pieces of rhodonite from the DJ project in Washington State, USA.

**Brendan M. Laurs** FGA, USA, for donating two reference books, *Simon & Schuster's Guide to Rocks & Minerals* and *Guide to Gems & Precious Stones*.

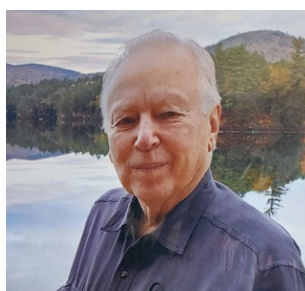
**Yianni Melas** (Greek gem explorer) and **Avant Chordia** (Jaipur, India) for donating five cabochons of chalcedony containing copper-mineral inclusions from Obi Island, Indonesia.

**Helen Serras-Herman** FGA, USA, for donating a copy of her 2022 book, *Carved Gems – Inspiration and Expertise*.

## OBITUARIES

### Dr Donald Hoover FGA

1930–2023



Donald Hoover DSC, FGA, FGAA, GG passed away on 22 January 2023. He was 92, although he still had plenty of energy and enthusiasm. Nothing else enthused him as much as geological and gemmological discovery,

whether it was opening new frontiers or re-discovering a lost technique.

Don was born on 17 June 1930 in Cleveland, Ohio, USA. As a young man, hikes looking for rocks with his father planted his long-time love of geology and minerals. He initially followed in his father's footsteps, becoming an electrical engineer, with his undergraduate studies completed at Case Western Reserve University in Cleveland, followed by a Master's degree at the University of Michigan, USA. After a brief stint with the U.S. Army, he then went on to his true calling in geophysics, completing his 'Doctor of Science' at Colorado School of Mines in Denver, Colorado, USA. At the time, because it was not a liberal arts school, a PhD was not considered the appropriate qualification, but as Don was all about science and not much for philosophy, this suited him well.

After graduating, he went on to a long career with the U.S. Geological Survey. His work with the Survey

covered seismology, volcanology, geothermal energy and nuclear waste disposal. It took him to numerous parts of the USA, including Alaska and Hawaii, as well as internationally to the Azores and Brazil. In Brazil he developed a long-lasting love for its geology, gems, natural history, people, language and food. His interest in gems led him to become a GG as well as an FGA. He was later awarded an honorary FGAA by the Gemmological Association of Australia. He inspired and mentored many younger gemmologists and was always willing to contribute to education. In retirement, he continued his gemmological research and writing, and he volunteered at local rock clubs and the Missouri Institute of Natural Science Museum, USA. He had a gift for explaining complex scientific concepts in a manner anyone could understand and treated no question as beneath him.

Don leaves behind a sizeable list of publications. He authored and co-authored numerous articles in various gemmological journals (as early as 1982 in *The Journal*) on topics such as refractometers, crossed-filter techniques, thermal properties of gems, magnetic susceptibility, dispersion, Cr-related fluorescence, dichromatism, colour change, Ethiopian opal, garnets and Brazilian diamonds. His final studies were dedicated to new theories on the genesis of Brazilian diamonds, which should be published in the near future.

**Cara Williams** FGA and **Bear Williams** FGA  
Stone Group Laboratories  
Jefferson City, Missouri, USA

## Christine Marie Woodward FGA 1943–2023



Chris Woodward FGA enjoyed both art and science, particularly the study of gemstones, until she was almost 80 years old. She was my most long-standing colleague, as she was already in the hydrogeology department of the

British Geological Survey (BGS) at South Kensington when I joined in 1965, where she was involved in early hydrogeological monitoring preparatory to the building of the Thames Barrier.

As she had received good training in both geology and the arts, and had enjoyed an Open University planetary science course, she was well placed to join me after I had moved to the Geological Museum, another BGS department, where she could put her talents to good use producing exhibitions and publications. Chris was an invaluable member of the team, with her curatorial skills and ability to interpret concepts and produce

concise writing aimed at the general public.

Chris studied gem materials at the Geological Museum since the 1970s, and produced all of the attractive descriptions of gem crystals with rough and cut stones in the display cases. Practical hands-on gemmology was bolstered by her work at Mrs Chang's renowned bead shop in West London for a few years. She co-authored *Gemstones* in the Museum's booklet series produced by Her Majesty's Stationery Office.

Chris was a member of the Gemmological Association of Great Britain (later renamed Gem-A), becoming a Fellow in 1980 and a Diamond Member in 1982. Chris joined Gem-A's Board of Examiners as a Diploma Theory Examiner and later acted as Chief Examiner. The Association benefitted greatly from her blend of detailed knowledge, meticulous care and dedication to the promotion of quality education.

I for one shall miss Chris's sense of humour, her quiet way of summing up situations, and her depth and breadth of useful scientific knowledge. I shall also miss her infectious laugh.

**Ian Mercer FGA**

Former Gem-A Director of Education  
Essex, United Kingdom



**Gem-A**  
THE GEMMOLOGICAL ASSOCIATION  
OF GREAT BRITAIN

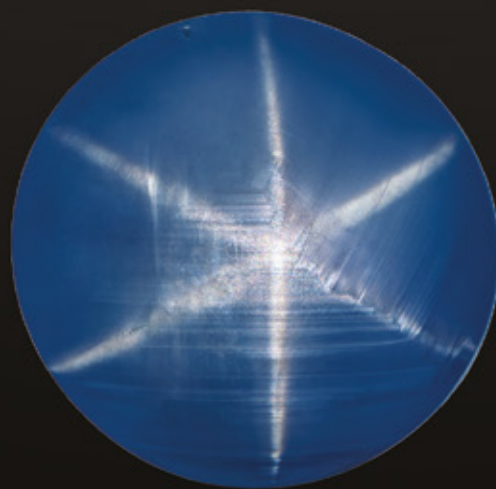
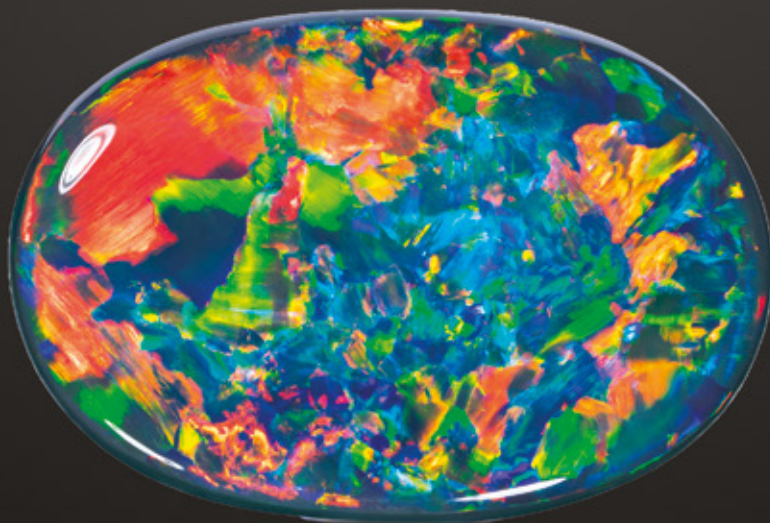
## Study gemmology online!

- Online class groups
- Virtual learning
- Interactive quizzes
- Start your journey to FGA Membership with online learning by leading provider, Gem-A



Contact [education@gem-a.com](mailto:education@gem-a.com) for more information

# SUPERNATURAL GEMS™



100%  
*Natural Ltd*

x

NASSI

 @GEMCOLLECTOR

VISIT US AT GEMGENÈVE

GEMSTONE PHOTO CREDIT: JEFF MASON PHOTOGRAPHY



# Learning Opportunities

## CONFERENCES AND SEMINARS

### 2023 Rochester Mineralogical Symposium

21–23 April 2023

Rochester, New York, USA

<https://www.rasny.org/mineral-section>

### Nineteenth Annual Sinkankas Symposium:

#### San Diego County Gems and Minerals

22 April 2023

Carlsbad, California, USA

<https://sinkankassymposium.net>

### Scottish Gemmological Association Conference

28 April–1 May 2023

Cumbernauld, Scotland

<https://www.scottishgemmology.org/conference-2023>

### American Gem Society Conclave

1–3 May 2023

Louisville, Kentucky, USA

<https://www.americangemsociety.org/conclave-2023>

### 18th Annual Conference of the Association for the Study of Jewelry and Related Arts

6–7 May 2023

Online

<https://www.jewelryconference.com>

### TECHNART 2023: International Conference on Analytical Techniques in Art and Cultural Heritage

7–12 May 2023

Lisbon, Portugal

<https://technart2023.com>

### First National Workshop on Fluid and Vitreous Inclusions

10–11 May 2023

Palermo, Italy

Email: [francescomarialoforte@gmail.com](mailto:francescomarialoforte@gmail.com)

### GemGenève

11–14 May 2023

Geneva, Switzerland

<https://gemgeneve.com>

*Note:* Includes a seminar programme

### Gemmological Association of Australia 76th Annual Federal Conference

19–21 May 2023

New South Wales, Australia

<https://www.gem.org.au/events>

### GAC-MAC-SGA Sudbury 2023

24–27 May 2023

Sudbury, Ontario, Canada

<https://event.fourwaves.com/Sudbury2023/pages>

*Session of interest:* Cratons, Kimberlites, and Diamonds

### JCK Las Vegas

2–5 June 2023

Las Vegas, Nevada, USA

<https://lasvegas.jckonline.com>

*Note:* Includes a seminar programme

### Sainte-Marie-aux-Mines Mineral & Gem Show

21–25 June 2023

Sainte-Marie-aux-Mines, France

<https://www.sainte-marie-mineral.com>

*Note:* Includes a seminar programme

### Jewellery & Gem Asia Hong Kong

22–25 June 2023

Hong Kong

<https://jga.exhibitions.jewellerynet.com>

*Note:* Includes a seminar programme

### NAJ Summit

24–26 June 2023

Northampton, East Midlands

<https://www.naj.co.uk/summit-2023>

### V National Conference of Gemmology

26–27 June 2023

Rome, Italy

<https://www.rivistaitalianadigemmologia.com/en/v-national-conference-of-gemmology-rome-2023>

**International Gemmological Research Industries – NCJV Conference**

30 June–3 July 2023

Brisbane, Australia

<https://ncjv.com.au/international-gemmological-research-industries-ncjv-conference>**Goldschmidt 2023**

9–14 July 2023

Lyon, France, and online

<https://conf.goldschmidt.info/goldschmidt/2023/meetingapp.cgi> *Session of interest:* The Awesome Foursome: Volatiles, Intraplate Magmatism, Mantle Metasomatism and Diamonds**Initiatives in Art and Culture's 13th Annual International Gold and Diamond Conference**

17–19 July 2023

New York, New York, USA

<https://artinitiatives.com/2023-gold-diamond-conference-maintaining-purpose>**Turquoise United 2023**

10–12 August 2023

Albuquerque, New Mexico, USA

<https://www.turquoiseunited.com>*Note:* Includes a seminar programme**2023 Chicago Responsible Jewelry Conference**

11–12 August 2023

Chicago, Illinois, USA

<https://chiresponsiblejewelryconference.com>*Note:* An accompanying 'responsible gem boutique' will be held 13 August.**Kimberley International Diamond Symposium**

23–27 August 2023

Kimberley, South Africa

<https://sadpo.co.za/symposium>**24th Federation for European Education in Gemmology (FEEG) Symposium**

3 September 2023

Barcelona, Spain

<http://www.feeg-education.com/symposium>**International Conference on the Application of Raman Spectroscopy in Art and Archaeology**

6–9 September 2023

Athens, Greece

<https://www.raa2023.ugent.be>*Note:* A pre-conference Raman Spectroscopy Training School will take place on 4–5 September and will include a session titled 'Application on Gemstones and Data Processing'.**Bangkok Gems & Jewelry Fair**

6–10 September 2023

Bangkok, Thailand

<https://www.bkkgems.com>*Note:* Includes a seminar programme**Maine Pegmatite Workshop**

6–10 September 2023

Bethel, Maine, USA

<http://www.maine-pegmatite-workshop.com>**JVA Registered Valuer Conference**

8–10 September 2023

Loughborough, Leicestershire

<https://thejva.org/jewellery-watch-valuer-conference>**33rd International Conference on Diamond and Carbon Materials**

10–14 September 2023

Palma, Mallorca, Spain

<https://www.elsevier.com/events/conferences/international-conference-on-diamond-and-carbon-materials>**HardRock Summit 2023**

15–18 September 2023

Denver, Colorado, USA

<https://hardrocksummit.com>*Note:* Includes a seminar programme**Jewellery & Gem World Hong Kong**

18–24 September 2023

Hong Kong

<https://jgw.exhibitions.jewellerynet.com>*Note:* Includes a seminar programme**13th Annual Portland Jewelry Symposium**

24–26 September 2023

Portland, Oregon, USA

<https://portlandjewelrysymposium.com>**20th Rendez-Vous Gemmologiques de Paris**

September 2023 (exact dates TBA)

Paris, France

<https://www.afgems-paris.com/rdv-gemmologique>

**86th Annual American Society of Appraisers (ASA) International Conference**

1–3 October 2023

New Orleans, Louisiana, USA, and online

<https://www.appraisers.org/asa-international-conference>**International Conference on Applied Mineralogy and Minerals (ICAMM 2023)**

9–10 October 2023

New York, New York, USA

<https://waset.org/applied-mineralogy-and-minerals-conference-in-october-2023-in-new-york>*Theme of interest:* Industrial Minerals, Gems, Ores, and Mineral Exploration**37th International Gemmological Conference**

23–27 October 2023

Tokyo, Japan

<https://www.igc-gemmology.org/igc-2023>*Note:* Includes a pre-conference jadeite excursion and a post-conference pearl excursion**Gem-A Conference**

5 November 2023

London

Email: [events@gem-a.com](mailto:events@gem-a.com)*Note:* Workshops and field trips (and a graduation ceremony for Gem-A students) will take place on 6 November.**GemGenève**

November 2023 (exact dates TBA)

Geneva, Switzerland

<https://gemgeneve.com>*Note:* Includes a seminar programme**AGTA Gemfair Tucson**

30 January–4 February 2024

Tucson, Arizona, USA

<https://agta.org/agta-gem-fair-tucson>*Note:* Includes a seminar programme**Tucson Gem and Mineral Show**

8–11 February 2024

Tucson, Arizona, USA

<https://www.tgms.org/show>*Note:* Includes a seminar programme**Inhorgenta Munich**

16–19 February 2024

Munich, Germany

<https://inhorgenta.com/en>*Note:* Includes a seminar programme**OTHER EDUCATIONAL OPPORTUNITIES****Gem-A Workshops and Courses**

Gem-A, London

<https://gem-a.com/education>**GemIntro Course**

Gem-A, online

<https://gemintro.gem-a.com>**Gemstone Safari to Tanzania**

5–22 July 2023 and 10–27 January 2024

<https://www.free-form.ch/tanzania/gemstonesafari.html>**Lectures with The Society of Jewellery Historians**

Society of Antiquaries of London, Burlington House

[https://www.societyofjewelleryhistorians.ac.uk/current\\_lectures](https://www.societyofjewelleryhistorians.ac.uk/current_lectures)

- Estelle Ottenwelter—Insight into Early Medieval Elite Jewellery from Bohemia  
23 May 2023
- Natasha Awais-Dean—Jewels Captured in Perpetuity: The Jewellery Book of Anne of Bavaria  
27 June 2023
- Sébastien Aubry—Greek and Latin Inscriptions on Antique Engraved Gems and Rings  
26 September 2023
- Cordelia Donohue—New Research on Tuareg Jewellery, and Kathleen Walker-Meikle—Pet Bling: Jewelled Animal Accessories in the Late Medieval and Early Modern Period  
24 October 2023
- John Benjamin—Jewellery from Anglesey Abbey  
28 November 2023



# Over 110 years of experience in gemmology education

**Our FGA and DGA Members are located around the world  
– join them by studying with Gem-A in one of three ways**

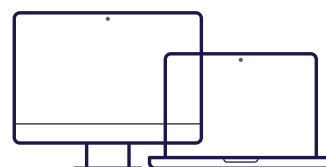
**AT GEM-A HQ**  
London



**WORLDWIDE**  
at one of our ATC's



**ONLINE**  
with in-person  
practical lab classes



**Find out more by contacting: [education@gem-a.com](mailto:education@gem-a.com)**

## Buy Gem-A Instruments online



**OVER 100  
PRODUCTS  
AVAILABLE**

View the full collection and offers at: **[shop.gem-a.com](http://shop.gem-a.com)**



# Gem-A

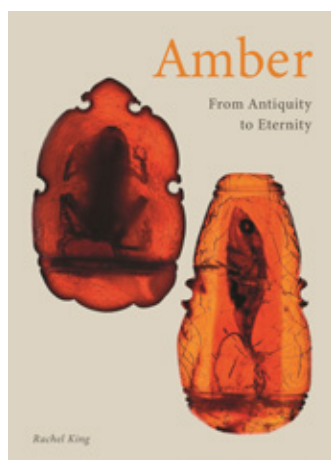
THE GEMMOLOGICAL ASSOCIATION  
OF GREAT BRITAIN



Gem-A, 21 Ely Place, London, EC1N 6TD, UK  
+44 (0)20 7404 3334 [www.gem-a.com](http://www.gem-a.com).  
Registered charity no. 1109555

CREATING GEMMOLOGISTS SINCE 1908

# New Media



## Amber: From Antiquity to Eternity

By Rachel King, 2022. Reaktion Books Ltd, London, <https://press.uchicago.edu/ucp/books/book/distributed/A/bo184798233.html>, 272 pages, illus., ISBN 978-1789145915, e-ISBN 978-1789145922 (ePub) or e-ISBN 978-1789145922 (PDF). GBP30.00 hardcover or eBook.

**M**any books have been written about amber, but this is the first one that this reviewer has come across that concentrates almost exclusively on the history of the material. It is not a standard gemmological reference book. There is some information on the physical and chemical aspects of amber, but that is secondary to the tale. As the author writes in the first paragraph, ‘This book is about the fascination and excitement surrounding amber and how it has attracted people of all backgrounds down the Ages.’ It is a very well-researched, comprehensive study of this beautiful gem, from thousands of years ago to the present day. It is well written in a style that is informal and very readable.

The book is divided into eight chapters covering various aspects of amber, and each one is subdivided into specific subjects. The extensive references are clearly marked in the text and are listed chapter by chapter at the end of the book. The text is illustrated with numerous good-quality photos, plus reproductions of maps and old prints.

The first chapter, ‘Amber: What, Where, When?’, is the most scientific one, giving a brief but concise explanation of what amber is. It deals with the definitions of the material, ancient and modern, and how it took hundreds of years of speculation to realise that amber

is a several-million-years-old plant resin. It looks at why some resins mature into copal and others amber, along with their various origins. Inclusions are discussed, as are the efforts to extract DNA from them.

Chapter 2, ‘Legend and Myth’, examines how people have admired amber for millennia. It further describes the conundrum posed by amber’s origins and some of the early beliefs, recounting the Greek tale of Phaeton’s chariot ride and the Tears of the Heliades, as well as the Lithuanian tale of Kastytis and Jūratė.

In Chapter 3, ‘Ancestors and Amber’, the author describes how amber has been regarded and used over the past 40,000 years, not only in Europe but also in other places such as China and the Middle East, and how it was traded far afield. Still not understanding the true origins of amber, many believed it to be connected to the sun, while others thought it was urine from a male lynx. But whatever the belief, it has been widely used for devotional objects for many centuries.

Chapter 4, ‘Unearthing Amber’, starts with Pliny the Elder, who came closest to understanding that amber was a plant resin, although not its age. As the title suggests, the chapter deals with methods of amber extraction, from fishing and diving to modern commercial mining, as well as the dangers involved. The extraction of amber was very closely guarded in northern Europe 600 years ago, and the act of collecting or trading it without permission could be punished by death.

Chapter 5, ‘Making and Faking’, begins with a 1,800-year-old Chinese recipe for faking amber, based on eggs. It goes on to describe the many colours and diaphaneities of true amber, and the difficulty of replicating its colour, weight and smell—problems that persisted until the advent of early plastics. Faked inclusions have been documented from the mid-nineteenth century, and a few notorious ones are mentioned.

In Chapter 6, ‘Accessorizing with Amber’, the author looks at amber as personal ornamentation in its various forms, from bead necklaces to sword hilts. She goes on to give examples of these various uses in different parts of the world where, in most cases, the amber was of Baltic origin, including some in India and China. The chapter also includes descriptions of trade, especially in the eighteenth century, and of amber being used for barter in Africa.

Chapter 7, ‘Artistic Ambers’, tells how, for thousands of years, amber has been used for works of art other than personal ornamentation. It has been used to make

free-standing carvings or as veneer or marquetry, often for devotional purposes. Large collections of beautiful artefacts were amassed, especially in the seventeenth century, by members of the nobility, and many of these collections were later passed to museums.

Chapter 8, 'Lost Ambers', covers some of the amber artefacts that have been lost over time, sometimes because they have degraded or—as was the case with the famous Amber Room in Russia—as the result of war. Some collections have also been lost to fire. In the last part of this final chapter the author discusses a few of today's known amber deposits, along with the laws or political situations affecting the amber mines.

This book allows the reader a glimpse into how amber has been perceived by people who lived hundreds—and indeed thousands—of years ago. And while the reader might initially feel knowledgeable on the history of amber, this book will probably prove otherwise.

When researching for and subsequently writing a

book, it is always difficult to know what to leave out. Too much information or too many facts can lead to overload, with the result that they become a blur and are difficult to absorb. If this reviewer has one criticism of the book, it is that it contains a surfeit of facts and descriptions, especially in the last chapters, and while every single one is of interest in its own right, the sheer volume makes them difficult to absorb. Perhaps the book should not be read cover-to-cover, but slowly and with breaks, in order to better take in its content.

However it is read, though, this is a fascinating book and well worth obtaining. Rachel King has done an enormous amount of research and written an excellent book, and Reaktion Books has produced a high-quality publication. The book is an absolute must for people interested in amber.

**Maggie Campbell Pedersen**

London



## **A Brilliant Commodity: Diamonds and Jews in a Modern Setting**

By Saskia Coenen Snyder, 2022. Oxford University Press, Oxford, 320 pages, illus., ISBN 978-0197610473 or e-ISBN 978-0197610503, <https://doi.org/10.1093/oso/9780197610473.001.0001>. GBP26.99 hardcover or GBP22.99 eBook.

**T**he history of South Africa's 1870s diamond rush, and the economic and power struggles that rose in the 1880s, have been documented in dozens of books. In more recent times, the narrative has shifted from derring-do and empire-building to colonialism and exploitation. The author of *A Brilliant Commodity*, Saskia Coenen Snyder, who is associate professor of Modern Jewish History at

the University of South Carolina, USA, recounts the former while acknowledging the latter in the story of the roles played in those events by Jews from Europe. Dr Coenen Snyder has meticulously combed through official documents, family records and contemporary press reports to create an objective and thoroughly researched account of their activities during this pivotal time that created the modern jewellery industry.

The discovery of diamonds in what had been a neglected corner of the British Empire quickly transformed South Africa into, if not the jewel in the crown, at least a major side stone worthy of a bloody war. When the news of diamonds being discovered in Kimberley broke in 1869, Jews joined the teeming thousands of fortune seekers aiming to start a new, hopefully more prosperous, life at the diamond diggings. Many trekked there to dig for their fortunes, but joining them were members of merchant families who set up shipping, transport and financing services. These businesses not only supported the diamond miners but also established the channels that aided the growth and expansion of the British Empire, by connecting African sources to European finance and manufacturing entities, and finally to consumer markets in the U.S. and Europe.

As in Europe, however, Jews were not fully accepted by the empire they were helping to build. They were 'White, but not quite.' They weren't colonisers, but they also weren't the colonised. A fitting example is that of Barney Barnato (Isaacs), who became one of the richest



men in the world after selling his diamond-mining concessions to Cecil Rhodes, but was still not accepted as an equal by the colonial business community. And because of such exclusions, Jews operated within their own networks, dispatching family members to open businesses and financing houses in Kimberley and Cape Town.

Accordingly, Dr Coenen Snyder bases her narratives on the movements and activities of families: the van Wezels, who expanded their diamond-cutting business beyond Amsterdam to Antwerp and New York; the Mosenthals, who established shipping and finance offices in the Cape Colony, as it was then referred to; and Anton Dunkelsbuhler, a gem merchant and partner with Mosenthal who sent a distant relative named Ernest Oppenheimer to Kimberley to set up a branch office to acquire diamonds.

The first chapter relates the initial chaos of the South Africa diamond rush of the early 1870s, noting that black miners from nearby tribes made up the majority of the claim holders in one area until discriminatory laws forced them to give up their holdings. Jewish merchants were attracted to the Kimberley area, both to trade in diamonds and to supply the rush with essential commodities, often in exchange for rough diamonds, because at the time there was no ‘coin of the realm’ in that region. By the end of the 1870s, lack of local financing forced many claim holders to sell out to ‘companies’ buying up claims. One such ‘company’ was the partnership of Mosenthal and Dunkelsbuhler, who had access to capital through their London connections. At the same time, a young claim broker named Bernard Isaacs, who called himself Barney Barnato, also began buying claims. He raised money by putting all his profits into buying new claims, and then engaging relatives to set up diamond-trading operations in London to avoid selling cheaply to the local dealers. This set the stage for the famed epic battle between Barnato and Cecil Rhodes for control of Kimberley. Rhodes finally outmanoeuvred Barnato, thanks in large part to financing by Jewish financial houses, but the deal made Barnato one of the world’s richest men.

After Rhodes formed the De Beers Consolidated Mining Company in 1888, the chaos that had prevailed in the diamond rush now carried over into the marketplace, where millions of carats flooded an industry that had been built around extreme scarcity of product. Along with Barnato’s associates and relatives—Alfred Beit, Solomon (Solly) Joel and others—Rhodes further worked to regulate the supply of rough diamonds to the market by funnelling all sales to a syndicate of ten designated trading houses, all based in London. The

London syndicate would, in turn, sell rough to cutters in a measured, orderly manner. All of the syndicate houses were Jewish owned, with names familiar from the battle over control of Kimberley—Barnato, Dunkelsbuhler, Mosenthal and Beit among them. Chapter 2 tells how, with full control over mining and distribution of South Africa’s diamonds in hand, De Beers and the syndicate squeezed supplies when they wanted to raise prices, creating extreme hardship within the large Jewish community in Amsterdam.

The third chapter describes the efforts of diamond worker Henri Polak, as antagonist to the owners of the cutting factories, who were often Jewish, to fight for better working conditions for the polishers. But their fortunes continued to rise or fall on the syndicate’s whims. Polak, however, eventually became a socialist labour leader and politician, active long enough to be seized by the Nazis in 1940. (He died in prison three years later.)

The remaining chapters follow the industry to New York, where a consumer buying boom was beginning in the USA. Jewish diamond dealers began opening facilities in that city, attracting so many Dutch workers that it became a second language of the jewellery district around Maiden Lane in Lower Manhattan. An 1894 tariff enacted by the U.S. Congress, which added 25% to the price of polished diamonds entering the country, hastened the emigration of Jewish-Dutch diamond workers to Maiden Lane factories.

The outsized involvement of Jews in the growing diamond industry played into the unfavourable anti-Semitic stereotypes held in Europe over the centuries. In South Africa, Jews were often handed the blame for much of the pervasive illicit diamond buying—trading stones purloined from diggings by miners or outright stolen from shipments. One of the chief targets of the anti-Semitic press was Barnato. Diamonds were, perhaps, a symbol of the British Empire’s might, but only after their Jewishness was polished away, as with the undesirable parts of a rough diamond.

All told, Dr Coenen Snyder’s work objectively relates how European Jews employed their families, and their commercial and financial networks, to bring South Africa’s diamonds to the world market. At the same time, however, they were opposed by other Jews who strove to wrest improved working conditions from their religious brethren, as well as by those who protested the syndicate’s stranglehold on supplies. All of this happened against the backdrop of anti-Semitic attitudes that equated diamonds with Jews, but consumers sought the commodity in spite of their prejudices. It is essential to mention again that the author builds the history from as

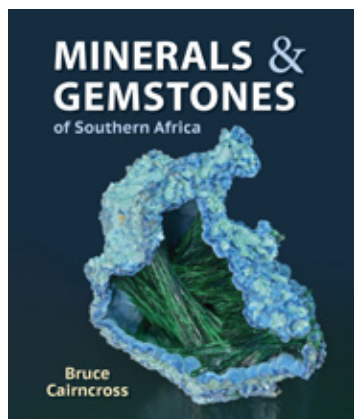
many objective, first-hand sources as possible—government and family records—to offer well-documented information, refraining from assumptions and biased points of view.

The author's scholarship is exceptional, the writing is

clear and concise, and the book is an essential account of that tumultuous time in history.

**Russell Shor**

Carlsbad, California, USA



## Minerals and Gemstones of Southern Africa

By Bruce Cairncross, 2022. Struik Nature, Cape Town, South Africa, <https://www.penguinrandomhouse.co.za/book/minerals-and-gemstones-southern-africa/9781775847533>, 296 pages, illus., ISBN 978-1775847533 or e-ISBN 978-1775847540. ZAR450.00 softcover or ZAR382.00 eBook.

**T**his publication is a complement to the author's *Minerals and Gemstones of East Africa* which was reviewed in *The Journal*, Vol. 37, No. 2, 2020. Similar in scope, this new book covers the basic geology and important localities of seven contiguous countries in southern Africa: Botswana, Eswatini (formerly Swaziland), Lesotho, (southern) Mozambique, Namibia, South Africa and Zimbabwe.

The minerals and gems are described alphabetically and illustrated with maps, diagrams and photographs. Many of the images were taken by the author himself, who is a renowned photographer of minerals and gems.

As he points out, 'During the past two decades, some southern African localities have impacted on the international mineral market by producing world-class specimens'. He also covers recent discoveries from other well-established mineral localities.

The book opens with an introduction, a two-page map showing the southern African region covered and a geological overview. This is followed by a brief description of each country in the region, with interesting observations and photos of each one. This reviewer has personally visited most of these countries and found that Cairncross is brilliant in succinctly describing their mineral legacies.

The alphabetical descriptions are arranged by mineral species, beginning on page 28 with aegirine and concluding on page 303 with zircon. To exemplify his statement about the past two decades producing incredible specimens, one mineral in particular is worth highlighting: page 174 shows world-class specimens of jeremejevite—figure 518 is of cut jeremejevite gemstones and figure 519 illustrates a jeremejevite crystal in matrix (unknown to most top mineral collectors).

The text on mineral species is followed with acknowledgements and a ten-page list of references. The book concludes with a comprehensive index.

I highly recommend this book for anyone who is serious about collecting minerals or gemstones. Taken together with his previous publication on East Africa, this book can familiarise the reader with nearly all of the gem and mineral commodities produced from this region of Africa.

**Bill Larson FGA**

Pala International, Fallbrook, California, USA

## Other Book Titles

### COLOURED STONES

#### Biominerals: Microbial Life in Agates and Other Minerals

By Marco Campos-Venuti, 2022. Edizioni DanzaSi,

Rome, Italy, 528 pages, ISBN 978-8894582789. EUR85.00 softcover.

#### Rubies and Implants: Aluminium Oxide and Its Diverse Facets

By Bozena Arnold, 2022. Springer, Berlin, Germany, viii + 97 pages, ISBN 978-3662661154 or e-ISBN 978-3662661161,

<https://doi.org/10.1007/978-3-662-66116-1>.  
USD29.99 softcover or USD19.99 eBook.

## CULTURAL HERITAGE

### **China Adorned: Ritual and Custom of Ancient Cultures**

By Deng Qiyao, 2023. Thames & Hudson, New York, New York, USA, 400 pages, ISBN 978-1760763015. USD70.00 hardcover.

### **Lapidarium: The Secret Lives of Stones**

By Hettie Judah, 2022. John Murray Press, London, 336 pages, ISBN 978-1529394948 or e-ISBN 978-1529394962. GBP20.00 hardcover or eBook.

### **Magic Rock Crystal**

By Manuela Beer, 2023. Hirmer Verlag GmbH, Munich, Germany, 448 pages, ISBN 978-3777440545. EUR55.00 hardcover.

### **Raman Spectroscopy in Cultural Heritage Preservation**

By Howell G. M. Edwards, Peter Vandenabeele and Philippe Colomban, 2023. Springer, Cham, Switzerland, xxxviii + 493 pages, ISBN 978-3031143786 (hardcover), 978-3031143816 (softcover) or e-ISBN 978-3031143793, <https://doi.org/10.1007/978-3-031-14379-3>. USD139.99 hardcover or USD109.00 eBook.

### **The Throne of the Great Mogul in Dresden: The Ultimate Artwork of the Baroque**

By Dror Wahrman, 2023. Yale University Press, New Haven, Connecticut, USA, 376 pages, ISBN 978-0300251937. USD40.00 hardcover.

## FAIR TRADE

### **Sustainable Jewellery: Principles and Processes for Creating an Ethical Brand**

By Jose Luis Fetolini, 2022. Hoaki Books, Barcelona, Spain, 204 pages, ISBN 978-8417656768. EUR27.00 softcover.

## GEM LOCALITIES

### **Frank C. Perham, Adventures in Maine Mining**

By Karen L. Webber, Raymond A. Sprague and William Skip Simmons, 2022. Rubellite Press, Cana, Virginia, USA, 200 pages, ISBN 978-0974061368. USD69.00 hardcover.

## GENERAL REFERENCE

### **Crystallography: Introduction to the Study of Minerals**

By Celia Marcos, 2022. Springer Nature, Cham, Switzerland, xv + 523 pages, ISBN 978-3030967826 or e-ISBN 978-3030967833, <https://doi.org/10.1007/978-3-030-96783-3>. USD109.99 hardcover or USD84.99 eBook.

### **Gemstones: Understanding, Identifying, Buying**

By Keith Wallis, 2023. ACC Art Books, Woodbridge, Suffolk, 160 pages, ISBN 978-1851496303. GBP20.00 hardcover.

## INSTRUMENTATION

### **Advances in Portable X-ray Fluorescence Spectrometry: Instrumentation, Application and Interpretation**

Ed. by B. Lee Drake and Brandi L. MacDonald, 2022. Royal Society of Chemistry, London, 547 pages, ISBN 978-1788014229, e-ISBN 978-1839162695 (PDF) or e-ISBN 978-1839162701 (ePub), <https://doi.org/10.1039/9781839162695>. USD275.00 hardcover or eBook.

### **Artificial Intelligence and Spectroscopic Techniques for Gemology Applications**

Ed. by Ashutosh Kumar Shukla, 2022. IOP Publishing Ltd, Glassfields, Bristol, 168 pages, ISBN 978-0750339254 or e-ISBN 978-0750339278, <https://doi.org/10.1088/978-0-7503-3927-8>. GBP120.00 hardcover or GBP99.00 eBook.

## JEWELLERY HISTORY

### **All the Queen's Jewels, 1445–1548: Power, Majesty and Display**

By Nicola Tallis, 2022. Routledge, New York, New York, USA, 360 pages, ISBN 978-1032065014 (hardcover), ISBN 978-1032065021 (softcover) or e-ISBN 978-1003202592. USD160.00 hardcover, or USD32.95 softcover or eBook.

### **Forever Jade: Chinese Jade Miniatures from Four Millennia**

Ed. by Alexandra von Przychowski, 2022. Scheidegger & Spiess, Zürich, Switzerland, 128 pages, ISBN 978-3039421022 (in English and German). CHF39.00 softcover.



## JEWELLERY AND OBJETS D'ART

### **B Is for Bvlgari: Celebrating 50 Years in America**

By Marion Fasel and Lynn Yaeger, 2022. Adventurine Limited Editions, New York, New York, USA, 96 pages, ISBN 979-8218012182. USD24.99 hardcover.

### **Cartier: 13 rue de la Paix**

By François Chaille, 2022. Flammarion, Paris, France, 268 pages, ISBN 978-2080280985 (English) or ISBN 978-2080281906 (French). EUR95.00 hardcover.

### **Cartier—Beautés du Monde: High Jewelry and Precious Objects**

By François Chaille, 2023. Flammarion, Paris, France, 256 pages, ISBN 978-2080287533. EUR95.00 hardcover.

### **Carved Gems: Inspiration and Expertise**

By Helen Serras-Herman, 2022. Gem Art Center (Rio Rico, Arizona, USA) and Xpo Press Inc. (Arvada, Colorado, USA), 160 pages, ISBN 978-0578323480. USD29.95 softcover.

### **Esther Brinkmann**

By Ward Schrijver, Philippe Solms, Fabienne X. Sturm and Elizabeth Fischer, 2022. Arnoldsche Art Publishers, Stuttgart, Germany, 208 pages, ISBN 978-3897906662. EUR38.00 hardcover.

### **Jewellery & Silverware Inspired by Architecture**

By Vicki Ambery-Smith, 2022. Unicorn Publishing Group, East Sussex, 144 pages, ISBN 978-1914414657. GBP30.00 hardcover.

### **Jewelry and Adornment of Libya**

By Hala Ghellali, 2023. Blikvelduitgevers Publishers, Zandvoort, The Netherlands, 288 pages, ISBN 978-9492940278. EUR45.00 hardcover.

### **Jewelry Guide: The Ultimate Compendium**

By Fabienne Reybaud, 2022. Assouline Publishing, New York, New York, USA, 324 pages, ISBN 978-1649800411. USD105.00 hardcover.

### **Jewels by Giulio Manfredi Celebrate Raphael: School of Light**

Ed. by Giulio Manfredi, Arnaldo Colasanti and Alberto Rocca, 2022. Silvana Editoriale, Milan, Italy, 113 pages, ISBN 978-8836652921. EUR38.00 hardcover.

### **New Brooches: 400 + Contemporary Jewellery Designs**

Ed. by Nicolás Estrada, 2022. Promopress, Barcelona, Spain, 240 pages, ISBN 978-8417656942. EUR27.00 softcover.

### **Tiaras: A History of Splendour**

By Geoffrey C. Munn, 2023. ACC Art Books, Woodbridge, Suffolk, 432 pages, ISBN 978-1788842129. GBP55.00 hardcover.

### **Tiffany & Co.: Vision and Virtuosity**

By Vivienne Becker, 2023. Assouline Publishing, New York, New York, USA, 256 pages, ISBN 978-1649800336. USD85.00 hardcover.

### **Yewn: Contemporary Jewels and the Silk Road**

By Juliet Weir-de La Rochefoucauld, 2023. ACC Art Books, Woodbridge, Suffolk, 276 pages, ISBN 978-1788841092. GBP75.00 hardcover.

## MISCELLANEOUS

### **Dans l'Intimité des Gemmes (The Intimacy of Gems)**

By Martine Philippe, 2022. Association Française de Gemmologie, Paris, France, 36 pages, no ISBN (in French). EUR18.00 softcover.

### **Le Musée de Minéralogie de L'École des Mines de Paris (The Mineralogy Museum of the School of Mines of Paris)**

By Didier Nectoux and Eloïse Gaillou, 2022. Gallimard (Collection Découvertes) and L'École, School of Jewelry Arts, Paris, France, 76 pages, ISBN 978-2072959431 (in French). EUR14.50 softcover.

### **Die Mysterien der Zeichen: Johannes Reuchlin, Schmuck, Schrift & Sprache**

Ed. by Matthias Dall'Asta, 2022. Arnoldsche Art Publishers, Stuttgart, Germany, 272 pages, ISBN 978-3897906709 (in German). EUR44.00 hardcover.

### **Rare Earth: Crystalline Treasures**

By Robert Lavinsky, Monica Kitt, Eugene Meieran and Thomas P. Moore, 2022. The Arkenstone Ltd, Dallas, Texas, USA, 85 pages, ISBN 979-8986166308. USD60.00 hardcover.

### **Vlad Yavorsky: A Gem Dealer's Story**

By Olena Levchenko with Vladyslav Y. Yavorsky, 2023. Yavorsky Co. Ltd, Hong Kong, 236 pages, ISBN 979-8218123857. USD200.00 hardcover.

# An innovator in gemstone reporting

• Identification of colored gemstones • Country of origin determination • Full quality and color grading analysis

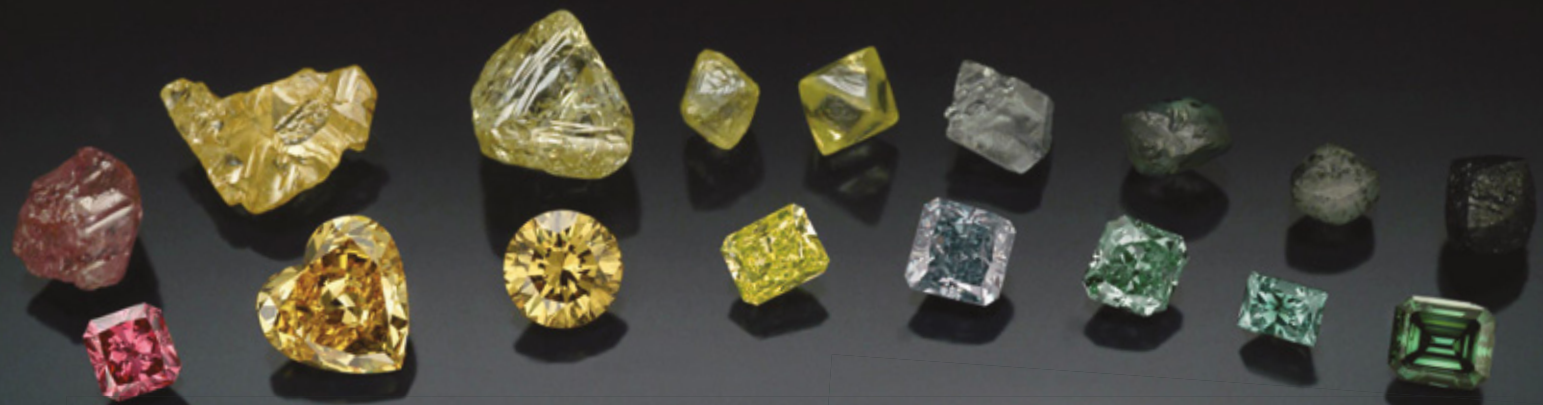


AMERICAN GEMOLOGICAL LABORATORIES

AGL

580 5th Ave • Suite 706 • New York, NY 10036, USA  
[www.aglgemlab.com](http://www.aglgemlab.com) • +1 (212) 704 - 0727





# REGISTER NOW!



## GemINTRO

*GemIntro* is a Level 2, online, entry-level course which will introduce you to the fascinating world of gemmology and the enormous variety of beautiful gems available. You can discover the basics of gemmology at your own pace - perfect for anyone looking to start or grow their career in the gems and jewellery trade, or for those completely new to gemmology and with an interest in gems.

Register now at [gem-a.com/gemintro](http://gem-a.com/gemintro)



### Gem-A

THE GEMMOLOGICAL ASSOCIATION  
OF GREAT BRITAIN





